# SYNTHESIS AND PROPERTIES OF SOME HIGH-SILICA ZEOLITES.

A thesis submitted to the University of Manchester
for the degree of Doctor of Philosophy
in the Faculty of Technology
by Elaine Mary Cooke.

Deparment of Chemistry
U.M.I.S.T.
1991

*This thesis is dedicated to my parents, Sheila and Leonard.*

No portion of the work referred to in this thesis has been submitted in support of an application for another degree or qualification at this or any other university or institute of learning.

Signed... E M Cooke

Date.... 30/7/91

## ACKNOWLEDGEMENTS.

I would like to thank my supervisor John Dwyer for his assistence during my Ph.D. research and I appreciate all the help given by past and present colleges in the zeolite research group at UMIST. In particular I thank Nic, Gaz, Arthur and Zhoa for all their help and support.

I am very grateful to Andy Wright for performing the EM studies in this thesis. I would also like to thank Ian Brough of the Material Science Dept at UMIST for the SEM studies and David Apperley for the MAS NMR work. I would also like to take this opportunity to thank my industrial supervisor David Walker and BP for financial support. I thank Dr.Ramdas for the theoretical studies and valuable discussions which were used in this work.

I thank my flat-mates Eevi, Daleen, Megan, Chris and Bella for their encouragment and support and I appreciate the guidence of Shen, throughout my Ph.D research.

To write a thesis is a difficult (heel moeilijk) time in anyone's life and without Edis it would have been much more distressing. Dus, hartelijk bedankt!!. Dank je wel voor de helpen, inspiratie, en motiverend fietsen.

## ABSTRACT

This thesis reports on the synthesis of several high-silica zeolites. In particular, the role of the organic additive during zeolite synthesis was studied. The structural character of pentasil zeolites was evaluated using several analytical and spectroscopic techniques.

From gels composed of TBP/DAO-$SiO_2$-$Na_2O$-$H_2O$ at 130°C silicalite-2, or at 175°C, ZSM-48 was synthesised. The optimum $OH^-/SiO_2$ ratio for both systems was 0.20. Reaction rates were enhanced when $Na^+$ ions were replaced by $K^+$ ions in the synthesis gel. At both 130°C and 175°C, with an initial $SiO_2/Al_2O_3$ ratio between 30-500, ZSM-11 was synthesised from gels containing DAO. In the $Na^+$ ion system with an initial $SiO_2/Al_2O_3$ ratio of 20, MOR, FER and ZSM-11 were obtained dependent upon the silica source. From the $K^+$ ion system, changes in the gel pH, dilution and reaction temperature resulted in the formation of TON, ZSM-5 or ZSM-11. In the absence of $M^+$ ions TON and ZSM-11 were synthesised from aluminous gels while ZSM-48 was obtained from an all-silica reaction system. On replacing DAO with TETA, DAH or DAB, zeolites TON, ZSM-5 and FER were synthesised, respectively. $^{13}C$, $^{15}N$ and $^{29}Si$ CP-MAS NMR revealed that DAO was incorporated into the zeolite pore system intact, either in a partially or fully protonated form, de pendent upon the zeolite framework and composition.

ZSM-11 and pentasil materials were synthesised from gels composed of DAO-, TBP-, TBA- and/or BAPZ-$SiO_2$-$Al_2O_3$-$Na_2O$. The pentasil content was dependent upon the nature of the organic additive and the reaction temperature. At 175°C the pentasil content increased from gels containing the organic additive in the order DAO>TBA>TBP>BAPZ. The product crystallinity increased from gels containing the organic additive in the order DAO≡TBP>TBA>BAPZ. In the mixed organic system DAO was preferentially incorporated into the zeolite pore system.

The structural content of ZSM-11, ZSM-5 and suspected intergrowths ECTBP and ECTBA were determined using a combination of analytical techniques. The phase purity was estimated using XRD, m-xylene adsorption and catalytic shape-selectivity. ECTBA and ECTBP had an intergrowth content between 20-40% and 70-90%, respectively. *In-situ* FTIR studies using the adsorption of pyridine and $H_2$ showed that the materials had equivalent Brønsted and Lewis acidity. Electron microscopy qualitatively distinguished intergrowths from physical mixtures. ECTBP was composed of ZSM-11 and ZSM-5 while ECTBA was made up of a broad range of random intergrowths. Electron diffraction, in contrast to x-ray data, revealed that ZSM-11 contained low levels of intergrowth. TEM studies and theoretical calculations were used to elucidate the polycrystallinity of the materials. This was related to the phase type and to the shape-selectivity in the methylation of p-xylene.

## LIST OF ABBREVIATIONS

Unless otherwise stated the following abbreviations will be used throughout this thesis:

| | | |
|---|---|---|
| atm | - | Atmosphere |
| BAPZ | - | N,N'Bis(3-aminopropyl)piperazine |
| BZA | - | British Zeolite Association |
| CP-MAS NMR | - | Cross-polarisation magic-angle-spinning nuclear magnetic resonance spectroscopy |
| DAB | - | Diaminobutane |
| DAH | - | Diaminohexane |
| DAO | - | Diaminooctane |
| DR | - | Double ring |
| ED | - | Electron diffraction |
| EM | - | Electron microscopy |
| FTIR | - | Fourier transform infrared |
| GLC | - | Gas liquid chromatography |
| HREM | - | High resolution electron microscopy |
| IR | - | Infrared |
| IZA | - | International Zeolite Association |
| $M^+$ ion | - | Inorganic metal cation |
| MR | - | Membered ring |
| PBU | - | Primary building unit |
| ppm | - | Parts per million |
| SBU | - | Secondary building unit |
| SEM | - | Scanning electron microscopy or micrograph |
| SR | - | Single ring |
| rpm | - | Revolutions per minute |
| T | - | Tetrahedra |
| TBA | - | Tetrabutylammonium |
| TBP | - | Tetrabutylphosphonium |
| TEM | - | Transmission electron microscopy |
| TETA | - | Triethylenetetraamine |
| TMS | - | Trimethylsilane |
| TPA | - | Tripropylammonium |
| WHSV | - | Weight hourly space velocity |
| XRD | - | X-ray diffraction |
| $\sigma$ | - | Mirror |
| i | - | Inversion |
| $2\Theta$ | - | Two theta |

## TABLE OF CONTENTS

### CHAPTER 1.

### General Introduction and Properties of Zeolites

## CHAPTER 2.

## Experimental Section

## CHAPTER 3.

## High-Silica Zeolite Synthesis Using 1,8-Diaminooctane as the Organic Additive



## CHAPTER 4.

## The Synthesis of ZSM-11 Using Several Organic Additives

## CHAPTER 5.

## The Characterisation of Pentasil Zeolites and Intergrowths

## CHAPTER 6.

## Future Work



## APPENDICES

# CHAPTER 1

## General Introduction and Properties of Zeolites

### 1.1. Introduction

Zeolites encompass a broad range of porous crystalline solids comprising of alumino-silicates of Group IA and Group IIA elements. The framework consists of an infinitely extended three-dimensional network of corner-sharing $SiO_4^{-4}$ and $AlO_4^{-5}$ tetrahedra (T). The structural formula of a zeolite is based on the crystallographic unit cell and is represented by:

$$M_{m/z}O \bullet [(AlO_2)_x(SiO_2)_y] \bullet qH_2O$$

where (x + y) is the total number of T per unit cell. M is the exchangeable cation with valency z and q is the amount of water per unit cell. In the case of high-silica zeolites y/x can vary between 20 to over 1000. The $SiO_2/Al_2O_3$ ratio is always equal to or greater than two. This is a consequence of Loewenstein's Rule [1]. Inorganic and/or organic cations are required to preserve charge-neutrality to compensate for the replacement of $Si^{+4}$ by $Al^{+3}$ T units. The cations M are mobile and may undergo ion-exchange. Water may be reversibly removed by the application of heat, which leaves the crystalline host structure intact. The void volume consists of regular micropores and cages which may amount to 50% of the crystals by volume. The zeolite framework should be viewed as somewhat flexible. The size and shape of the pore system responds to changes in temperature and interaction with guest molecules.

As a result of the physical and chemical nature of zeolites a number of properties and characteristics arise [2] such as:

- reversible water loss,
- thermal framework stability,
- cationic exchange capabilities,
- Brønsted and Lewis acidity,
- adsorption of gases and vapours,
- conductiometric abilities.

## 1.2. Zeolite Classification and Structure

### 1.2.1. The Building Units of Zeolite Frameworks

Over 50 topologically distinct, naturally occurring and synthesised zeolites are known [3]. They exhibit pore sizes from 0.3nm to 1.5nm comparable to the sizes of small hydrocarbons such as $C_1$ to $C_6$ alkanes. Breck [4] first proposed a method of classifying zeolite frameworks based on common subunits. The primary building unit (PBU) is a tetrahedron, centered on either a silicon or aluminium with bonds to four oxygen atoms located at the vertices. In turn each oxygen is bonded to two T atoms. Secondary building units (SBUs) are generated when a specific array of T units are linked through T-O-T bridges as shown in Figure 1.1. Meier postulated eight key SBUs as the smallest number of subunits to describe zeolite frameworks [5].

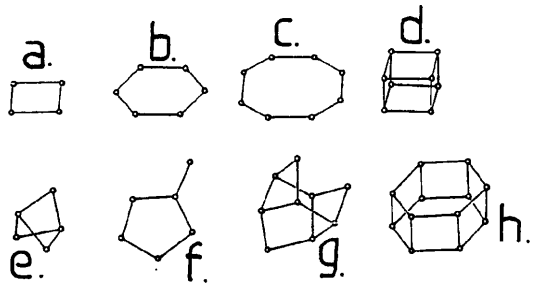


**Figure 1.1. SBUs: SR-single ring, DR-double ring a. S4R, b. S6R, c. S8R, d. D4R, e. complex 4-1 ($T_5O_{10}$ unit), f. complex 5-1 ($T_8O_{16}$ unit), g. complex 4-4-1 ($T_{10}O_{20}$ unit) and h. D6R.**

For zeolite A and faujasite (zeolite X and Y), S4- and S6Rs are joined together and form a cuboctahedron. This is also referred to as a sodalite unit or β-cage. If sodalite units are connected by oxygen bridges between the S6R the faujasite structure is obtained. Zeolite A has S4R connections between the sodalite cages as depicted in Figure 1.2.

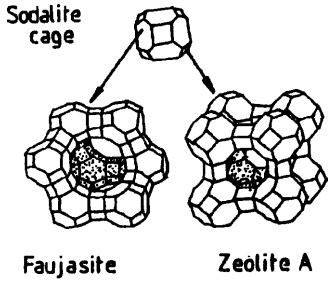


**Figure 1.2. The structural generation of zeolite A and faujasite.**

These arrangements create cages in the framework of zeolite A and faujasite with entrances of 8- and 12-MR windows, respectively. The free diameter of the pore aperture in zeolite A is around 4.2nm and in faujasite approximately 7.5nm.

Structural investigations of zeolites are complicated by two factors. Firstly, the micro-crystallinity of the materials in the order of microns precludes the use of single crystal techniques. Secondly, the distribution of Si and Al over T sites in the lattice is often disordered. Thus only an average description of the structure can be obtained. Although x-ray techniques are greatly enhanced by the use of synchrotron x-ray sources and Rietveld analysis techniques [6], a variety of techniques are necessary to deduce the lattice structures of zeolites. In this regard, high resolution solid-state Magic Angle Spinning Nuclear Magnetic Resonance (MAS NMR) spectroscopy [7] has emerged as an important complementary technique to diffraction methods. This technique reflects local environments of Si and Al atoms, connectivity and short-range orderings compared with the long-range orderings and periodicities to which diffraction methods are most sensitive. The structures of several high-silica zeolites relevant to this work are described in the following sections.

### 1.2.2. The Structure of ZSM-5, ZSM-11 and their Intergrowths

ZSM-5 and ZSM-11 have been defined as the structure types MFI and MEL, respectively [8]. They form the end members of a series of high-silica zeolites known as pentasils [9]. Crystallographic studies [10, 11] have shown that both structures are composed of 96 T atoms and based upon identical basic building units made up of 8- and 5-MRs joined along [001] as depicted in Figure 1.3. These form chains which pack laterally along [010] generating a pentasil sheet as shown in Figure 1.4. The structure of ZSM-5 is generated when adjacent (100) planes or sheets are related to one another by inversion (i) symmetry. In contrast, the structure of ZSM-11 is formed when the (100) sheets are associated by mirror symmetry ($\sigma$).

In ZSM-5, two orthogonal sets of intersecting 10-MR aperture channels or pore systems occur. The channels, that run along [010] are straight with nearly circular diameter of 5.5Å, whilst those along [100] follow a sinusoidal course and possess an

elliptical cross-section of approximately 5.1 x 5.5Å. The unit cell dimensions of ZSM-5 based on orthorombic (Pnma) symmetry are a=20.02Å, b=19.90Å and c=13.38Å. For ZSM-11 the two orthogonal sets of channels are equivalent, straight and elliptical about 5.1 x 5.5 Å in diameter. The unit cell dimensions of ZSM-11 based on tetragonal (I4m2) symmetry are a=20.07Å, b=20.07Å and c=13.41Å.

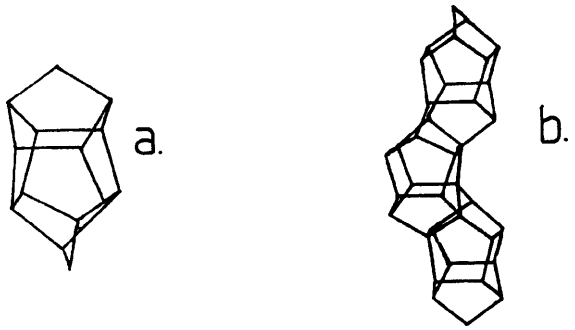


**Figure 1.3. Basic pentasil building unit (a) and chain (b).**

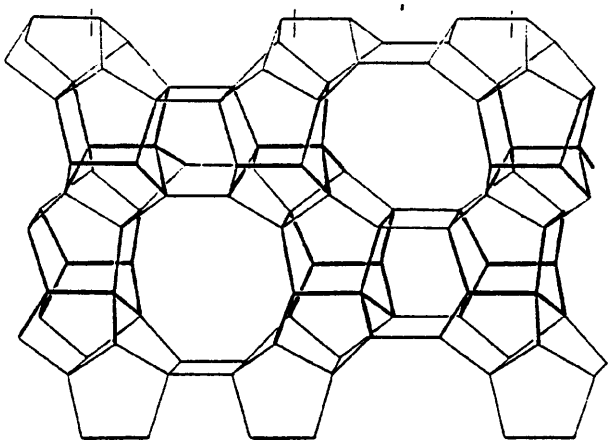

**Figure 1.4. Characteristic pentasil layer.**

All cavities formed at the intersections of the channels in ZSM-5 are equivalent. In ZSM-11 there are two distinct types [10], one similar to that found in ZSM-5, the other larger by approximately 30%. The net result is a decrease in the channel tortuosity and an increase in the volume available within the intra-crystalline pore structure of ZSM-11 compared to ZSM-5. This duality of cavity geometry is of particular significance in determining the precise nature of the shape-selective catalytic characteristics of the two materials [12].

Kokotailo and Meier [10] suggested that due to the subtle differences in the framework nature of ZSM-5 and ZSM-11 an almost infinite variety of related compounds could be synthesised, intermediate in structure between ZSM-5 and ZSM-11. By a regular and random sequencing of the σ and i planes, pentasil intergrowth materials are generated as depicted in Figure 1.5. A schematic representation of the pore systems of ZSM-5, ZSM-11 and an intergrowth are given in Figure 1.6.

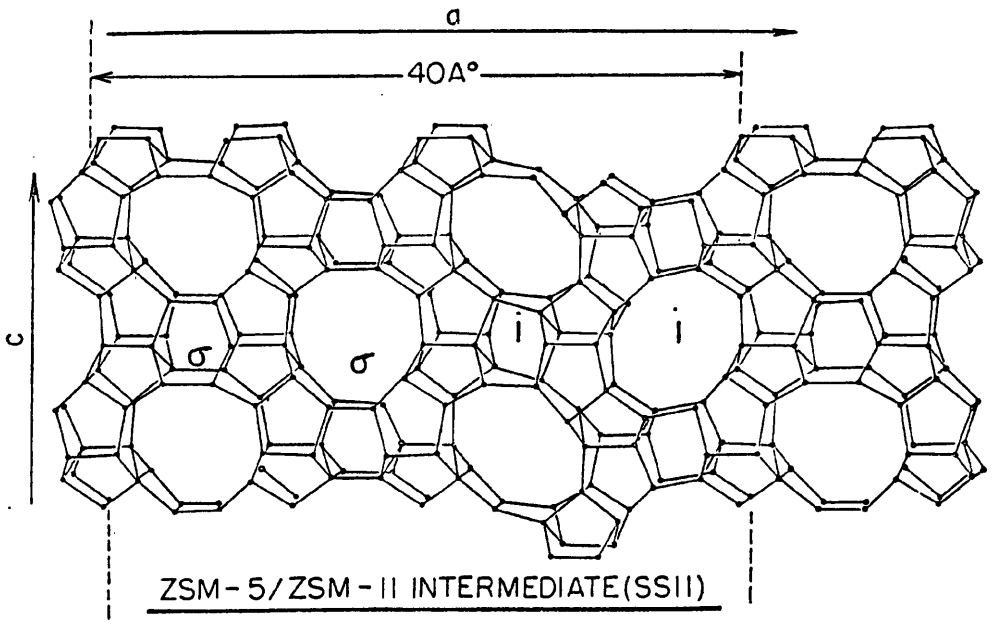


**Figure 1.5. Skeletal framework diagram of a (σσii) pentasil intergrowth and subsequent pore system projected along the [010].**

Millward et al.[13] successfully used high-resolution electron microscopy (HREM) to identify intergrown pentasil materials and the occurrence of a pentasil *super-lattice* composed of a regular array of i and σ planes. Intergrowths of other zeolite structures such as those associated with zeolite beta have been reported [14]. The uniqueness of the ZSM-5 and ZSM-11 structures was shown by Fyfe et al.[7] using $^{29}Si$ MAS NMR studies. The spectra of highly dealuminated samples showed that the stacking sequence of the i and σ planes considerably alters the local T environment. There are 24 (orthorombic symmetry) inequivalent T sites in MFI but only seven in MEL. Similarly, line-broadening associated with the $^{29}Si$ MAS NMR spectra of intergrowth materials may yield information concerning their local structural environment [7].

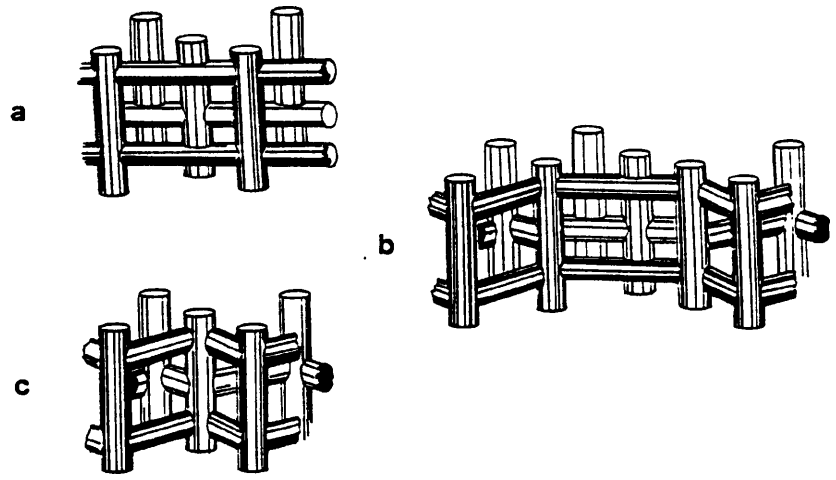


**Figure 1.6. The pore systems of a. ZSM-11, b. a related intergrown pore system and c. ZSM-5.**

### 1.2.3. The TON Structure Type

In the early 1980s, Theta-1, then a new high-silica zeolite, was synthesised by Barri et al.[15]. Several other proprietary zeolites such as Nu-10 [16], ZSM-22 [17], ISI-1 [18], and KZ-2 [19] have comparable XRD data to Theta-1. Consequently, according to IUPAC rules, this family of zeolites is designated as the TON structure type [8]. The TON framework is composed of 24 T atoms per unit cell arranged in of 5-, 6- and 10-MRs. The structure consists of chains of double 5-MRs extended along [100]. These chains are alternately linked by 6-MRs along [010] which generates a straight and one-dimensional channel system running parallel to [001]. The basic TON structure is shown in Figure 1.7.

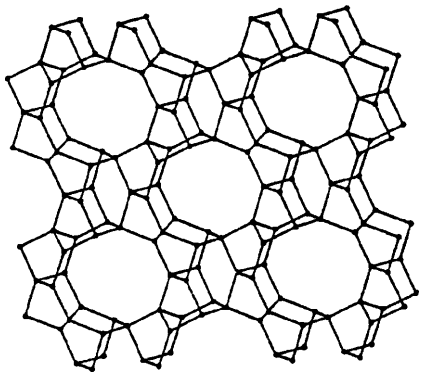

**Figure 1.7. A skeletal framework diagram of TON projected along [001].**

The shape and size of the channels are determined by ten-membered, elliptical rings of approximately 5.5 x 4.5Å. The unit cell dimensions of TON based on orthorombic (Cmcm) symmetry are a=13.86Å, b=17.42Å and c=5.04Å [17]. Recently, structural studies revealed that the framework of ZSM-23 arises from the recurrent twinning of TON [20].

### 1.2.4. ZSM-48: A Disordered Ferrierite-Type Structure

Essentially, ZSM-48 [21], EU-2 [22], EU-11 [23] and ZBM-30 [24] have analogous structural data and only differ intrinsically by their method of synthesis. The structure of ZSM-48 is composed of 48 T atoms and consists of 4-, 5- and 6-MRs. These SBUs join to form ferrierite sheets linked by bridging oxygen in the mirror plane. This results in a one-dimensional, linear 10-MR channel system whose dimensions are 5.3 x 5.6Å. Schenkler et al.[21] noted that the walls of the channel system are composed purely of distorted 6-MRs as shown in Figure 1.8. The unit cell dimensions of ZSM-48 based on orthorombic (Pmma) are a=14.24Å, b=20.14Å and c=8.40Å [21].

Diffraction studies [21] have shown that by varying the distribution of 4-MR elements in the basic structure, two topologically different, ZSM-48 lattices are generated as summarised in Figure 1.9 and Table 1.1. Consequently, both the two structural polymorphs and random intergrowths of ZSM-48 can be synthesised and contribute to the structural data.

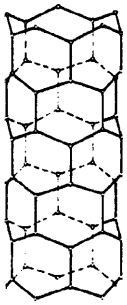

**Figure 1.8. The channel system of ZSM-48.**

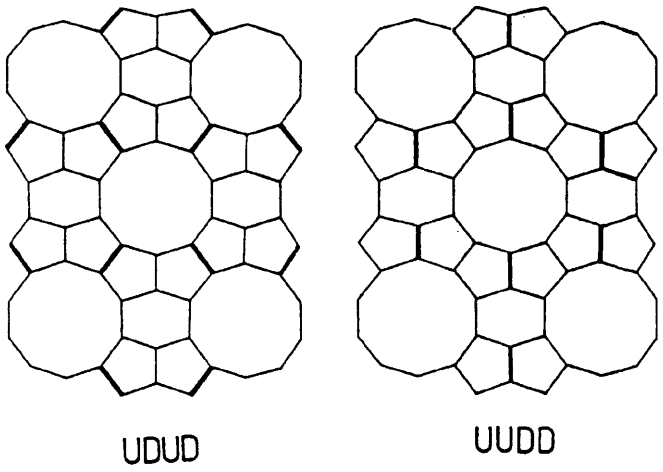


**Figure 1.9. Distribution of 4-MRs in ZSM-48. U-up and D-down position, of neighbouring T in FER sheet. Edges of the 4-MRs are shown as bold lines whose planes are perpendicular to the plane of the diagram.**

| LATTICE SYMMETRY | UNIT CELL DIMENSIONS Å a | b | c | PORE CHARACTERISTICS |
|---|---|---|---|---|
| CmCm (UUDD)* | 14.24 | 20.14 | 8.40 | Equivalent 10 MR's |
| Imma (UDUD)* | 8.40 | 14.24 | 20.14 | Equivalent 10 MR's |

* - U,D: Up, Down position, respectively of neighbouring 4 MR's in the ferrierite sheet

**Table 1.1. The structural differences present in ZSM-48.**

## 1.3. Zeolite Application and Technology

The estimated zeolite usage for the USA, Western Europe and Japan was approximately 550,000 metric tons in 1988 [25]. Figure 1.10 shows a representation of zeolite consumption in terms of commercial usage.

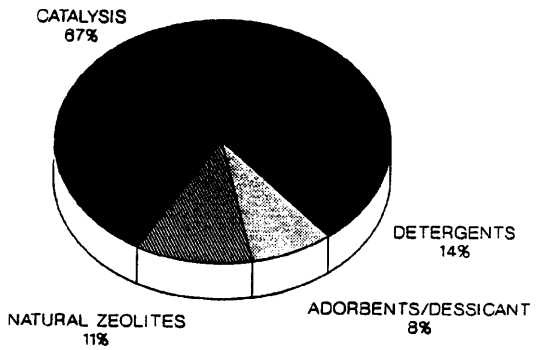


**Figure 1.10. Zeolite consumption and applications in 1988.**

Although most zeolite research and development is aimed at these *traditional* areas, recently considerable effort has been directed at new uses of zeolites as advanced materials. Research areas include heat and energy transformation, electrochemistry, fast ion conductors, semiconductors, chemical sensors, imaging and data storage, lasers and membranes [26]. The most significant utilisation of high-silica zeolites is acid catalysis, which will be discussed in more detail in the following section.

### 1.3.1. Catalytic Usage and Acidity of Zeolites

Like conventional solid catalysts, zeolites offer numerous advantages in process usage over liquid catalysts as they:

- reduce the corrosion of reaction vessels
- offer no waste or disposal problems
- are easily used in continuous processes in fixed-bed reactions
- have high thermostability
- are adaptable and modifiable.

Over recent years the most significant catalytic development was that of zeolite ZSM-5. No other catalyst matches its stability, activity, selectivity and versatility for the conversion of intermediate-size molecules [27]. Table 1.2 lists some of the commercial uses of ZSM-5 type catalysts.

| Process | Objective |
|---|---|
| 1. Selectoforming<br>-selective n-paraffin cracking. | To increase the Octane number in gasoline or to produce LPG. |
| 2. Dewaxing<br>-cracking ofhigh MW n-paraffins and mono-methyl paraffins. | To produce light fuel oil from heavy oil or to reduce pour point of lube oils. |
| 3. Xylene Isomerisation<br>-also production of xylene from toluene and methanol. | To obtain high yield of the p-isomer. |
| 4. Making Ethyl benzene<br>-alkylation of benzene with ethylene. | To produce mono-ethyl benzene selectively and in high yeild. |
| 5. Toluene Disproportionation. | Convert toluene to benzene and xylenes. |
| 6. Methanol to Gasoline (MTG). | To generate high grade gasoline from methanol |

**Table 1.2. Commercial processes using ZSM-5 catalysts.**

Although reactions do occur on the surface of the zeolite crystal, the majority of the reactants are transformed at active sites within the intra-crystalline void system. Access to the interior of the zeolite crystals is controlled by the aperture size of the pore system. The reactant molecule, typically organic, enters the zeolite and is then subject to the geometry environment of the pore system. In the case of ZSM-5 and ZSM-11 the internal pore system consists of channels linked by channel intersections. The pore geometry has important consequences for the diffusion and shape-selective catalysis in zeolites.

The majority of zeolite catalytic processes involves acid-catalysed hydrocarbon transformations. It is generally accepted that hydroxyl groups associated with the framework aluminium provide the active Brφnsted sites [28]. Such framework acidity is usually introduced by the thermal decomposition of the ammonium ion-exchanged form of the zeolite [28]. The hydroxyl groups may be regarded as protons bonded to negatively charged framework oxygen associated with the $AlO_4^-$ tetrahedra. At reaction temperatures above 200°C the protons are mobile and move between sites [29].

The presence of another type of acid site, namely a *true* Lewis site, have been identified. Such sites are thought to be composed of alumino-hydroxyl species, thermally dislodged from the framework at temperatures above 500°C [28]. Although still open to speculation, several workers have suggested the presence of *super-acid* sites [30]. These are believed to be enhanced Brφnsted acid sites arising from the synergism between dislodged alumino-hydroxyl species and framework hydroxyls such as:

$$TO_n(OH)_m \ldots\ldots (AlO)^+_p ,$$

where T represents Si and Al atoms and n, m and p are integral numbers. Hence, the acidic properties of zeolites as a consequence of framework composition, depends on the number and concentration of acid sites as well as their relative strengths [31].

The matching the size and configuration of reacting molecules, intermediates and products with the geometry and tortuousity of the zeolite channel or cavity provides the basis for controlled *shape selectivity* [28]. *Reactant selectivity* is observed when only a fraction of the reactant has access to the active sites because of molecular

sieving effects. *Product selectivity* occurs when only some of the product species with the correct dimensions or configuration can diffuse out of the zeolite intra-crystalline volume. *Restricted transition state selectivity* takes place when certain transitions states cannot be formed due to steric restrictions.

### 1.3.2. Adsorbent Usage

Zeolites have become firmly established in industry as a means of performing a host of separations and purifications [2]. Purification technology is dependent on the surface selectivity for polar or polarisable molecules such as water, carbon dioxide and toxic compounds of sulphur. Most bulk separations are based on molecular sieving principles such as the separation in the liquid phase of n- from i-paraffins, ethylbenzene from toluene and in the gaseous phase, nitrogen from oxygen, and n- from i-butyl olefins. The processes involve selectively absorbing molecules based upon their molecular size and shape relative to the particular pore size dimensions of the zeolite [28]. Other factors, such as the polarity of the absorbates, also influence the adsorption selectivity. Figure 1.11 shows the correlation between window size of the zeolite and the molecular diameter of some sorbate molecules. Similar stereospecific effects occur in both catalysis and ion-exchange. The effective pore size of a particular sorbate can be changed to suit a particular separation process by varying the exchangeable cation.

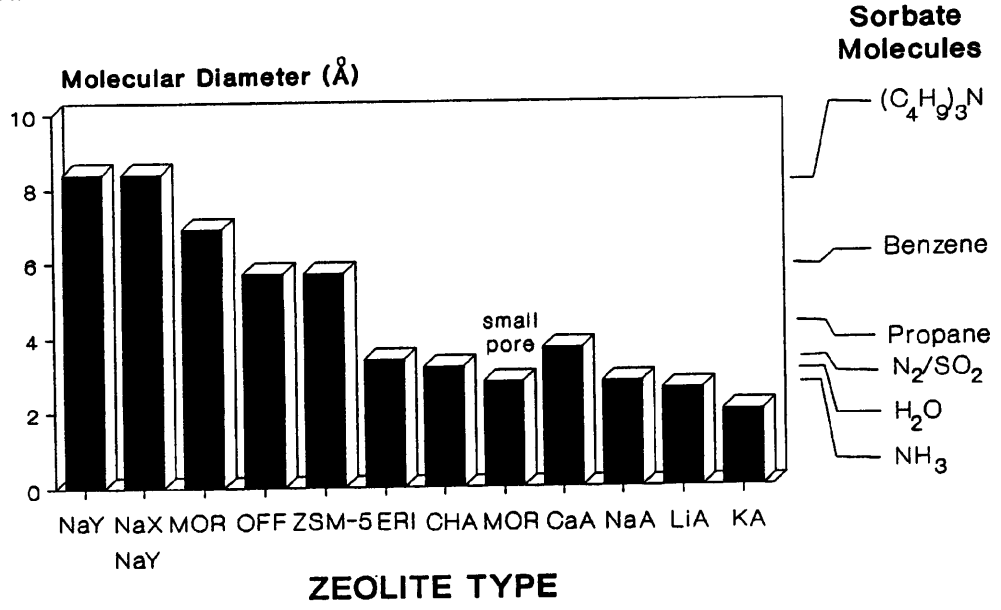


**Figure 1.11. Sorption characteristics in zeolites.**

### 1.3.3. Ion-Exchange Applications

Cation exchange of zeolites is used routinely in modifying the properties of zeolite products used in adsorption. A summary of present day applications of synthesised and natural zeolites is given in Table 1.3.

| Application | Advantage |
|---|---|
| 1. Detergent Builder. | Removes $Ca^{2+}$ and $Mg^{2+}$ from hard water instead of unecological sodium tripolyphosphate. |
| 2. Nuclear Waste Treatment. | Removes $^{137}Cs$ other high level radioisotopes and fixation for long term storage. |
| 3.Waste Water Treatment. | Removal of $NH_4^+$ and trace heavy metal impurities. |
| 4. Fertilisers. | Provides soil nutrients such as $NH_4^+$, $K^+$, moisture and pH. |
| 5. Livestock Nutrition. | Dietary supplementation reduces intestinal $NH_4^+$ by selective exchange to non-toxic levels. |

**Table 1.3. Ion exchange applications.**

The mobile non-framework inorganic cations associated with the zeolite pore system can be replaced by other cations as long as neutralisation of the anionic framework is maintained. The exchange behaviour depends upon several factors [32] such as the:

- cationic radius and charge,
- solution temperature and cation concentration,
- anionic species present in solution,
- type of solvent used for the exchange,
- structure and chemical composition of the zeolite.

## 1.4. Zeolite Synthesis

### 1.4.1. Historical Development of Molecular Sieves

The aim of research over the last 40 years concerning molecular sieve technology has been the synthesis of new structures and compositions. The major advances over this

period are given in Table 1.4. The pioneering synthesis work of Barrer [33] in the 1940s, inspired Milton of the Linde Division of Union Carbide Corporation to initiate the first industrial investigation into zeolite synthesis. The reactions involved the hydrothermal crystallisation of reactive alkali metal aluminosilicate gels at temperatures below 100°C. This led to the discovery of zeolites A and X [34] (Si/Al=1), later used commercially in adsorptive and catalytic applications. However, the framework aluminium provided a site of thermal instability and was attacked by steam and acids. These practical problems provided the impetus to find more stable siliceous materials.

During the 1950s and 1960s such materials were reported including zeolite Y [35] (Si/Al=1.5-3) and large pore mordenite, commercially known as *Zeolon* [36] (Si/Al=5). In comparison to zeolite X, zeolite Y has superior thermal stability and enhanced activity. It is today one of the most commercially successful hydrocarbon cracking catalysts [37]. In the early 1960s a significant development in zeolite synthesis was the introduction of quaternary ammonium ions, such as tetramethylammonium (TMA), during gel preparation [38]. This lead to the synthesis of materials such as ZK-4 [39] with *intermediate* Si/Al ratios between 5 and 10.

The first high-silica zeolites were obtained by Mobil Research Laboratories, exemplified by zeolite beta [40] and later ZSM-5 (Zeolite Socony Mobil Five) [41], using tetrapropylammonium ions (TPA) as the organic additive. Further work led to the discovery of other zeolites such as ZSM-11 [42], ZSM-12 [43], ZSM-34 [44] and ZSM-21 [45]. These highly siliceous zeolites with Si/Al ratios ranging from 10-100 or higher, had somewhat contrasting properties to the previously reported materials. This is linked to their organophilic and hydrophobic nature.

Later the compositional ranges of these material and others were extended and essentially *all-silica* zeolites were synthesised. Examples are ferrierite [46], silicalite-1 [47] and silicalite-2 [48]. The latter two materials are the structural analogues of ZSM-5 and ZSM-11, respectively. In the 1980s a further proliferation of new members of the high-silica zeolite family such as Eu-1 [49] and Eu-2 [22], and Theta-1 [15] were produced. Synthesis chemists discovered that by changing the chemical and/or physical nature of the organic additive an extended range of zeolites and compositions

could be achieved [50]. For example, Zones et al.[51] reported the synthesis of a whole range of new zeolites such as SSZ-23, SSZ-13 and SSZ-24 using adamantane derived organic additives. A silica-rich (Si/Al=5) faujasite material was also reported using a crown-ether as the organic additive [52]. Several zeolites have been synthesised with non-aqueous solvents such as glycerol, alcohols and dimethylsulphoxane [53]. Organic additives act as structure-directing agents during synthesis, which will be discussed later in this Chapter.

| Molecular Sieve Class | Si/Al Range | Example | ERA |
|---|---|---|---|
| "Low" Si/Al Zeolites | 1 to 1.5 | A, X | Late 40s, early 50s |
| "Interme .diate" Si/Al Zeolites | 2 to 5 | Y, L, Omega<br>large pore mordenite | 50s and 60s |
| "High" Si/Al Zeolites | 10-1000 | ZSM-5, ZSM-11 | 70s |
| | | Isomorphous substitution | 70s and 80s |
| | >1000 | All-silica Systems - e.g MFI, MEL & FER | 70s and 80s |
| New Materials | | $AlPO_4$s<br>SAPOs<br>MeAlPOs | 80s and 90s |

**Table 1.4. Evolution of molecular sieves.**

Similarly, considerable effort in synthesising metallosilicate molecular sieves was reported, where Fe, B, Cr, Ga, Ti, Ge and other metals were incorporated into the silica and aluminosilicate frameworks, typically with ZSM-5 topology [54]. Others include metallosilicate analogues of ZSM-11, ZSM-12, Theta-1, ZSM-34 and beta. In only a limited number of these studies has sufficient characterisation been presented to establish isomorphous substitution [54].

In 1982 a major discovery of a new class of aluminophosphate molecular sieves was described by Wilson et al.[55]. By 1986 some 13 elements were reported to have been incorporated into the aluminophosphate frameworks. These include Li, Zn, As, Be, B and Ti [56]. These materials were designated as $AlPO_4$ based molecular sieves comprising of more than two dozen structures of two hundred compositions. Table 1.5 lists some of the typical $AlPO_4$ based materials and the organic additives used for

their synthesis including VPI-5, the first very-large-pore framework material. It has a one-dimensional channel system defined by an 18-MR with a free pore diameter of 1.25nm [57]. Recently it was noted that another material, MCM-9, was a physical mixture of Si-VPI-5 and SAPO-11 [57].

Further research [3] led to the synthesis of silicoaluminophosphates (SAPO), metalaluminophosphates (MeAPO) and metalaluminophosphosilicates (MeAPSO). Like SAPOs the MeAPOs exhibit both structural diversity and an even more extensive compositional variation. The metal species include the divalent forms of Co, Fe, Mg, Mn and Zn and trivalent Fe.

| STRUCTURE | ORGANIC ADDITIVES USED FOR SYNTHESIS | IZA CODE |
|---|---|---|
| 5 | Tripropylamine ($Pr_3N$) | AFI |
| 8 | Di-n-butylamine | 14MR Structure |
| 11 | Di-n-propylamine ($nPr_2NH$) | AEL |
| 14 | Isopropylamine | |
| 16 | Quinuclidine | AST |
| 17 | Quinuclidine | ERI |
| 18 | Tetraethylammonium hydroxide (TEAOH) | |
| 20 | Tetramethylammonium hydroxide (TMAOH) | SOD |
| 31 | $nPr_2NH$ | |
| 33 | TMAOH | ATT |
| 34 | TEAOH | CHA |
| 35 | Quinuclidine | LEV |
| 36 | $Pr_3N$ | |
| 37 | Tetrapropylammonium hydroxide & TMAOH | FAU |
| 39 | $nPr_2NH$ | |
| 41 | $nPr_2NH$ | |
| 46 | $nPr_2NH$ | AFS |
| 52 | $Pr_3N$ & TEAOH | AFT |
| VPI-5 | $nPr_2NH$ | VFI |

**Table 1.5. Selected $AlPO_4$ based materials synthesised in the 1980s.**

### 1.4.2. Overview of High-Silica Zeolite Synthesis

A simple representation of a high-silica synthesis method is given in Figure 1.12. The characteristics of the synthesis of aluminosilicates include [58]:

- reactive starting materials such as freshly co-precipitated inhomogenous gels or amorphous solids,
- relatively high pH (> 10) introduced in the form of an alkaline metal hydroxide or other strong base,
- low temperature hydrothermal conditions (100-200°C) with concurrent low

autogeneous pressure at saturated water vapour pressures,

- a high degree of supersaturation of reagents leading to nucleation and subsequent crystal growth,
- crystallisation time from a few hours to many days.

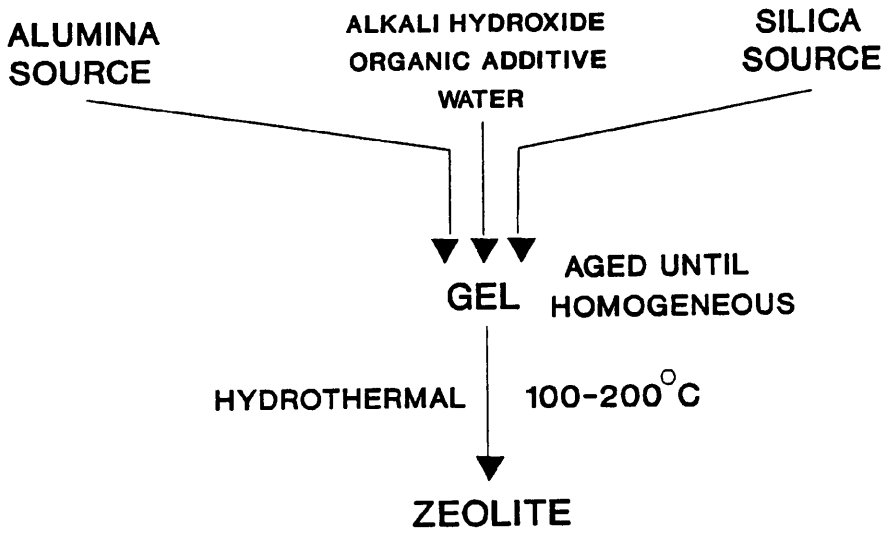


**Figure 1.12. General outline of a high-silica zeolite synthesis.**

Even though the preparation of zeolite gels is relatively simple, the chemistry involved in the formation of the zeolitic phase is extremely complex. This is due to variables [58] such as the:

- differences in the rates of reactant dissolution,
- formation of an intermediate gel phase,
- presence of structure-directing organic additives,
- nucleation phenomena provoked by supersaturation,
- occurrence of transformation and metastable phases.

The events occurring from gel preparation to zeolite crystallisation are summarised in Table 1.6. Routinely, synthesis gels are prepared at ambient temperatures in a highly alkaline environment. Several analytical methods have been used to investigate the physiochemical changes occurring in the reaction mixture. These include the trimethylsilation method [59], attenuated total reflectance infrared spectroscopy [60] and solution NMR spectroscopy [61]. However, it is difficult to apply these techniques truly *in-situ* from gel preparation through to zeolite crystallisation and consequently

the processes involved remain open to conjecture.

| TEMPERATURE | PROCESS | SUBSEQUENT EVENTS |
|---|---|---|
| <60°C | gel preparation | Reactant Solution<br>Reactant mixture |
| <60°C to < 200°C | autoclaved reaction rises to reaction temperature | Gel rearrangment<br>Dissolution of gel<br>Dissolution of silicate |
| <200°C | reaction temperature stable | Pre-nucleation phase<br>Nucleation<br>Crystallisation |
| <60°C | sampling of cooled autoclave | Isolation |

**Table 1.6. Events occurring during zeolite preparation.**

### 1.4.3. Initial Gel Processes

#### 1.4.3.1. Aluminate Solutions

Aluminate solutions with a pH of above approximately 10.5 consist exclusively of $Al(OH)_4^-$ ions. However, at pH values less than seven species such as, $Al(OH)_3nH_2O$, $[Al(OH)_2(H_2O)_n]^+$ and $[Al(H_2O)_6]^{3+}$ occur [58]. The tetrahedral configuration of the aluminate ion $Al(OH)_4^-$ favours tectosilicate formation with silicate species [62].

#### 1.4.3.2. Silicate Solutions

NMR studies of silicate gels revealed that as the pH is increased the colloidal silica particles form a range of dissolved and polymeric species [61]. The demarcation between silicate solutions containing particles and those which are free of such particles can be illustrated on a plot of silica concentration versus pH as shown in Figure 1.13. The following two important processes govern the distribution of silicate species [63]:

**1. Hydrolysis**

$$\equiv Si\text{-}OH \longleftrightarrow \equiv Si\text{-}O^- + H^+$$

Above pH values of nine this dissolution step is dominant and monomeric silicate ions can be released from the gel via hydrolysis. Below pH values of nine the

solubility of silica rapidly falls.

**2. Condensation.**

$$\equiv Si\text{-}OH + HO\text{-}Si\equiv \longleftrightarrow \equiv Si\text{-}O\text{-}Si\equiv + H_2O$$

Condensation reactions also occur at high pH forming a range of silicate species [61]. A dynamic equilibrium exists between the silicate species and the gel, which is affected by temperature, pH, the presence and type of inorganic cations and organic additives [61].

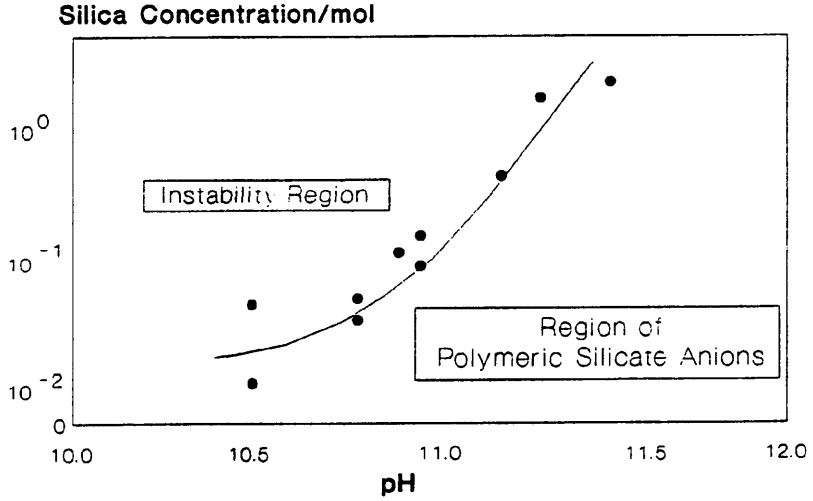


**Figure 1.13. PH dependence of silicate species in solution.**

### 1.4.3.3. Aluminosilicate Solutions.

On mixing, silicate and aluminate solutions form an amorphous gel, which is soluble and reactive in the alkaline environment. The (alumino)silicate gel phase consists of either a homogeneous dispersed phase of branched chains of sol particles or a more separate solid phase of an ordered aggregate of sol particles in equilibrium with a liquid phase [63]. The composition and reactivity of the silicate and aluminosilicate species released into solution are dependent upon several variables such as the original gel ingredients, gel precipitation processes and overall reaction stoichiometry [64]. The formation of aluminosilicate anions such as $Al(OSiO_3)_4^{-13}$ have been suggested via the condensation reaction [65]:

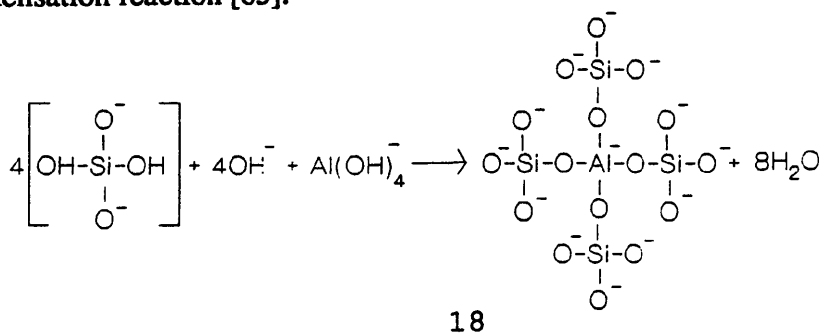

Subsequently, further condensation with a dimeric species of the $Al(OSiO_3)_4^{-13}$ anion would explain the formation of the S5R system as follows:

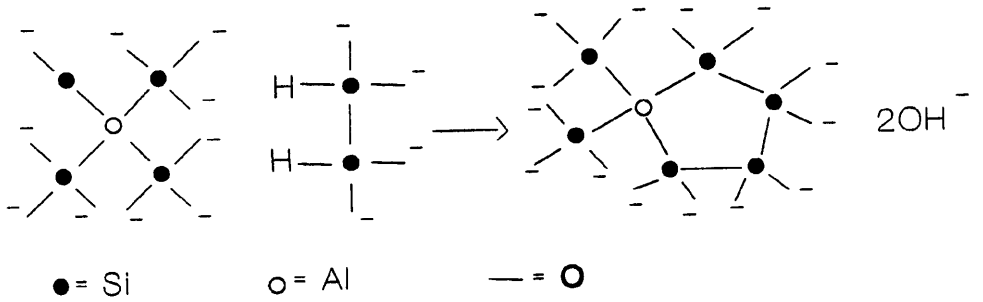


Similar pathways may result in the formation of more complex precursors involved in the synthesis of ZSM-5. These were proposed by van Santen et al.[66] and are illustrated in Figure 1.14. However, more recently the same workers concluded after comprehensive gel studies that the D5R silicate condensation mechanism is not generally operative in the synthesis of MFI structures. It is now believed that smaller units such as monomers and dimers play a significant role in the formation of precursor species under the influence of structure-directing agents [67].

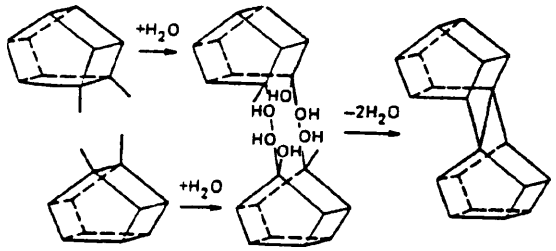


**Figure 1.14. Condensation of D5R silicates to form a ZSM-5 precursor species.**

There are many indications that the aging process of the (alumino)silicate gel is important and markedly influences the rate of zeolite crystallisation [68]. Brontic et al.[69] suggested that the aging step may result in the formation of viable nuclei which effectively lie dormant until the temperature is raised. The chemical composition of the gel is also an important factor influencing reaction rates in the synthesis of high-silica zeolites [62]. The incorporation of aluminium into the framework of ZSM-5 is a disruptive process requiring the presence of counter-balancing ions to preserve electroneutrality. Nonetheless, an optimum initial $SiO_2/Al_2O_3$ ratio exists for the synthesis of a particular high-silica zeolite [70]. This suggests that the type or concentration of (alumino)silicate species determines the nature of the zeolite formed.

### 1.4.4. Events Occurring During the Attainment of Reaction Temperature

The primary events occurring over this period of time suggested by Jansen [64] include:

- an accelerated dissolution of the gel to monomeric and dimeric species in solution,
- the dissociation of silicate oligomers and increase of monomers as measured by NMR up to around 100°C,
- an increase in concentration and mobility of monomeric and dimeric (alumino)silicate species,
- the formation of metastable nuclei,
- a decrease in pH due to the hydrolysis and condensation of precursor species in solution.

Several workers have shown that nucleation and crystallisation processes are sensitive to physical variables such as the heating rate, the material and physical characteristics of the autoclave and the aging and mixing procedure [25].

### 1.4.5. Events Occurring at the Reaction Temperature

#### 1.4.5.1. Nucleation

Zeolite synthesis appears to be a kinetically rather than thermodynamically controlled process [58]. Generally, these transformational processes can be mathematically expressed by the simple kinetic equation [69]:

$$f_c = K.t_c^q$$

where $f_c$ is the fraction of zeolite formed at crystallisation time $t_c$ and **K** and **q** are constants for a given set of experimental conditions. The value of the exponent **q** may point to the nature of the nucleation process. For instance, if **q** equals three or four then nucleation is probably heterogeneous on foreign surfaces or homogeneous from solution, respectively. However, practically the estimate of **q** lies between these two values.

The period during which no crystallisation can be detected is termed the induction time. As proposed by Barrer [71] metastable germ nuclei appear in the supernatant

liquid composed of a few lattice-forming units (j) but are unstable because of positive free energy terms. Initially the germ nuclei are not viable i.e. the sum of the positive free energy terms is dominant. Eventually, in the supersaturated gel, a critical size is reached when spontaneous nucleation occurs and the addition of more lattice-forming units occurs with a reduction in free energy. The size of critical nuclei for ZSM-5 was suggested by Jacobs et al.[72] to lie in the region of 20Å. Figure 1.15 shows a simple representation of zeolite nucleation.

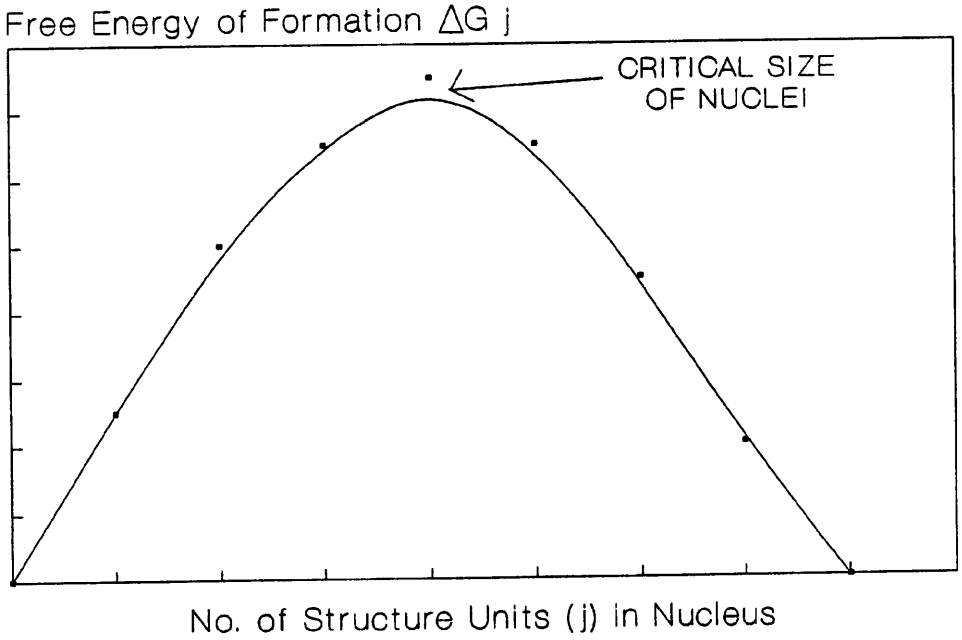


**Figure 1.15. A simple representation of nucleation.**

It is generally accepted that once nucleation occurs, the remaining chemical nutrients are used for crystal growth purposes. However, in the later stages of the synthesis *secondary nucleation* is occasionally observed. This results from the presence of crystalline material (surface) in the medium which with a satisfactory level of super-saturation, allows viable nuclei to form [73].

### 1.4.5.2. Crystallisation

Zeolite crystallisation may occur in one or more of the following manners [64]:

-**Solution** - crystallisation occurs from clear synthesis solutions. This implies that nucleation and crystal growth occurs via a phase-ion transportation process [74].

-**Dispersed low density gel** - nucleation occurs at the liquid interface (heterogeneous-

ly) of dispersed gel mixtures and crystallisation occurs in all directions.

-**Separated high density gel** - crystallisation proceeds after surface nucleation *into* the gel. As a liquid phase is present, crystallisation is a solvent mediated process.

-**Solid Phase** - according to Ostwald's rule of successive transformation [74], the zeolites formed undergo transformation to denser phases. This suggests that the zeolite which is least different in stability from the aqueous gel, nucleates most readily, i.e. in the shortest time.

Crystallisation mechanisms are still an area of debate and the processes occurring in a real synthesis mixture may involve several of the above suggestions. Lowe [75] applied a simple equilibrium model for the crystallisation of high-silica zeolites from gels to explain the accompanying change in pH. For crystallisation the solubility of the zeolite, $K_{s,zeolite}$, must be less than that of the amorphous gel $K_{s,gel}$. The free energy change $\Delta G$ for the conversion of the gel solid to the zeolite for a chosen reaction temperature T with **R** representing the gas constant, is given by the equation,

$$\Delta G = -RT\ln(K_{s,gel}/K_{s,zeolite}).$$

Assuming that the cation concentration $[Q^+]$ remains constant, the change in pH ($\Delta pH=pH_f-pH_{si}$), which occurs on crystallisation, is given by the equation,

$$pH = -F.\log(K_{sf}/K_{si})$$

where $K_{si}$ is the solubility of the solid gel phase and $K_{sf}$ is that of the zeolite. The factor F varies between 1 for low pH and 0.5 for high pH mixtures. Consequently, when a reaction mixture gives several different zeolites in succession, each transformation produces a material which is more stable (lower $K_s$) than the proceeding one and there will be an increase in pH.

The type of (alumino)silicate species or building units and processes involved in crystal growth on a molecular level are the subject of much debate. The general view from crystal growth theories is that crystals are formed via PBUs [64] and that larger dissolved polymeric species such as the SBUs are probably not involved [67]. Furthermore, the incorporation of guest molecules such as water, inorganic metal cations and/or an organic additives lowers the chemical potential and stabilises the growing zeolite crystal. This thermodynamic relationship was termed by Barrer the *guest-host* interaction [71].

### 1.4.6. Factors Affecting High-Silica Zeolite Synthesis

This final section discusses the roles played by both chemical and physical reaction parameters in the synthesis of high-silica zeolites.

#### 1.4.6.1. The Role of the Organic Additive

The introduction of organic additives in the early 1960s [38] for zeolite synthesis has resulted in the formation of new zeolites, the broadening of compositional ranges, the enhancement of crystallisation rates and changes in crystal size and morphology. In general the roles of the organic additive relates to one or more of the following definitions.

-**Structure-directing agent**, a general term describing how the formation of a particular zeolite structure is promoted or favoured by the presence of a certain organic additive.

-**Template**, a very specific interaction similar to the behaviour of water clathrates [51]. The organic is incorporated into a part of framework where its geometry directly relates to or matches the zeolite structure i.e. *hand-in-glove*.

-**Pore-filler**, here the organic occupies and stabilises the zeolite pore system by lowering the chemical potential of the structure. The organic additive is thought to prevent unfavourable interactions between water and the hydrophobic framework [71].

-**Counter- or charge-balancing agent**, the organic additive functions as efficient charge-balancing ions with respect to incorporated framework aluminium [76].

There is a general ambiguity in the use of these terms in the literature describing the functions of the organic additive during zeolite synthesis. Consequently, throughout this particular work, unless otherwise stated, the organic additive will be referred to as a structure-directing agent.

Extensive solution NMR studies have shown that tetraalkylammonium (TAA) ions exert specific structure-forming effects on silicate ions present in aqueous TAA silicate solutions [77]. Similarly Boxhoorn et al.[78] observed a drastic redistribution of

silicate species in a TPA silicate solution after the addition of methanol, ethanol and/or dimethyl sulphoxide (DMSO). A D5R silicate species was identified from these solutions, and it was suggested to be involved in the nucleation of ZSM-5. Solid-state MAS NMR studies have detected organic additives sited specifically in the intra-crystalline cages, channels and pore systems of several zeolites [79].

Alternatively, organic molecules are known to substantially affect the gel chemistry of the synthesis mixture [51]. Mostly basic in nature, they assist in the dissolution of the reactant (alumino)silicate species and promote reaction. It has been argued that structure directing effects may only become operative when the right gel chemistry is present [67].

Although the *templating* specificity of some organics is clear, anomalies are widely reported. Frequently, one organic additive, such as TMA, directs the formation of a number of zeolites. Conversely, one structure, such as ZSM-5, can be synthesised with a multitude of organic additives of chemical diversity and size [51]. Table 1.7 lists a range of organic additives used for the synthesis of ZSM-5. In contrast, ZSM-5 can also be formed in the absence of an organic additive. In this case, the structure-directing role of the inorganic cations was emphasised [80]. These materials are usually *Al-rich* where $Na^+$ ions and water molecules stabilise a more hydrophilic framework. Clearly the situation is not as simple as first thought and the influence of other chemical and physical factors as discussed in this section, influence the ultimate zeolite formed.

| ORGANIC ADDITIVE | ORGANIC ADDITIVE |
|---|---|
| Neopentylamines | Trialkylmethylammonium ions |
| Dioxan, Dioxolane | Triethyl-n-propylammonium ions |
| Morpholine | 2-9 C Primary monoalkylamines |
| Crown ethers | 5-6 C Alkylamines |
| Triethylenetetraamine | 3-12 C Alkylenediamines |
| Dipropylenetriamine | Glycerol, Inisitol, Mannitol |
| 3-6 C Diols | Methylquinuclidine |
| Pentaerythritol | Pyridine, 2-aminopyridine |
| Di- and Tri-alkylamines | Ethylenediamine |
| Ethylene, Propylene glycols | Alcohols and Ammonia |

**Table 1.7. Organic additives other than TPA used for the synthesis of ZSM-5 [50].**

### 1.4.6.2. The Role of Inorganic Cations

The type of inorganic cation $M^+$ has been shown to influence phase development [81], the rates of nucleation and crystallisation and the crystal size and morphology [82]. However, several high-silica zeolites have been synthesised in the absence of an inorganic cation source [83]. Literature offers contradicting views concerning the function of the inorganic cation $M^+$ during zeolite synthesis. It has been suggested that the inorganic cation

- acts as counter balancing ions with respect to the incorporation of framework aluminium,
- when incorporated, lowers the chemical potential and stabilises the zeolite [71] formed,
- changes the viscosity and supersaturation level of the synthesis gel [63],
- promotes agglomeration and precipitation of precursor species during synthesis i.e. a *salting-out* effect [63],
- has either a structure-directing ($Li^+$ and $Na^+$) or structure-breaking ($K^+$, $Rb^+$ and $Cs^+$) effect on the precusors for zeolite synthesis [84].
- depending upon their ionic radius (r) i.e.electrostatic potential (1/r), interact with the various (alumino)silicate species during nucleation and crystal growth [72]. This relates to the charge-neutralising efficiency of the inorganic cation.

MAS NMR studies suggested that inorganic cations affect the structure-directing properties of organic additives [85]. This was shown by the presence of a tetrahedral coordination complex at the channel intersection of ZSM-5 of a $Na^+$ cation with diamine organic additives.

### 1.4.6.3. Role of Mineralising Agents and Gel Alkalinity

The pH and solubility of the reactants in the synthesis mixture are governed by the presence of hydroxide ions ($OH^-$) in solution. Changes in the alkalinity at constant temperature, directly influence the mechanisms occurring during nucleation and crystal growth. Hydroxide ions are powerful mineralisers [72] decreasing the gel viscosity, which results in a more homogeneous reaction mixture, promoting the dissolution

of reactant species. Thus the rates of nucleation and crystallisation are enhanced.

The gel alkalinity can, however, inhibit nucleation and crystal growth and an optimum $OH^-/SiO_2$ ratio exists for a given zeolite synthesis [86]. This ratio represents a pH which is sufficient to maintain a high level of reactant species without inhibiting subsequent nucleation and crystal growth. Synthesis studies have also shown a dependence on phase type with respect to the $OH^-/SiO_2$ ratio [70]. As shown by solution NMR [61], the dynamic equilibrium between various (alumino)silicate species is sensitive to changes in pH and temperature. This suggests that variations in the concentration and distribution of (alumino)silicate species may influence the nucleation of a particular phase. Alternatively, changes in the alkalinity of the reaction mixture alter the ionic strength of the various species in solution [87]. Thus the hydration sphere of the $M^+$ ion, the local charge and geometry of the organic additive and reactivity of the (alumino)silicate species will be modified.

Over recent years, fluoride ions ($F^-$) have also been used for the synthesis of high-silica zeolites [88]. There are several advantages of using $F^-$ ions rather than $OH^-$ ions in the synthesis of zeolites [64]. For example, the solubility of metal ions such as $Fe^{3+}$, $Ti^{4+}$ and $Ti^{3+}$ is increased, which assists in isomorphous substitution. The pH of the synthesis gel is significantly reduced by replacing $F^-$ ions for $OH^-$ ion. Typically, the gel pH of the former and latter system range between 3-10 and 10-13, respectively. Consequently, fluoride synthesis is a less corrosive process. Larger zeolite crystals between 100-500μm in length are obtained from fluoride media. These are useful for structural studies, fundamental diffusion work and catalytic applications. However, too high a concentration of $F^-$ ions prevents the polycondensation of (alumino)silicates species during nucleation. A compromise between solubility of certain elements and inhibition of zeolite crystallisation results in $F^-$ ion synthesis systems which are less supersaturated than in hydroxide media.

### 1.4.6.4. The Nature of the Silica Source

In zeolite synthesis the silica sources are carefully chosen as different reaction rates and zeolitic phases may occur despite a common starting stoichiometry [89,90].

Usually a gel containing monomeric forms of silica, such as sodium silicate, crystallise faster than gels in which the silica is present in a highly polymeric form such as colloidal silica. Similarly the rates of dissolution of the silica source alter the nucleation period. It follows that the nature of the silica source alters the viscosity of the gel, thus affecting the mobility and diffusion of precursor species.

### 1.4.6.5. The Reaction Temperature

In general, the rate of nucleation and crystallisation of high-silica zeolites increases with reaction temperature [89]. Other studies have shown that the phase type [81] and crystal size and morphology [89] are also affected by temperature. Franklin et al.[91] based such changes on thermodynamic principles, where the more thermodynamically stable and denser structure forms at lower synthesis temperatures. Alternatively, changes in the motion of the organic additive with temperature are thought to influence product development [92].

### 1.4.6.6. Agitation

High-silica zeolites can be synthesised under agitated and static conditions. The rates of nucleation and crystallisation are, in general, enhanced by agitation. The process promotes the dissolution of the reactants and homogeneity of the gel, assuring a more mutual mixing of reactant species. A phase dependence of some high-silica zeolites was shown to be sensitive to the mixing process [15,51].

## REFERENCES.


1. W.Loewenstein, *Am.Mineral.*, **39**, 92 (1954)

2. E.M.Flanigen in Proc.5th Int.Zeolite Conf., (Ed.Rees, Butterworths) Naples, Italy, 760 (1980)

3. E.M.Flanigen in *Introduction to Zeolite Science and Practice*, Stud.Surf.Sci. Catal.No.**58**, (Eds.van Bekkum, Flanigen & Jansen, Elsevier) 13 (1991)

4. D.W.Breck, *Zeolite Molecular Sieves* (Wiley Interscience, 1974)

5. W.M.Meier in *Molecular Sieves*, Soc.Chem.Ind., London, 12 (1968)

6. L.B.McCusker & C.Baerlocher in Proc.6th Int.Zeolite Conf., (Eds.Olson & Bisio, Butterworths) Reno, USA, 812 (1983)

7. C.A. Fyfe, H. Gies, G.T. Kokotailo, Y. Feng, H. Strob, B.Marler & D.E.Cox in *Zeolites: Facts, Figures, Future*, Proc.8th Int.Zeolite Conf., (Eds.Jacobs & van Santen, Elsevier) Amsterdam, The Netherlands, 545 (1989)

8. R.von Ballmoos & J.B.Higgins, *Collection of Simulated X-Ray Powder Patterns for Zeolites*, IZA Special Publication, (Butterworths, 1990)

9. G.T.Kokotailo & W.M.Meier, *Chem.Soc.Special Publ.*, **33**, 33 (1980)

10. H.van Koningsveld, J.C.Jansen & H.van Bekkum, *Zeolites*, **10**, 235 (1990)

11. C.A.Fyfe, H.Gies, G.T.Kokotalio, C.Pastor, H.Strobl & D.E.Cox, *J.Am.Chem. Soc.*, **111**, 2470 (1989)

12. P.A.Jacobs & J.A.Martens, *Pure Appl.Chem.*, **58** No.10, 1329 (1986)

13. G.R.Millward, S.Ramdas & J.M.Thomas, *J.Chem.Soc.Farad.Trans.2*, **79**, 1075 (1983)

14. M.M.J.Treacy & J.M.Newsam, *Nature*, **332**, 249 (1988)

15. S.A.Barri, G.W.Smith, D.White & D.Young, *Nature*, **312**, 533 (1984)

16. A.Araya & B.M.Lowe, *Zeolites*, **4**, 280 (1984)

17. D.H.Olson, E.M.Valocsik & R.B.Calvert, *Eur.Pat.Appl.* 010 2716 (1984)

18. K.Takastsu & N.Kaweta, *Eur.Pat.* 0 087 017 (1982)

19. C.M.Parker & D.M.Bibby, *Zeolites*, **3**, 8 (1983)

20. J.M.Thomas, R.W.Millward, D.White & S.Ramdas, *J.Chem.Soc.Chem.Commun.*, 436 (1988)

21. J.L.Schlenker, W.J.Rohrbaugh, P.Chu, E.W.Valyocsik & G.T.Kokotailo, *Zeolites*, **5**, 355 (1985)

22. G.W.Dodwell, R.P.Denkewicz & L.B.Sand, *Zeolites*, **5**, 153 (1985)

23. A.Araya & B.M.Lowe, *J.Catal.*, **85**, 135 (1985)

24. L.Marosi, M.Schwarzmann & J.Stabenow, *Eur.Pat.* 46 504 (1981)

25. L.Moscou in *Introduction to Zeolite Science and Practice*, Stud.Surf.Sci. Catal.No.**58**, (Eds.van Bekkum, Flanigen & Jansen, Elsevier) chpt.1 (1991)

26. G.A.Ozin, A. Kuperman & A.Stein, *Angrew.Chem.*, **28**, No.3, 359 (1989)

27. S.L.Meisel, *CHEMTECH*, p.32 (1988)

28. J.Dwyer, *Chem.Ind.*, **7**, 258 (1984)

29. M.M.Mestdach, E.E.W.Stone & J.J.Fripiat, *J.Chem.Soc.Farad.Trans.1*, **72**, 154 (1976)

30. A.G.Ashton, J.Dwyer, I.S.Elliot, F.R.Fitch, G.Qin, M.Greenwood & J.Speakman in *Proc.6th Int. Zeolite Conf.*, (Eds.Olson and Bisio, Butterworths) Reno, USA 704 (1983)

31. A.F.H.Wielers, M.Vaarkamp & M.F.M.Post, *J.Catal.*, **127**, 51 (1991)

32. R.P.Townsend, *Chem.Ind.*, **7**, 246 (1984)

33. R.M.Barrer, *J.Chem.Soc.Ind.*, **64**, 130 (1945)

34. R.M.Milton, *US.Pats.* 2 882 243 (1959) & 2 882 244 (1959)

35. W.Breck, *US.Pat.* 3 130 007 (1964)

36. Anon., *Chem.Eng.News*, **12**, (1962)

37. A.Corma in *Zeolites: Facts, Figures, Future*, Proc.8th Int.Zeolite Conf., (Eds. Jacobs & van Santen, Elsevier) Amsterdam, The Netherlands, 49 (1989)

38. R.M.Barrer & P.J.Dempsey, *J.Chem.Soc.*, 971 (1961)

39. G.T.Kerr, *Inorg.Chem.*, **5**, 1573 (1966)

40. R.L.Wadingler, G.T.Kerr & E.J.Rosinski, *US.Pat.* 3 308 069 (1967)

41. R.J.Argauer & G.R.Wadlinger, *US.Pat.* 3 702 886 (1972)

42. P.Chu, *US.Pat.* 3 709 979 (1973)

43. E.J.Rosinski & M.K.Rubin, *US.Pat.* 3 832 449 (1974)

44. M.K.Rubin, E.J.Rosinski & C.J.Plank, *US.Pat.* 4 086 186 (1978)

45. C.J.Plank, E.J.Rosinski & M.K.Rubin, *US.Pat.* 4 046 859 (1977)

46. H.Gies & R.P.Gunawardane, *Zeolites*, **7**, 442 (1987)

47. E.M.Flanigen, J.M.Bennet, R.W.Grose, J.P.Cohen, R.L.Patton, R.M.Kirchner & J.V.Smith, *Nature*, **271**, 512 (1978)

48. D.M.Bibby, N.B.Milestone & L.P.Aldridge, *Nature*, **280**, 664 (1979)

49. J.L.Casci, B.M.Lowe & T.V.Whittam, *Eur.Pat.Appl.* 42226 (1981)

50. B.M.Lok, T.R.Cannan & C.A.Messina, *Zeolites*, **3**, 282 (1983) and E.M.Moretti, S.Contessa & M.Padovan, *La Chimica El' Industria*, **67**, N.1-2, 21 (1985)

51. S.I.Zones, R.A.van Nostrand, D.S.Santilli,D.M.Wilson, L.Yuen & L.D.Scampavia in *Zeolites: Facts, Figures, Future*, Proc.8th Int.Zeolite Conf., (Eds. Jacobs & van Santen, Elsevier) Amsterdam, The Netherlands, 229 (1989)

52. F.Delprato, L.Delmotte, J.L.Guth & L.Huve, *Zeolites*, **10**, 546 (1990)

53. X.Wenyang, L.Jianquan & L.Guanghuan, *Zeolites*, **10**, 753 (1990)

54. R.Szostak in *Molecular Sieves, Principles of Synthesis and Identification*, (Publ. van Nostrand Reinhold) 205 (1989)

55. S.T.Wilson, B.M.Lok, C.A.Messina, T.R.Cannon & E.M.Flanigen, *J.Am.Chem. Soc.*, **104**, 1146 (1982)

56. E.M.Flanigen, B.M.Lok, R.L.Patton & S.T.Wilson in *New Developments in Zeolite Science and Technology*, Proc.7th Int.Zeolite Conf., (Eds. Murakami, Ijima & Ward, Elsevier) Tokyo, Japan, 103 (1986)

57. M.E.Davies, P.E.Hathaway & C.Montes, *Zeolites*, **9**, 436 (1989)

58. R.M.Barrer in *Hydrothermal Chemistry of Zeolites*, (London Academic Press, 1982)

59. C.W.Lentz, *Inorg.Chem.*, **3**, 574 (1964)

60. E.J.J.Groenen, C.A.Emeis, J.P.van den Berg & P.C.de Jong-Versloot, *Zeolites*, **7**, 474 (1987)

61. A.V.McCormick and A.T.Bell, *Catal.Rev.Sci.Eng.*, **31** (1&2) 97 (1989)

62. V.N.Romannikov & V.M.Mastikin, *Zeolites*, **3**, 311 (1983)

63. R.K.Iler, *The Colloid Chemistry of Silica and Silicates*, (Publ.Cornwell Uni.Press, 1955)

64. J.C.Jansen in *Introduction to Zeolite Science and Practice*, Stud.Surf.Sci.Catal. No.**58**, (Eds.van Bekkum, Flanigen & Jansen, Elsevier) 77 (1991)

65. E.J.J.Groenen, A.G.Kortbeek, M.Mackay & O.Sudmeijer, *Zeolites*, **6**, 403 (1986)

66. R:A.van Santen, J.Keijsper, G.Omms & A.G.Kortbeek in *New Developments in Zeolite Science and Technology*, Proc.7th Int.Zeolite Conf., (Eds. Murakami, Iijima & Ward, Elsevier) Tokyo, Japan, 169 (1986)

67. J.J.Keijsper & M.F.M.Post in *Zeolite Synthesis*, ACS Symp.Ser., **398**, (Eds.M.L. Occelli & H.E.Robin) 617 (1988)

68. S.P.Zhdanov and N.N.Samulevich in Proc.5th Int.Zeolite Conf., (Ed.Rees, Butterworths) Naples, Italy, 75 (1980)

69. J.Brontic, B.Subotic, I.Smit & L.J.A.Despotovic in *Innovations in Zeolite Materals and Science*, Stud.Surf.Sci.Catal.No.**37**, (Eds.P.J.Grobet, Mortier, Vansant & Schulz-Ekloff) 107 (1988)

70. K.Suzuki, Y.Kiyozumi, S.Shin, K.Fujisawa, H.Watanabe, K.Saito & K.Noguuchi, *Zeolites*, **6**, 518 (1989)

71. R.M.Barrer in *Surface Organometalic Chemistry:Molecular Approaches to Surface Catalysis*, (Eds.J.M.Basset & B.C.Gates, Kluwer) 221 (1989)

72. A.Jacobs & J.A.Martens in *Synthesis of High-Silica Aluminosilicate Zeolites*, Stud.Surf.Sci.Catal.No.**33**, (Publ.Elsevier) chpts.2-4 (1987)

73. R.D.Edelman, D.V.Kuldalkar, T.Ong, J.Warzywoda & R.W.Thompson, *Zeolites*, **9**, 496 (1989)

74. Z.Gabelica, E.G.Derouane & N.Blom in *Catalytic Materials: relationship between structure and reactivity*, ASC Symp.Ser., **248**, (Eds.Whyte, Dalla Betta, Derouane & Baker) 219 (1984)

75. B.M.Lowe, *Zeolites*, **3**, 300 (1983)

76. E.W.Valyocsik & L.D.Rollmann, *Zeolites*, **5**, 123 (1985)

77. G.Engelhardt & D.Michel in *High Resolution Solid-State NMR of Silicates and Zeolites*, (Publ.Wiley & Sons) 92 (1987)

78. G.Boxhoorn, O.Sudmeijer & P.H.Gastern, *J.Chem.Soc.Chem.Commun.*, 1416 (1983)

79. J.B.Nagy, Z.Gabelica & E.G.Derouane, *Zeolites*, **3**, 43 (1983)

80. P.Shiralkar & A.Clearfield, *Zeolites*, **9**, 363 (1989)

81. A.Araya and B.M.Lowe, *J.Chem.Research (S)*, 192 (1985)

82. A.Erdem & L.B.Sand, *J.Catal.*, **60**, 241 (1979)

83. K.R.Franklin & B.M.Lowe in *Zeolites: Facts, Figures, Future*, Proc.8th Int.Zeolite Conf., (Eds. Martens & van Santen, Elsevier) Amsterdam, The Netherlands, 179 (1989)

84. J.B.Nagy, P.Bodart, E.G.Derouane, Z. Gabelica & A. Nastro in *New Developements in Zeolite Science and Catalysis*, Proc.7th Int.Zeolite Conf.Zeolites, (Eds.Murakami, Ijima & Ward, Elsevier) Tokyo, Japan, 231 (1986)

85. S.Tianyou, X.Ruren, L.Liyun & Y.Zhaohui in *New Developments in Zeolite Science and Catalysis*, Proc.7th Int.Zeolite Conf., (Eds.Murakami, Ijima & Ward, Elsevier) Tokyo, Japan, 201 (1986)

86. S.B.Kulkarni, V.P.Shiralkar, A.N.Kotasthane & R.B.Ratnasamy, *Zeolites*, **2**, 313 (1982)

87. P.W.Atkins in *Physical Chemistry*, 3rd Edn., (Oxford University Press, 1978)

88. J.L.Guth, H.Kessler & R.Wey in *New Development in Zeolite Science and Catalysis*, Proc.7th Int.Zeolite Conf., (Eds.Murakami, Ijima & Ward, Elsevier) Tokyo, Japan, 121 (1986)

89. R.Mostowitz & L.B.Sand, *Zeolites*, **2**, 144 (1982)

90. F.Y.Dai, K.Deguchi, M.Suzuki, T.Hiroshi & Y.Saito, *Chem.Lett.*, 869 (1988)

91. K.R.Franklin & B.M.Lowe, *Zeolites*, **8**, 495 (1988)

92. R.P.Gunawardane, H.Gies & B.Marler, *Zeolites*, **8**, 127 (1988)

# CHAPTER 2.

## Experimental Section

### 2.1. Zeolite Synthesis

In this work several zeolites have been synthesised and characterised using the following methods.The chemicals for the synthesis of the zeolite materials are listed in the following.

#### 2.1.1. Reagents

**a. Silica Sources**

-Ludox AS40 colloidal silica (40% wt/wt $SiO_2$, 60%wt/wt $H_20$), Du Pont Chemicals.

-Pyramid sodium silicate (29.3% wt/wt $SiO_2$, 8.8% wt/wt $Na_2O$, 61.9% wt/wt $H_2O$), Crossfield Chemicals.

-Cab-O-Sil/M-5, fumed silica (100% $SiO_2$), BDH Chemicals.

**b. Mineralising Agents**

-Sodium (NaOH) and potassium (KOH) hydroxide pellets, BDH Chemicals.

**c. Alkali metal salts**

-Aluminium Nitrate ($Al(NO_3)_3.9H_2O$), BDH Chemicals

**d. Acids**

-Nitric (70% wt/wt $HNO_3$, 30% wt/wt $H_2O$), BDH Chemicals.

-Sulphuric (98% wt/wt $H_2SO_4$, 2% wt/wt $H_2O$), BDH Chemicals.

**e. Organic additives**

All of the organic additives used were obtained from Aldrich Chemicals Company.

-N,N'Bis(3-aminopropyl)piperazine (BAPZ, $C_{10}H_{24}N_4$)

-1,8-Diaminooctane (DAO, $C_8H_{20}N_2$)

-1,6-Diaminohexane (DAH, $C_6H_{16}N2$)

-1,4-Diaminobutane (DAB, $C_4H_{12}N_2$)

-Tetrabutylammonium bromide (TBA, $[C_4H_9]_4NBr$)

-Tetrabutylphosphonium bromide (TBP, $[C_4H_9]_4PBr$)

-Tetrapropylammonium bromide (TPA, $[C_3H_7]_4NBr$)

-Triethylenetetraamine (TETA, $C_6H_{16}N_4$)

### 2.1.2. Gel Preparation

Considerable care was taken to ensure that all the reaction mixtures were prepared in the same manner by the addition of the appropriate amount of mineralising agent, alkali metal salt, silica, organic additive, acid and distilled water. Details of the calculations concerning the initial starting stoichiometry and molar ratios are summarised in Appendix I. In the reactions referred to as *all-silica* it must be appreciated that, in practice, aluminium may be present as a trace impurity in the starting materials. Prior to synthesis, in order to remove any residual zeolite deposits the autoclaves were treated with sodium hydroxide solution (10% wt/wt), heated to the synthesis temperature for eight hours and washed successively with deionised water then dried ready for use.

The reactions studied at and above 130°C were performed in stainless steel 120ml capacity autoclaves. The autoclaves were then heated at the stated temperature (+/- 2°C), under static conditions or rotated in a purpose built oven. Low temperature syntheses at 90°C were performed in 100ml capacity polypropylene bottles and shaken. Before being charged to the autoclaves the pH of the gels was recorded using a *Hand* (BDH Chemicals Ltd.) pH meter fitted with a PYE Unicam Ingold electrode.

The reactions were timed from the moment the autoclaves were placed in the preheated oven. The nucleation and crystallisation rates of the crystalline products were monitored by sampling and recording the pH of the synthesis mixture from the same quench-cooled autoclave at allocated intervals. After sampling, the autoclave was immediately returned to the oven and the white bulk products were separated from their mother liquors by filtration, thoroughly washed with distilled water and dried at 120°C for eight hours.

## 2.2. Elemental Analysis

The elemental composition of the *as-made* and calcined zeolites were performed by the UMIST Chemical Analysis Service using standard procedures. The methods used can be summarised as follows,

- carbon and nitrogen - gravimetry,

- sodium and potassium - atomic absorption,
- silicon, aluminium and phosphorus - inductively coupled plasma emmision.

The inorganic and organic content (per unit cell) of the crystalline materials was calculated using methods as outlined in Appendix II.

## 2.3. Calcination Procedure

The organic additives were removed from the *as-made* zeolites by a careful by calcination procedure in a temperature-programmable furnace. In order to avoid any thermal disruption of the framework the zeolites were carefully heated from room temperature to 550°C at a rate of 1°C $min^{-1}$ and held for eight hours in a stream of purified dry air.

## 2.4. Ion Exchange

The ammonium form of the calcined zeolite was produced by thrice, refluxing 5g of zeolite in 50ml of 1.5 molar ammonium nitrate solutions at 80°C for two hours. After each exchange the zeolite was filtered an thoroughly washed five times with 300ml of deionised water. After ion exchange the sample was left to dry at 120°C overnight.

## 2.5. X-Ray Diffraction (XRD)

For a powder sample, a random orientation of crystals exists. An incident monochromatic x-ray is diffracted by an angle ($\Theta$) under the Bragg diffraction condition [1] by the various crystallographic planes in the powder sample. The diffraction pattern so formed is composed of maxima at specific angles (relating to d, the interplanar spacing) and intensities. This enables the crystal structure to be identified by matching against standard spectra i.e. *finger-printing*. Similarly, the crystallinity and purity were estimated from x-ray analysis.

### 2.5.1. Sample Preparation and Analysis

The zeolite sample (*as-made* or calcined) was ground into a fine powder and placed into a square groove on a silicon glass or aluminium plate. The powder was then packed using a flat strip of plastic into the indentation until self-supporting. Any excess of powder was tapped away from the plate leaving a smooth flat surface and carefully mounted, vertically, into the diffractometer. The diffractograms were ob-

tained using a Philips model diffractometer using nickel filtered copper Kα radiation from a long fine-focus x-ray tube operating at 40KV and 50 mA and a Philips PW 1380 goniometer. Samples were step-scanned between the Bragg angles 5-50° two-theta (2Θ).

Phases were identified by comparing their diffraction patterns to those of standard zeolite materials and x-ray data quoted in the literature [2]. The literature XRD data corresponding the materials synthesised in this work are listed in Appendix III. Crystallinity was calculated by comparing the area of the largest x-ray intensity of a given pattern with that obtained from the highly crystalline reference material. The major d-spacing intensities used to calculate crystallinity for a given phase are summarised in the Table 2.1.

| Structure / Å d-spacing |
|---|
| ZSM-11 / 3.85 |
| ZSM-5 / 3.85 |
| ZSM-48 / 3.86 |
| TON / 10.85 |
| FER / 9.58 |
| MOR / 3.48 |
| *Mag [1] / 3.44 |
| *α-Q [2] / 3.33 |
| *Cris [3] / 4.08 |

* - Dense Phases
1. Magadiite
2. α-Quartz
3. Cristobalite

Table 2.1. D-spacing values used to calculate phase crystallinity.

## 2.6. Fourier Transform Infrared (FTIR)

The acidic nature of zeolites can be assessed by adsorbing various basic molecules such as pyridine, ammonia and hydrogen utilising *in-situ* FTIR studies. Two infrared cells based on a novel design [3] were used differing in window material, one quartz and the other silicon. The former cell has a spectral range of between 2,000-10,000cm$^{-1}$ and the latter 10-10,000cm$^{-1}$. As the cells are composed of different materials they are suitable for different experiments. The silicon window cell was used to study interactions such as those between pyridine and Brφnsted acid sites

($1545cm^{-1}$) and Lewis acid sites ($1454cm^{-1}$) as well as the nature of the physical and chemical interactions of organic additives encapsulated within the zeolite pore system. Alternatively, the quartz cell has a lower reflectivity and higher energy throughput and sensitivity compared to the silicon cell in the hydroxyl region. In addition, the quartz cell could be cooled in liquid nitrogen and used for the low temperature adsorption of hydrogen.

### 2.6.1. Sample Preparation

For sorption studies a self-supporting disc (1.1cm diameter) of approximately 10mg of ammonium exchanged zeolite was prepared by pressing to 4 tons for 3-6 minutes. The disc was mounted into a silica cell, evacuated to $10^{-6}$ Torr and heated *in-situ* to 370°C at 2.0°C per minute and held for two to three hours. The disc was then cooled to room temperature before recording the infrared spectum. For studies involving investigations concerning the occlusion of the organic additive within the zeolite pore system a self-supporting disc of the *as-made* zeolite was prepared as outlined above. The disc was mounted into the silica cell and evacuated to $10^{-6}$ Torr after which the spectra was recorded. The sample was then incrementally heated, cooled and spectrum recorded until the organic additive was removed from the zeolite framework.

### 2.6.2. Experimental Outline using Probe Molecules

#### 2.6.2.1. Low Temperature Hydrogen Adsorption

The hydrogen adsorption experiments were performed by N. Thompson using the following outline [3]. The quartz transmission cell was mounted into the spectrometer centered in a quartz dewar. The system was then purged to remove any water vapour which would interfere with spectral recordings. The sample was heated as previously described. Hydrogen of a known pressure (measured using a pressure transducer) was carefully introduced into the vacuum system. After allowing ten minutes for equilibration, liquid nitrogen was poured into the dewer above the height of the zeolite disc. The temperature of the cell was left to stabilise at approximately -190°C before the spectra was recorded. The hydrogen pressure was then increased and after equilibrium was achieved the next spectra was recorded. This was then repeated over a series of hydrogen pressures.

#### 2.6.2.2. Brønsted and Lewis Acid Strength Determination by Pyridine Adsorption.

The disc was preheated as described earlier and cooled to 150°C, at which temperature the sample was exposed to one atm of gaseous pyridine for five minutes. After the excess pyridine was pumped off and disc cooled to room temperature the spectra was recorded. Additional spectra were collected at higher desorption temperatures to study the relative pyridine retention on both Brønsted and Lewis acid sites.

### 2.6.3. Spectrometer Set-Up

All infrared spectra were collected using a Mattson Cygnus 100 FTIR spectrometer at a resolution of $4cm^{-1}$. The spectra were obtained using a potassium bromide beam-splitter (KBr substrate and Ge semi-reflector) and a mercury-cadmium-tellurium (MCT) type detector. Between 100 and 500 interferograms were collected for the spectra.

## 2.7. Electron Microscopy

### 2.7.1. Scanning Electron Microscopy (SEM)

SEM involves the scanning of a zeolite sample with a fine electron beam, which results in the emission of secondary electrons [4]. The resultant emitted electrons are collected, amplified and imaged on to a phosphor screen or photographic plate. Elemental analysis can also be performed by the examination of the x-rays associated with the energy emission of core electrons that are displaced by the electron beam. This mode is called energy dispersive x-ray analysis or EDAX.

#### 2.7.1.1. Sample Preparation

The samples are required to be mounted on a conducting aluminium stub connected to earth. The zeolites, previously ground into a fine powder form were mounted onto the stubs and degassed to $10^{-2}$ Torr. The sample was then coated with a thin layer of gold to prevent charging under the electron beam using an Edwards splutter coater, Model 5150B. For EDAX studies the samples were coated with carbon using a similar technique. The crystal size and morphology was investigated using a Philips scanning electron microscope, Model 505, fitted with an EDAX energy-dispersive spectrometer.

### 2.7.2. Electron Microscopy (EM)

This is a powerful technique for the detailed analysis of the structure of materials [4]. However, zeolite materials suffer from the serious disadvantage of low resistance to beam damage as discussed in Chapter 5. This is partly overcome by operating the microscope with a minimum beam current, or by use of a high-accelerating potential which reduces the ionisation and other damaging processes. The instrument operates in several modes including: **transmission (TEM)** - producing morphological details, **diffraction (ED)** - producing crystallographic information and **high resolution (HREM)** - where the intricate details of the crystal surface are recorded.

#### 2.7.2.1. Sample Preparation

The samples were prepared by grinding the zeolite powder in acetone using a small agate mortar and pestle. The resultant slurry was diluted with acetone and dispersed ultrasonically. A small drop of the fine dispersion was then placed on a 3.5mm carbon-coated, copper microscope grid, dried under a light bulb and placed in a dessicator until used. All micrographs and diffraction patterns were collected using the Phillips EM430 facility with an accelerated potential of 300kV. THe diffraction patterns were viewed using a Gatan 622YAG image pick-up system. For lattice imaging the procedure adopted involved finding a crystal area of interest using the image intensifier. Once an area had been selected, the plate is exposed to the beam, whilst the beam transversed across the sample. This allows the image of an unexposed and undamaged zeolite to be recorded.

### 2.8. Xylene Adsorption

Adsortion measurements with molecules of different size give direct information about the dimensions of the zeolite pore system [5]. The diffusivity and relative uptake of m-xylene was determined using a Robal microbalance as represented in Figure 2.1. Between 50-100mg of the ammonium form of the zeolite was weighed into a small aluminium foil bucket on the balance. The system was then carefully closed and degassed to $10^{-5}$ Torr. Prior to adsorption the sample was dehydrated by heating under vacuum from ambient temperature to 400°C at 2°C $min^{-1}$ and held for eight hours. The sample was then cooled to 120°C, sealed from the main vacuum system and dehydrated zeolite accurately weighed before the balance was *tar ed* to

zero. The sorbate, held at a constant temperature of 0°C, was first expanded into the shaded area of the isolated system as shown in Figure 2.1. After allowing 15 minutes for the vapour to equilibrate the vapour was admitted into the microbalance section and the sample weight increase noted as a function of time.

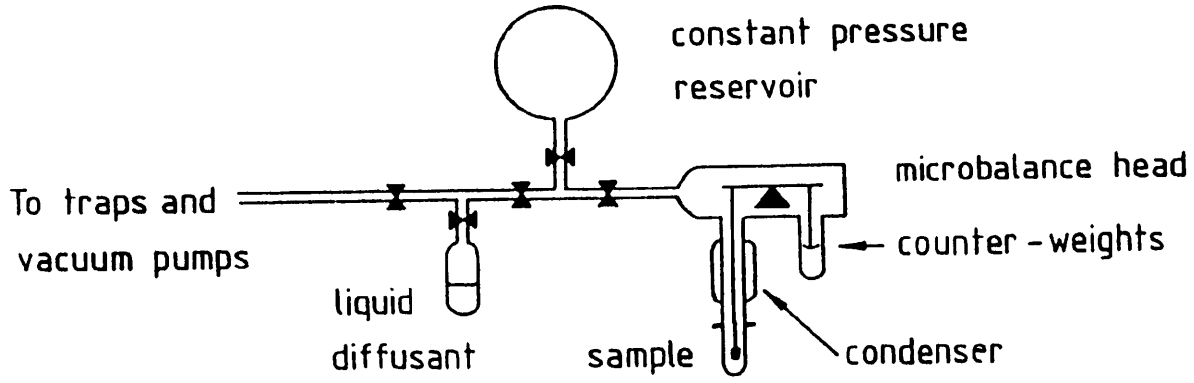


Figure 2.1. Experimental set-up for sortion of m-xylene.

## 2.9. Solid State Magic Angle Spinning Nuclear Magnetic Resonance (MAS NMR) Spectroscopy

High resolution solid state NMR spectroscopy is an effective and widely used means of elucidating subtle details of the structural properties of zeolite materials [6]. The basis of NMR is concerned with the behaviour of the magnetic moment of a given atomic nucleus under the influence of a magnetic field [6]. Spectra of both *as-made* and calcined materials were obtained at Durham University using a Varian VXR-300 Multinuclear spectrometer. The experimental conditions were as follows:

| CONDITIONS | NUCLEI | | | |
|---|---|---|---|---|
| | $^{27}Al$ | $^{29}Si$ | $^{13}C$ | $^{15}N$ |
| Observed Frequency/MHz | 78.2 | 59.6 | 75.4 | 30.4 |
| Spin Rate/KHz | 3.0 | 2.8 | 4.8 | 4.5 |
| Acquisition Time/μm | 4.8 | 49.9 | 14.4 | 19.2 |
| Relaxation Delay/s | 1.0 | 2.0 | 1.0 | 1.0 |
| Reference for Chemical Shift | $Al(H_2O)_6^{3+}$ | TMS[a] | TMS | $NH_4NO_3$ |

a. TMS=Tetramethylsilane

## 2.10. Catalysis - Alkylation of P-Xylene with Methanol

Catalysis is a method frequently used to characterise both the acidic and shape-selective properties of zeolites [7].

### 2.10.1. Sample Preparation

The ammonium form of the zeolite was compacted into a small cake using 3 ton.cm$^{-2}$ of pressure. After grinding, 20-40 mesh size (0.84-0.42mm) pellets were sieved for catalysis.

### 2.10.2. Reactor System and Reaction Procedure

A schematic representation of the catalytic reactor system used for this work is given in Figure 2.2. Under normal (atmospheric) operating conditions approximately 1.0g of pelleted catalyst was positioned in a fixed-bed continuous flow, electrically heated reactor. The reactor consisted of a cylindrical quartz tube (1.5 x 80cm) with a porous quartz sinter positioned 25cm along its length. A quartz thermowell containing a NiCr/NiAl thermocouple was placed 0.5cm above the sinter support which, allows the temperature measurement at the centre of the catalyst bed. A second thermocouple was placed adjacent to the fixed bed along the wall of the reactor tube. The temperature of the bed was controlled to 1°C by a temperature programmer designed at UMIST.

The catalysts was first activated *in-situ* in a stream of dried nitrogen with a flow rate of 20ml min$^{-1}$ heated from room temperature to 410°C at 2°C min$^{-1}$. The sample was held at the final temperature for 10 hours before being cooled to and stabilised at the reaction temperature of 305°C in a readjusted nitrogen flow of 30ml min$^{-1}$. A (2:1) molar mixed feed of methanol and p-xylene (Aldrich Chemicals, HPLC Grade), respectively, was delivered at a rate at 3ml hr$^{-1}$ by a precalibrated syringe pump (ex. Braun, Perfusor VI Model) into the reactor tube.

The total *weight hourly space velocity* (WHSV) of the liquid feed can be calculated using the following expression.

$$\text{WSHV} = \frac{\text{WEIGHT OF LIQUID FEED (g.hr}^{-1}\text{)}}{\text{WEIGHT OF CATALYST (g)}}$$

Unless otherwise stated the reactions in this study were performed with a WHSV of 3.0 $hr^{-1}$. After reaction the reactor system was cooled to room temperature before dry air was admitted into the system. This avoids any unnecessary damage to the zeolite framework such as dealumination. The catalyst was then regenerated to remove coking deposits by heating to 410°C at 2°C $min^{-1}$ and held at the top temperature for eight hours.

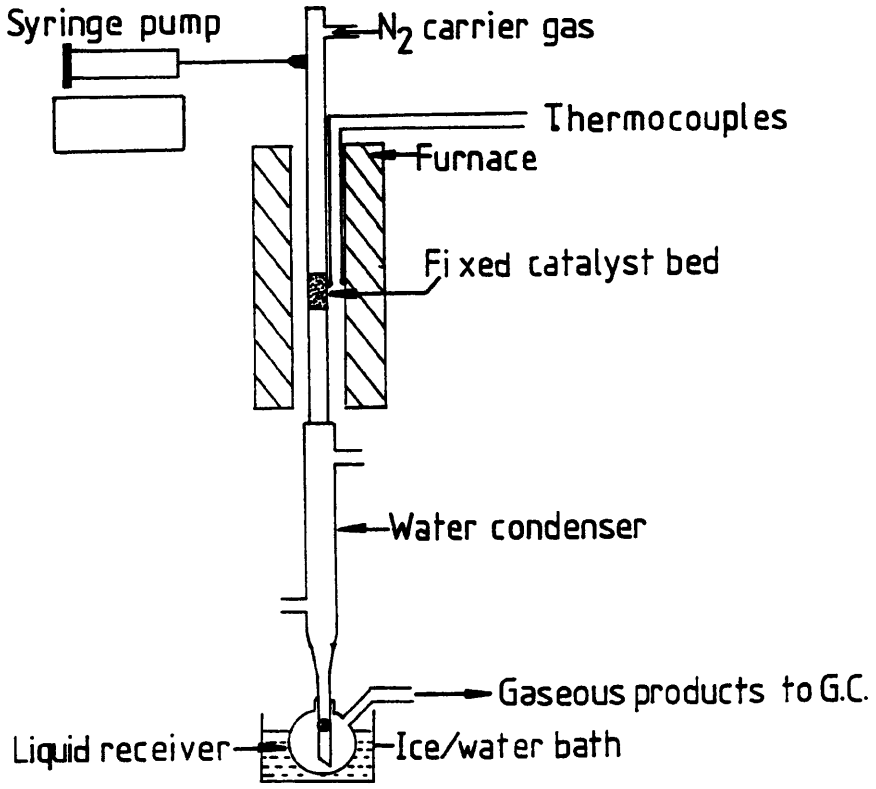


**Figure 2.2. Catalytic Reaction Design**

### 2.10.3. Product Analysis

The resultant product gases were condensed and the liquid aromatic and aqueous products were collected in a spherical flask situated in an iced water bath. Uncondensed gases were piped via heated lines to an on-stream GLC (Gas Liquid Chromatography) for immediate analysis. Changes in the bed temperature and the gaseous product flow rate were noted corresponding to both gaseous and liquid sampling periods. The aromatic and aqueous components were first separated then weighed and refrigerated ready for GLC analysis. The gaseous and liquid products were analysed using the conditions outlined in Table 2.2.

The corresponding peak retention times for the various hydrocarbon products were qualified using standard mixture supplied by BP Research *Hydrocarbon Bank* and their GLC/mass spectrometry (MS) facility [8]. The response factors for all the hydrocarbon products were found to be close to unity. Thus the integrated peak percentage area was assumed to be equivalent to the percentage weight of each product in a given mixture. Consequently the mass balance, reactant conversion and product selectivity were accurately estimated using the relationships as oulined Appendix IV.

| ANALYSIS CONDITIONS | GASEOUS | ORGANIC LIQUIDS | AQUEOUS |
|---|---|---|---|
| INITIAL TEMP/$^{o}$C | 80 | 80 | 120 |
| INITIAL HOLD TIME/min | 2 | 10 | - |
| FINAL TEMP/$^{o}$C | 220 | 180 | 120 |
| TEMP RATE/$^{o}$C.min$^{-1}$ | 8 | 10 | ISOTHERMAL |
| FINAL HOLD TIME/min | 20.5 | 10 | - |
| INJECTOR TEMP/$^{o}$C | 210 | 210 | 180 |
| DETECTOR TEMP/$^{o}$C | 280 | 290 | 200 |
| CARRIER GAS | $N_2$ | $N_2$ | $N_2$ |
| COLUMN DIMENSIONS | 50M x 0.3mm | 20M x 0.25mm | 1.5M x 4mm |
| COLUMN PACKING | POT ALUMINA/KCl | CARBOWAX | 10% CARBOWAX 90% CHROMASORB W |

Table 2.2. Analysis of products from the alkylation of p-xylene with methanol.

## REFERENCES

1. G.N.Gilmore, *A Modern Approach to Comprehensive Chemistry*, 2nd Edn, (Publ. Stanley Thornes) chapt.3 (1979)

2. R.von Ballmoos & J.B.Higgins, *Collection of Simulated X-Ray Powder Patterns for Zeolites*, IZA Special Publication, (Butterworths, 1990)

3. N.Thompson, Ph.D Thesis, UMIST (1991)

4. G.Thomas & M.J.Goringe in *Transmission Electron Microscopy of Materials*, (Publ.J.Wiley & Sons, New York, 1979)

5. M.F.M.Post in *Introduction to Zeolite Science and Practice*, Stud.Surf.Sci.Catal. No.58, (Eds.van Bekkum, Flanigen & Jansen, Elsevier) 392 (1991)

6. G.Engelhardt & D.Michel in *High Resolution Solid-State NMR of Silicates and Zeolites*, chpt.4 (Publ.Wiley & Sons, 1987)

7. P.A.Jacobs & J.A.Martens, *Pure Appl.Chem.*, **58**, No.10, 1329 (1986)

8. BP Research Center, Middlesex.

# CHAPTER 3.

## High-Silica Zeolite Synthesis using 1,8-Diaminooctane as the Organic Additive

### 3.1. Introduction

Alkyl quaternary compounds have been successfully as structure-directing agents for the synthesis of many high-silica zeolites and in expanding their conventional compositional ranges [1]. More recently, amine derived materials have been used as an alternative source of organic additive [2,3]. Functioning also as structure-directing agents or void fillers they have the added advantage over quaternary compounds of being cheaper and a more diverse number of structures are available. Due to their basic nature, reagent dissolution is enhanced and the requirement of alkali metal hydroxides in the initial reaction mixture diminished [4]. As a result, the necessity for ion exchange or acid pre-catalytic treatments to remove trace alkali cations which can damage the zeolite framework is avoided. Diamines can be represented by the simple formula, where n is an integer number,

$$NH_2\text{-}[\,CH_2\,]_n\text{-}NH_2$$

By varying the length (n) of the diamine molecule a range of zeolites can be synthesised [3]. Alternatively, changing the chemical composition of the synthesis gel or the reaction temperature with respect to a specific diamine several high-silica zeolites result such as ZSM-5, ZSM-48, Nu-10 and ZSM-11 [5].

The aim of this work was to clarify the role of the organic additive 1,8-diaminooctane (DAO) during the nucleation and crystallisation of high-silica zeolites. This was achieved by studying the effects of a wide range of reaction conditions and starting stoichiometries. The initial studies involved the all-silica systems DAO-$SiO_2$-$H_2O$ and DAO-$SiO_2$-$Na_2O$-$H_2O$. Aluminous gel systems were also investigated in order to present a comprehensive picture of the processes occurring during synthesis. This included a synthesis study where the physical and chemical nature of the organic additive was changed.

## 3.2. Experimental

Details of the chemical sources and the synthesis and sampling procedures used in this work are given in Chapter 2. The method for formulating a typical gel, unless otherwise stated, can be described by the example in the following section.

### 3.2.1. Gel Preparation

To a stirred solution of sodium hydroxide (4.56g) in distilled water (150.00g), fumed silica (11.36g) was slowly added over a period of 30 minutes. Once a uniform consistency was achieved a solution of DAO (6.96g) in distilled water (50.00g) was added dropwise together with the remaining distilled water and washings (24.00g). The resulting white slurry was stirred for 15 minutes before nitric acid (70.00%, 7.83g) was added and then aged for a further hour. The pH of the mixture was recorded before it was charged to a 120ml capacity stainless steel autoclave where it was heated, statically at 175°C for a total reaction time of 48 hours. The initial gel starting stoichiometry unless otherwise stated, can be represented by the following equation in terms of molar oxides,

$$11.4Na_2O - 37.8SiO_2 - 0.0Al_2O_3 - 9.6(DAO)_2O - 2515.0H_2O$$

1. $Na_2O/SiO_2=0.30$
2. $SiO_2/Al_2O_3 > 2000$*
3. $H_2O/SiO_2=66.50$
4. $(DAO)_2O/SiO_2=0.25$
5. $OH^-/SiO_2=0.14$

(* essentially an all-silica system).

Details of the stoichiometric and molar ratio calculations are given in Appendix I. After an allocated reaction time the autoclaves were quench-cooled and a sample of the contents taken, filtered, thoroughly washed several times with deionised water and dried overnight at 120°C. The solid products were characterised using several methods including XRD, SEM, FTIR, MAS NMR and wet chemical analysis as described in Chapter 2.

## 3.3. Results and Discussion

In order to investigate the reaction system the initial synthesis procedure was modified as described below.

### 3.3.1. The Effect of Reaction Temperature

The initial gel was prepared and heated statically at either 175, 130 or 90°C for a period of 75, 120 or 340 hours, respectively.

The results show that the synthesis of a particular phase depends upon the reaction temperature. A longer reaction period was necessary in order to obtain products of equivalent crystallinity as the synthesis temperature was lowered. The x-ray diffraction patterns of the *as-made* zeolites formed at each temperature are compared in Figure 3.1. The data show that at 90°C and 130°C, silicalite-2 is obtained while at 175°C, ZSM-48 is the crystalline product. The product d-spacings compare well to literature values [6,2] of the structures as quoted in Appendix III. The wet chemical analysis of the materials formed at each reaction temperature are given in Table 3.1 in a unit cell form. The molar C/N ratio of both silicalite-2 and ZSM-48 is four, therefore DAO is assumed intact and sited in the zeolite pore system. The number of DAO molecules per unit cell is 1.4 for ZSM-48 and between 3.8 and 4.0 for silicalite-2.

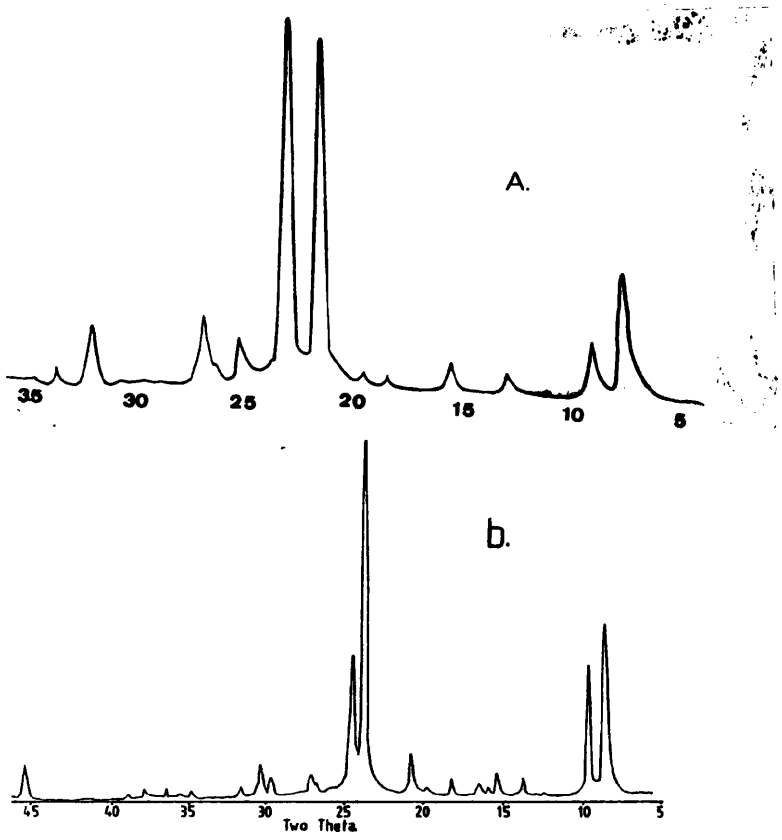


**Figure 3.1. XRD data of *as-made* a. ZSM-48 and b. silicalite-2 synthesised at 170°C and 130°C, respectively.**

| Run No | Reaction Temp | Phase Type | Stoichiometry (puc) *as-made* Zeolite |
|---|---|---|---|
| 1. | 175°C | ZSM-48 | 1.4DAO - 0.0Al - 48.0Si - 0.4Na |
| 2. | 130°C | Silicalite-2 | 3.8DAO - 0.0Al - 96.0Si - 1.9Na |
| 3. | 90°C | Silicalite-2 | 4.0DAO - 0.0Al - 96.0Si - 2.1Na |

**Table 3.1. Wet chemical analysis of *as-made* zeolites synthesised at various reaction temperatures.**

The pore-filling capacity of DAO for each zeolite was estimated from the calculations proposed by Nagy et al. [7], relating the molecular size of DAO to the length of the channel system for a particular zeolite. The total channel length per unit cell, estimated from the known structures of ZSM-48 and silicalite-2 [6] equals 1.7 and 8.0nm, respectively. The length of DAO was calculated to be 1.5nm using the CHEM-X system [8]. Hence, the theoretical maximum number of DAO molecules per unit cell, assuming a complete filling of the channels and an end-to-end configuration of the diamine chain is:

$$n(\text{DAO}) \text{ per unit cell} = \frac{1.7}{1.5} = 1.1 \text{ for ZSM-48}$$

and

$$n(\text{DAO}) \text{ per unit cell} = \frac{8.0}{1.5} = 5.3 \text{ for silicalite-2.}$$

Comparing the theoretical and experimental data, *as-made* ZSM-48 experiences a near-maximum pore-filling by DAO. This is in agreement with similar calculations [7]. Silicalite-2 (Run No.2) is partially occupied by the organic additive at around 70%. The physical and chemical nature of DAO in silicalite-2 and ZSM-48 will be discussed later in section 3.3.8. These data show that the organic additive does not have to occupy the available pore volume in order to be an efficient structure-directing agent.

Trace levels of aluminium (<0.01-0.02 wt%) were detected with chemical analysis giving an indication of their siliceous nature. The $Na^+$ ion content of silicalite-2 and ZSM-48 is approximately 1.9-2.0 and 0.4 per unit cell, respectively. The amount of $Na^+$ ions in both materials is in excess of that required to balance the negative charge on the tetrahedral aluminium trace impurities. Fegan et al.[9] remarked on a similar $Na^+$ ion content of silicalite-1. It was suggested that these ions together with the organic additive were associated with negatively charged framework defect sites. These results suggest that there are less defect sites in the framework of ZSM-48 than silicalite-2.

Franklin et al.[10] reported a similar temperature dependence for the synthesis of silicalite-1 and ZSM-48 using DAH as the organic additive. They inferred that the more thermodynamically stable structure ie. silicalite-1, preferably forms at the lower synthesis temperature. However, theoretical studies have shown negligible differences between the thermodynamical stability of zeolite structures [11]. Despite this, in this present study a correlation between framework density and reaction conditions was observed. In agreement with the general principles of synthesis, under more demanding or prolonged reaction conditions there was a tendency for the denser phase to form [12]. In this particular study a higher reaction temperature favoured the denser phase of ZSM-48 over silicalite-2. The reported framework densities in terms of T, for ZSM-48 and silicalite-2 are 19.9 and 17.7 T/1000 Å, respectively [13]. Other workers suggested that $Na^+$ ions, sited at channel intersections of ZSM-5 form tetrahedral complexes with water and diamines during the synthesis of ZSM-5 [14]. The bonding interactions of such species are disturbed by increases in reaction temperature. As a result the synthesis of one-dimensional structures such as ZSM-48 are favoured over silicalite-2 which has a two dimensional structure [15].

The micrographs of ZSM-48 formed at 175°C after 60 hours and silicalite-2 at 130°C after 120 hours are shown in Figure 3.2 and Figure 3.3, respectively. ZSM-48 is composed of large, single, bow-tie-shaped crystals of 40μm in length with a centre-neck width of around 10μm. A large amount of twinned phase is also present composed of large, regular aggregates approximately 40 x 40μm in size. On closer inspection, as revealed in Figure 3.2c, the crystals are made up of tightly packed rod-

like crystallites. The uniform size distribution of the phase suggests a homogeneous nucleation of stable nuclei followed by a constant growth rate mechanism [16]. The morphology of these crystals is comparable to EU-2, a structural analogue of ZSM-48 [17].

Assuming that there is adequate room for DAO to be sited along the major 10-MR channels of ZSM-48, an end-to-end packing DAO along the channel system can be envisaged. This promotes the formation of needle-like crystals. Similar crystallisation processes have been suggested for other zeolites such as TON [18]. Alternatively, the relative growth rates of the faces of a crystal can be altered by various solution factors. For example, rapid or quench-cooling generally results in the formation of acicular or needle-like crystals [19]. A similar aggregate formation to ZSM-48 has been observed during crystallisation of various salt solutions. This results from a phenomenon known as *parallel growth* [19]. During this process, frequently associated with undisturbed media, individual forms of the same crystalline material grow on top of one another. Consequently, the corresponding edges of the individual forms are parallel.

Silicalite-2 synthesised at 130°C consisted of monodispersed, tablet-like crystals, 8.5 x 6.5μm in size. The surface of the material is smooth and without visible defects. The crystal morphology compares to that reported in other MEL synthesis studies [20]. Silicalite-2 synthesised at 90°C (not shown) consists of ill-defined, sub-micron crystallite aggregates. Their morphology is difficult to ascertain, possibly due to presence of unreacted amorphous material. At such a relatively low synthesis temperature nucleation and crystallisation of high-silica zeolites are inhibited [21].

### 3.3.2. The Influence of Gel Basicity

The initial reaction mixture was prepared with various amounts of nitric acid added in order to vary the initial $OH^-/SiO_2$ ratio between 0.00 and 0.60 as outlined in Appendix I. All the other initial molar ratios were as described in section 3.2. The gels were heated statically at 175 or 130°C for a total of three and five days, respectively.

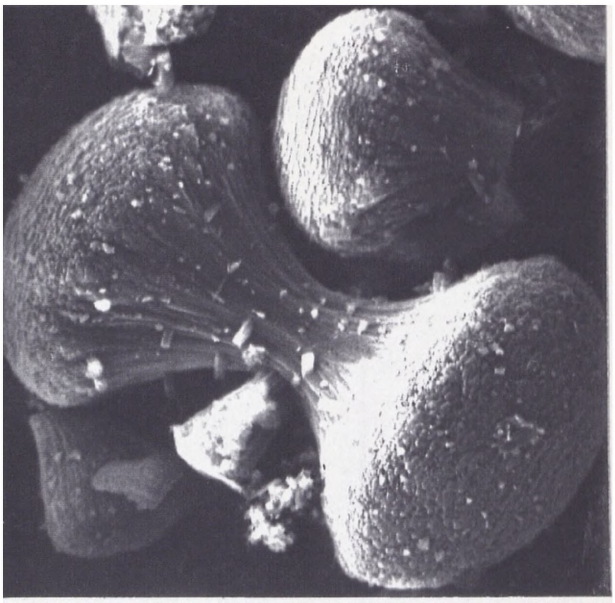

SCALE
10μm

3.2a. Single crystal of ZSM-48.

SCALE
10μm

3.2b. Twinned crystal morphology of ZSM-48.

**Figure 3.2. SEM of ZSM-48 synthesised at 175°C after 60 hours.**

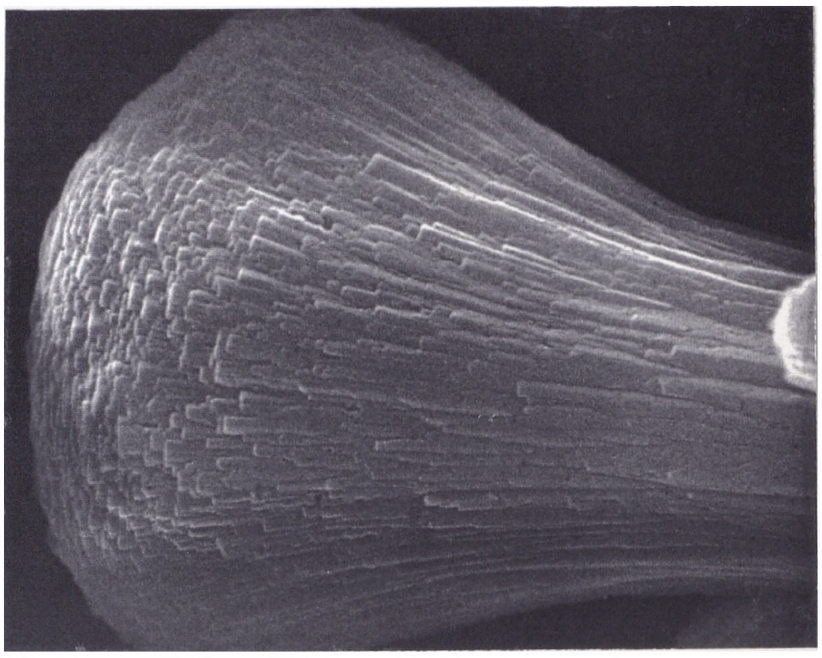

SCALE
2μm

3.2c. Close-up of ZSM-48 crystal morphology.

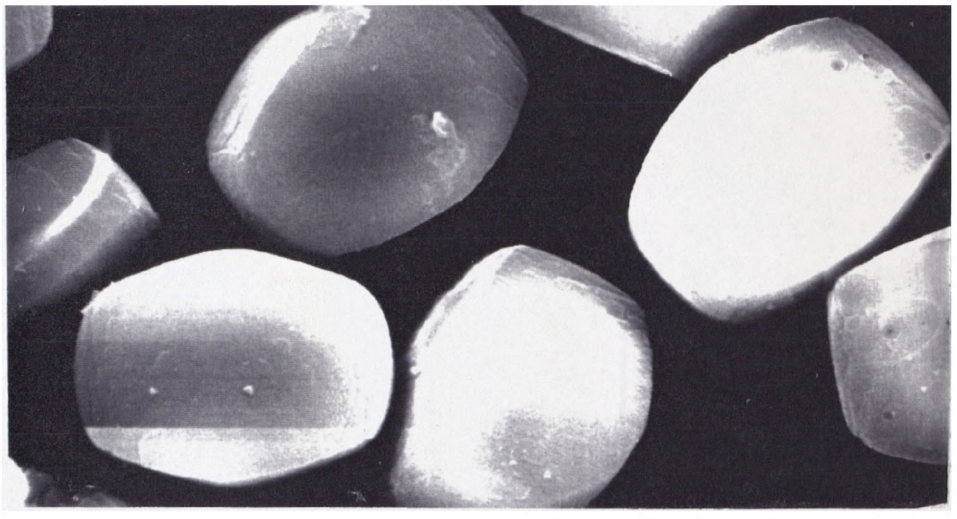

SCALE
5μm

Figure 3.3. SEM of silicalite-2 synthesised at 130°C after 120 hours.

X-ray analysis of the various products revealed that ZSM-48 and silicalite-2 were the only crystalline phases synthesised. The nucleation and crystallisation rates of these zeolites were dependent upon the initial $OH^-/SiO_2$ ratio and reaction temperature. Other dense phases such as magadiite, cristobalite and α-quartz also appeared subject the reaction conditions used. The effect of the initial gel basicity on the nucleation and crystallisation rates of ZSM-48 is summarised in Figure 3.4. It shows that both rates are optimised using an initial $OH^-/SiO_2$ ratio of 0.20. On reducing this ratio below 0.2, both the nucleation and crystallisation rates decrease significantly.

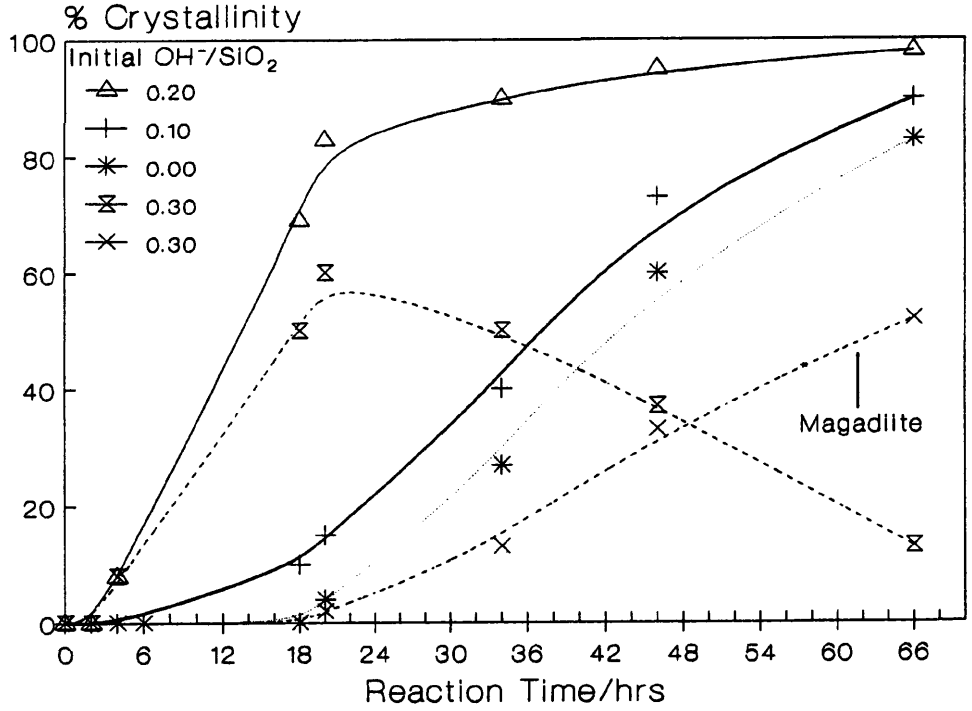


**Figure 3.4. Effect of the initial $OH^-/SiO_2$ ratio on ZSM-48 synthesis.**

A similar nucleation period to the optimised synthesis was found when the initial $OH^-/SiO_2$ ratio was 0.3. However, as the reaction proceeded ZSM-48 was found to be metastable and gradually transformed to magadiite. An optimum reaction alkalinity for the synthesis of several high-silica zeolites using amine-derived organic additives has been reported [23]. Barrer [12] emphasised that, in general, increases in the $OH^-$ ion concentration of the initial gel enhances the dissolution of the silica source. Consequently the degree of supersaturation of reactive species is increased promoting nucleation and crystal growth. However, if the optimum gel alkalinity is exceeded nucleation is inhibited as there is a tendency for the nuclei to become unstable and redissolve into the solution/gel phase. High alkalinities also promote metastable

transformations, assisting the dissolution of the crystalline phase and the recrystallisation of more denser phases [12].

There were no significant changes in the $Na^+$ ion or organic content of ZSM-48 synthesised between the initial $OH^-/SiO_2$ ratios of 0.00-0.30. This implies that reaction rates are more dependent on parameters such as the dissolution of the silica source than on the relative incorporation of DAO or $Na^+$ ions.

A highly crystalline ZSM-48 was obtained at or below an initial $OH^-/SiO_2$ ratio of 0.2. No other material appeared over the crystallisation period studied. On increasing the initial basicity ratio of the gel above 0.2 increasing amounts of kenyaite and magadiite co-crystallised with ZSM-48. With an initial $OH^-/SiO_2$ ratio of 0.4 the solid product consisted of a 1:1 mixture of magadiite and kenyaite phases with trace amounts of ZSM-48. In the latter stages of this reaction these materials transformed to the more thermodynamically stable phases of cristobalite and α-quartz. No zeolite phases were obtained from gels with very high initial $OH^-/SiO_2$ ratios (> 0.5). Cris tobalite and α-quartz appeared throughout the crystallisation period. Figure 3.5 summarises the changes in phase development with respect to initial reaction basicity.

The change in pH of the gel at various stages of the reaction is frequently used as an indication for the onset of zeolite crystallisation [24]. Figure 3.6 shows the corresponding changes in the pH of the gel over the reaction period for several initial $OH^-/SiO_2$ ratios. During the nucleation period the initial pH remained approximately constant but with the onset of crystallisation a corresponding sharp rise in pH was observed. This increase was most pronounced at the optimum initial $OH^-/SiO_2$ ratio 0.2.

Prior to nucleation amorphous silica, being more concentrated than the zeolite precursor species, controls the silicate ion concentration [9]. At the begining of crystallisation the precursor species become more influential and start to govern the pH of the reaction mixture. This results in a decrease of the silicate ion concentration. However, this is insufficient to offset the drop in base ion concentration and the pH suddenly rises. Other workers have shown that at higher alkalinities the concentration of

monomeric silicate species increases at the expense of higher polymeric species [25]. It is believed that these polymeric species do not participate in the nucleation and crystal growth processes. Consequently, gels containing a greater number of monomeric species, associated with a greater pH rise, promote the reaction processes [26].

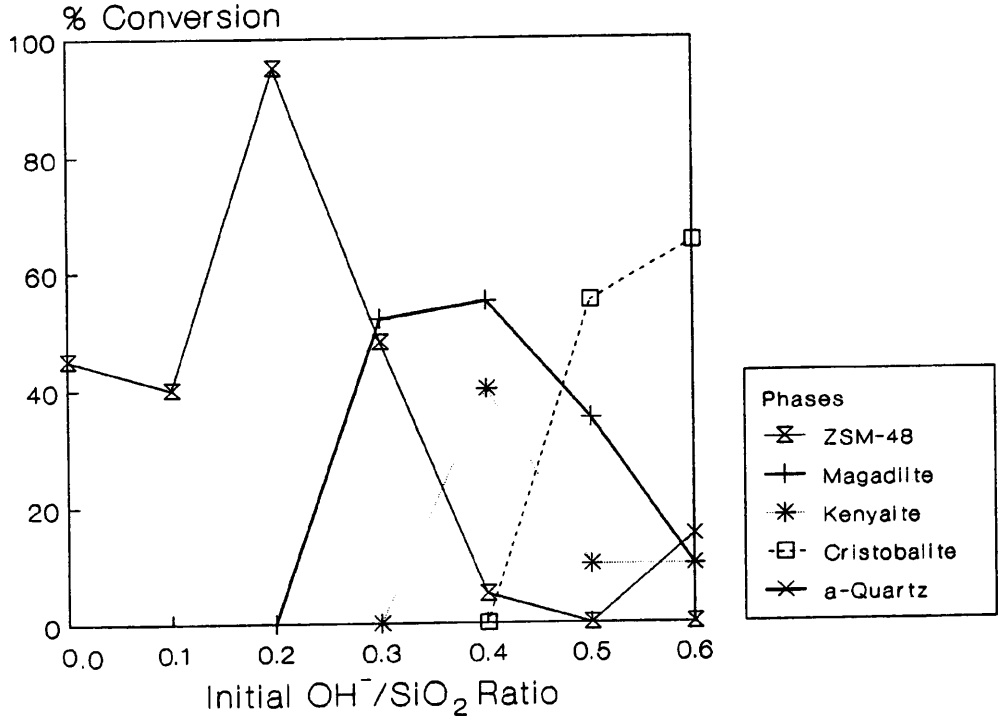


**Figure 3.5. Effect of the initial $OH^-/SiO_2$ ratio on the product distribution at 175°C.**

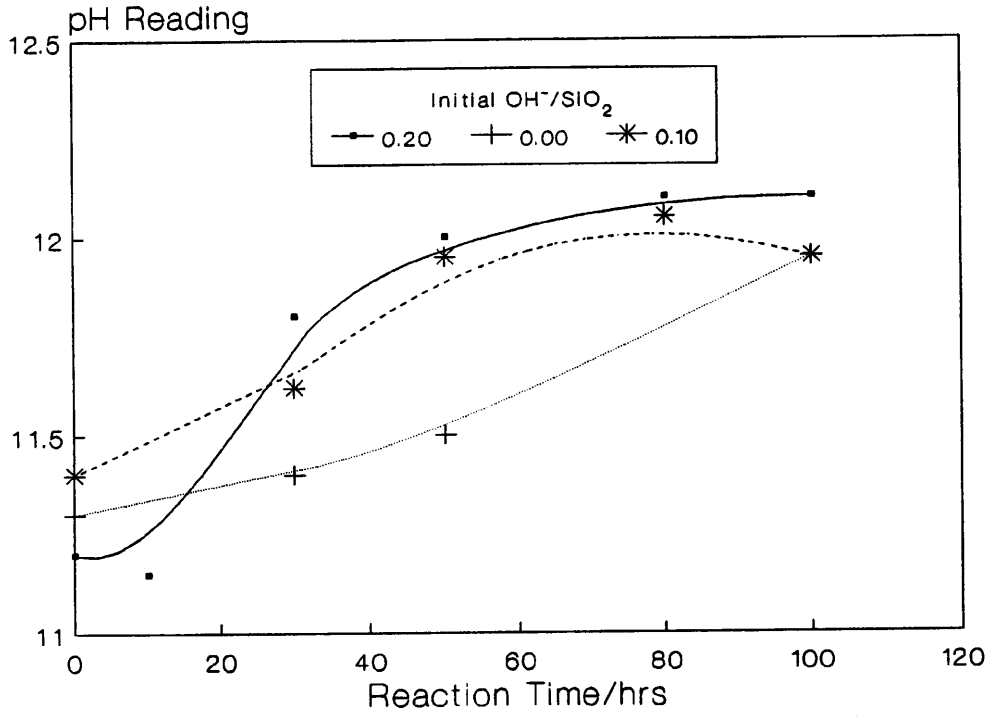


**Figure 3.6. Change in pH during the synthesis of ZSM-48 at 175°C.**

SEM studies revealed that changes in the initial $OH^-/SiO_2$ ratio influence the crystal size and morphology of ZSM-48. Figure 3.7 shows the series of micrographs for the initial $OH^-/SiO_2$ ratios of 0.10, 0.20 and 0.30 after 48 hours. When the initial $OH^-/SiO_2$ ratio was 0.10 the crystalline phase was composed of either single and twinned large bow-tie-shaped crystal aggregates around 30μm in length or of regular cylindrical crystal collections 3 x 10μm in size. Similar to the crystal morphology of ZSM-48 previously described in section 3.31 these aggregates were composed of linear, single, needle-like crystallites. The development of such a bimodal crystal distribution may arise from secondary nucleation processes [27]. During the course of the reaction at two periods of time, sufficient levels of supersaturation occurred to initiate nucleation.

At the optimum initial $OH^-/SiO_2$ ratio of 0.2 both single crystals, 6 x 13-15μm in size, and twinned crystals, 13-15$\mu m^2$ in size, were found. These are noticeable less *necked* than the crystals produced at lower alkalinity. This may be a result of the differences in gel composition and dissolution processes. Above the optimum basicity ratio the crystalline phase is associated with leaf-like collections of magadiite as shown in Figure 3.7c.

Impurities in the crystallising solution often inhibits the growth of a crystal in given crystallographic direction [27]. This may explain the accentuated crystal morphology of ZSM-48 especially at lower $OH^-/SiO_2$ ratios. Hayhurst et al.[28] reported an increase in the *aspect ratio* (crystal length/width) of silicalite-1 with increases in the gel hydroxide ion concentration. It was suggested that differences in the growth rate along a particular crystallographic axis corresponded to different silicate species participating in the crystal growth processes.

The alkalinity of the initial reaction gel also influenced the synthesis of silicalite-2. Figure 3.8 shows the effects of the initial $OH^-/SiO_2$ ratio on the reaction kinetics of silicalite-2 together with corresponding pH changes over the reaction period. The product conversion with respect to the initial $OH^-/SiO_2$ ratio after 120 hours is shown in Figure 3.9.

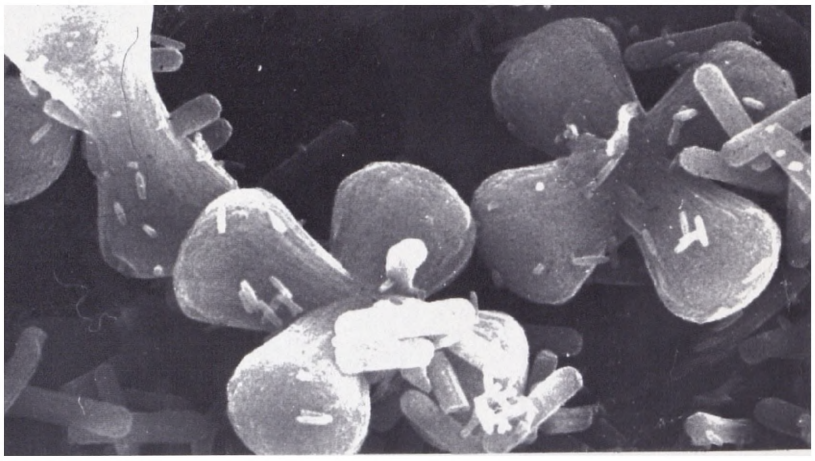


a. Initial $OH^-/SiO_2$=0.10


b.Initial $OH^-/SiO_2$=0.20

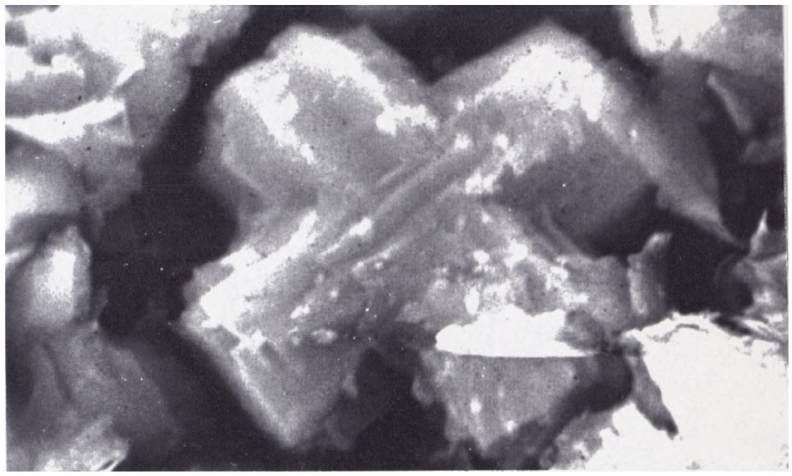


c. Initial $OH^-/SiO_2$=0.3

**Figure 3.7. SEMs of ZSM-48 synthesised at 175°C after 48 hours with several initial $OH^-/SiO_2$ ratios.**

Highly crystalline silicalite-2 was obtained between the initial $OH^-/SiO_2$ ratios of 0.15 to 0.30 after 120 hours. Previously only an impure silicalite-2 phase using DAO as the organic additive had been reported [4]. The effects of the initial gel basicity on the nucleation and crystallisation rates of the zeolites synthesised can be summarised as follows:

| NUCLEATION RATE | CRYSTALLISATION RATE |
|---|---|
| Rate decreases in the order of Initial $OH^-/SiO_2$ Ratio | |
| 0.20 > 0.15 > 0.30 | 0.20 > 0.30 > 0.15 |

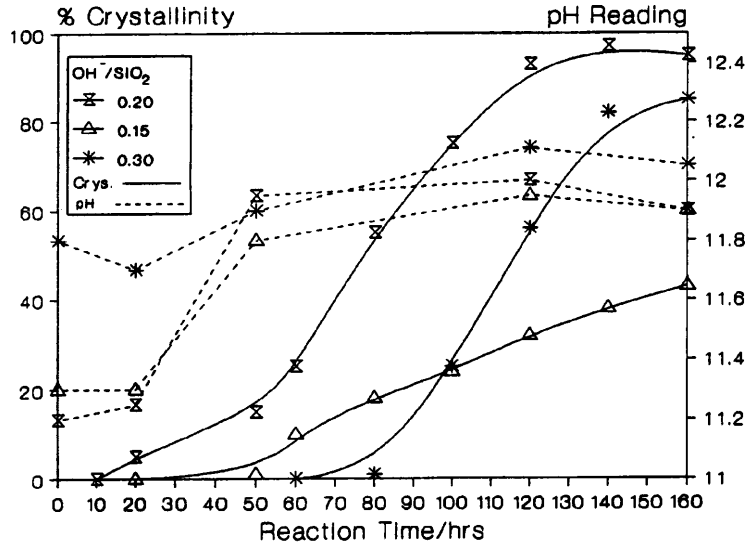


**Figure 3.8. Effect of initial $OH^-/SiO_2$ ratio on the reaction kinetics of silicalite-2 at 130°C.**

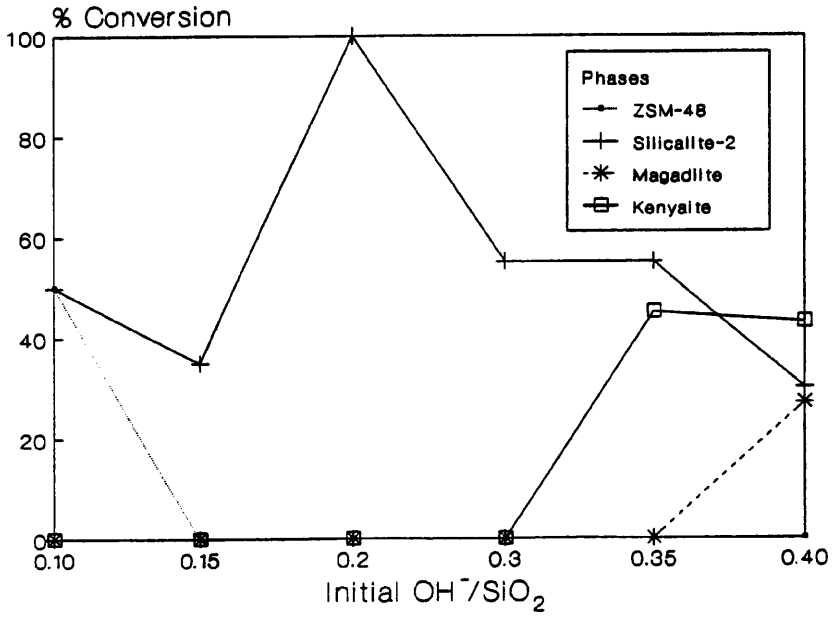


**Figure 3.9. Phase development as a function of gel alkalinity after 120 hours at 130°C.**

The optimum $OH^-/SiO_2$ ratio in terms of the nucleation and crystallisation rates for the synthesis of silicalite-2 is 0.20. In comparison to the synthesis of ZSM-48, the largest change in gel pH was experienced in this reaction system. Comparing results obtained at the other basicity ratios, nucleation is more favoured at the lower value of 0.15. In contrast, the crystallisation rate is enhanced at the higher ratio value of 0.3. Although there are a greater number of monomers available at a higher alkalinity for crystal growth, such an environment can prevent the formation of stable nuclei. When the $OH^-/SiO_2$ ratio was decreased to 0.10 the synthesis product was composed of a physical mixture of silicalite-2 and ZSM-48. This was confirmed by SEM analysis as shown in Figure 3.10. The micrograph clearly shows a bimodal distribution of crystalline products consisting of either smooth rectangular crystals, 4 x 10μm in size, or single and twinned and aggregated bow-tie-shaped crystals of varying size between 10-20μm in length. The morphologies compare well to those previously described in section 3.31 for silicalite-2 and ZSM-48, respectively. A similar product development was noted in similar synthesis studies of Rollmann et al.[2].

Raising the initial $OH^-/SiO_2$ ratio above 0.3, denser phases such as magadiite and kenyaite were increasingly associated with silicalite-2 from nucleation. However, transformation of all these phases to cristobalite and α-quartz took place in the later stages of the crystallisation period. Samples of the solid products were taken over the reaction period and studied by XRD. The results revealed an equivalent rate of nucleation and crystallisation for both phases.

The micrographs of silicalite-2 synthesised at an $OH^-/SiO_2$ ratio between 0.20 and 0.30 after 120 hours are depicted in Figure 3.11. At the optimum initial $OH^-/SiO_2$ ratio of 0.2 silicalite-2 is made that consists of monodispersed, smooth-surfaced, tablet-shaped crystals. They are approximately 3 x 7μm in size. Similarly shaped crystals were obtained from reactions where the basicity ratio was increased to 0.3. However, the average crystal size is reduced to 3 x 5μm. Generally, the nucleation period is increased in more basic environments [16] so a larger number of stable nuclei is formed. Thus smaller crystals are synthesised and the available silicate species are rapidly consumed during crystallisation [28].

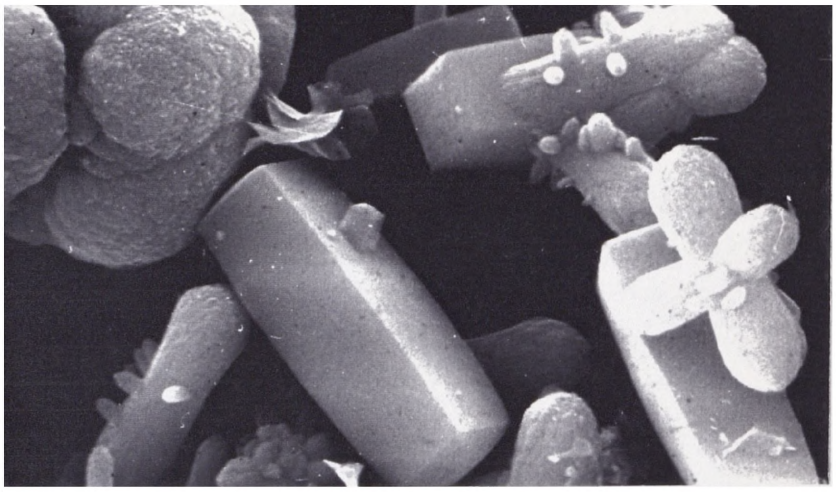


**Figure 3.10. SEM of physical mixture of silicalite-2 and ZSM-48 synthesised at 130°C after 120 hours with an initial $OH^-/SiO_2$=0.10.**

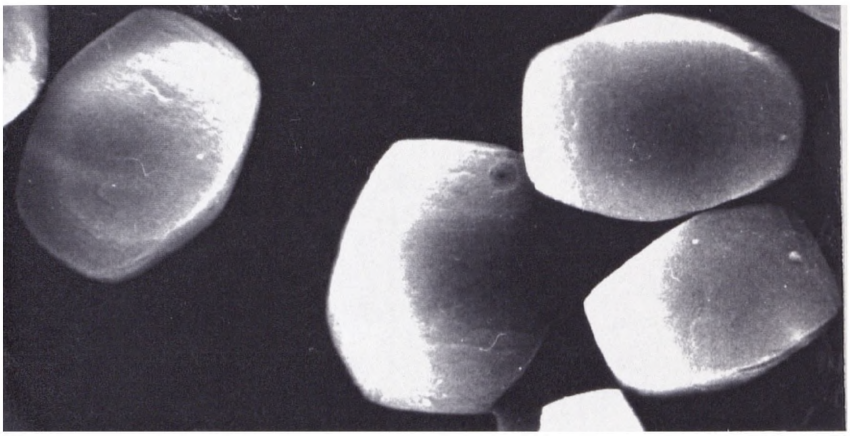


**Figure 3.11a. Initial $OH^-/SiO_2$=0.2.**

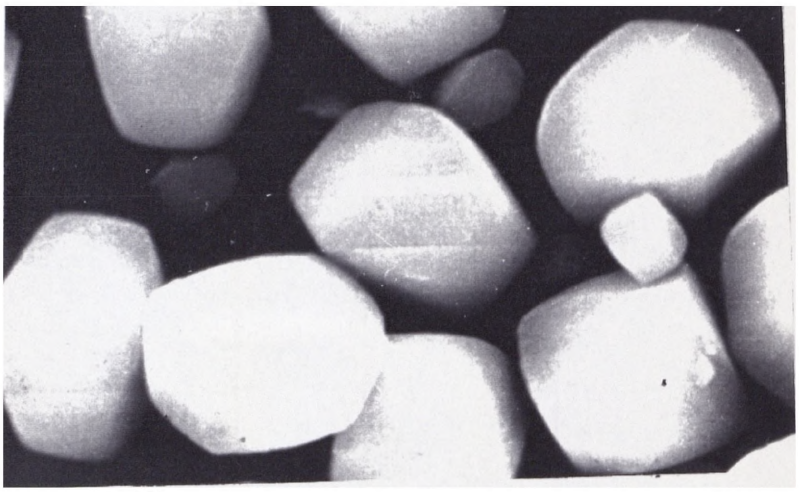


**Figure 3.11b. Initial $OH^-/SiO_2$=0.3.**

**Figure 3.11. SEMs of silicalite-2 synthesised at 130°C after 120 hours at various initial $OH^-/SiO_2$ ratios.**

Franklin et al. [10] suggested that the synthesis of ZSM-48 at low $OH^-/SiO_2$ ratios does not require very stringent reaction conditions. As a result the growth mechanism can readily accommodate a variety of silicate building units. In contrast, the development of silicalite-2 requires a greater concentration of monomeric silicate ions associated with gels at higher alkalinity. Similarly in this work, the synthesis of silicalite-2 required stricter reaction conditions than that of ZSM-48. It is worth noting that the optimum $OH^-/SiO_2$ ratio for the synthesis both ZSM-48 and silicalite-2 was 0.2. This suggests there is an optimum pH for the structure-directing ability of DAO.

### 3.3.3. The Effect of Inorganic Cation Variation in an All-Silica Reaction System

During the initial gel preparation equimolar amounts of either NaOH, KOH or NaOH/KOH (1:1, mol:mol) were added. The initial $M_2O/SiO_2$ molar ratio was 0.3 or 0.15. The gels were heated at 130°C, statically or agitated by revolving at approximately 80 rpm. for a total reaction time of 120 hours. A series of syntheses were performed in the absence of a mineralising agent.

The starting stoichiometry of these reactions can be represented as follows,

$$37.8SiO_2 - 0.0Al_2O_3 - x(DAO)_2O - 2488.3H_2O$$

where x equals 18.9 or 9.45. The gels containing no $M^+$ ions were heated statically at 130°C or 175°C for 800 hours.

In both the $Na^+$ and $K^+$ ion systems, x-ray analysis revealed that silicalite-2 was the only zeolite synthesised. The wet chemical analysis of the crystalline product is summarised in Table 3.2. Figure 3.12 reveals the effect of the $M^+$ ion type on the crystallinity of silicalite-2. With the addition of $K^+$ ions both the nucleation and crystallisation rates were enhanced. In agreement with silicalite-1 synthesis studies [7], the crystallinity of silicalite-2 is increased by raising the initial $Na_2O/SiO_2$ ratio from 0.15 to 0.30. The use of static rather than agitated reaction conditions also reduced the product crystallinity. Agitation increases the homogeneity of the reaction mixture assisting a more mutual contact of reactant species and rate of gel dissolution. Consequently, reaction rates are enhanced.

| $M^+$ Ion Used in Synthesis | Percent[a] Crystallinty | Molar C/N Ratio | Unit Cell Contents M | DAO |
|---|---|---|---|---|
| Na | 73 | 4.4 | 2.4 | 4.5 |
| Na s | 60 | 4.0 | 2.0 | 3.0 |
| K | 98 | 4.6 | 0.2 | 4.6 |
| K/Na | 80 | 4.0 | 0.2(Na) <0.05 (K) | 4.9 |

a. Percentage crystallinity after 120 hours.

s. Synthesised under static conditions

**Table 3.2. Wet chemical analysis of $M^+$-silicalite-2.**

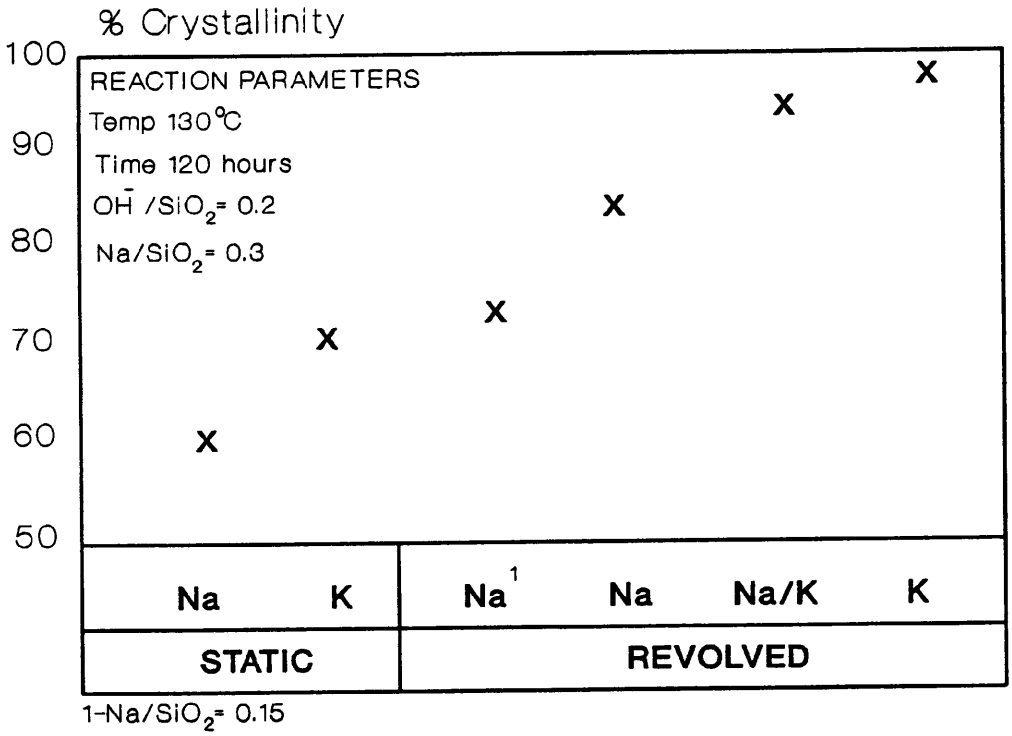


**Figure 3.12. Effect of the $M^+$ ion type on silicalite-2 synthesis.**

In all cases DAO is assumed to be intact, as the C/N molar ratio is approximately 4, and sited within the pore system of silicalite-2. Independent of the $M^+$ ion source the crystalline materials synthesised from the agitated reaction experienced an approximate 85-90% DAO pore-filling capacity. There are clear differences, however in the

$M^+$ ion content of the crystalline material depending on the type of $M^+$ ion used. The results show that far less $K^+$ than $Na^+$ ions are present within the structure of silicalite-2. Similarly, the presence of $K^+$ ions in the $Na^+$ ion system reduced the overall $M^+$ ion content together with a corresponding increase in crystallinity of the materials. Overall, the results imply that the $M^+$ ion source is more influential in the events taking place during nucleation.

There are several ways of interpreting the role of the $M^+$ ion during zeolite synthesis, but literature provides only contradicting views [16]. Erdem et al.[29] found a similar enhancement of reaction rates on the replacement of $Na^+$ by $K^+$ ions in the synthesis of ZSM-5. They suggested that the increase in rates could be a potassium selectivity for the building units of the framework structure. However, Jacobs et al.[16] related a decrease in the activation energy for nucleation of zeolites proportional to a increase in the electrostatic potential (1/r) of the cation, where r is the ionic radius of the $M^+$ ion ($Na^+$=1.04Å and $K^+$=1.38Å). Consequently, at the same moment the overall rate of nucleation also rises. In view of this, the increase in nucleation rate of the $K^+$ ion system, in this study, may be explained by a less efficient competition of $K^+$ ions for DAO compared with $Na^+$ ion which simply reflects a more efficient use of DAO.

Alternatively, physical nature of the gel is known to influence reaction rates as discussed in Chapter 1. During the preparation of the zeolites it was noticed that the viscosity of the $Na^+$ ion gel was greater than in the presence of $K^+$ ions. This can be related to the larger hydration sphere experienced by the $Na^+$ ions in solution [30]. Consequently, $K^+$ ion gels promote the dissolution of the silica. A more mutual interaction of reaction species enhances the reaction rates during zeolite synthesis.

Figure 3.13 summarises the micrographs obtained from the agitated $Na^+$, $K^+$, and $Na^+/K^+$ ion synthesis systems after 120 hours. Although smaller in size, the crystal morphology of products from each reaction system is similar to that of the $Na^+$ ion system previously described in section 3.31. The zeolites are composed of single monodispersed, tablet-like and cuboid crystals. The crystal sizes obtained from the $K^+$ ion system are slightly irregular ranging between 3-5μm in length. Occasionally, some smaller crystal approximately 1.0$\mu m^2$ were observed.

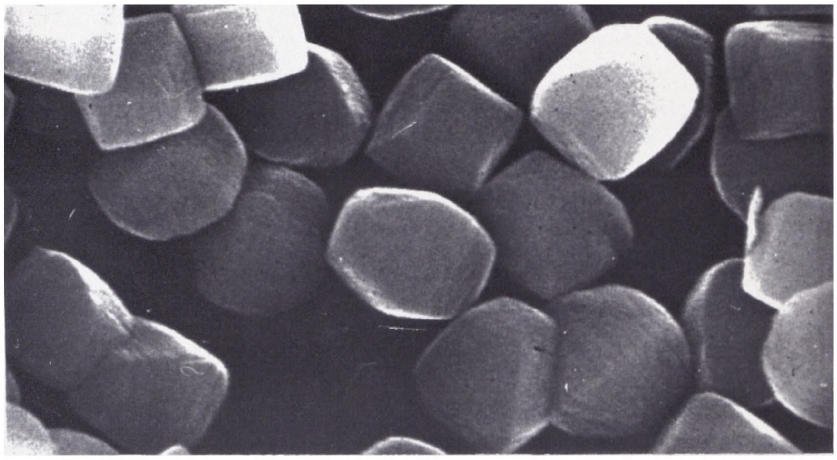


**Figure 3.13a. $Na^+$ ion system crystalline products.**

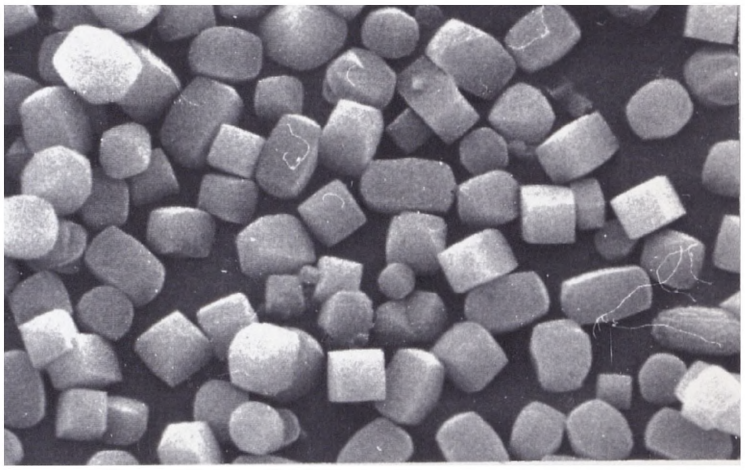


**Figure 3.13b. $K^+$ ion system crystalline products.**

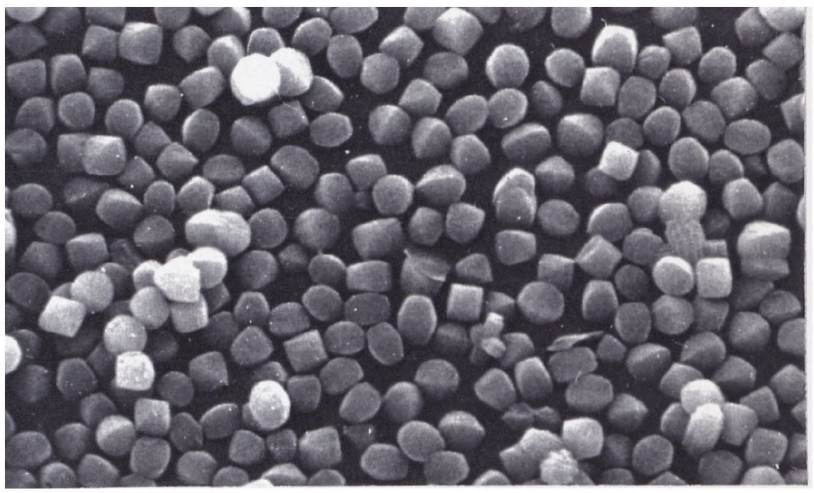


**Figure 3.13c. Mixed $Na^+/K^+$ ion system.**

**Figure 3.13. SEMs of silicalite-2 synthesised at 130°C after 120 hours with various $M^+$ ions.**

Overall, more regularly sized and smaller crystals are obtained from the $Na^+$ and mixed ion reaction systems which have a typical length of 1.75-2.0μm. A similar crystal size dependency for the synthesis of ZSM-5 using a variety of $M^+$ ions was reported by Nagy et al.[31].

Gels prepared excluding a mineralising agent (NaOH/KOH) were sufficiently basic for the depolymerisation of the silica source and zeolite formation. However, both the nucleation and crystallisation rates of the reaction systems were severely inhibited. In agreement with similar studies [10] the crystallinity of the materials is enhanced by increasing the initial $R_2O/SiO_2$ ratio. XRD analysis, as summarised in Table 3.3, revealed that ZSM-48 is the only product obtained at either 130 or 175°C after 800 hours. At the lower temperature the crystallinity of ZSM-48 is approximately 30%, whereas at the higher temperature, depending on the initial gel organic content, the crystallinity of ZSM-48 is between 85-95%.

Although the autoclaves were not frequently sampled, it was established that the nucleation of the zeolites formed at 175 and 130°C occurred after 300 and 500 hours, respectively. This suggests that inorganic cations assist in the nucleation processes. The absence of silicalite-2 in the synthesis product at 130°C suggests that $M^+$ ions facilitate the formation of more open structures. As mentioned in section 3.3.1, under more demanding reaction conditions denser phases, in this case ZSM-48, are synthesised. These results show a limit to the structure-directing abilities of DAO.

| Reaction Temp/°C | Initial $(DAO)_2O/SiO_2$ | % Crystallinity of ZSM-48[b] | Unit Cell Contents | |
|---|---|---|---|---|
| | | | DAO | M |
| 175 | 0.50 | 95 | 1.0 | <0.01 |
| 175 | 0.25 | 86 | 0.8 | <0.03 |
| 130 | 0.50 | 36 | a | a |
| 130 | 0.25 | 50 | a | a |

a. Chemical analysis not performed
b. Percentage crystallinity after 800 hours

**Table 3.3. Products obtained from *$M^+$ free* synthesis at 130°C and 175°C after 800 hours.**

Wet chemical analysis of the crystalline materials are previously given in Table 3.3. The results show that the $M^+$ ion and aluminium content of the crystalline phases are negligible. The trace amounts present are probably a result of impurities associated with the starting reagents. The DAO pore-filling capacity of ZSM-48 synthesised with an initial $(DAO)_2/SiO_2$ ratio of 0.50 or 0.25 is around 91 or 73%, respectively. These results compare to those obtained for the ZSM-48 synthesised from $Na^+$ ion system, where all the available channel space is occupied by DAO. In agreement with Barrer [12] a more crystalline material is obtained when a greater percentage of the zeolite's pore volume is occupied and stabilised by *guest* species.

The series of micrographs of ZSM-48 synthesised at 130 and 175°C are shown in Figure 3.14. At either reaction temperature the crystalline material was composed of either individual needle-like crystallites varying in size between 10-20μm in length and irregular aggregates of the needle-like crystals up to 50μm in length. ZSM-48 synthesised at 130°C is also associated with a large amount of amorphous deposits or unreacted material.

### 3.3.4. The Influence of the Initial $SiO_2/Al_2O_3$ Ratio

The original gel was prepared with various amounts of aluminium nitrate dissolved in the sodium hydroxide solution before the addition of fumed silica. The initial $OH^-/SiO_2$ ratio was controlled by the corresponding incremental addition of nitric acid (70%) as outlined in Appendix 1. The starting stoichiometries can be summarised by the following equation:

$$\mathbf{18.4Na_2O - 61.1SiO_2 - xAl_2O_3 - 15.5(DAO)_2O - 4032.6H_2O.}$$

The amount of x was varied between 3.0 and 0.12. The molar ratios were as stated in section 3.2 apart from,

1. $OH^-/SiO_2$ = 0.10 or 0.30.
2. $SiO_2/Al_2O_3$= 500*, 240, 200*, 150*,120, 90, 60, 40, 30, 20,

(* - Only performed at 130°C).

The gels were heated under static conditions at either 130 or 175°C for a total reaction time between 100 and 800 hours or 48 and 500 hours, respectively.

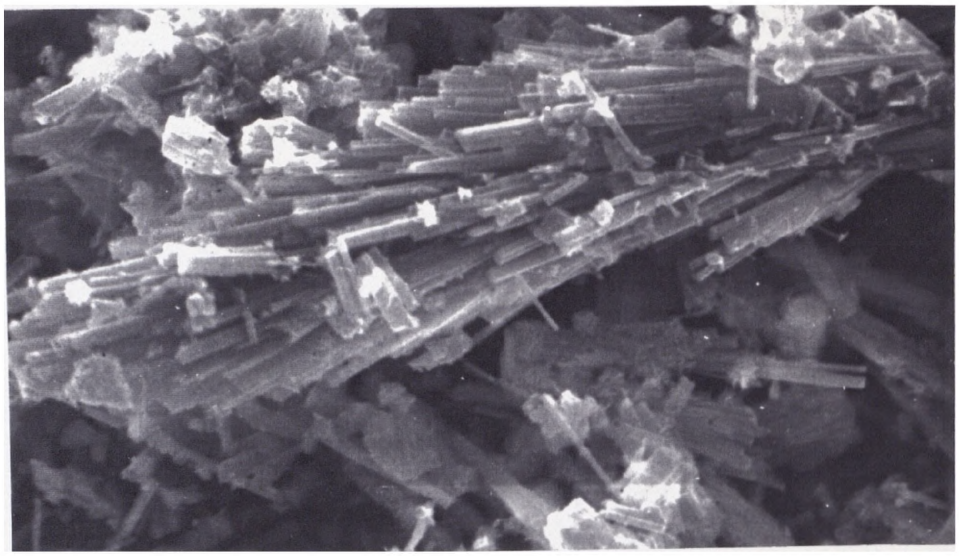

SCALE
10μm

**Figure 3.14a. Products synthesised at 175°C.**

SCALE
10μm

**Figure 3.14b. Products synthesised at 130°C.**

**Figure 3.14. SEM of crystalline products obtained from the all-silica reaction system in the absence of a $M^+$ ion after 800 hours.**

Compared to the all-silica studies described in section 3.31, the presence of aluminium during synthesis resulted in changes in the product distribution and reaction rates. Figure 3.15 compares the x-ray diffractograms of the crystalline products obtained at 175°C after 48 hours and at 130°C after 100 hours with those of the products obtained with the initial $SiO_2/Al_2O_3$ and $OH^-/SiO_2$ ratio of 200 and 0.10, respectively. In agreement with Rollmann et al.[3] the results show that ZSM-11, the structural analogue of silicalite-2 [32], was synthesised at either reaction temperature in the presence of DAO. Moreover, ZSM-11 is the only zeolite obtained at either reaction temperature or initial $OH^-/SiO_2$ ratio between the $SiO_2/Al_2O_3$ ratios of 20-500. In contrast to the all-silica systems, throughout the study there is no evidence of ZSM-48 in the crystalline product. The effects of aluminium incorporation into the zeolite framework overrides the influence of framework density on the nature of the zeolite formed. This probably reflects a change in the role of DAO moving from a siliceous to an aluminous reaction environment.

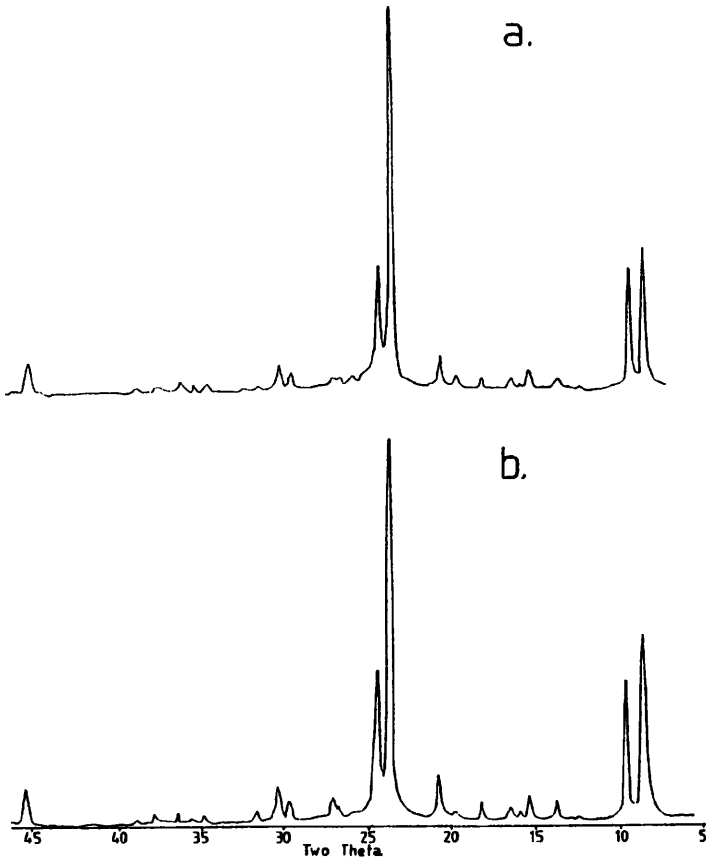


**Figure 3.15. XRD of crystalline products synthesised at a. 130°C after 100 hours and b. 175°C after 48 hours.**

Other workers [33] have noted the difficulties in synthesising aluminous ZSM-48 with diamines. Diquats, organic additives such as diquat-6, $(CH_3)_3N^+(CH_2)_6N^+(CH_3)_3$, [34] have been used as effective structure-directing agents for the synthesis of ZSM-48 over a range of $SiO_2/Al_2O_3$ ratios. These organic additives are thought to be more efficient than diamines in complexing aluminium species and incorporating them into the lattice due to a comparably higher positive charge density.

On repeating the high temperature synthesis with an initial $SiO_2/Al_2O_3$ ratio of 20, ferrierite (FER) [6] co-crystallised with ZSM-11 in the initial stages of crystallisation. In the latter stages of the reaction the FER content in the reaction product was reduced by phase transformation to ZSM-11. This reaction was investigated further and is discussed in section 3.35. The syntheses performed at 130°C with an initial $OH^-/SiO_2$=0.3 were only partially successful. Increasing the initial $SiO_2/Al_2O_3$ ratio above 150 gave rise to greater amounts of magadiite in the solid product and a longer crystallisation period was required for the synthesis of ZSM-11. Consequently, the following discussions are mainly concerned with ZSM-11, synthesised at 175°C with an initial $OH^-/SiO_2$ ratio of 0.10. As in the synthesis of ZSM-5 [21], increases in the aluminium content of the initial gel coincided with an increase in both the nucleation and crystallisation rates of ZSM-11. This is illustrated in Figure 3.16.

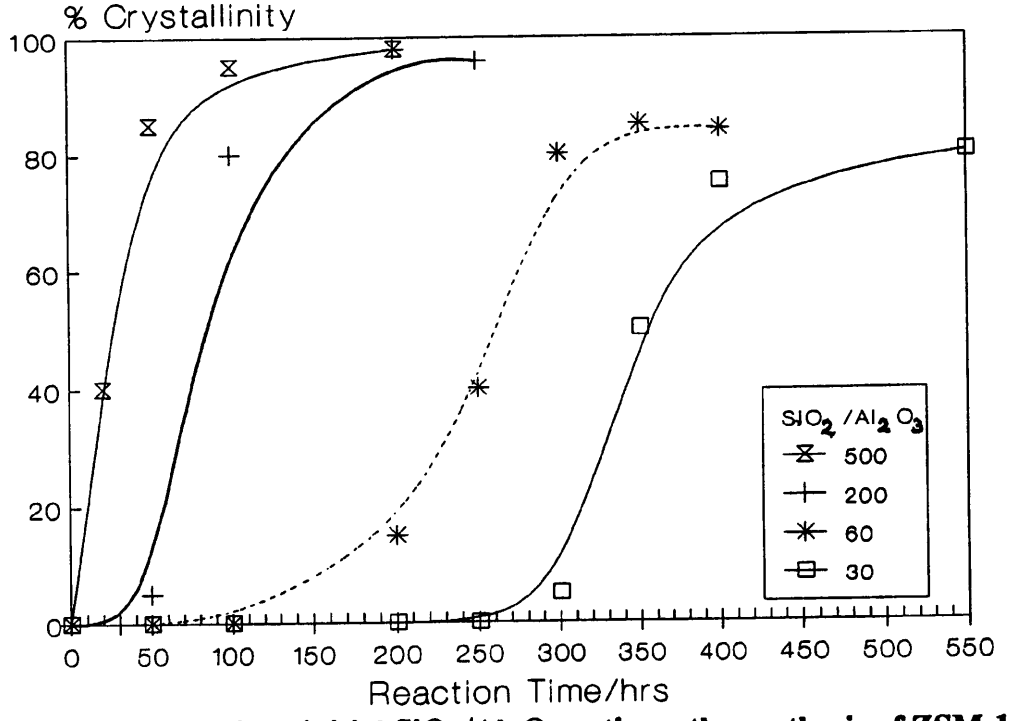


**Figure 3.16. Effects of the initial $SiO_2/Al_2O_3$ ratio on the synthesis of ZSM-11.**

The incorporation of aluminium into the pentasil framework is thought to be a disruptive process [35]. Alternatively, aluminate ions in solution consume $OH^-$ ions to form $Al(OH^-)_n^{(3-n)}$ species. Consequently, there is a decrease in $OH^-$ ions available for the depolymerisation of the gel resulting in an increase in the reaction period [21]. Chemical analysis of the crystalline phases revealed that the insertion of aluminium into the framework of ZSM-11 is efficient. This corresponds to a linear relationship between the aluminium content in the gel and the zeolite as depicted in Figure 3.17. In agreement with similar studies [3], this shows that DAO is a very effective structure-directing agent as ZSM-11 was synthesised over a wide range of compositions. The chemical analysis also shows that irrespective of the product Si/Al ratio, around 4.0-4.5 intact DAO molecules per unit cell are associated with the crystalline phase. This compares to the organic content silicalite-2 synthesised previously. This shows that due to the size of DAO and the structure of MEL the maximum pore-filling of DAO is around 75-85%.

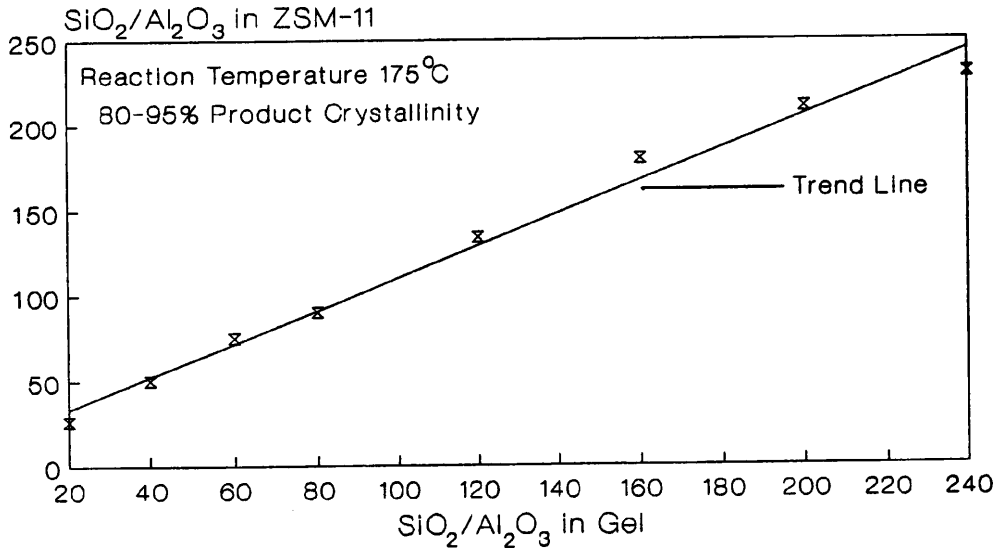


**Figure 3.17. Comparison of gel and crystalline ZSM-11 aluminium content.**

Independent of the product $SiO_2/Al_2O_3$ ratio, the molar Al/Na ratio of the crystalline products is always greater than unity. This suggests that DAO is present in the zeolite pore system in a partially protonated form, functioning as both a charge-balancing ion and structure-directing agent. However, as illustrated in Figure 3.18, the $Na^+$ ion content of ZSM-11 increased with a decrease in the product $SiO_2/Al_2O_3$ ratio. A similar trend was reported for the synthesis of

ZSM-5 [29]. This illustrates a limit to the charge-balancing abilities of DAO, which is likely to be a geometric effect. $Na^+$ ions are more efficient in this role, especially when associated with zeolites with a high aluminium content. The alkali cations are believed to assist the redispersion of the Al-bearing species into tetrahedrally coordinated aluminium in the gel [29]. It is also assumed that the $Na^+$ ion can access all Al sites, whereas the access to a site for DAO may be blocked by another DAO molecule.

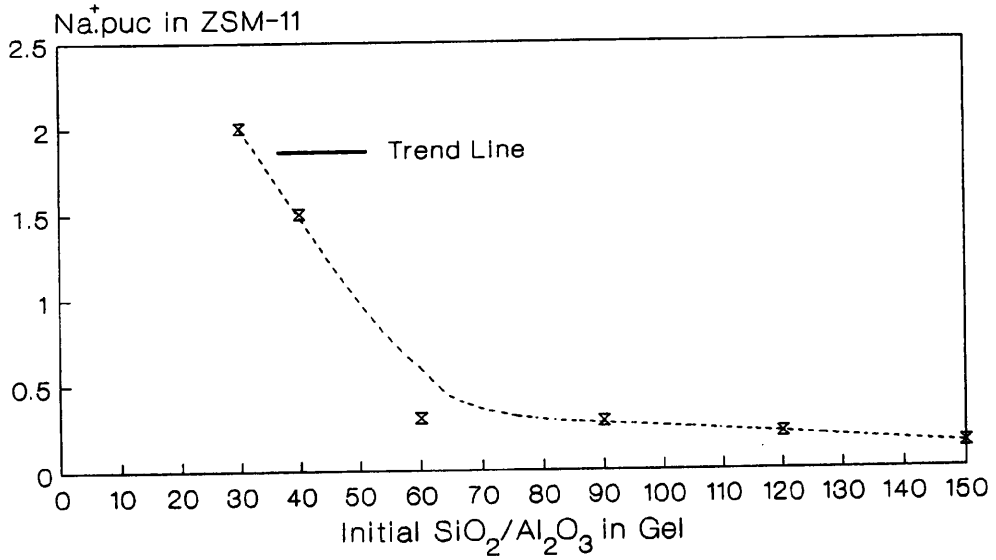


**Figure 3.18. Correlation of the aluminium and $Na^+$ ion content of ZSM-11.**

Several changes in crystal size and morphology were observed from SEM analysis of several ZSM-11 products of equivalent crystallinity (> 90%) dependent upon the initial $SiO_2/Al_2O_3$ ratio. The appearance of the crystals also contrasted to that of silicalite-2, described in section 3.31., but are comparable to ZSM-11 described in the literature. The micrograph of a ZSM-11 product obtained after 48 hours at 175°C with an initial $SiO_2/Al_2O_3$ ratio of 240 is shown in Figure 3.19a. The product is composed of a bimodal distribution of spherical single crystals either 12 or 3μm in diameter which is indicative of secondary nucleation.

Figures 3.19b and 3.19c show the micrographs of ZSM-11 obtained using initial $SiO_2/Al_2O_3$ ratios of 120 or 60 after 100 and 150 hours, respectively. Both products are composed of heavily twinned and multifaceted, spherical crystals. The crystal diameter of the former product is approximately 10μm; the latter product ranged

between 1-6μm. This reflects the disruptive effect of increasing the aluminium content of the gel on crystal growth processes. Interestingly, at the lower initial $SiO_2/Al_2O_3$ ratio of 40 the crystal morphology was altered. After a reaction period of 200 hours monodispersed, smooth, spherical crystals with an approximate diameter of 10μm were obtained, as shown in Figure 3.19d.

Changes in the crystal size of ZSM-5 with the aluminium content of the initial gel have been reported [36]. The gel-dissolution process is directly influenced by the aluminium content of the reaction mixture [21]. Consequently, both the rate of nucleation and the nature of crystal growth processes are affected [28]. In this study, the morphological differences altered in an unpredictable manner, highlighting the complicated processes occurring during crystallisation.

### 3.3.5. The Effect of Inorganic Cation Variation in an Aluminous Reaction System

The gels were prepared as outlined in section 3.34 using NaOH or KOH as the mineralising agent. The initial starting stoichiometry can be represented by the following equation:

$$18.4M_2O - 61.0SiO_2 - xAl_2O_3 - 15.5(DAO)_2O - 4032.0H_2O$$

where M represents the inorganic cation $K^+$ or $Na^+$ and x varied between 8.2 and 0.3. The initial $OH^-/SiO_2$ ratios were between 0.00 and 0.30. The gels were then heated, unless otherwise stated, statically at 130 or 175°C for six and four days, respectively. Reactions were also investigated excluding an $M^+$ ion source. In this case the gels were composed of fumed silica, aluminium nitrate, DAO and distilled water with initial $SiO_2/Al_2O_3$ ratios of 146 and 315. For these syntheses the total reaction period was 35 days and 60 days at 175 and 130°C, respectively.

Results were obtained from a single sample study. Therefore the reaction kinetics of the $M^+$ ion systems will not be discussed. In contrast to the all-silica system, x-ray analysis of the crystalline products revealed that changing the $M^+$ ion source resulted in the synthesis of a number of zeolites in addition to ZSM-11. The results are summarised in Table 3.4. Araya et al.[5] found a similar phase dependence on the inorganic cation source with high-silica zeolites synthesised with diamines.

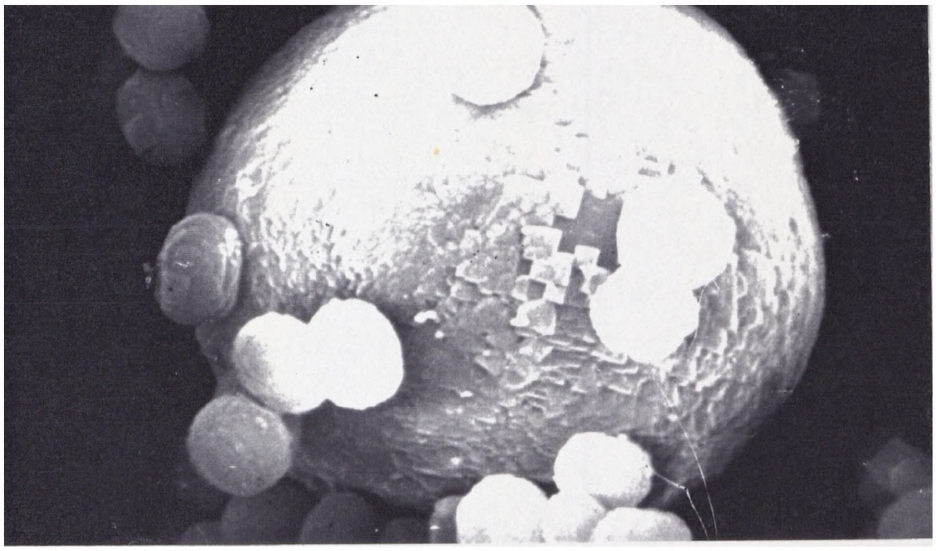

SCALE
3μm

**Figure 3.19a. Initial $SiO_2/Al_2O_3$=240 after 48 hours.**

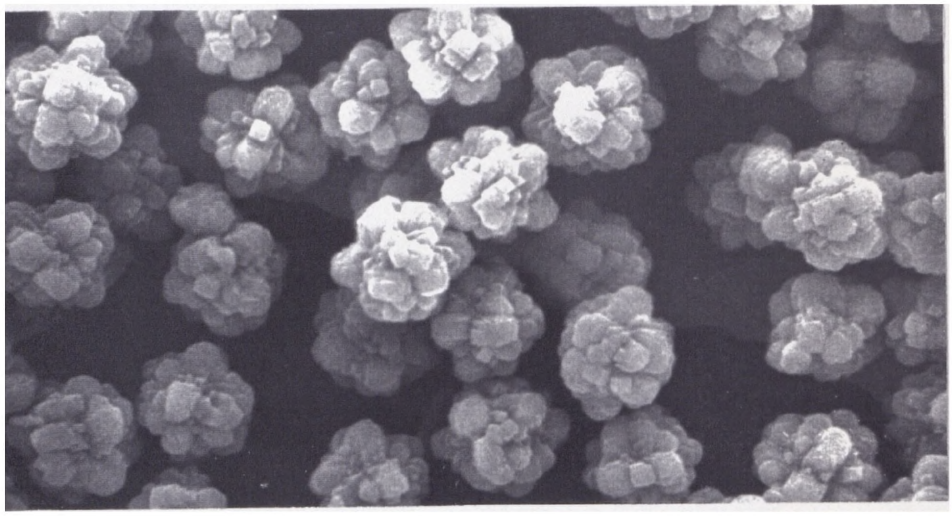

SCALE
10μm

**Figure 3.19b. Initial $SiO_2/Al_2O_3$=120 after 100 hours.**

**Figure 3.19. SEMs of ZSM-11 synthesised at 175°C with various initial $SiO_2/Al_2O_3$ ratios.**

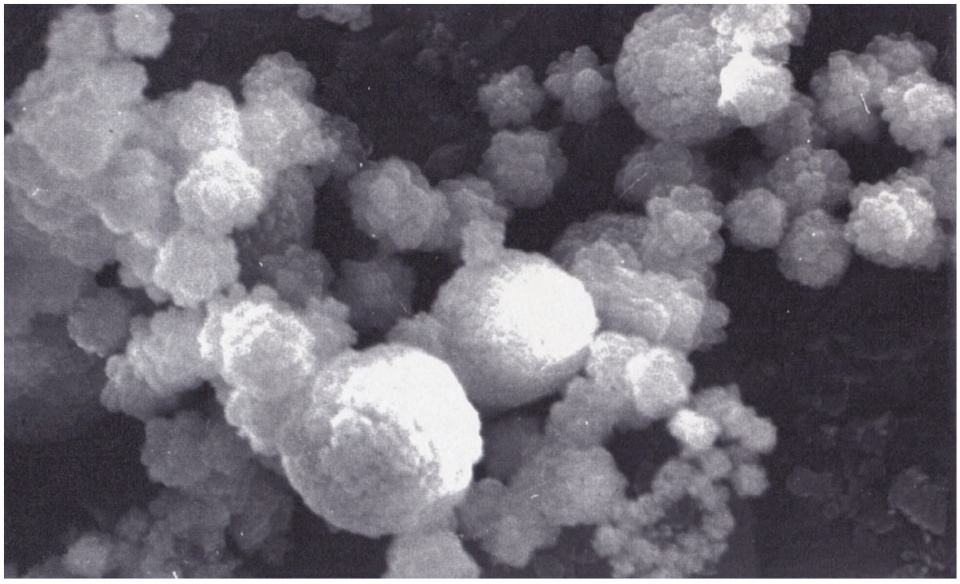

SCALE
5μm

**Figure 5.19c. Initial $SiO_2/Al_2O_3$=60 after 150 hours.**

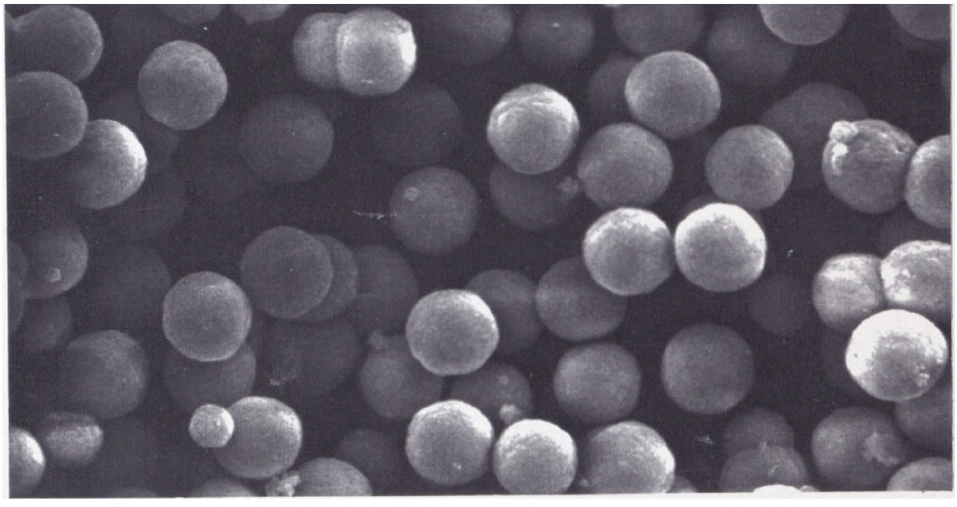

SCALE
20μm

**Figure 5.19d. Initial $SiO_2/Al_2O_3$=40 after 200 hours.**

As in the $Na^+$ ion system studied, x-ray analysis revealed that ZSM-11 was synthesised at 175°C in the presence of $K^+$ ions when the initial $OH^-/SiO_2$ ratio was 0.10 and the initial $SiO_2/Al_2O_3$ ratios varied between 250 and 80. Overall, the crystallinity of the ZSM-11 decreased with increasing aluminium content of the initial gel as summarised in Figure 3.20. In contrast, when the initial $SiO_2/Al_2O_3$ ratio was reduced to 28 and the $OH^-/SiO_2$ ratio was reduced from 0.10 to 0.05 TON [6,44] co-crystallised with ZSM-11. At the higher initial $OH^-/SiO_2$ ratio of 0.3, ZSM-5 and α-quartz were synthesised.

| $M^+$ Ion Type | Initial Ratios $SiO_2/Al_2O_3$ | Initial Ratios $OH^-/SiO_2$ | S/R [1] | Products |
|---|---|---|---|---|
| Na | 500-20 | 0.10-0.30 | S | ZSM-11 |
| K | 250-80 | 0.10 | S | ZSM-11 |
| Na | 30 | 0.05,0.10 | S | ZSM-11 |
| K | 28 | 0.10,0.20 | R | ZSM-11 + Trace TON |
| K | 28 | 0.05 | R | ZSM-11 + TON (2:1) |
| $K_2$ | 28 | 0.05 | S | ZSM-11 + TON (5:1) |
| $K_3$ | 28 | 0.05 | R | TON |
| K | 28 | 0.30 | R | ZSM-5 + quartz (2:1) |

1. Static or revolved
2. Synthesis performed at 130°C
3. Gel dilution increased to $H_2O/SiO$ =80.0

**Table 3.4. Phases synthesised at 175°C from $Na^+$ and $K^+$ ion systems.**

A similar phase development of NU-4 (a ZSM-5 family zeolite), with Nu-10 at higher basicity values in the presence of polyamines, has been reported [38]. In the present study, the content of TON in the crystalline product is increased either by stirring or diluting the synthesis gel. In the latter case, the initial $H_2O/SiO_2$ ratio was increased from 66 to 80. Figure 3.21 shows the XRD of TON synthesis under these conditions. Several workers have shown that the synthesis of TON is favoured with $K^+$ ions compared to $Na^+$ ions and that it is sensitive to small changes in the reaction parameters [5].

A decrease in reaction temperature from 175 to 130°C favoured the crystallisation of ZSM-11 over TON. Araya et al.[5] reported that a reduction in reaction temperature promoted the synthesis of TON over ZSM-5 when DAH was used as the organic additive. This reflects the structure-directing abilities of diamines for zeolite synthesis. In the present work a decrease in the initial $OH^-/SiO_2$ ratio or $OH^-$ ion concentration favoured the synthesis of TON over ZSM-11. A similar effect was described in section 3.33 concerning the crystallisation of ZSM-48 with silicalite-2. These results support the view that denser phases are more favourably synthesised under more demanding reaction conditions. The reported framework density of TON is 19.7 T/1000 Å while for ZSM-11, 17.7 T/1000 Å [13].

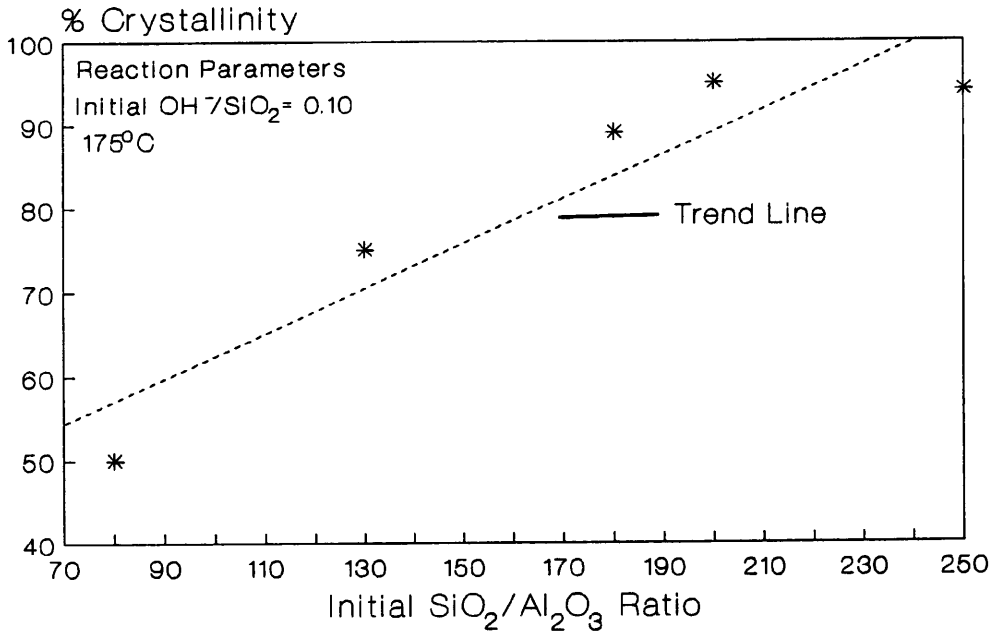


**Figure 3.20. Effect of the initial $Al_2O_3/SiO_2$ ratio on the crystallinity of ZSM-11 after 100 hours.**

Alternatively, theoretical studies suggest that organic additives possess an *exclusive volume* [39], dependent upon their physical and electronic nature. During synthesis the (alumino)silicate chains polymerise or organise around the organic additive. Changes in the physical and chemical environment of the organic additive will directly affect its structure directing properties. Alternatively, changes in the gel basicity will also shift the equilibrium of the various aluminosilicate precursor species available in solution which may influence the zeolite formed [25].

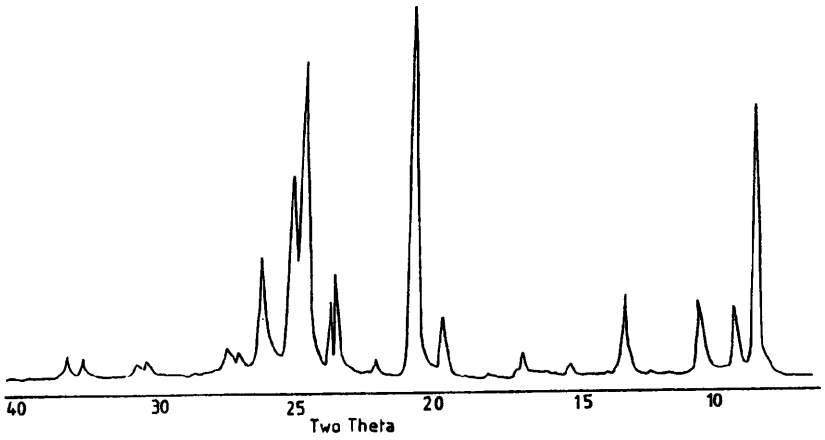


**Figure 3.21. XRD of TON synthesised at 175°C using a diluted synthesis gel.**

In comparison to the all-silica system studied in section 3.3, zeolites were also synthesised in the absence of an $M^+$ ion source as summarised in table 3.5. Two crystalline products were identified with x-ray analysis and SEM studies. At 175°C after 35 days with the initial $SiO_2/Al_2O_3$ ratios of 146 and 315 a physical mixture of TON and ZSM-11 were synthesised in an approximate product conversion ratio of (8:3). An increase in the initial aluminium content of the gel gave rise to a corresponding reduction in the product crystallinity. The percentage crystallinity of TON is approximately 85% or 60% when the initial $SiO_2/Al_2O_3$ ratios was 315 or 146. Highly crystalline ZSM-11 was synthesised after 60 days at 130°C when the initial $SiO_2/Al_2O_3$ ratio was 146. The chemical analysis of the $M^+$ ion free ZSM-11 synthesised at 130°C can be summarised as follows:

1.$SiO_2/Al_2O_3$=175 2.Molar C/N=4.1 3.DAO(puc)=4.7

Only negligible amounts of sodium are associated with the crystalline phase. The molar C/N ratio is 4 and DAO assumed intact, occupying the maximum possible pore volume available. As the product is more siliceous than the original gel it suggests that the charge-compensating ability of DAO is not as effective as $Na^+$. In the absence of an $M^+$ ion the reaction period required to obtain a crystalline product was prolonged by a factor of ten. Although the gel stoichiometries of these two systems are not strictly comparable the results suggest that the $M^+$ ion has a vital role in the nucleation of these zeolites. In agreement with section 3.1, the results reflect the difficulty in synthesising a more open structure in the absence of $M^+$ ions.

| Initial $SiO_2/Al_2O_3$ Ratio | Product and % Crystallinity | |
|---|---|---|
| | 175°C after 35 days | 130°C after 60 days |
| 146 | ZSM-11/30 + TON/85 | ZSM-11/96 |
| 315 | ZSM-11/23 + TON/60 | No reaction[a] |

a. Autoclave leakage

**Table 3.5. Zeolites synthesised in the absence of a $M^+$ ion source.**

Nonetheless, this study shows that the synthesis of TON and ZSM-11 with DAO as the organic additive does not require the presence of a $M^+$ ion. This has not been previously noted. The results also contrast to the all-silica $M^+$ ion free system where ZSM-48 was synthesised. As described in section 1.2, the topology of ZSM-48 and TON are similar, in that both zeolites are composed of a one-dimensional, 10-MR channel system. However, unlike ZSM-48, the structure of TON contains no 4-MRs. Jacobs et al.[37] suggested that aluminium atoms are preferentially located in the 4-MRs of ZSM-48. These results suggest that the structure-directing and charge-balancing properties of DAO depend on the framework aluminium siting.

The micrographs of the crystalline products obtained at 130 and 175°C with an initial $SiO_2/Al_2O_3$ ratio of 146 are shown in Figure 3.22. ZSM-11, synthesised at 130°C, shows a very uniform distribution of spherical crystal aggregates around 16μm in size (see Figure 3.22a). This suggests that a single nucleation point occurred during synthesis, followed by a homogeneous crystal growth mechanism. On closer inspection it becomes evident that the crystals are heavily twinned and multifaceted. Two types of crystal morphologies were found in the crystalline product obtained at 175°C (see Figure 3.22b and c). One phase composed of near-spherical agglomerates made up of heavily twinned, cuboid and rectangular crystallites approximately 20μm in diameter. This morphology compared to ZSM-11 synthesised at 130°C as described in Figure 3.19b and c. The other crystalline product is made up of collections of rod-like crystals, which is indicative of TON [40]. The individual crystals ranged in size from around 8-20μm in length and 0.5-4μm in width. The aggregated TON phase is composed of collections between 10 and 80μm in size.

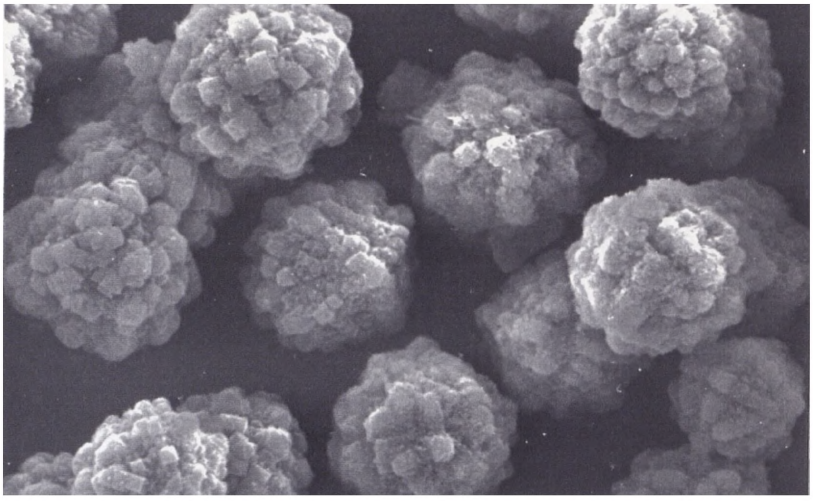


**Figure 3.22a. Product obtained at 130°C after 65 days.**

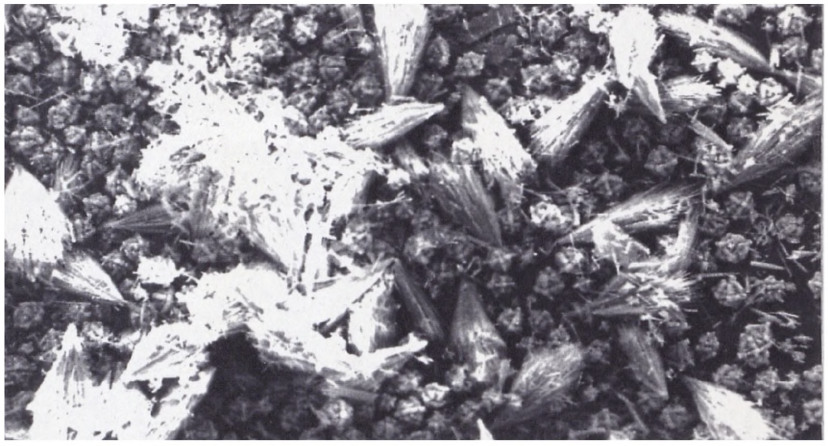


**Figure 3.22b. Phases synthesised at 175°C after 35 days.**

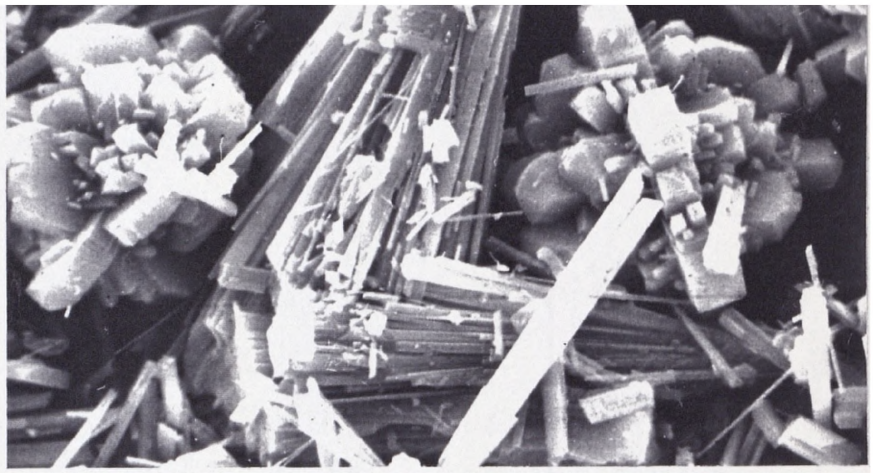


**Figure 3.22c. Close-up of high temperature products.**

**Figure 3.22. SEM of zeolites synthesised in the absence of $M^+$ ions with initial $SiO_2/Al_2O_3$=146.**

### 3.3.6. The Effect of Changes in the Silica Source

The original synthesis gel was prepared with Ludox AS40 (colloidal silica), sodium silicate or Cab-O-Sil (fumed silica). The overall starting stoichiometry in terms of molar oxides was:

$$6.1Na_2O - 20.1SiO_2 - 1.0Al_2O_3 - 5.2(DAO)_2O - 1344.2H_2O$$

The important initial molar ratios were, $OH^-/SiO_2$=0.10, $SiO_2/Al_2O_3$=20.1. The prepared gels were heated either statically or under agitated conditions at 175°C for a total reaction time of 300 hours. In agreement with other workers, varying the silica source resulted in the synthesis of different zeolite phases [41] and changes in the reaction rates [42]. Figure 3.23 shows the x-ray diffraction patterns of the crystalline materials obtained after 300 hours from the agitated sodium silicate and colloidal silica systems.

The d-spacings of the product synthesised with sodium silicate or fumed and colloidal silica compare with those quoted in the literature [6] for mordenite (MOR) and ferrierite (FER), respectively. The literature d-spacings for MOR and FER are listed in Appendix III. Previously MOR has been synthesised with a variety of large organic molecules such as 1,4-diazabicyclo[2.2.2]octane [43] or pyridine [44]. DAH, however, was until now the largest diamine to have been used to synthesise FER [5].

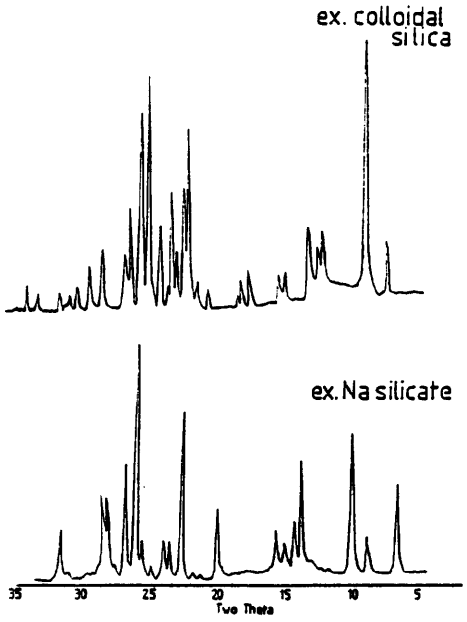


**Figure 3.23. X-ray data of zeolites obtained using colloidal or sodium silicate silica sources.**

Under static reaction conditions ZSM-11 was synthesised when fumed and colloidal silica were used (the sample from the sodium silicate reaction was lost due to autoclave leakage). Figure 3.24 shows the changes in the product development from each silica system under static and agitated conditions. The nucleation and crystallisation rates of the zeolites were enhanced by agitation and promoted the crystallisation of FER over ZSM-11. This is illustrated in Figure 3.25. The data revealed that ZSM-11 and FER nucleated at same time but that, in the latter stages of the reaction, FER transformed to the ZSM-11 in the static colloidal silica system. ZSM-11 was the stable crystalline product throughout the reaction period involving fumed silica where FER appeared only as a trace impurity. The process of agitation has been shown to affect both the reaction kinetics and phase development of several zeolites [10]. In a static environment it is possible that localised areas of high aluminium content encouraged in the nucleation of FER over ZSM-11.

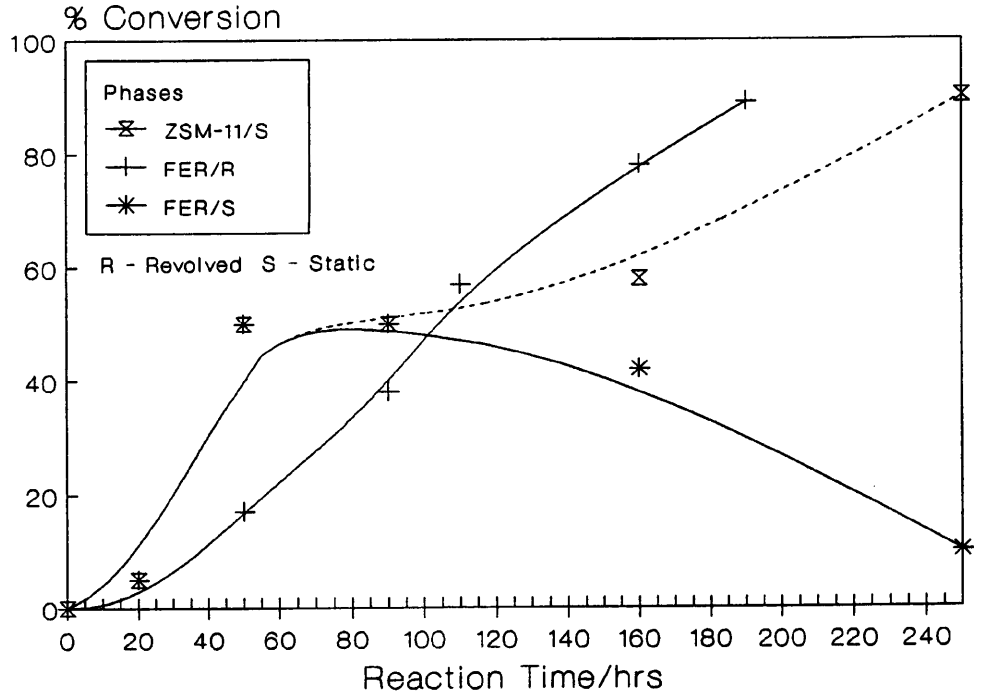


**Figure 3.24. Effect of agitation on zeolite development.**

In agreement other studies [45], both the rate of nucleation and crystallisation during zeolite synthesis are affected by the silica source. This can be summarised as follows:

**Nucleation/Crystallisation Rate**

**Increases in the order**

**SODIUM SILICATE > LUDOX > FUMED**

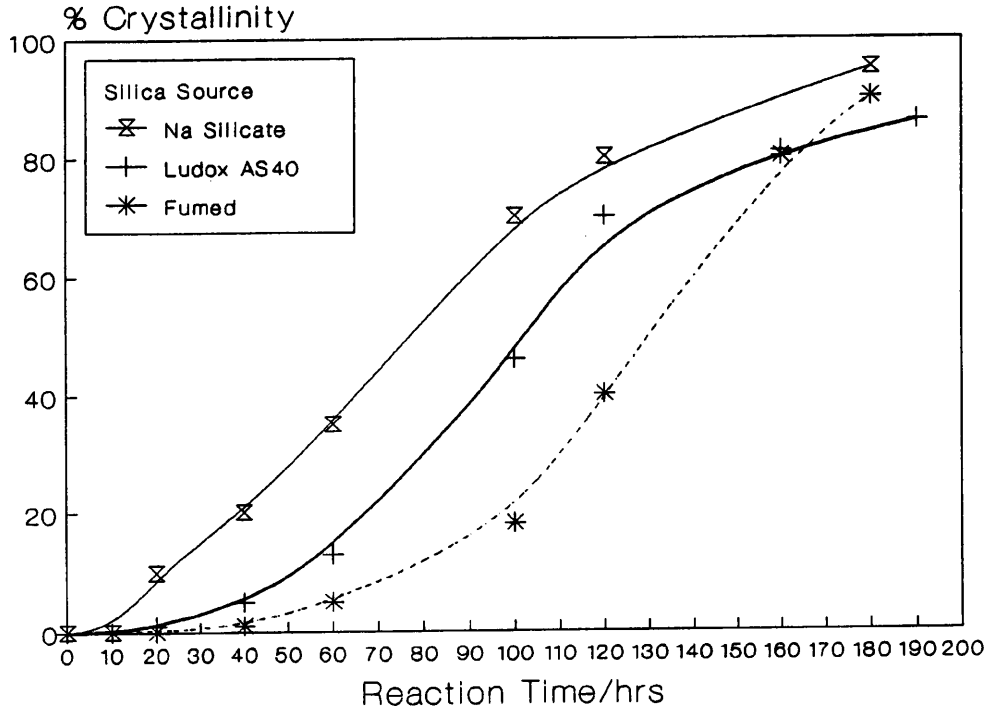


**Figure 3.25. Kinetic study of the agitated silica reaction systems.**

The rate of nucleation and crystal growth are primarily dependent upon the availability of reactive silicate and aluminosilicate species. Reactions involving sodium silicate quickly form highly saturated, hydrogels composed of monomeric silica and alumina species. Both $Na^+$ ion and DAO species are closely associated with the hydrogel, favouring rapid nucleation. In contrast, the depolymerisation of the active silica i.e. fumed or colloidal, to yield monomeric silicate anions is the essential rate limiting step [20,50].

There is a little ambiguity in the chemical composition of the materials assessed by standard wet chemical analysis and EDAX studies, as shown in Table 3.6. Both analytical methods have experimental errors in the region of ± 10%. The molar C/N ratio is approximately four in all the materials studied. This indicates that DAO is intact and sited within the zeolite pore systems. By assuming DAO is situated along the major 10-MR and 12-MR channels of FER and MOR, respectively, both zeolites experience a near maximum, end-to-end, organic pore-filling. Overall, MOR and FER have a lower product Si/Al ratio than ZSM-11 synthesised using the same starting stoichiometry. Noticeably, the EDAX analysis revealed that MOR with a Si/Al ratio of 5.3 is more aluminous than FER. The molar Al/Na ratio for all the materials is

greater than unity. However, the sodium content of MOR was noticeably higher than FER. The compositional data suggests that DAO is a protonated form functioning as a counter-balancing agent in both MOR and FER.

| Silica Source | Phase Type | EDAX Si/Al | Wet Chemical Analysis Molar Ratios Si/Al | Al/Na | C/N | p.u.c. DAO | Na |
|---|---|---|---|---|---|---|---|
| Ludox | FER | 8.9 | 10.0 | 1.6 | 4.0 | 1.0 | 1.9 |
| Fumed | FER | 9.9 | 9.9 | 1.7 | 4.1 | 1.1 | 2.0 |
| Na Silicate | MOR | 5.3 | 9.9 | 1.4 | 4.2 | 1.7 | 3.0 |
| Fumed * | ZSM-11 | 10.9 | 15.0 | 1.1 | 4.6 | 4.5 | 2.1 |

* Static reaction system

**Table 3.6. Chemical analysis of zeolites synthesised with different silica sources.**

The results show that $Na^+$ ions played an important role in the synthesis of MOR. The use of sodium silicate in zeolite synthesis allows the $Na^+$ ions to be more directly involved in the nucleation and crystallisation processes [2]. The nature of the silica source has been shown by other workers to alter the distribution of silicate species present in solution [49,31,18]. This suggests that the changes in phase development are related to the interaction of DAO and $Na^+$ ions with different (alumino)silicate species.

The coordination of aluminium in MOR and FER was assessed using $^{27}Al$ MAS NMR. The spectra are reproduced in Figure 3.26. Both consist of a single signal at 52.25ppm for FER and 53.03ppm for MOR, which corresponds to tetrahedrally coordinated aluminium in the zeolite framework. No extra-framework aluminium was detected in either zeolite. Other synthesis studies [46] have shown that generally, MOR can be synthesised in more aluminous environments than FER. This is a result of a preferential occupation of aluminium in the 4MRs associated with the MOR structure [46]. A similar phase development to these results was reported in the order ZSM-5, FER to MOR with decreasing initial $SiO_2/Al_2O_3$ ratio [44]. The 4MRs of MOR form part of both the 8MR and 10MR pore systems. It is probable that DAO is

more readily accommodated along the latter channel. Consequently, protonated DAO can act as an efficient charge-balancing species for the incorporated framework aluminium.

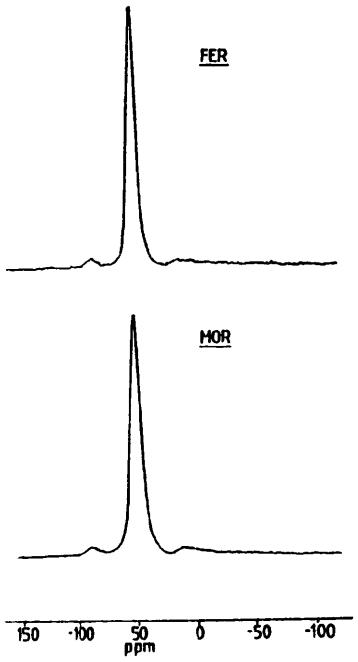


**Figure 3.26. $^{27}$Al MAS NMR spectra of *as-made* MOR and FER.**

The crystal morphologies of FER and MOR synthesised from the sodium silicate and colloidal silica systems are shown in Figures 3.27 and 3.28, respectively. MOR was composed of highly twinned large aggregates ranging in size between 30 x 40μm and 10 x 30μm. The aggregates are made up of tightly-packed rod-like crystallites 1 x 30μm in dimension. FER, obtained from both the colloidal and the fumed silica systems, was composed of very small, aggregated, square platelets of approximately 1$\mu m^2$. The morphology of FER and MOR compare to those reported by Smith et al.[44].

The physical and chemical interaction of the organic used in the synthesis was studied using *in-situ* FTIR as described in section 2.6. The experiment involved studying the gradual thermal degradation of the organic from the as made MOR and FER materials. The physical and chemical nature of DAO in FER was further studied using MAS NMR as discussed in section 3.3.8. By comparison with reported FTIR spectra for diamines [47], DAO was found to be intact and sited in the channel system of FER.

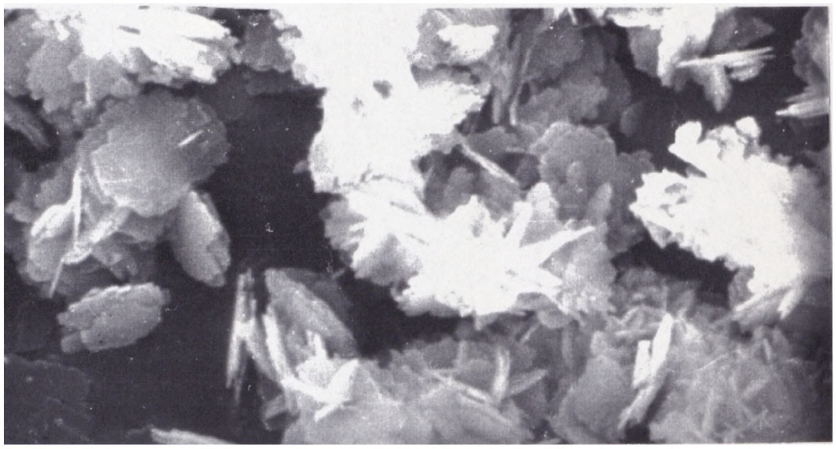


**Figure 3.27. SEM of FER synthesised with colloidal silica at 175°C after 300 hours with an initial $SiO_2/Al_2O_3$=20.**

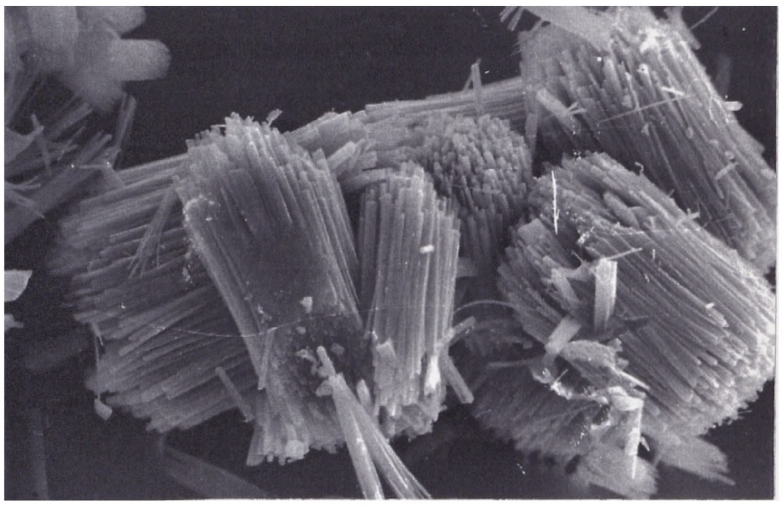


**Figure 3.28. SEM of MOR synthesised with sodium silicate at 175°C after 300 hours with initial $SiO_2/Al_2O_3$=20.**

Figure 3.29 shows the FTIR spectra of FER recorded at the various degradation temperatures.

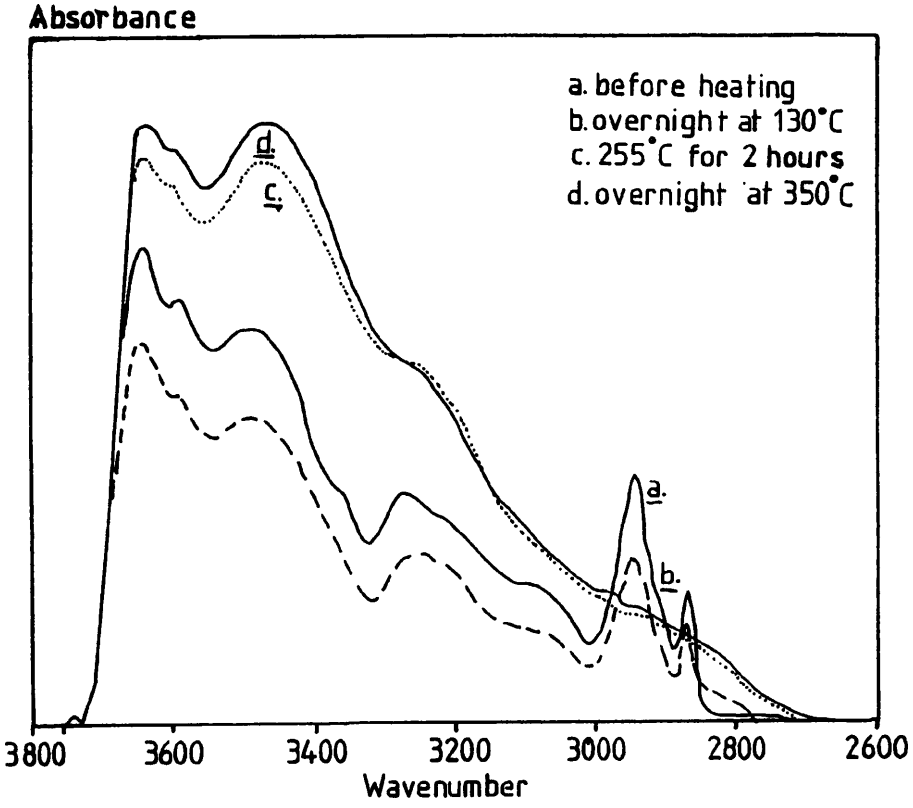


**Figure 3.29. FTIR spectra of *as-made* FER at several degradation temperatures.**

The finer detail of the diamine spectra is masked by the broad hydroxyl bands associated with the zeolite [22] framework. However, the various $\nu$C-H asymmetrical and symmetrical vibrational stretching frequencies of the diamine are evident. Tentative assignments are summarised in Table 3.7. The most significant assignment is that of the small shoulder around 3050cm$^{-1}$, which is indicative of the Zwitter-ion ($RNH_3^+$) [48]. This suggests that the diamine is, at least in part, present in a protonated within the zeolite pore system.

With an increase in the degradation temperature of between 25-185°C DAO remained intact within the zeolite pore system. Only dehydration occurred over this temperature range, which was accompanied by a significant reduction of the $\nu$O-H band around 3400 - 3500cm$^{-1}$. Above temperatures of 200°C, DAO was removed from the zeolite as shown by the significant reduction of the $\nu CH_3$ and $\nu RNH_3^+$

stretching frequencies. Noticeably, as the organic was degraded, the band intensity of the free silanol (Si-OH) around 3750cm$^{-1}$ increased correspondingly, as shown in Figure 3.30. Unfortunately, no information could be obtained from the FTIR spectrum of MOR obtained under the same experimental conditions. The hydroxyl stretches and associated hydration bands are very broad and mask any finer detail of the retained organic.

| Wave Number cm$^{-1}$ | Band Assignment and Appearance$_1$ |
|---|---|
| 2850 | Symmetrical C-H str - sharp |
| 2950 | Asymmetrical C-H str - sharp |
| 3250 | Asymmetrical N-H Str - broad |
| 3050 | $RNH_3^+$ Zwitter ion - small/broad |

1. Spectra recorded at room temperature
2. Str - Stretching frequency.

**Table 3.7. Summary of the FTIR band assignment of DAO sited in FER.**

The FTIR data obtained for FER suggests that a number of the internal silanols, or framework defect sites, were associated with protonated DAO. As suggested by Fegan et al.[9], the processes occurring during organic degradation can be summarised as follows,

$$\equiv\text{Si-OH}\ \ RNH_3^+ \bullet\bullet\bullet\ {}^-\text{O-Si}\equiv \ \xrightarrow{\qquad\qquad}\ \equiv\text{Si-OH} + \text{HO-Si}\equiv$$

During calcination the organic additive is removed and hydroxyl species are created. Hydroxyl nests of this nature are known to undergo a framework healing processes at high calcination temperatures. However, this was not observed during the FER degradation study.

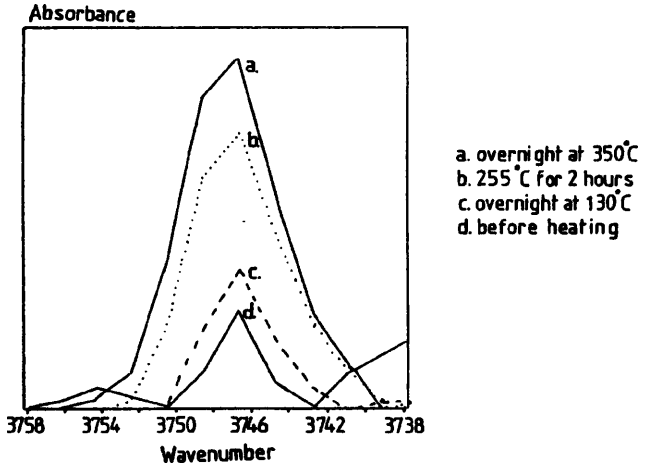


**Figure 3.30. Effect of degradation temperature on the development of silanols in FER.**

The FTIR spectra of the calcined sodium form FER and MOR are shown in Figure 3.31. The spectra of both materials contain a sharp hydroxyl stretch around 3750cm$^{-1}$. This band is due to both the internal defect and external surface non-acidic silanol group stretching frequencies [49]. The main difference in the two spectra is a band associated with the FER framework around 3607cm$^{-1}$, which is assigned to the fundamental vibration of the acidic hydroxyls [49]. The presence of this band indicates that the protonated diamine functions in part as a counter-balancing ion for framework aluminium in FER. Such a band is absent in MOR, and it appears that $Na^+$ is the preferred counter-balancing ion in MOR. It must be appreciated that the calcination procedure may not have removed all of the DAO the zeolite or there is an element of error in the chemical analysis data given in Table 3.7. The spectra of the hydrogen forms (via ammonium-exchange and calcination) of MOR and FER are shown in Figure 3.32. In both cases the acidic hydroxyl band around 3604cm$^{-1}$ overshadows the terminal silanol band at 3748cm$^{-1}$.

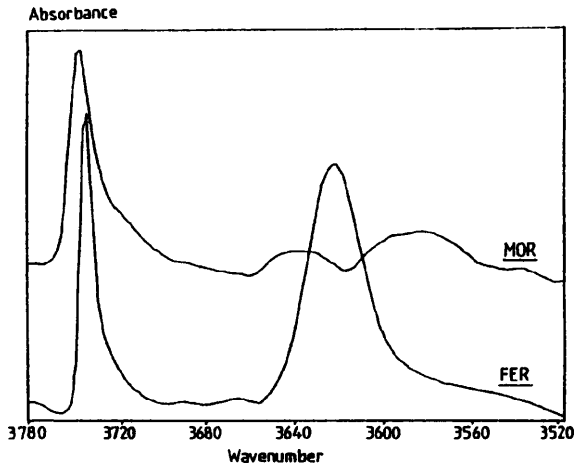


**Figure 3.31. FTIR spectra of the calcined $Na^+$ forms of MOR and FER.**

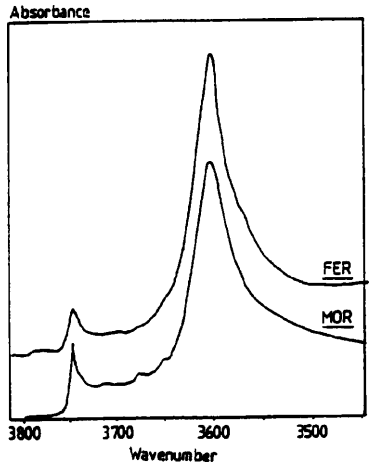


**Figure 3.32. FTIR spectra of the calcined hydrogen forms of MOR and FER.**

### 3.3.7. The Effect of Changes in the Chemical and Physical Nature of 1,8-Diaminooctane

The gels were prepared as previously outlined in section 3.34 using Ludox AS40 as the silica source. The starting stoichiometry can be represented by the following equation:

$$17.8Na_2O - 78.0SiO_2 - xAl_2O_3 - 19.6R_2O - 2353.3H_2O$$

where x was 0.0, 1.0 or 2.0 and R represents the organic additives DAO, diaminobutane (DAB), diaminohexane (DAH) and triethylenetetraamine (TETA). The changed molar ratios were a.$SiO_2/Al_2O_3$=80,135 or ∞, b.$OH^-/SiO_2$=0.15, c.$H_2O/SiO_2$=30.0. The gels were heated at 175°C under agitated conditions for a total reaction period of 75 hours. Syntheses involving the organic additive DAO and TETA were also performed at 130°C with a total reaction period of 100 hours.

X-ray analysis revealed that several zeolites were synthesised depending on the length of the diamine molecule and the initial $SiO_2/Al_2O_3$ ratio. Table 3.8 summarises the crystalline products obtained from each of the diamine reaction systems. Silicalite-2, with traces of magadiite, was the only zeolite synthesised from the all-silica system using DAO as the organic additive. Denser phases, such as cristobalite and α-quartz, formed in the presence of DAH and DAB.

| Organic Additive | Initial $SiO_2/Al_2O_3$ Ratio | | |
|---|---|---|---|
| | ALL SILICA | 80 | 135 |
| DAB | Cristobalite + $t_q$ | ZSM-5 + $t_c$ | ZSM-5 + FER (50:50) + $t_c$ |
| DAH | Quartz | ZSM-5 | ZSM-5 + $t_q$ |
| DAO | Silicalite-2 + $t_m$ | ZSM-11 | ZSM-11 |

Trace (t) q - quartz c - cristobalite m - magadiite

**Table 3.8. Products obtained using diamines as the organic additives after 48 hours at 175°C.**

As other workers have used DAH for the synthesis of silicalite-1 [4,50] under similar reaction conditions, the denser phases associated with this study may have resulted from the transformation of crystalline material synthesised at an earlier stage of the

reaction. In the absence of an organic additive, only amorphous solids were obtained throughout the synthesis programme.

When the initial $SiO_2/Al_2O_3$ ratio was 80 and 135, ZSM-5 was synthesised using DAH and DAB as the organic additive. At the higher ratio with the latter organic additive, FER formed 50% of the crystalline product. ZSM-11 was synthesised in all reaction systems involving DAO. Rollmann et al.[3] reported a similar phase development with an increase in size of the diamine additive. However, ZSM-5 has only been synthesised with diamine molecules longer than DAB, such as DAP, DAH and 1,10-diaminodecane (DAD) [3].

When TETA was used as the organic additive the nature of the crystalline phase was dependent upon the initial $SiO_2/Al_2O_3$ ratio and the reaction temperature. At 175°C, after a reaction period of 75 hours, ZSM-5 was synthesised independent of the initial gel composition. Alternatively, after 100 hours at 130°C, highly crystalline TON and ZSM-5 were obtained when the initial $SiO_2/Al_2O_3$ ratio was respectively, 135 and 80. The XRDs of the TON and ZSM-5 synthesised at 130°C are shown in Figure 3.33. Previously, both zeolites have been synthesised using TETA [28,51] as the organic additive.

It is worth noting that under the same reaction conditions in the all-silica reaction systems, magadiite was formed at 130°C and cristobalite resulted at 175°C. The wet chemical analysis of the crystalline products gave the following unit cell contents:

**ZSM-5** **2.1 TETA - 94.7 Si - 1.3 Al - 0.5 Na**

**TON** **0.7 TETA - 23.6 Si - 0.4 Al - 0.4 Na**

The molar C/N ratio of TETA for both structures is 1.6 showing that the organic molecule is intact. In TON the molar Na/Al ratio is one, whereas in ZSM-5 the ratio is less than unity. This indicates that TETA functions in part as a charge-balancing ion during the synthesis of ZSM-5. In TON, the 10MR channel is uni-dimensional along the c-axis with a repeat distance of 5.0Å [53]. Assuming that the length of TETA is 14.6Å[8], the pore-filling capacity of the organic additive is 102 and 35% for TON and ZSM-5, respectively. The result shows that TETA completely fills the pore

volume of TON, while in ZSM-5 the pore-filling is incomplete. TETA is probably more favourably sited along the straight rather than zig-zag 10-MR channels of ZSM-5.

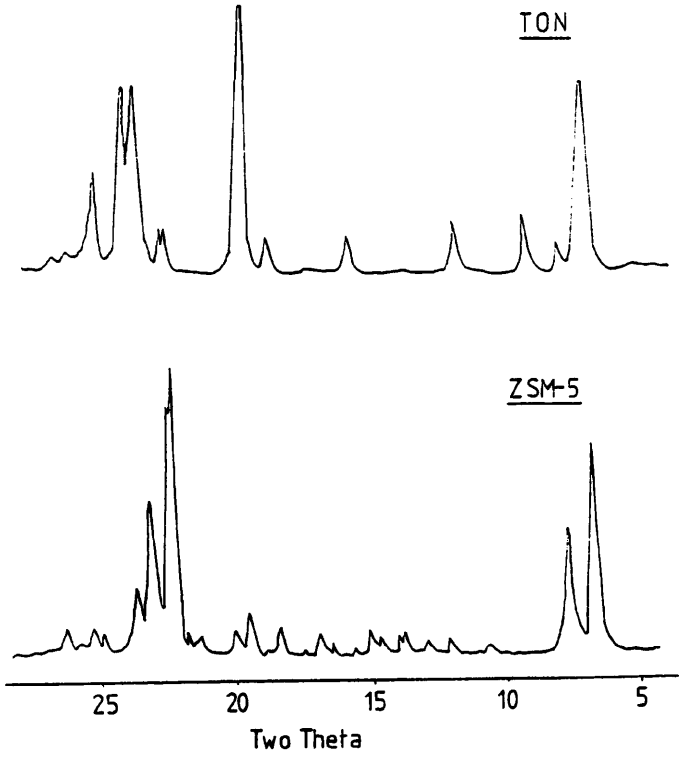


**Figure 3.33. XRD of a. TON and b. ZSM-5 synthesised with TETA at 130°C with an initial $SiO_2/Al_2O_3$ ratio of 135 and 50, respectively.**

The micrographs of TON and ZSM-5 synthesised at the lower reaction temperature in the presence of TETA are shown in Figures 3.34 and 3.35, respectively. In agreement with similar observations [15] TON composed of needle-like crystals averaging 0.2 x 1.5μm in size. ZSM-5 is made up of a collection of spheric aggregates varying in size between 0.2-2.0μm in diameter. This morphology has often been reported in the literature [16].

TON is generally synthesised using organic additives with the general formula,

$$HX\text{-}CH_2\text{-}CH_2\text{-}Y\text{-}CH_2\text{-}CH_2\text{-}ZH,$$

where X, Y and Z are oxygen and/or CH2 or NH groups [54]. Changing the chemical nature of DAO by increasing the amino ($NH_2$) content of the molecule promotes the nucleation of TON over ZSM-11.

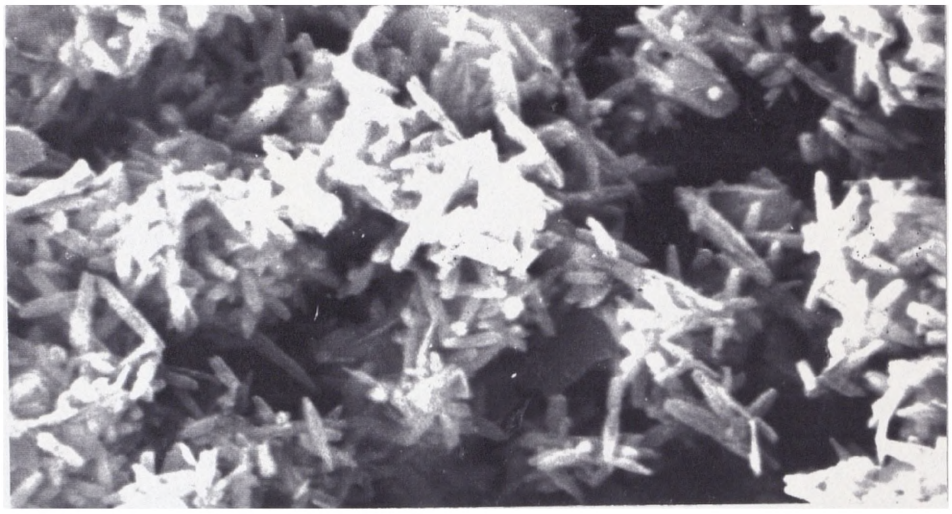

SCALE
2μm

**Figure 3.34. SEM of TON synthesised using TETA as the organic additive at 130°C after 100 hours and initial $SiO_2/Al_2O_3$=135.**

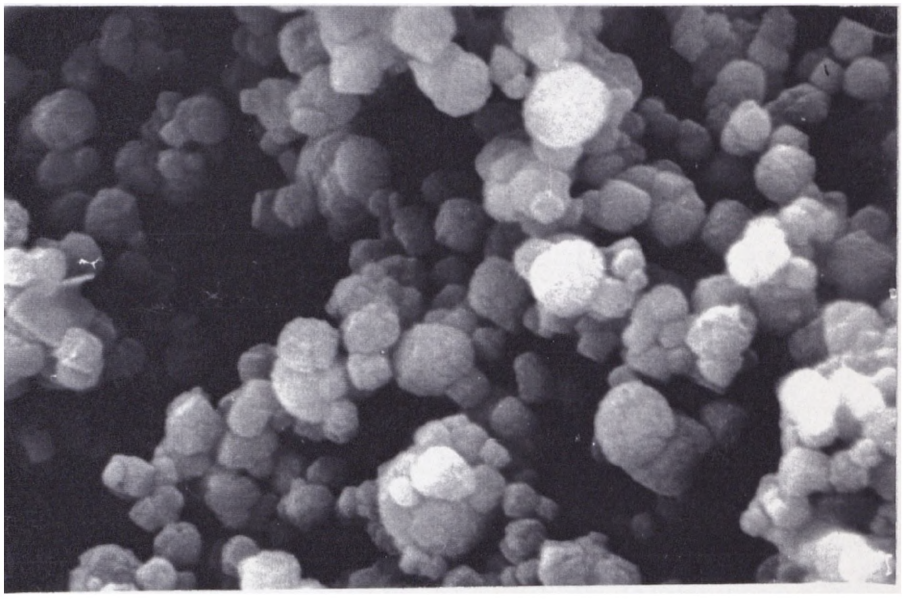

SCALE
2μm

**Figure 3.35. SEM of ZSM-5 synthesised using TETA as the organic additive at 130°C after 100 hours and initial $SiO_2/Al_2O_3$=80.**

Such changes will alter the charge-balancing nature of the organic additive and its ability to incorporate aluminium into the framework. It is unlikely that TETA is sited along the channels of the zeolites in a linear conformation, but rather takes a shape which optimises the interaction of the organic with the framework [8]. The increased thermal motion of the organic at a higher reaction temperature will directly affect such interactions [15].

### 3.3.8. NMR Evaluation of the Chemical and Physical Nature of 1,8-Diaminooctane in the Pore Systems of High-Silica Zeolites

*As-made* zeolites silicalite-2, ZSM-48 and FER as described in sections 3.1 and 3.6 were analysed using $^{13}C$, $^{15}N$ and $^{29}Si$ MAS NMR. Details of the experimental procedure are given in section 2.33. Internal silanol groups as structural defects in high- silica zeolites can be identified using $^{1}H$-$^{29}Si$ cross-polarisation CP-MAS NMR [55]. Polarisation transfer preferentially occurs from the protons of the organic additive to the silicon tetrahedra lining the 10-MR channel system [56]. Figure 3.36a shows the $^{29}Si$ MAS NMR spectra (without cross-polarisation) of the *as-made* silicalite-2 and ZSM-48. The chemical shift values are quoted in ppm from TMS.

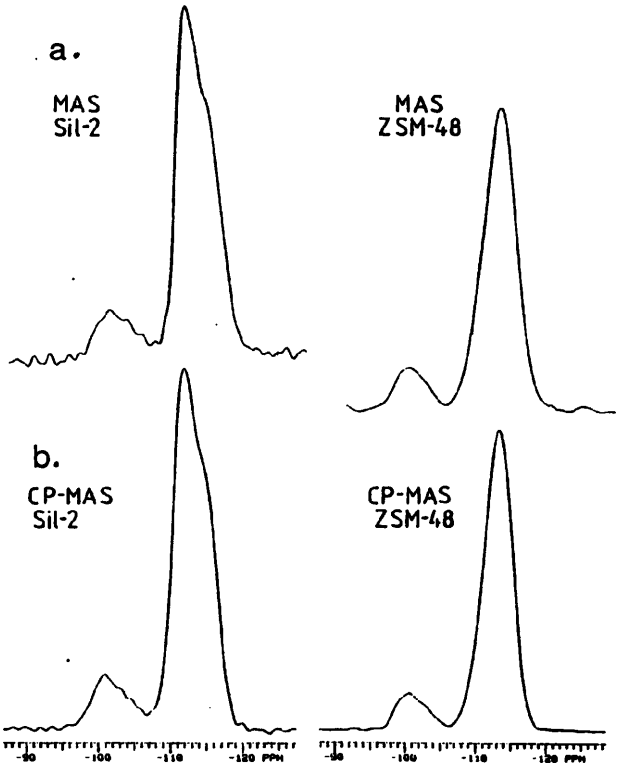


**Figure 3.36. a.$^{29}Si$ MAS NMR and b. $^{29}Si$ CP-MAS NMR spectra of *as-made* ZSM-48 and silicalite-2.**

Both spectra show a broad, strong intensity centred around -112ppm with a shoulder at -115ppm. A weaker broad intensity is also present at around -101ppm. The peak intensities associated with chemical shifts between -112 to -115ppm have been previously attributed to Si(OAl) units. This is indicative of an essentially aluminium-free zeolite framework. The other line at -101ppm can be ascribed to one or both of two possible silanol or defect centres, namely $Q^3$(0Al) and $Q^3$(1Al) [55].

The $^{29}Si$ CP-MAS NMR spectra of ZSM-48 and silicalite-2 are shown in Figure 3.36b. The data from both zeolites compare well to the original spectra with no significant change in the intensity around -101ppm. In other studies concerning Na,TPA-ZSM-5 the defect intensities were removed with cross-polarisation. It was suggested that the defect sites were not $SiO^-H^+$ or $SiO^-TPA^+$ but $SiO^-Na^+$ for which direct cross-polarisation is not possible [57]. Given this, the NMR data in this present study imply that defect sites in ZSM-48 and silicalite-2 are present in the form of $SiO^-$ $DAO^+$ interactions. It follows that during synthesis DAO was incorporated into the pore system in a partially protonated form. Since the changes in defect intensity were not quantitatively assessed, the presence of some $SiO^-Na^+$ defect species, as suggested from chemical analysis, cannot be ruled out completely.

The physical and chemical effects on DAO due to inclusion in the pore system of ZSM-48, silicalite-2 and FER was further substantiated using $^{13}C$ CP-MAS NMR. Figure 3.37 compares the $^{13}C$ solution NMR and solid CP-MAS NMR spectra of DAO to the CP-MAS NMR spectra of *as-made* silicalite-2, ZSM-48 and FER. The corresponding chemical shift information in ppm from TMS is summarised in Table 3.9. Unlike $^1H$ NMR, the results obtained from $^{13}C$ NMR are non-quantitative and give no information concerning the relative number of carbon nuclei.

Both the solution $^{13}C$ NMR and solid CP-MAS NMR spectra of DAO consist of four sharp intensities. These represent the four carbon positions which are incrementally deshielded with respect to nitrogen (see Table 3.9). The chemical shifts of the solution spectrum are, respectively, 41.7, 33.2, 30.0 and 27.6ppm, while in the solid state they are 43.4, 39.1, 32.5, and 29.4ppm. The protonation of DAO (pH=1.0) in solution was achieved by the addition of HCl. A relative up-field chemical shift is obtained

with respect to each equivalent carbon to 40.6, 28.7, 27.5 and 26.3ppm. The results clearly show the effect on the magnitude of the chemical shift with respect to the physical state of the organic and its protonation.

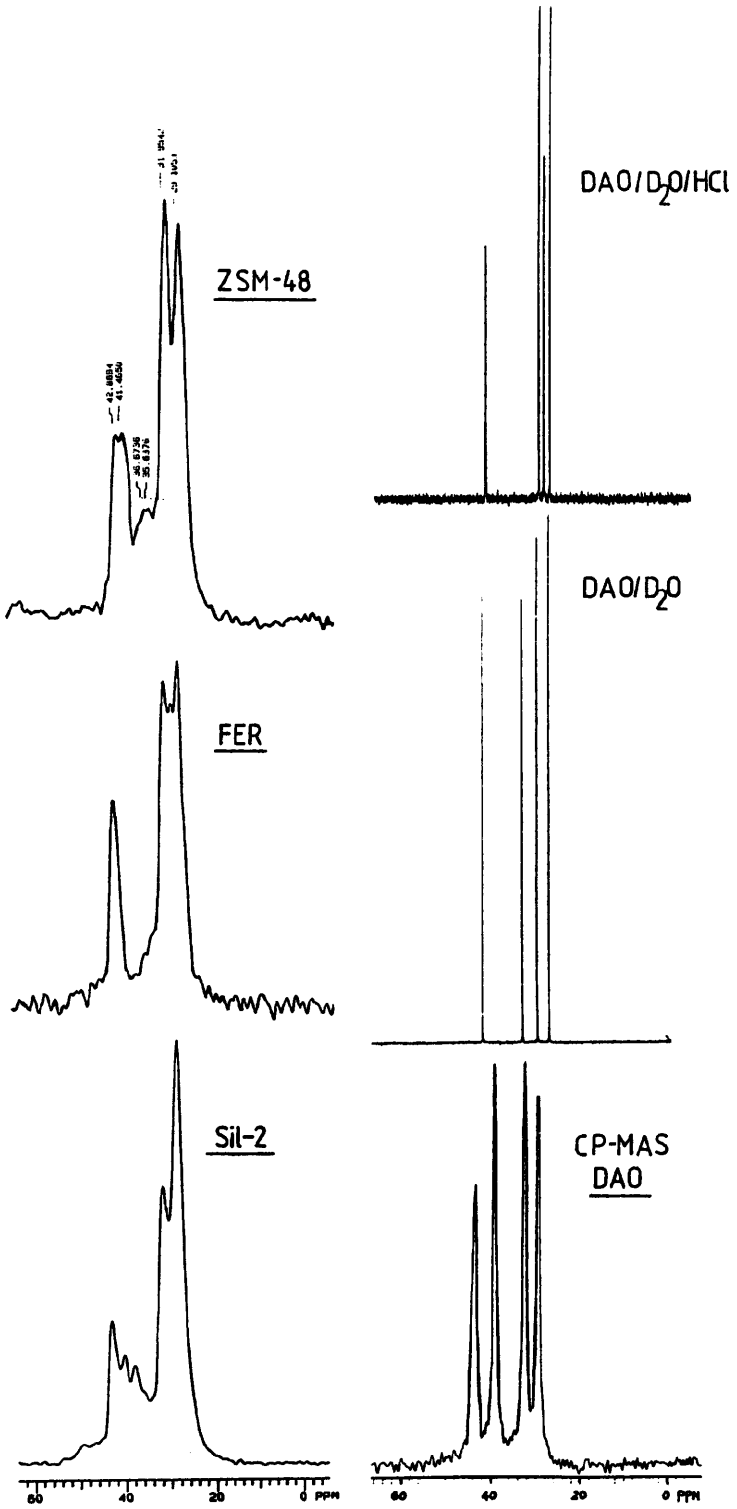


**Figure 3.37. Comparison of $^{13}C$ CP-MAS and solution NMR spectra of DAO (* fully protonated).**

The $^{13}C$ CP-MAS NMR spectra of DAO sited in silicalite-2 and ZSM-48 both consist of six broad intensities. In contrast, the spectrum of DAO in FER is composed of four broad intensities. For silicalite-2 the chemical shifts are 43.0, 40.2, 38.0, 36.5, 31.6 and 28.5ppm and for ZSM-48 they are 42.9, 41.5, 36.7, 35.6. 31.9 and 29.1ppm. The chemical shifts for FER are 42.1, 30.7, 29.2 and 27.5ppm. There is no evidence from the zeolite CP-MAS NMR spectra of any products such as n-butylamine from the decomposition of DAO [58].

| Phase Type | $^{13}C$ Chemical Shifts in ppm from TMS [a] | | | |
|---|---|---|---|---|
| | 1[b] | 2 | 3 | 4 |
| DAO/Solution | 41.7 | 33.3 | 30.0 | 27.6 |
| DAO/$H^+$ Solution | 40.6 | 28.7 | 27.5 | 26.3 |
| DAO/CP-MAS | 43.4 | 39.1 | 32.5 | 29.4 |
| FER | 42.1 | 30.7 | 29.2 | 27.5 |
| ZSM-48 | 42.9<br>41.5 | 36.7<br>35.6 | 31.9 | 29.1 |
| Silicalite-2 | 43.0<br>40.2 | 38.0<br>36.5 | 31.6 | 28.5 |

a. T.M.S.- Trimethysilane

b. Numbering sequence of the carbon atoms in DAO.

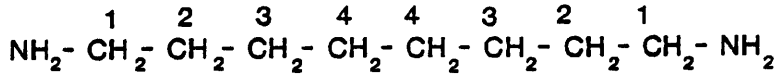


**Table 3.9. $^{13}C$ CP-MAS and solution NMR chemical shift data of DAO.**

The $^{13}C$ spectra of DAO in FER is near comparable while there are differences in the spectra obtained for Sil-2 and ZSM-48 to the corresponding solution NMR and CP-MAS NMR spectra for DAO. Other workers have reported similar changes in chemical shift of organic additives on incorporation into the zeolite pore system [57]. The present results suggest that DAO molecules are sited intact within the pore system of ZSM-48, silicalite-2 and FER. Interestingly, although FER and ZSM-48 have similar frameworks the chemical shifts are noticeably different. The chemical shift data for ZSM-48 and silicalite-2 are closest to those for DAO in the solid state. In contrast, the chemical shifts for FER are closer to those of DAO in solution. A significant effect of the incorporation into the pores is observed in the multiplicity intensities of

the $C_1$ and $C_2$ carbon nuclei in silicalite-2 and ZSM-48. Interestingly, the intensities of these intensities are not the same in both spectra. In contrast, the spectrum of FER shows no such multiplicity.

The differences in the $^{13}C$ NMR spectra of DAO in solution and of DAO incorporated into the zeolite pores, result from variations in the electronic configuration of the diamine molecule. This can result from chemical modification such as protonation [56], coordination with $M^+$ ions [14] and conformational changes imposed by the zeolite framework [7]. It is difficult to identify the specific contribution of each interaction to the chemical shift of the carbon nuclei. The spectral line-broadening of the diamine sited in the zeolite pore system may result from the close proximity of a given $CH_2$ group to the framework. This gives rise to a series of unresolved chemical shifts caused by framework disorder such as defect sites. Alternatively, differences in the magnitude of the $T_2$ relaxation time between the carbon atoms can also contribute to line-broadening [56].

Such structural differences are known to affect the multiplicity and chemical shift of resonances observed in the $^{13}C$ NMR spectra [7]. By comparing the spectra of DAO in ZSM-48 and silicalite-2 the contribution of structural differences to the chemical shift can be estimated to 1-2ppm. In the case of FER, which has a framework similar to that of ZSM-48, the differences in the chemical shift data appear to be too large to be accounted for by purely structural effects. The data suggest that the chemical environment of DAO in FER is different from that experienced in ZSM-48 and in silicalite-2.

The solution $^{13}C$ NMR spectrum shows that protonation of DAO results in a noticeable up-field chemical shift of the $C_2$ carbon nuclei. Although smaller in magnitude, a similar trend occurs for DAO in both ZSM-48 and silicalite-2. However, in the case of DAO in FER the shift is more noticeable. In agreement with the $^{29}Si$ CP-MAS results, this data suggests that DAO occupies the pore system of ZSM-48 and silicalite-2 in a partially-protonated form. On the other hand, it appears that DAO is incorporated into the pore system of FER in a fully-protonated form. The $Na^+$ ion and DAO unit cell contents together with the Si/Al ratio of FER were given previously in

Table 3.6. The chemical analysis revealed that in order to achieve framework neutrality DAO must be fully protonated. FTIR studies previously discussed in section 3.3.6 gave other evidence of a protonated form of DAO in the pore system of FER.

Challoner et al.[56] reported similar results for high-silica TON synthesised with diethylamine. They suggested the existence of localised domains of defect sites. Similarly, Engelhardt et al.[59] reported differences between the $^{13}C$ MAS NMR spectrum of sorbed butylamine on calcined ZSM-5 and the corresponding spectra of the *as-made* zeolite where butylamine was used as the organic additive. Additional lines were due to the protonated $BuNH_3^+$ species. Tianyou et al.[14] did not observe splitting in the $^{13}C$ CP-MAS NMR spectrum of ZSM-5 synthesised with 1,6-diaminohexane. The $Na^+$ ion content of this material was far in excess of the framework $Al^{3+}$ indicating that the diamine was sited in the channels of ZSM-5 in an unprotonated form.

The chemical and physical nature of DAO was further studied by recording $^{15}N$ CP-MAS NMR. The low natural abundance of the $^{15}N$ isotope makes its detection difficult. However, by increasing the number of scans reasonable spectra were recorded. These are the first reported $^{15}N$ CP-MAS spectra for diamines in zeolites. Chemical shifts are referenced in ppm with respect to solid ammonium nitrate and the results are summarised in Table 3.10. Figure 3.38 shows the $^{15}N$ CP-MAS NMR of the *as-made* zeolites and solid DAO together with DAO in a partially acidified solution. The chemical shift for DAO in the solid state is -349.6ppm while in acidified solution shifts at -342.8 and -340.4ppm are observed. Two resonances are found at -341.3 and -344.7ppm for silicalite-2 and at -339.5 and -345.7ppm for ZSM-48. In contrast, the FER spectrum shows one intensity at -341.5ppm.

Parallel to the observations using $^{13}C$ CP-MAS NMR, the $^{15}N$ spectra show that the terminal nitrogens of the diamine chain in ZSM-48 and Silicalite-2 are electronically non-equivalent. In contrast, they are all chemically equivalent in FER. Similarly, changes in the $^{15}N$ chemical shift also depend upon the nature of the zeolite framework. However, the difference in chemical shift of the intensities in the spectra of the zeolites appear too large to reflect purely structural effects [60]. There are many

similarities in the way the $^{15}N$ and $^{13}C$ chemical shifts alter with the electronic environment. However, the corresponding changes in chemical shift are less predictable for $^{15}N$ than $^{13}C$. The effect of protonation on the chemical shift cannot be predicted and is best compared to experimental rather than theoretical values. Generally, however, such a decrease in electronic shielding results in an up-field shift [61]. This is reflected in the results for the partially acidified solution of DAO and zeolite samples. Consequently, the $^{15}N$ CP-NMR spectra of silicalite-2 and ZSM-48 can be tentatively assigned to the unprotonated and protonated terminal nitrogen. These species relate to resonances between -345.7 to -344.7ppm and -341.3 to 339.5ppm, respectively. In the case of FER the only resonance observed is at -341.5ppm this supports the conclusion from $^{13}C$ NMR results that DAO resides the pore system in a fully protonated form.

Combining the information from the $^{29}Si$, $^{13}C$ and $^{15}N$ CP-MAS NMR and results from the literature it can be tentatively concluded that DAO is intact, partially protonated and encapsulated in the pore systems of ZSM-48 and silicalite-2. In the pore system of FER only protonated diamine molecules are present. The subtle differences in the MAS NMR data show that the chemical and physical nature of DAO is not equivalent in FER, ZSM-48 and silicalite-2. Due to the limited availability of the spectrometer only a restricted study could be made. Consequently, in order to substantiate these results further investigations are required.

| Phase Type | $^{15}N$ Chemical Shift[1] | |
|---|---|---|
| DAO/CP-MAS | -346.4 | |
| DAO/SPMAS | -349.6 | |
| DAO/$H_2O$ + HCl | -342.8 | -340.4 |
| FER | -341.5 | |
| ZSM-48 | -345.7 | -339.5 |
| Silicalite-2 | -344.7 | -341.3 |

1. in ppm from $NH_4NO_3$

**Table 3.10. $^{15}N$ CP-MAS and solution NMR data for DAO in various physical environments.**

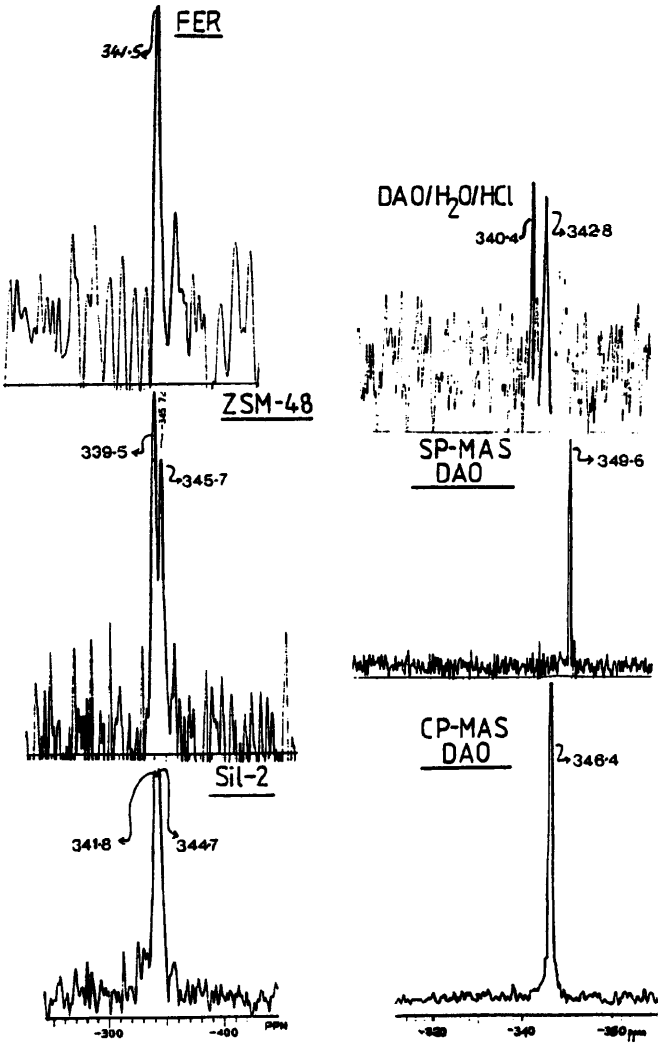


**Figure 3.38. CP-MAS NMR $^{15}N$ spectra of DAO and the *as-made* zeolites ZSM-48, silicalite-2 and FER with the solution spectra of partially acidified DAO.**

## 3.4. Conclusions

By varying the physical and chemical reaction conditions a variety of zeolites have been synthesised in the presence of DAO, which brings into question the structure-directing abilities of the organic additive. Structural details of these materials are listed in Table 3.11. All the zeolites synthesised have major channel systems defined by 10- or 12-MRs. There is no appreciable geometrical limitation on DAO being sited along the linear channel system of any of the materials obtained.

All uni-dimensional zeolites experience a maximum pore-filling with DAO. In the MEL type materials and ZSM-5 a limit the pore filling capacity was between 70-80% and 40%, respectively. This relates to the size of DAO and the dimensionality and/or

the tortuosity of the framework. Generally, under more demanding reaction conditions such as high temperature, very low $OH^-/SiO_2$ ratio and in the absence of inorganic cation phase changes occurred. These particular results showed a trend between the synthesis product with an increase in framework density.

| PHASE TYPE | FWD T/1000 Å | CRYSTAL DATA a(Å) | b(Å) | c(Å) | D | MAJOR PORE | CHANNEL CHARACTERISTICS(Å) | |
|---|---|---|---|---|---|---|---|---|
| ZSM-5 | 17.9 | 20.06 | 19.80 | 13.36 | 3 | 10 | [010] 5.8X5.2 | S |
| | | | | | | 10 | [100] 5.4X5.4 | ZZ |
| ZSM-11 | 17.7 | 20.10 | 20.10 | 13.40 | 2 | 10 | [010] 5.8X5.2 | S |
| MOR | 17.7 | 18.10 | 20.50 | 7.50 | 2 | 12 | [010] 6.7x7.0 | S |
| | | | | | | 8 | [100] 4.8x3.5 | S |
| FER | 17.2 | 19.20 | 14.10 | 7.50 | 2 | 10 | [001] 5.5x4.3 | S |
| | | | | | | 8 | [010] 4.8x3.5 | S |
| ZSM-48 | 19.9 | 14.24 | 20.14 | 8.40 | 1 | 10 | [001] 5.3x5.6 | S |
| TON | 19.7 | 13.84 | 17.42 | 5.04 | 1 | 10 | [001] 4.5x5.5 | SS |

FWD-FRAMEWORK DENSITY
D-DIMENSIONALITY
S-STRAIGHT CHANNEL
SS-SLIGHTLY SINUSOIDAL CHANNEL
ZZ-ZIG-ZAG CHANNEL

**Table 3.11. Zeolites synthesised using DAO as the organic additive.**

MASNMR, FTIR and chemical analysis show that DAO resides in the zeolite pore system, intact and in a partially or fully protonated form. This is qualitative evidence for the counter-balancing nature of DAO. In the case of silicalite-2 and ZSM-48, DAO resides in the pore system in a partially protonated form mostly associated with framework defect sites. In contrast, it was tentatively suggested DAO is in a fully protonated state within the pore system of FER required to counter-balance the charge created by framework aluminium.

ZSM-48 and MEL type materials were synthesised over a wide range of gel compositions. On changing the length of the diamine, or its chemical nature, other zeolites were synthesised. This reveals the structure-directing nature of organic additives.

However, other zeolites were obtained within narrow compositional ranges and products were strongly dependent on other reaction variables. These include the nature of the silica source, inorganic cation type, mixing procedure and/or reaction temperature. In this respect the zeolite synthesised were not attributable to the physico-chemical or structure-directing nature of DAO.

Changes in the synthesis temperature altered both reaction rates and phase development. In the all-silica reaction system, silicalite-2 was preferably synthesised over ZSM-48 on reducing the reaction temperature. This is related to differences in the thermal motion of the organic molecule and framework density. However, in the aluminous systems, ZSM-11, FER and MOR, rather than ZSM-48, were obtained. This shows that the structure-directing and charge-balancing properties of DAO are intrinsically linked to the incorporation of tetrahedral aluminium into the zeolite framework during synthesis.

Changing the alkalinity of the gel, and consequently the distribution of (alumino)silicate species, altered both reaction rates and phase development. For example, the results suggest that the synthesis of MEL requires a greater concentration of monomeric silicate species, as associated with higher alkalinities. In a similar manner reaction rates for the synthesis of silicalite-2 and ZSM-48 optimised at an initial $OH^-/SiO_2$ ratio of 0.2, which allowed the greatest pH change during the reaction to occur. Presumably, such an increase in pH would generate a smaller silicate species suitable for crystal growth processes. However, the species required for nucleation are not necessarily those essential for crystal growth.

By varying the inorganic source and gel aluminium content different zeolite phases were obtained. This indicates that the inorganic cations have structure-directing properties. Reactions performed in the absence of an $M^+$ source resulted in a substantial increase in the reaction period. This shows that the $M^+$ ions play a vital role during zeolite nucleation. Inorganic cations are able to complex and incorporate aluminium into the zeolite framework and may also assist in the inclusion of water and DAO into the pore system. Replacing $Na^+$ for $K^+$ ions enhanced zeolite nucleation, but the crystalline product had a noticeably lower $K^+$ ion content. This implies

that the $K^+$ ions assist more favourably in the formation of the (alumino)silicate species required for nucleation. Alternatively, the change in rate of nucleation depend on physical properties of the gel such as viscosity, which was lower in the $K^+$ than $Na^+$ reaction system. A lowering of the gel viscosity allows a more intimate mixing of reagents which assists gel dissolution and encourages nucleation.

By changing the silica source, changes in the nucleation and crystallisation rates and phase development were observed. This is related to differences in the equilibrium concentration of the reactive (alumino)silicate species during the nucleation period. No single reaction variable was dominant and the effect of any variable was dependent upon the values of the other variables. In general, DAO was an efficient structure-directing agent for the synthesis of MEL and ZSM-48. However, as a series of materials were obtained, DAO must also function an efficient a pore- or space-filler. Due to these structure-directing abilities, DAO cannot be regarded as a *template*.

These results highlight the importance of investigating a synthesis system over a range of reaction conditions. Consequently, the *true* structure-directing properties of an organic additive can be uncovered and new materials synthesised.

## REFERENCES.


1. B.M.Lok, T.R.Cannan & C.A.Messina, *Zeolites*, **3**, 282 (1983)

2. L.D.Rollmann, E.W.Valyocsik & J.A.Cooper, *Eur.Pat.Appl.*, 0 015 132 (1980)

3. E.W.Valocsik & L.D.Rollmann, *Zeolites*, **5**, 123 (1985)

4. K.R.Franklin & B.M.Lowe in *Zeolites: Facts, Figures, Future*, Proc.8th Int.Zeolite Conf., Stud.Surf.Sci.Catal.No.**49**, (Eds.Jacobs & van Santen, Elsevier) Amsterdam, The Netherlands, 179 (1989)

5. A.Araya & B.M.Lowe, *J.Chem.Res.(S)*, 192 (1985)

6. R.von Ballmoos & J.B.Higgins, *Collection of Simulated X-Ray Powder Patterns for Zeolites*, IZA Special Publication, (Butterworths, 1990)

7. J.B.Nagy, Z.Gabelica & E.G.Derouane, *Zeolites*, **3**, 43 (1983)

8. Chem-X User Guide (Chemical Design Ltd., Oxford 1986)

9. S.G.Fegan & B.M.Lowe, *J.Chem.Soc.Farad.Trans.1*, **82**, 785 (1986)

10. K.R.Franklin & B.M.Lowe, *Zeolites*, **8**, 495 (1988)

11. G.J.Kramer, A.Z.M.de Man & R.A.van Santen, *J.Am.Chem.Soc.*, in press (1991)

12. R.M.Barrer, *Hydrothermal Chemistry of Zeolites*, (London Academic Press, 1982)

13. D.E.Akporiaye & G.D.Price, *Zeolites*, **9**, 321 (1989)

14. S.Tianyou, X.Ruren, L.Liyun & Y.Zhaohui in *New Developments in Zeolite Science and Technology*, Proc.7th Int.Zeolite Conf., (Eds.Murakami, Iijima & Ward,Elsevier) Tokyo, Japan, 201 (1986)

15. R.P.Gunawardane, H.Gies & B.Marler, *Zeolites*, **8**, 127 (1988)

16. A.Jacobs & J.A.Martens in *Synthesis of High-Silica Aluminosilicate Zeolites*, Stud.Surf.Sci.Catal.No.33, (Publ.Elsevier) chpt.2 (1987)

17. G.W.Dodwell, R.P.Denkewicz & L.B.Sand, *Zeolites*, **5**, 153 (1985)

18. B.Marler, *Zeolites*, **7**, 393 (1987)

19. R.K.Iler, *The Colloid Chemistry of Silica and Silicates*, (Publ. Cornwell Uni.Press, 1955)

20. D.M.Bibby, N.B.Milestone & L.P.Aldridge, *Zeolites*, **280**, 664 (1979)

21. K.J.Chao, T.S.Tasi, M.S.Chen & I.Wang, *J.Chem.Soc.Farad.Trans.1*, **3**, 547 (1981)

22. J.C.Jansen, F.J.van der Gaag & H.van Bekkum, *Zeolites*, **4**, 369 (1984)

23. R.A.Febre, H.W.Kouwenhoven & H.van Bekkum, *Zeolites*, **8**, 60 (1988)

24. J.L.Casci & B.M.Lowe, *Zeolites*, **3**, 186 (1983)

25. A.V.McCormack & A.T.Bell, *Catal.Rev.Sci.Eng.*, **31(1 & 2)**, 97 (1989)

26. J.B.Nagy, P.Bodart, H.Collette, C.Fernandez, Z.Gabelica, A.Nastro & R.Aiello, *J.Chem.Soc.Farad.Trans.1*, **85** (9), 2749 (1989)

27. J.C.Jansen in *Introduction to Zeolite Science and Practice*, Stud.Surf.Sci.Catal. No.**58**, (Eds.van Bekkum, Flanigen & Ward, Elsevier) 77 (1991)

28. D.T.Hayhurst, A.Nastro, R.Aiello, F.Crea & G.Giordano, *Zeolites*, **8**, 415 (1988)

29. A.Erdem & L.B. Sand, *J.Catal.*, **60**, 241 (1979)

30. K.M.Mackay & R.A.Mackay in *Introduction to Modern Inorganic Chemistry*, 2nd Edn. (Publ.Intertext Books, London 1973)

31. J.B.Nagy, P.Bodart, H.Collette, J.El Hage-Al Asswad, Z.Gabelica, R.Aiello, A.Nastro & C.Pellegrino, *Zeolites*, **8**, 209 (1988)

32. *US.Pat.*, 4 061 724 (1977)

33. A.Araya & B.M.Lowe, *J.Catal.*, **85**, 135 (1984)

34. J.L.Casci, B.M.Lowe & T.V.Whittam, *Eur.Pat.Appl.*, 42 226 (1981)

35. V.N.Romannikov, V.M.Mastikhin, S.Hocevar and B.Drazaj, *Zeolites*, **3**, 311 (1983)

36. S.S.Pollack, J.W.Adkins, E.L.Wetzel & D.Newbury, *Zeolites*, **4**, 181 (1984)

37. P.A.Jacobs & J.A.Martens in *Synthesis of High-Silica Aluminosilicate Zeolites*, Stud.Surf.Sci.Catal.No.**33**, (Publ.Elsevier) chpt.8 (1987)

38. P.J.Hogan, T.V.Whittam, J.J.Birtill & A.Stewart, *Zeolites*, **4**, 275 (1984)

39. J.Dwyer, private commun. (U.M.I.S.T, Manchester, 1991)

40. S.A.I.Barri, G.W.Smith, D.White and D.Young, *Nature*, **312**, 533 (1984)

41. F.Y.Dai, K.Deguchi, M.Suzuki, H.Takahashi & Y.Saito, *Chem.Lett.*, 869 (1988)

42. Z.Gabelica, E.G.Derouane & N.Blom in *Catalytic Materials, Relationship Between Structure and Reactivity*, (Eds.Whyte, Dalla Betta, Derouane & Baker) ACS Symp.Ser., **248**, 219 (1984)

43. R.H.Daniels, G.T.Kerr & L.D. Rollmann, *J.Am.Chem.Soc.*, **100**, 3097 (1978)

44. W.J.Smith, J.Dywer & J.Dewing, *J.Chem.Soc.Farad.Trans. 1*, **85**(11), 3623 (1989)

45. R.Mostowicz & L.B. Sand, *Zeolites*, **2**, 143 (1982)

46. G.Debras, J.B.Nagy, Z.Gabelica, P.Bodart & P.A.Jacobs, *Chem.Lett.*, 199 (1983)

47. C.J.Pouchert, *The Aldrich Library of Infrared Spectra*, (1970)

48. K.Nakanishi & P.H.Solomon, *Infrared Absorption Spectroscopy*, 2nd Edn. (Publ.Holden-Day Inc., 1977)

49. N.Y.Topsoe, K.Pedresen & E.G.Derouane, *J.Catal.*, **70**, 41 (1981)

50. L.D.Rollmann, *US.Pat.*, 4 108 881 (1981)

51. P.J.Hogan, A.Stewart & T.V.Whittam, *Eur.Pat.Appl.*, 0 065 400

52. G.T.Kokotalio, J.L.Schenker, F.G.Dwyer & E.W.Valyocsik, *Zeolites*, **5** 349 (1985)

54. P.A.Jacobs & J.A.Martens in *Synthesis of High-Silica Aluminosilicate Zeolites*, Stud.Surf.Sci.Catal.No.**33**, (Publ.Elsevier) 243 (1987)

55. M.Hunger, J.Kärger, H.Pfeifer, J.Caro, B.Zibrowisius, M.Bülow & R.Mostowicz, *J.Chem.Soc.Farad.Trans.1*, **83 (11)**, 3459 (1987)

56. R.Challoner, R.K.Harris, K.J.Packer & M.J.Taylor, *Zeolites*, **10**, 539 (1990)

57. K.F.M.G.J.Scholle, W.S.Veeman, P.Frenkel & G.P.M.van der Velden, *Appl.Catal.*, **17**, 233 (1985)

58. G.C.Levy & G.L.Nelson, *Carbon-13 Nuclear Magnetic Resonance for Organic Chemists*, (Publ.Wiley-Interscience, 1972)

59. G.Engelhardt & D.Michel in *High Resolution Solid-State NMR of Silicates and Zeolites*, chpt.4 (Publ.Wiley & Sons 1987)

60. D.Apperley, private commun. (Uni.Durham Ind.Res.Lab., 1991)

61. W.Kemp, *NMR in Chemistry: A Multinuclear Introduction*, (Publ.Macmillan, 1986)

# CHAPTER 4

## The Synthesis of ZSM-11 using Several Organic Additives

### 4.1. Introduction

ZSM-11 and ZSM-5, structure types MEL and MFI respectively, form the two end members of the pentasil structure family [1]. Possessing an intermediate pore size and consequently, shape-selective properties, these zeolites are attractive candidates for many catalytic applications [2]. As described in section 1.2.2, both materials are structurally closely related. Intergrowths of the two structures can be generated and it has been postulated that an almost infinite series of intermediate structure types exist [3].

The original patent literature indicates that the synthesis of ZSM-11 requires the use of quaternary salts, specifically with four carbon atoms per alkyl chain. Such organic salts include tetrabutylammonium bromide (TBA) or tetrabutylphosphonium bromide (TBP) [4]. However, there are difficulties in synthesising ZSM-11 in a structurally pure form using these organic additives. The intergrowth content is influenced by synthesis variables such as the inorganic ion type [5] and the reaction temperature [6]. A particularly useful development in this respect was the use of comparatively inexpensive organic additives such as diamines and polyamines [7]. As well as enhancing the reaction rates during synthesis, these additives, DAO for example, improved the purity of the ZSM-11 products [8].

In contrast to ZSM-5, ZSM-11 can only be synthesised using fewer different types of organic additives [9]. This suggests a more stringent structure-directing requirement of the organic additive in the formation of ZSM-11. Recently, however, ZSM-11 was synthesised using the novel organic additive, N,N'-Bis(3-aminopropyl)piperazine (BAPZ) [10].

The aim of this work was to assess the structure-directing abilities of BAPZ, TBP, TBA and DAO for the synthesis of ZSM-11. Syntheses were performed using gels of

equivalent stoichiometry containing each or mixtures of the organic additives. The resultant solid products were assessed in terms of crystallinity and phase purity.

## 4.2. Experimental

All the gels were prepared in the same fashion using the reagents and procedure outlined in Chapter 2. A typical preparation of a gel for the synthesis of ZSM-11 proceeded as outlined in the following sections.

### 4.2.1. Gel Preparation

To a stirring solution of sodium hydroxide (20.52g) and aluminium nitrate (16.20g) in distilled water (260.00g), a mixture of Ludox AS40 colloidal silica (192.00g) and distilled water (130.00g) was added over a period of 20 minutes. Once homogeneous in appearance a solution of BAPZ (64.98g) in distilled water (130.00g) was carefully added to the stirring slurry. After aging for 15 minutes dropwise addition of nitric acid (70.00%, 20.83g) followed to control the initial $OH^-$ concentration as outlined in Appendix I. After a further aging period of one hour the slurry was charged to four, 120ml capacity stainless steel autoclaves and heated to 175°C, 165°C, 155°C or 130°C for a total reaction period of 50, 60, 150, and 200 hours, respectively. Several syntheses were performed in sealed polypropylene bottles at 90°C for 420 hours. The reactions performed at 130°C and 90°C were heated under static conditions while at the other temperatures the autoclaves were revolved at 80 rpm. The initial gel stoichiometry can be represented by the simple oxide formula,

$$11.9Na_2O - 59.2SiO_2 - Al_2O_3 - 15.0(BAPZ)_2O - 16688H_2O$$

where the initial molar ratios were,

1. $SiO_2/Al_2O_3=59.2$ 2. $Na_2O/SiO_2=0.20$
3. $OH^-/SiO_2=0.09$ 4. $H_2O/SiO_2=28.2$
5. $R_2O/SiO_2=0.25$

After an allocated reaction time the autoclaves were quench-cooled and a sample of the contents taken, filtered, thoroughly washed several times with deionised water and dried overnight at 120°C. All the solid products were characterised using XRD, SEM and chemical analysis as outlined in Chapter 2.

## 4.3. Results and Discussion

In order to investigate the reaction system the initial synthesis procedure was modified as outlined below.

### 4.3.1. Effect of the Initial $SiO_2/Al_2O_3$ Ratio and Reaction Temperature

The original gel was prepared except various amounts of aluminium nitrate were added to the initial sodium hydroxide solution. Subsequently, the initial $OH^-/SiO_2$ ratio was controlled with the corresponding addition of nitric acid (70.00%) as outlined in Appendix I. The initial starting stoichiometries can be represented by the following equation:

$$11.9Na_2O - 59.4SiO_2 - xAl_2O_3 - 15.1R_2O - 1656.7H_2O,$$

where x equals 1.2, 1.0 and 0.8. This corresponds to initial $SiO_2/Al_2O_3$ ratios of 70.0, 59.4 and 50.0, respectively. The reactions were performed at the temperatures previously outlined.

All the crystalline phases were identified by comparing the XRD data of the calcined materials with literature data [11]. The quantitative determination of intergrown materials is a difficult task. As discussed in Chapter 5, a number of analytical methods have been employed for this purpose. In this study, due to the large number of samples involved, XRD was used as semi-quantitative method to determine phase purity [12]. This procedure takes into account the relative intensities of the peaks around $2\Theta$ of 23.19 and 24.48, associated with d-spacings (d) of 3.84 and 3.64, respectively.

However, XRD cannot distinguish intergrown materials from physical mixtures of the end members. Due this ambiguity, in this study the quantity of ZSM-5 to ZSM-11 in the crystalline product from the x-ray data will be know as the pentasil content. In a similar manner, such materials will be referred to as a pentasils. The pentasil content of the sample can be assessed using the relationship of the d-spacings:

$$\% \text{ Pentasil} = (I_{3.64} / I_{3.84}) \times (100 / 0.5)$$

The peak at 3.64 is absent in ZSM-11 and the value of 0.5 refers to the maximum

value obtained for the relationship $I_{3.64}/I_{3.84}$ for the ZSM-5 standard used in this study. Consequently, all the results are normalised to the pure ZSM-5 standard. Table 4.1 summarises the x-ray data obtained of the calcined materials in terms of product crystallinity and pentasil content. The results reveal that ZSM-11 and pentasil materials were synthesised from gels using any one of the organic additives. No other zeolite phases were obtained in this synthesis study. Figure 4.1 compares the XRD patterns of the materials obtained using each organic additive after 50 hours with an initial $SiO_2/Al_2O_3$ ratio of 70. The data show that both the phase purity and crystallinity are dependent upon the organic additive.

| REACTION | | INITIAL $SiO_2/Al_2O_3$ RATIO | | | | | | | | | | | |
|---|---|---|---|---|---|---|---|---|---|---|---|---|---|
| TEMP /°C | TIME /hrs | TBA | | | TBP | | | DAO | | | BAPZ | | |
| | | 50 | 60 | 70 | 50 | 60 | 70 | 50 | 60 | 70 | 50 | 60 | 70 |
| 90 | 420 | - | - | 55 | - | - | 65 | - | - | 65 | - | - | D |
| 130 | 200 | - | - | 60 | - | - | 70 | - | - | 68 | - | - | D |
| 155 | 160 | 57 | 63 | 65 | 63a | 67b | 87b | 66 | 73 | 79 | 47c | 53c | 70a |
| 165 | 60 | 69a | 68a | 76a | 80b | 70b | 88b | - | 82 | 76 | 63 | 72b | 65a |
| 175 | 50 | 69a | 66 | 83a | 69b | 66b | 94b | 70 | 59 | 94 | 75b | 70b | 66a |

a. 20-30% Intergrowth
b. 60-70% Intergrown
c - associated with clay type materials
D - Amorphous

**Table 4.1. Summary of the XRD results of calcined zeolites synthesised using several organic additives.**

As the organic additives differ in both physical and chemical nature it is worth noting that similar zeolites were synthesised under the same reaction conditions. Consequently, these reactions do not necessarily represent the optimum reaction stoichiometry and conditions for the synthesis of MEL for each organic system. This was reflected in the comparative crystallinity of the synthesis products under a given set of reaction conditions. Figure 4.2 compares the reaction kinetic plots for each organic system synthesised at 175°C with an initial $SiO_2/Al_2O_3$ ratio of 70.

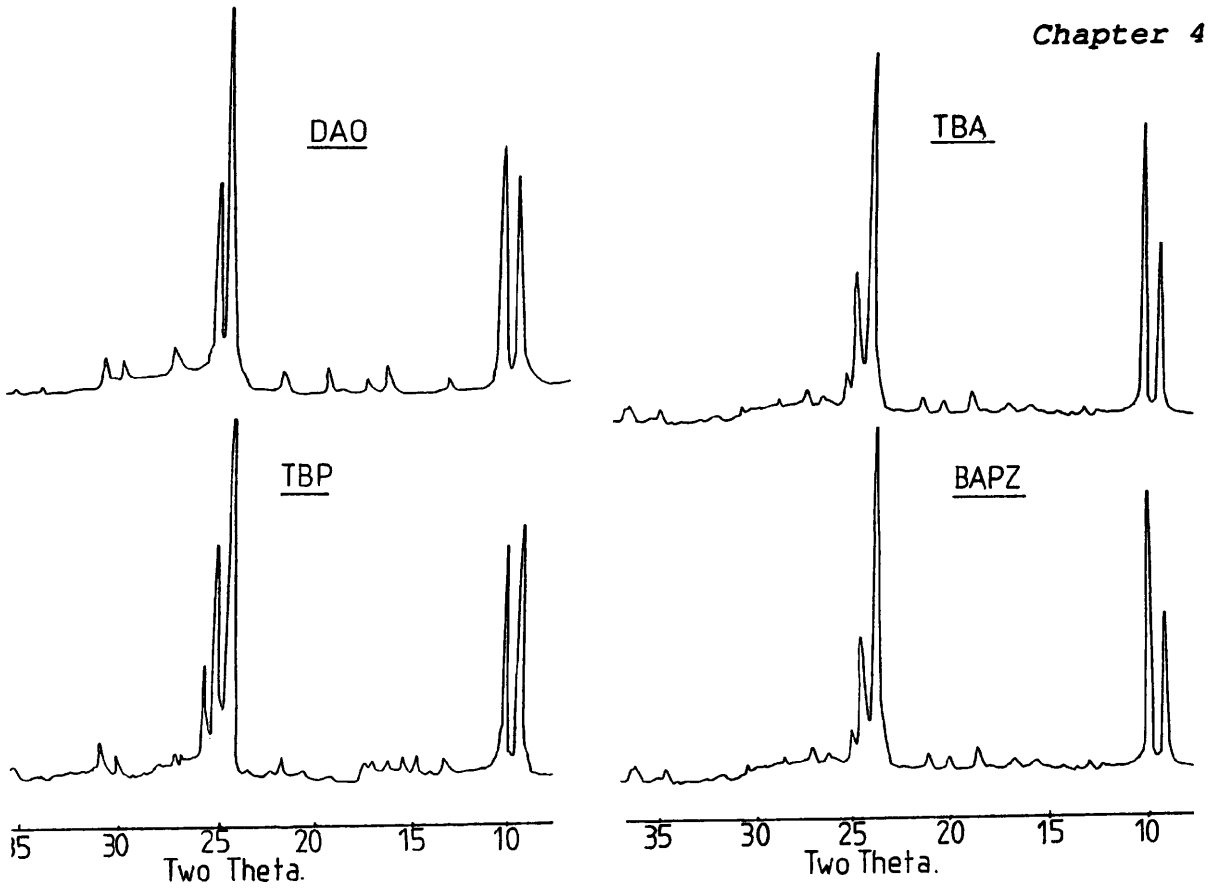


**Figure 4.1. XRD data of calcined zeolites produced with several organic additives with an initial $SiO_2/Al_2O_3$ of 70 at 175°C after 50 hours.**

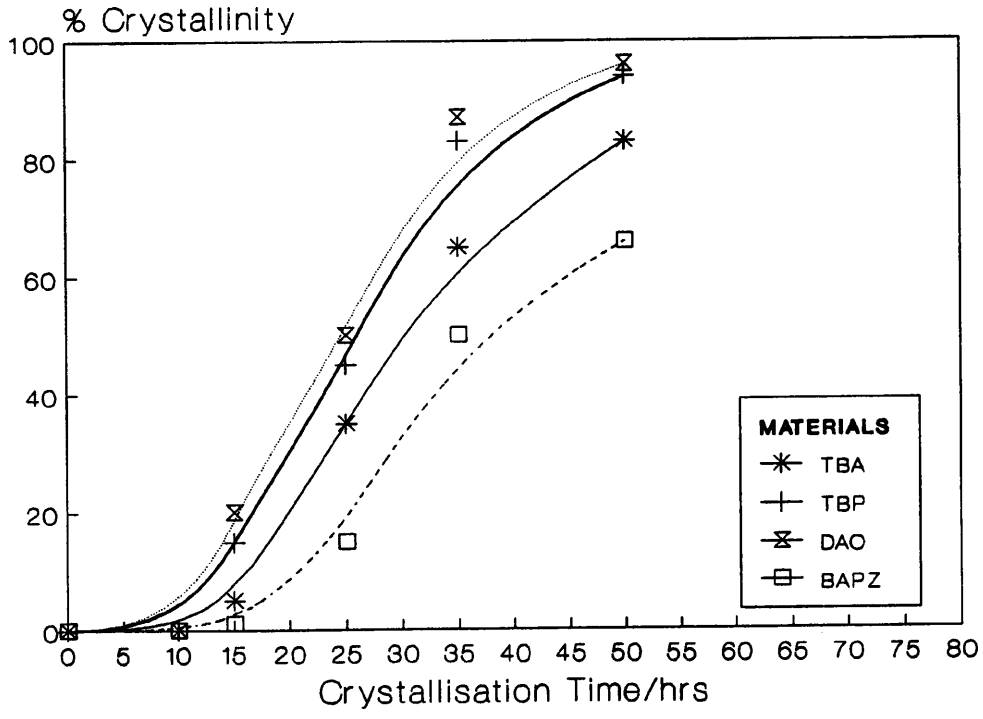


**Figure 4.2. Reaction kinetic data for pentasil synthesis using several organic additives at 175°C with an initial $SiO_2/Al_2O_3$ of 70.**

In agreement with similar MEL synthesis studies [12], a faster nucleation rate and highly crystalline zeolites were obtained from reaction systems involving TBP and DAO as the organic additive. Both systems had an equivalent nucleation period of less than ten hours followed by rapid crystallisation. The crystallinity of the final samples taken from both reaction systems after 50 hours was approximately 95%. Pure ZSM-11 was obtained using DAO as the organic additive. However, a pentasil 60-70%, was synthesised involving TBP. In contrast, the reaction rates of the TBA synthesis were slower. The estimated nucleation period was less than 15 hours and the crystallinity of the final sample taken after 50 hours was around 83%. In this case, the crystalline material was richer in ZSM-11 with an estimated pentasil content between 20-30%. The reaction kinetics were most inhibited where BAPZ was used as the organic additive. After a nucleation period of greater than 20 hours the product crystallinity after a reaction period of 50 hours was approximately 66%. The pentasil content of this material was estimated between 20-30%.

In general, synthesis involving a particular organic additive experienced similar trends with respect to reaction kinetics and phase purity. For a given reaction temperature the shortest nucleation periods and most crystalline materials were obtained from gels containing TBP and DAO. Pure ZSM-11 was always synthesised where DAO was the organic additive, independent of the gel composition or reaction temperature. The majority of synthesis performed using TBP as the structure-directing agent resulted in a range of crystalline products with a pentasil content, between 20-70%.

Although the reaction rates were comparatively slower in the TBA system, the pentasil content of the materials was below 30%. Independent of the gel composition, pure ZSM-11 was obtained in this reaction system by decreasing the reaction temperature. The slowest nucleation and crystallisation rates were associated with reaction systems containing BAPZ. Depending on the reaction temperature the pentasil content of the crystalline products from this system varied between 20-70%.

Previously, BAPZ has only been used as the organic additive for the synthesis of ZSM-48 using an all-silica reaction system [13]. In this work using an aluminous system, ZSM-11 type materials were synthesised. A similar trend was noticed in the

DAO synthesis studies discussed in Chapter 3. Although not as efficient, this shows BAPZ has a similar structure-directing nature to DAO. In other studies, silicalite-1 [14] and clathrasils, ZSM-39, Eu-19 and Eu-20 [15] were synthesised with piperazine as the organic additive. This highlights the structure-directing effect of changing the dimensions of the organic additive on the zeolite synthesis.

Once nucleated the pentasil zeolites were *phase stable*, ie.their pentasil content remained constant, throughout the reaction period. Transformations to ZSM-5-rich or denser materials such as α-quartz or cristobalite were not apparent. In this work the reaction times were not prolonged where transformations to more thermodynamically stable phases might have occurred.

The crystallinity of the final products for each set of reaction conditions can be summarised by the general trend:

INCREASE IN PRODUCT CRYSTALLINITY



**DAO ≡ TBP > TBA > BAPZ**

Overall, the phase purity of ZSM-11 was a function of the reaction temperature and the nature of the organic additive. In agreement with other studies concerning the synthesis of ZSM-11 [5], the purity of ZSM-11 increased with a decrease in the reaction temperature, independent of the gel composition. At 130 and 90°C, ZSM-11 was the only product formed from gels involving TBA, TBP, and DAO. The decrease in reaction temperature also corresponded to a reduction in the nucleation and crystallisation rates of the systems. Indeed, only amorphous solids were found in reactions performed below 155°C involving BAPZ as the organic additive. This reveals the limitations of this organic additive as a structure-directing agent. Such kinetic trends are in agreement with other pentasil synthesis studies [6]. Figure 4.3 shows the effect of reaction temperature on the reaction kinetics involving TBP as the organic additive.

As discussed in section 3.31, lower synthesis temperatures encourage the synthesis of more symmetrical structures. This is due several factors such as the thermodynamics of the reaction system and/or the reduced thermal motion of reactant species. Consequently, the nature of the zeolite formed is directly influenced by the pore-filling nature of the organic additive [16]. Kaucic et al.[17] suggested that, due to its larger

size compared to TBA, TBP stabilises the zeolite structure more effectively and promotes crystallisation. The effect of these organics with respect to phase purity was not fully discussed by the authors.

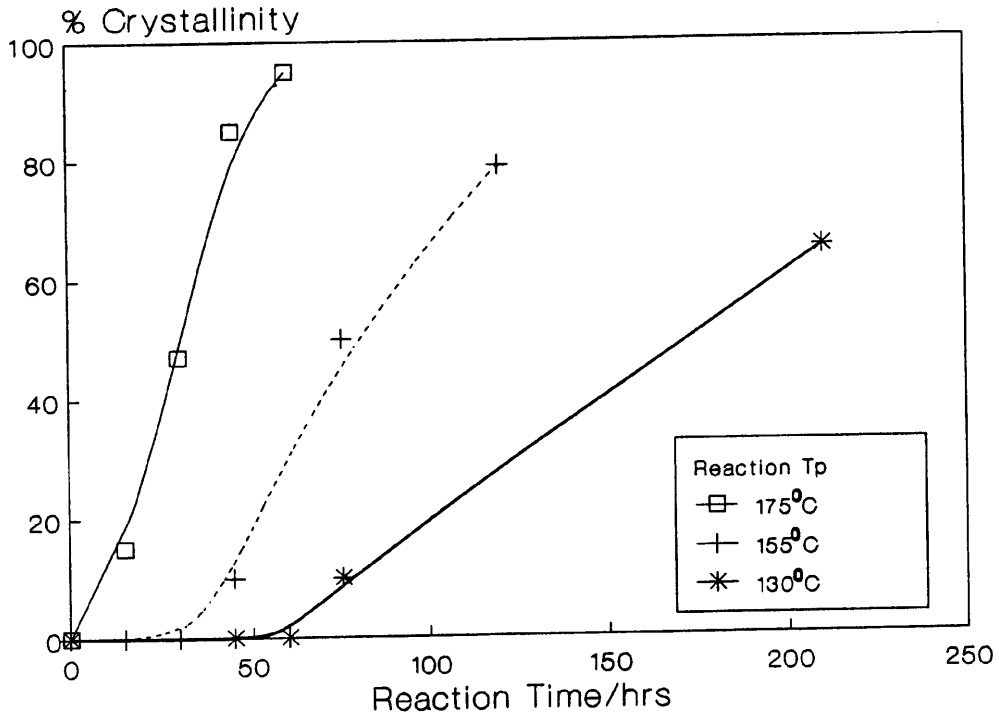


**Figure 4.3. Effect of reaction temperature on pentasil synthesis with TBP as the organic additive with an initial $SiO_2/Al_2O_3$ ratio of 70.**

It has been shown that the specific length or size of the diamine molecule directly influences phase development. For example, Valyocsik et al.[18] found that a diamine chain containing eight or nine carbon atoms enhances the nucleation and crystallisation of ZSM-11. In contrast, BAPZ is a comparatively bulky organic additive and as a result has a limited pore-filling capacity (discussed later). Consequently zeolite formation is inhibited, as reflected in this and other work [10] by the narrow compositional ranges within which ZSM-11 was synthesised.

For the reactions performed between 155 and 175°C, the overall pentasil content with respect to organic additive can be summarised as follows:

**INCREASING ZSM-11 PURITY**

**TBP < BAPZ < TBA < DAO**

**INCREASING pentasil CONTENT**

Consistent with other pentasil studies [19], product crystallinity was generally enhanced with an increase in the initial $SiO_2/Al_2O_3$ ratio. This is indicative of the disruptive nature of aluminium incorporation into the zeolite framework [19]. In contrast to other studies [20], there was no clear indication that the aluminium content of the initial gel affected the pentasil content of the zeolite. However, in this work the range of initial $SiO_2/Al_2O_3$ ratios investigated was comparatively narrow and possibly not sufficient to show such phase changes.

The micrographs of the products obtained after 150 hours with an initial $SiO_2/Al_2O_3$ ratio of 50 at 155°C are shown in Figure 4.4. The morphology and crystal sizes are all very similar irrespective of the phase purity and the nature of the organic additive. Indeed, an equivalent crystal morphology (not shown) was found for the crystalline products obtained at 175°C, but some amorphous material is present with the crystalline phase obtained from the reaction containing BAPZ. The phases are composed of crystalline egg-shell- and sheet-like aggregates around 10-15μm in size. The aggregates are made up very small spherical crystallites approximately 0.5-1.5μm in diameter.

The homogeneity of the crystal morphology and size suggests that similar crystal growth processes occurred during each synthesis. These results show that morphological similarities are by no means an indication of phase purity. Several studies, as mentioned in section 1.4, have suggested that an interface or site is required for nucleation to occur [21]. A process termed *Method B* was suggested Gabelica et al.[16] to describe the processes of nucleation and crystal growth occurring at the gel/solution interface during pentasil synthesis. The initial nuclei are sited at the surface of the gel and gradually grow by the incorporation of soluble species originating from the gel. The egg-shell aggregate morphology represents the latter stages of the reaction where the spherical crystals are held together by the remaining amorphous *gel-glue*.

The chemical analyses of most of the crystalline products are summarised in Table 4.2. Generally, the ratio of the $SiO_2/Al_2O_3$ ratio in the gel to that in the solid phase is approximately unity for all of the crystalline products.

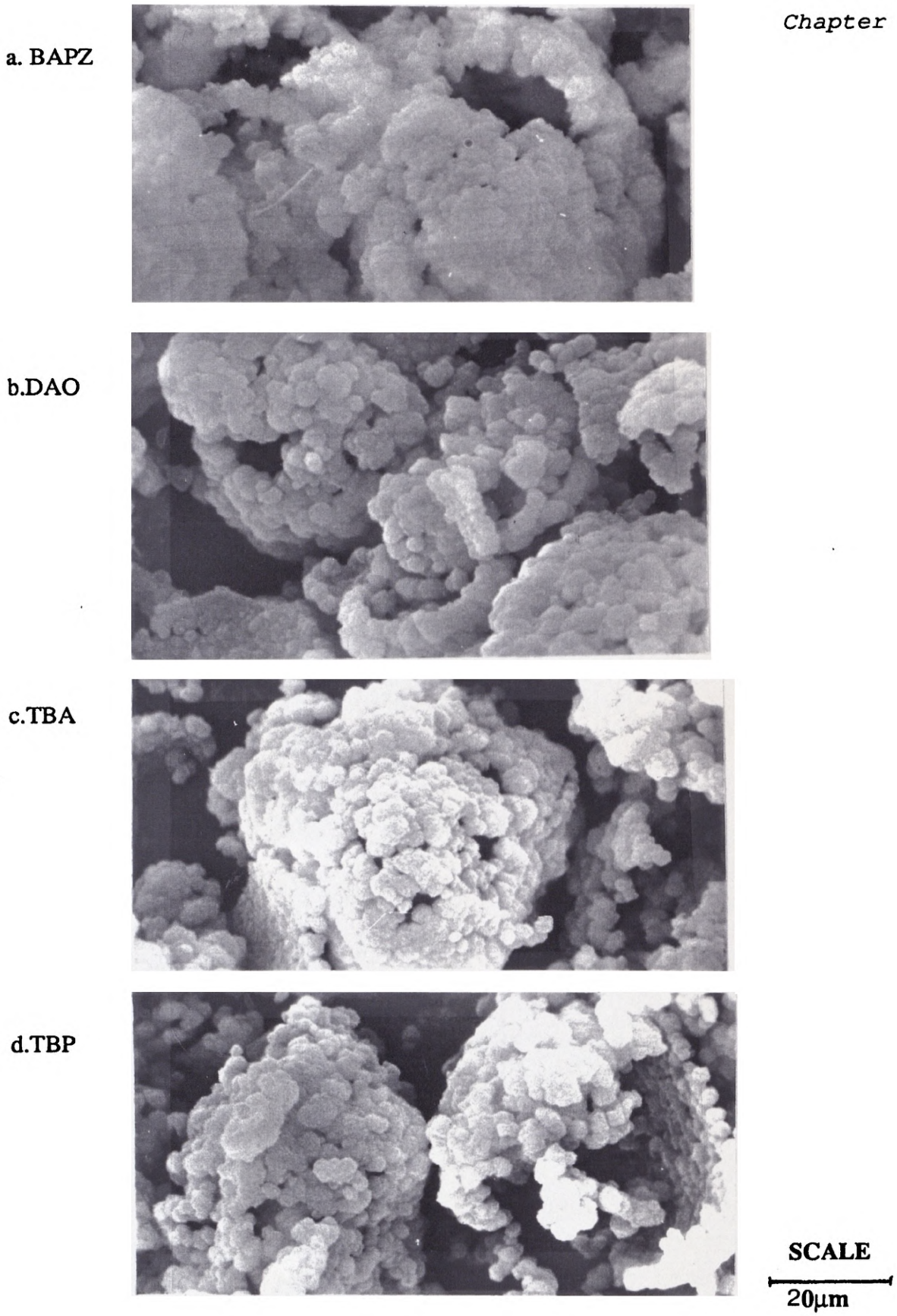


**Figure 4.4. SEM of zeolites obtained at 155°C after 150 hours with an initial $SiO_2/Al_3O_2$ of 50.**

This indicates an efficient up-take of aluminium into the framework. For all samples, the molar Na/Al ratio was less than one. This suggests that the organic additives function as both charge-balancing ions as well as structure-directing agents during synthesis. This assumes that both DAO and BAPZ were incorporated into the zeolite pore system in a protonated form [18]. For reactions involving the quaternary ions and BAPZ the crystalline product contained two $Na^+$ ions per unit cell. In contrast, ZSM-11 products synthesised with DAO contained one $Na^+$ ion per unit cell. This indicates that DAO is more favoured as a charge-balancing species than the other organic additives.

| Organic Additive | $SiO_2/Al_2O_3$ Initial Ratio | Molar Product Ratios | | | R | Na |
|---|---|---|---|---|---|---|
| | | Na/Al | C/N | $Si_2O/Al_2O_3$ | p.u.c | p.u.c |
| TBP | 70 | 0.66 | 14.4 | 64.8 | 2.8 | 1.9 |
| TBA | 70 | 0.55 | 14.5 | 66.0 | 2.8 | 1.9 |
| BAPZ | 70 | 0.76 | 2.5 | 61.4 | 3.7 | 1.9 |
| DAO | 70 | 0.33 | 7.0 | 68.2 | 4.7 | 0.9 |
| TBP | 50 | 0.50 | 12.6 | 51.2 | 2.8 | 1.8 |
| TBA | 50 | 0.51 | 13.0 | 56.0 | 2.8 | 1.8 |
| BAPZ | 50 | 0.40 | 2.0 | 43.4 | 3.7 | 1.8 |
| DAO | 50 | 0.23 | 7.0 | 46.1 | 4.9 | 0.9 |
| $TBP_a$ | 70 | 0.96 | 17.5 | 74.6 | 1.9 | 2.8 |
| TBA | 70 | 0.50 | 16.5 | 65.0 | 2.9 | 1.9 |
| $DAO_a$ | 70 | 0.40 | 7.5 | 68.0 | 5.1 | 0.9 |

a. Synthesised at 130°C

**Table 4.2. Chemical analysis of crystalline products synthesised 175°C after 50 hours.**

Noticeably, ZSM-11 synthesised at 130°C using TBP as the organic additive is comparatively more siliceous than the product synthesised at 175°C with a high pentasil content. The former zeolite also contains more $Na^+$ ions and less TBP species than the latter product. This suggests that the incorporation of TBP cations encourages the development of ZSM-5. In contrast, there was no difference in the inorganic or Si/Al composition of the zeolites obtained with TBA. Franklin et al.[22] noticed a similar decrease in organic up-take of the zeolite with increasing size of the quater-

nary ammonium species. This suggests that TBA is a more favourably incorporated into the pore system of ZSM-11 than TBP. This may relate to the smaller dimensions of TBA and/or its more efficient counter-balancing properties.

In contrast, the composition of ZSM-11 synthesised at 130°C in the presence of DAO has a similar chemical composition to ZSM-11 formed at 175°C. This highlights the efficiency of DAO as both a charge-balancing ion and a structure-directing species in the synthesis of ZSM-11.

In general, the product C/N molar ratios denote that each organic additive is intact and sited in the pores of the zeolite. The corresponding organic unit cell organic content is approximately 5.0, 3.7 and 2.8 for systems containing DAO, BAPZ and quaternary cations, respectively. However, the molar C/N ratio of between 13 and 14 of the zeolites containing quaternary ions is slightly lower than the expected value of 16. It has been demonstrated that tetraalkylammonium ions under synthesis conditions can undergo a base catalysed Hoffmann Elimination type reaction [23]. For example, using TBA the reaction proceeds as follows,

**Hoffmann Elimination**

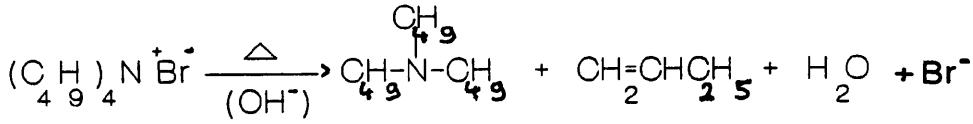

Tributylamine formed during the elimination reaction is a known structure-directing agent for ZSM-5 [16]. It is possible that this product interferes with the reaction processes involved in the synthesis of ZSM-11. Consequently, this may result in the nucleation of ZSM-5 type species.

The chemical and physical nature of TBA sited in the zeolite pore system was investigated using $^{13}C$ CP-NMR MAS. The $^{13}C$ CP-MAS NMR spectrum of the pentasil material synthesised with an initial $SiO_2/Al_2O_3$ of 50 at 175°C is illustrated in Figure 4.5. Table 4.3 compares the corresponding chemical shifts (in ppm from TMS) to TBA in solution and reported data from a similar study [24]. Chemical shift variations are towards lower fields in the butyl chains of TBA relative to the corresponding values in water. The respective shift changes are +1.8 ($C_1$), +0.1 ($C_2$), +0.4 ($C_3$), +0.8

($C_4$) and -1.2ppm ($C_4$). There is no contribution to the spectra of degraded products such as tributylamine. However, a splitting of the $C_4$ terminal methyl resonance is found. The chemical shift data compares well to that previously reported by Nagy et al.[24] and shows that TBA is incorporated into the channel system in an intact form. The splitting of the terminal methyl resonances is due to environmental effects i.e. the position of TBA in the framework [24].

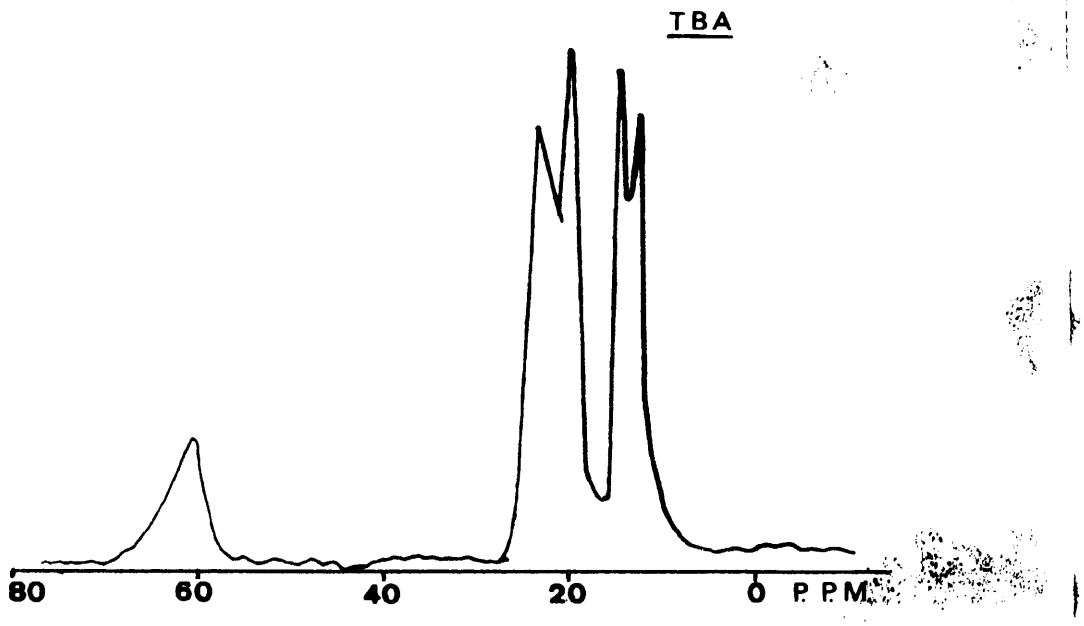


**Figure 4.5. $^{13}C$ CP-MAS NMR of the as-made pentasil after 50 hours synthesised with TBA at 175°C with an initial $SiO_2/Al_2O_3$ Ratio of 50.**

| SAMPLES | CHEMICAL SHIFT(ppm form TMS)[a] | | | |
|---|---|---|---|---|
| | $C_1$[b] | $C_2$ | $C_3$ | $C_4$ |
| TBABr 0.6M in $H_2O$ | 58.9 | 24.0 | 20.0 | 13.9 |
| TBA in Intergrowth | 60.7 | 24.1 | 20.4 | 15.0, 12.7 |
| TBA in ZSM-11 [25] | 60.6 | 24.1 | 20.8 | 14.7, 12.7 |

a. TMS - Tetramethylsilane

b. Numbering sequence of the carbon atoms in TBA

$$N^{+}(\overset{1}{CH_2}\text{-}\overset{2}{CH_2}\text{-}\overset{3}{CH_2}\text{-}\overset{4}{CH_3})_4$$

**Table 4.3. Chemical shift assignment for TBA in various physical environments.**

The framework of ZSM-11 consists of two types of channel intersections, one similar to that in ZSM-5 and another approximately 30% larger. Chemical analysis revealed that 2.8 TBA cations occupy the channels of a unit cell of the ZSM-11-rich pentasil containing four cavities. These cations preferentially occupy the larger cavities [24]. This is reflected by the different $C_4$ intensities and is in agreement with other studies. The remaining 0.8 organic cations take up positions in the remain two smaller cavities. A similar $C_4$ methyl resonance splitting would be experienced by TBA incorporated into the pore system of ZSM-5. This is due differences in the channel geometry where both zig-zag and straight channels are present. Consequently this method cannot be used to differentiate pentasil intergrowths from physical mixtures ZSM-5 and ZSM-11.

As outlined in Chapter 3, the pore-filling capacity of an organic additive can be estimated by relating the length of the hydrocarbon in question to the total channel length (per unit cell) of the corresponding zeolite framework. The molecular lengths of the organic additives were calculated from an energy-minimised structural representations using CHEM-X [17]. The molecular dimensions of the various organic additives are given in Figure 4.6. Small changes in the conformation of the organic additive are expected when incorporated into the pore system [25]. However, these values are thought to reasonably represent the dimensions of the organic additives. The total channel length for ZSM-11 and ZSM-5 is 8.0nm and 8.8nm, per unit cell, respectively [24]. The channel length of the pentasil was calculated using the structural composition of ZSM-11 and ZSM-5 estimated from the x-ray analysis.

Hence, for example, the theoretical maximum number of TBA cations per unit cell of ZSM-11 (20% pentasil content), can be represented as follows.

**Theoretical Number (n) of TBA cations per unit cell,**

$$n(TBA)/\text{Unit Cell}=[(8.8 - 8.0) \times 0.2] + 8.0/(4_a \times 0.72_b)$$

**a. calculated length of a n-butyl chain in nm**
**b. takes into account the four n-butyl chains per TBA cation**

This formula assumes complete pore-filling by TBA and an end-to-end configuration

of the butyl chains. The theoretical pore capacity of the other organic additives can be calculated likewise. Table 4.4 lists the pore-filling capacities of the zeolites synthesised at 175°C with the initial $SiO_2/Al_2O_3$ ratio of 70. The calculations show that the pore-filling capacity of the quaternary ions and DAO is between 85-100%.

In contrast, products containing BAPZ had a lower organic content of approximately 75%. These results support the reaction kinetic data suggesting that the structure-directing abilities of BAPZ are less pronounced than those of the other organic additives. However in the case of DAO, the data show that the organic does not have to occupy all the pore space available in order to be an efficient structure-directing agent.

If the pentasil materials are indeed intergrowths, planar faults occur parrallel to the [010] channel system [26]. The quaternary ammonium ions can be assumed to be sited at the centre of channel intersection. Their butyl chains extend along the channel system [24]. By the same analogy for the BAPZ molecule, the piperazine ring may occupy the channel intersection with the amino-n-propyl groups pointing along the 10-MR channels. In the case of DAO the molecule can occupy the total [010] and [100] channel system of ZSM-11. The accommodation of the organic along the channel system, rather than at the channel intersection, should prevent the development of fault planes in ZSM-11.

| | Physical Data | | | Theoretical Data | | |
|---|---|---|---|---|---|---|
| Organic Additive | % INTERG[a] from XRD | R[b] p.u.c. | % Pore Filling Capacity | R p.u.c ZSM-11 | INTERG[a] | ZSM-5 |
| TBA | 20-30 | 2.8 | 100 | 2.8 | 2.9 | 3.0 |
| TBP | 60-70 | 28 | 100 | 2.8 | 2.9 | 3.0 |
| DAO | Pure ZSM-11 | 4.7 | 90 | 5.3 | 5.6[c] | 5.9 |
| BAPZ | 20-30 | 3.7 | 75 | 4.8 | 4.9 | 5.3 |

a. Intergrowth
b. Chemical analysis
c. Theoretical 50% intergrowth

**Table 4.4. Calculated pore-filling capacity of organic additives used for pentasil synthesis.**

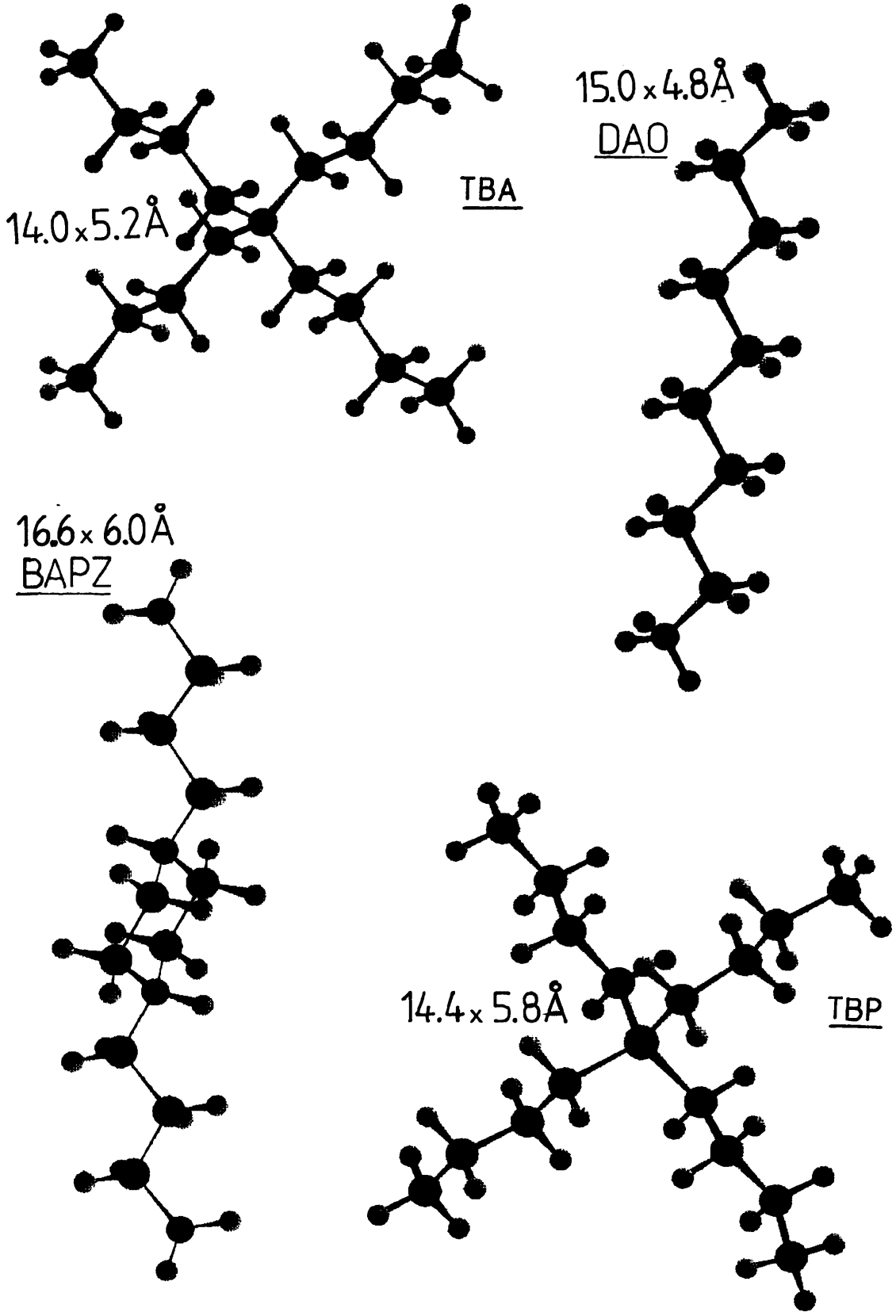


**Figure 4.6. CHEM-X energy minimised view of the organic additives used for pentasil synthesis.**

### 4.3.2. The Influence of Inorganic Cation Variation

The effects of the inorganic cation were studied using an all-silica reaction system. The initial gel was prepared, except that aluminium nitrate was excluded and either sodium hydroxide, potassium hydroxide or mixtures of the two metal hydroxides were added. Synthesis were also performed excluding a mineralising agent. The initial gel stoichiometry can be summarised as follows:

$$35.0M_2O - 29.3R_2O - 115.8SiO_2 - 0.1Al_2O_3 - 7778.0H_2O$$

where, M=K, Na or K/K+Na=0.05 , R=TBP, TBA, DAO or BAPZ. The initial oxide molar ratios were as previously stated except for $OH^-/SiO_2$ which varied between 0.10 and 0.30. All reactions were heated statically at 130°C and 175°C for a total reaction time of 140 and 42 hours, respectively.

Phases were identified by comparing their respective x-ray data to literature values [11]. The results showed that ZSM-48, silicalite-1 and silicalite-2 were obtained dependent upon the nature of the organic additive and reaction temperature. In contrast to Jabolonski et al.[5], the phase synthesised was independent of the inorganic cation type. Table 4.5 lists all products and their related crystallinity obtained at both reaction temperatures when the initial $OH^-/SiO_2$ ratio was 0.3.

| REACTION TEMP/°C | REACTION TIME/hrs | $M^+$ Ion | ORGANIC ADDITIVE(% Crystallinity) TBP | TBA | DAO | BAPZ |
|---|---|---|---|---|---|---|
| 130 | 140 | Na | [1]Sil-2(45)$_m$ | Sil-1(11) | Sil-2(66)$_m$ | AMP |
| | | K | Sil-2(35)$_m$ | [3]AMP | Sil-2(100)$_m$ | AMP |
| 175 | 42 | Na | [2]Sil-1(87) | Sil-1(76)$_q$ | ZSM-48$_k$ | AMP |
| | | K | Sil-1(95) | Sil-1(90)$_c$ | Q+C | AMP |

Trace Products - m-magadiite q-quartz c-cristobalite k-kenyaite
1. Sil-2 - Silicalite-2
2. Sil-2 - Silicalite-2
3. AMP - Amorphous Materials

**Table 4.5. Zeolites synthesised with an initial $OH^-/SiO_2$ ratio of 0.3 at 130°C and 175°C.**

At 130°C after 140 hours, silicalite-2 was synthesised in the presence of $Na^+$ or $K^+$ ions and gels containing DAO or TBP. The crystallinity of silicalite-2 was markedly greater in systems containing DAO, showing that it is a very efficient structure-directing agent for the synthesis of MEL. In contrast, silicalite-1 with low crystallinity was synthesised from gels containing TBA and $Na^+$ ion and amorphous solids were associated with the $K^+$ ion system. This reflects the less efficient structure-directing abilities of TBA as compared to TBP, as discussed in section 4.31. Reactions involving BAPZ were unsuccessful throughout this synthesis study. This may be related to the basicity of the initial gel as previously, zeolites were only synthesised when the initial $OH^-/SiO_2$ ratio was below 0.15 [10].

At 175°C after 42 hours, highly crystalline silicalite-1 was obtained from both quaternary ion systems. This is in agreement with the work of Bibby et al.[27], who found that silicalite-2 was only synthesised using TBA in the absence of inorganic cations. With inorganic cations silicalite-1 formed, suggesting that such additives possess some structure-directing abilities. ZSM-48, together with kenyaite, was synthesised from gels containing DAO and $Na^+$ ions which compares to the results discussed in Chapter 3. Denser phases such as cristobalite and α-quartz were found in the $K^+$ ion system. This may reflect a faster reaction rate as compared to the $Na^+$ ion system where the initial crystalline products have transformed to denser phases. Supporting the findings of other workers [28], these results show that branched organic additives such as TBA and TBP favour the formation of a two- and three-dimensional framework containing channel intersections. In contrast, DAO and other linear molecules are accommodated along the pore system of the zeolite and promote the formation of one-dimensional frameworks, such as ZSM-48.

The effect of the initial gel basicity on the crystallinity of MEL at 130°C after 140 hours with TBP as organic additive is evident from Figure 4.7 The results show that in both, the $Na^+$ and $K^+$ ion systems, the most crystalline was synthesised when the $OH^-/SiO_2$ ratio was 0.2. Below this value, reaction rates were slow and a longer crystallisation period was required for an equivalent crystallinity. At higher basicity values the crystalline phase was associated with denser phases such as magadiite. The development of denser phases at higher alkalinities has also been noted by other

workers [17,28]. Similar results were obtained when DAO was used as the organic additive for the synthesis of silicalite-2, as discussed in section 3.32.

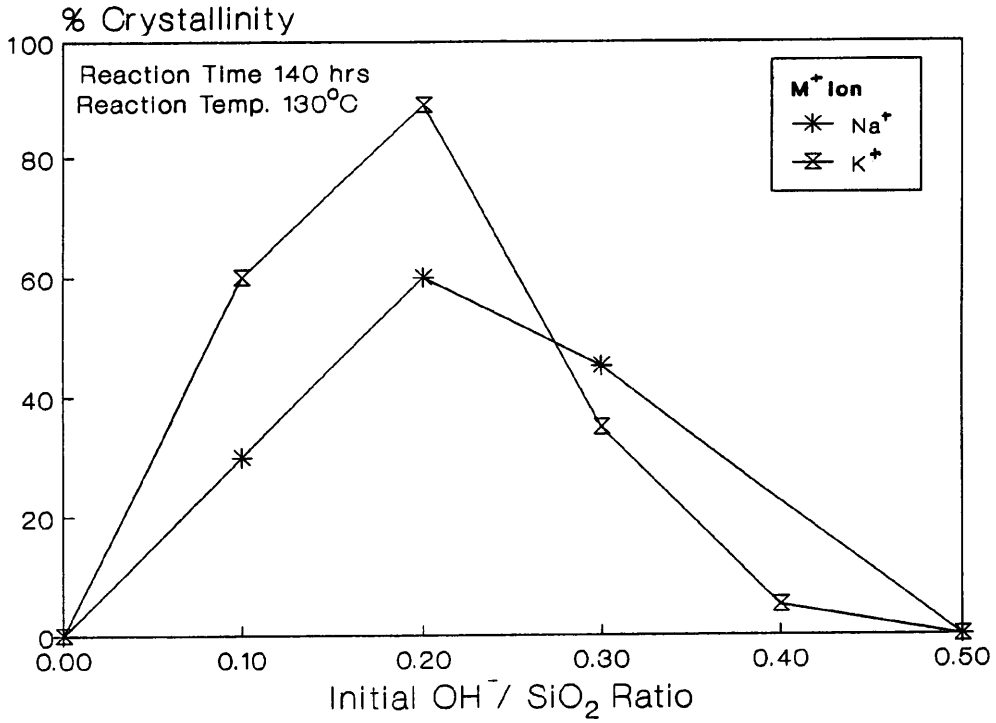


**Figure 4.7. Effect of the initial $OH^-/SiO_2$ ratio on the crystallinity of silicalite-2 with TBP as the organic additive.**

The reaction kinetics of gels containing TBP and $Na^+$, $K^+$ or $K^+/Na^+$ ions (where $K^+/(K^+ + Na^+)=0.05$) were investigated. The gels were synthesised at the optimum basicity ratio at 130°C and the results are summarised in Figure 4.8. In agreement with the results discussed in section 3.3.3 and by others [29], both the nucleation and crystallisation rates of MEL were enhanced by the presence of $K^+$ ions. This was highlighted by the mixed ion system where the addition of $K^+$ ion (5%) to the $Na^+$ ion systems resulted in a significant increase in the reaction rates. The estimated nucleation period from the crystallisation data for the $K^+$, $K^+/Na^+$ and $Na^+$ systems was 15, 30 and 40 hours, respectively. After nucleation, the crystallisation was rapid in all the reaction systems and less dependent on the nature of the inorganic cation. It appears from this kinetic data that the $K^+$ ions are most influential during the nucleation period of silicalite-2. Silicalite-2 was phase-stable throughout the reaction period. However, trace impurities of MFI (<5%), developed in the latter stages of all the syntheses after 120 hours.

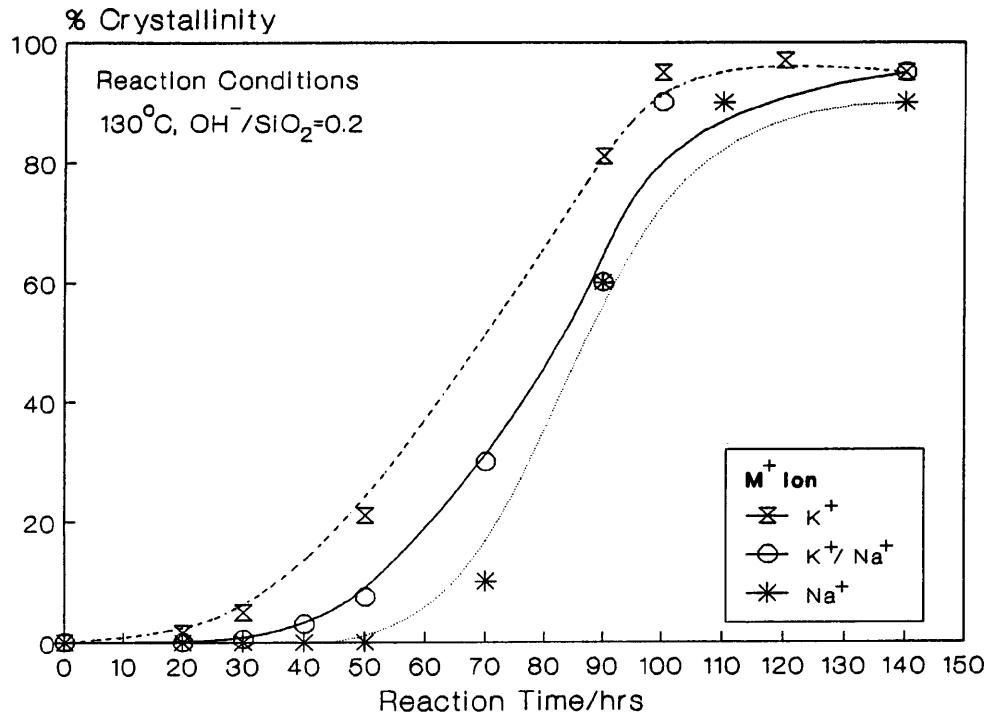


**Figure 4.8. Effect of the $M^+$ ion on the synthesis of MEL at 130°C.**

The micrographs of silicalite-2 synthesised at 130°C after 120 hours in the $Na^+$, $K^+$ and $Na^+/K^+$ ion systems are shown in Figure 4.9. The crystals obtained in the $Na^+$ ion system have an regular morphology. The majority of the crystalline phase is composed of lozenge-shaped crystals with an average size of 6 x 12μm. A large amount of these crystals are twinned with a random multifaceted nature. The surface of a crystal can offer an active site for secondary nucleation [30] which leads to a crystal morphology of this type. There is also a nominal amount of small, irregular and lozenge-like crystallites between 1 and 2μm in length. A range crystal sizes were observed in the $K^+$ ion system. All the material was composed of lozenge type crystals. In contrast to the $Na^+$ ion system they are virtually free from twinning and surface defects. The crystal sizes can be separated into two categories. The first contains crystals of approximately 6 x 13-14μm and accounts for around 30% of the crystalline phase. The other, and the majority of the solid product (@70%), consists of appreciably smaller crystals between 1.5-7.0 x 0.5-3.0μm. Such a clear division in crystal size is again an indication of secondary nucleation.

**a. $Na^+$-Silicalite-2**

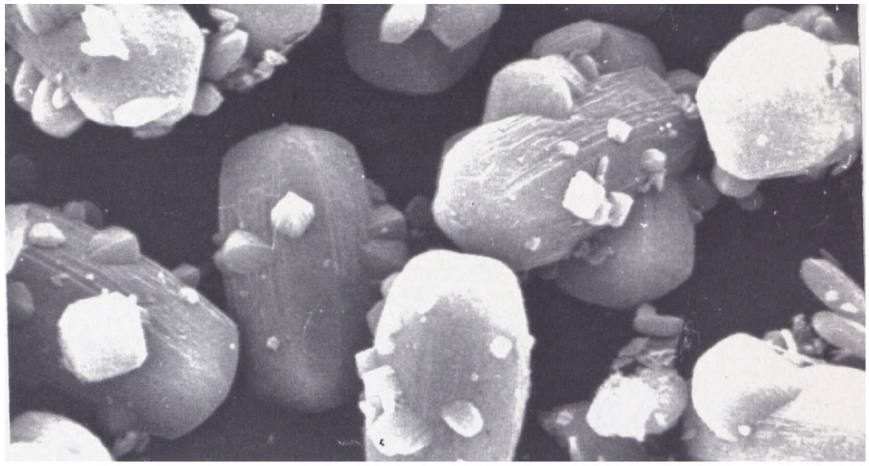


**b.$K^+$-Silicalite-2**

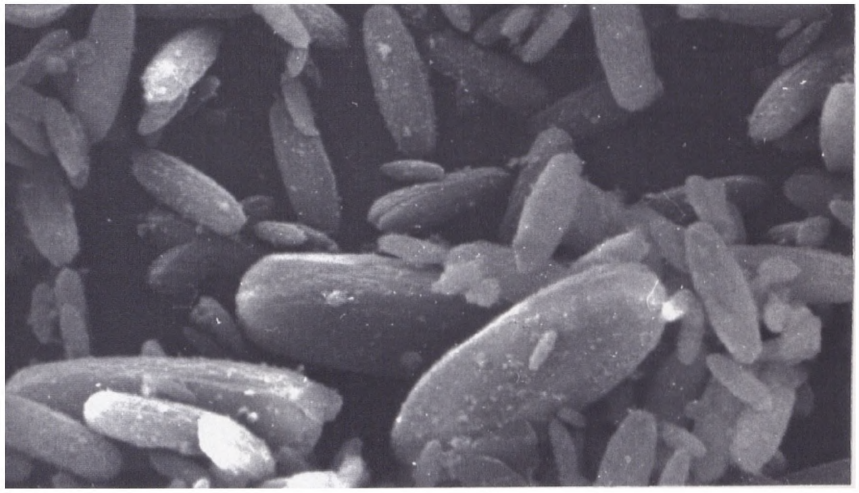


**c.$Na^+$/$K^+$-Silicalite-2**

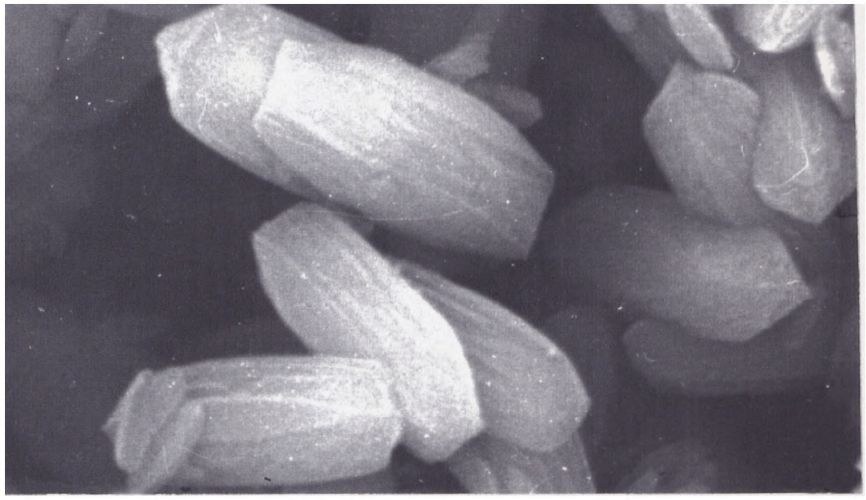


**Figure 4.9. SEM of silicalite-2 synthesised after 140 hours at 130°C with TBP as the organic additive.**

Alternatively, Si-rich heterogeneous domains associated with the gel phase, can also lead to crystals of varying size [16]. A smaller range of crystal sizes was obtained in the mixed ion system. The crystals are again lozenge-like in appearance. The largest crystals are around 2 x 4μm in size but the crystal dimensions varied to as small as approximately 0.3 x 1μm.

Other workers have reported a similar crystal morphology with respect to silicalite synthesis [31]. However, from the mixed ion system, there is a noticeable reduction in the crystal size and twinning of the crystalline phase. The size of the crystals is determined by experimental factors which alter the relative rates of nucleation and crystal growth. Generally, high nucleation rates followed by crystal growth will tend to produce smaller crystals as experienced in the $K^+$ and mixed ion system [8]. However, such processes are not necessarily predictable. For example, silicalite-2 synthesised with DAO, discussed in section 3.3, showed an opposite $M^+$ ion crystal size dependence. Reaction variables such as the nature of the organic additive and silica source, the degree of gel dissolution and mixing procedures have been reported by other workers to affect the crystal growth processes [16]. Consequently, it is difficult to compare morphological results of zeolites synthesised under different reaction conditions.

The chemical analyses of the crystalline materials after 120 hours are summarised in Table 4.6. Irrespective of the inorganic cation source 1.0 TBP molecule was associated with a unit cell of silicalite-2. This value is noticeable lower than for ZSM-11 discussed in section 4.31 where the TBP content per unit cell was 2.5. This indicates that for aluminium-free systems, TBP functions as a structure-directing agent rather than a charge-balancing ion, as suggested by other authors [32]. The pore-filling capacity of TBP in silicalite-2 is around 36%. This shows that it is not necessary for TBP to occupy all the available pore volume for synthesis of silicalite-2 synthesis. The data also includes the chemical analysis of TBP-silicalite-1 synthesised at 175°C. In this case the pore-filling capacity of TBP is approximately 80%. The change in the TBP content with phase and pentasil content was noted in the previous section. These results indicate that the incorporation of TBP favours the formation of MFI over MEL.

| PHASE TYPE | $M^+$ ION | % CRYSTALLINITY | MOLAR C/N RATIO | $M^+$ p.u.c | TBP |
|---|---|---|---|---|---|
| SIL-$2_1$ | Na | 91 | 15 | 1.2 | 1.0 |
| SIL-2 | K | 96 | 16 | 0.3 | 1.0 |
| SIL-2 | K/K+Na=5% | 95 | 14 | <0.03/K 0.3/Na | 1.0 |
| SIL-$1_2$ | Na | 87 | 15 | 1.0 | 2.1 |

1. Silicalite-2
2. Silicalite-1 synthesied at 175°C

**Table 4.6. Chemical analysis results of silicalite-2 synthesised at 130°C after 140 hours with TBP as the organic additive.**

Furthermore chemical analysis revealed differences in the $M^+$ ion content of the silicalite-2 materials synthesised with TBP. Significantly more $Na^+$ than $K^+$ ions were associated with the zeolite, respectively 1.2 and 0.3 per unit cell. These results compare to those obtained when DAO was used as the organic additive as discussed in section 3.33. In the mixed ion system the respective $M^+$ ion contents are markedly reduced. It appears that $K^+$ ions are less involved in the crystal growth process. These results agree with the work of Kungang et al.[31] who found that the stability of silicalite-2 synthesised with TBA was increased with the ionic size of the $M^+$ ion in the following order,

**INFLUENCE OF THE ALKALI METAL CATION**

$$Li^+ < Na^+ < K^+ < Rb^+ < Cs^+$$

In the absence of aluminium and associated electrostatic charge the hydrated alkali metal cations interact with the framework in several ways. These include defect site interactions [33] and via hydrogen-bonding with the oxygen atoms of the $SiO_4$ tetrahedra [32].

### 4.3.3. The Use of Mixtures of Organic Additives

The original gel was prepared as outlined in section 4.2 but with a series a bimolar additions of TBA, TBP, DAO, TPA and BAPZ. The initial starting stoichiometry can be summarised as follows:

$$11.9Na_2O - 59.4SiO_2 - 0.8Al_2O_3 - 15.1R_2O - 1657.6\ H_2O$$

where R is a 1:1 molar mixture of two organic compounds. The organic mixture studied can be summarised as follows,

| Code | Organic Mixture | Code | Organic Mixture |
|---|---|---|---|
| A - | TBA/TBP | E - | TBA/DAO |
| B - | TBA/BAPZ | F - | TBP/DAO |
| C - | TBP/BAPZ | G - | DAO/TPA |
| D - | DAO/BAPZ | H - | *DAO/TPA |

* molar ratio equivalent to (4:1)

All the reactions in this study were heated statically at 175°C for a total reaction period of 75 hours.

X-ray analysis revealed that ZSM-11, ZSM-5 and pentasils were synthesised in this study. A summary of the zeolites synthesised in terms of crystallinity and phase purity are given in Table 4.7. In general, for the equivalent reaction period, the overall crystallinity of all the products was lower than the those obtained using a single organic additive as discussed in section 4.32. In contrast to the previous work, the reactions in this study were performed under static conditions. This may account for the decrease in reaction rates.

| CODE | ORGANIC MIXTURE | % CRYSTALLINITY 49 Hrs | 75 Hrs |
|---|---|---|---|
| A | TBP/TBA | 11 a | 78 b |
| B | TBP/BAPZ | 31 a | 75 c |
| C | TBA/BAPZ | 68 a | 76 a |
| D | DAO/TBA | 66 a | 80 a |
| E | BAPZ/DAO | 54 a | 66 c |
| F | TBP/DAO | 89 b | 98 a |
| G | DAO/TPA | 97 d | 97 d |
| H | DAO/TPA | 96 d | 98 d |

a - Pure ZSM-11
b - 20-30 > % Intergrowth ZSM-5 in ZSM-11
c - 30-40 >
d - Pure ZSM-5

**Table 4.7. XRD analysis of the crystalline phases obtained at 175°C with organic additive mixtures.**

Some general trends in the phases obtained could be identified from the x-ray results. The crystallisation curves for the mixed template systems are illustrated in Figure 4.10. The shortest nucleation and crystallisation periods were observed with synthesis involving TPA as the organic additive. In these reactions ZSM-5 was the only crystalline product, independent of the DAO content in the initial synthesis gel. The efficient structure-directing properties of TPA for the synthesis of ZSM-5 under a variety of reaction conditions are well known [8].

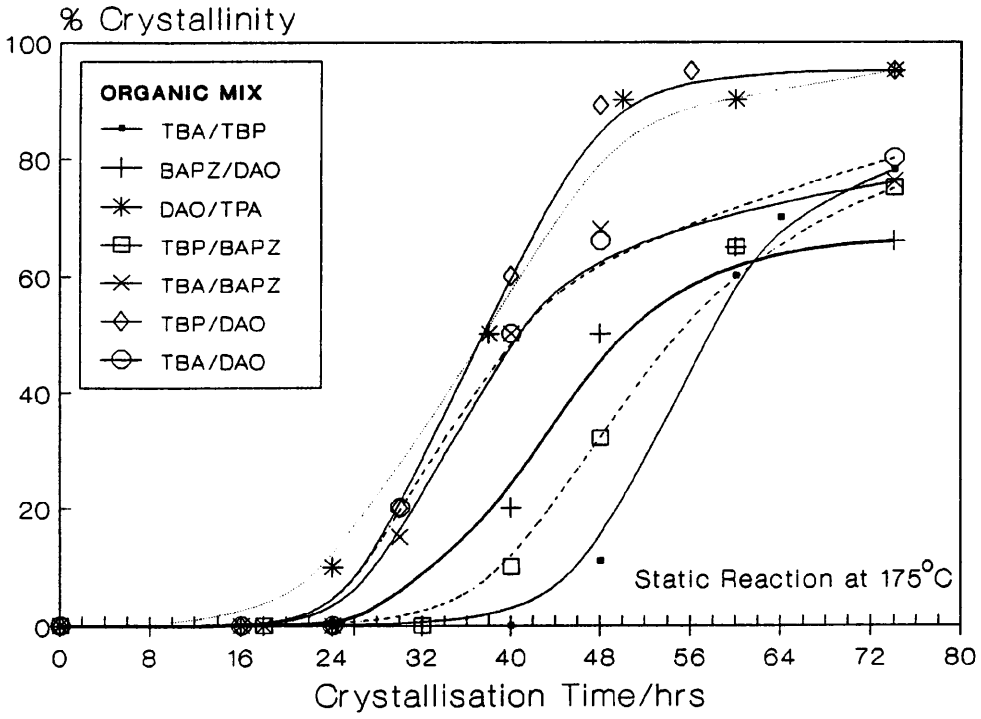


**Figure 4.10. Reaction kinetic plots for synthesis involving mixtures of organic additives.**

Generally, in the early stages of synthesis, the initial semi-crystalline product was ZSM-11 in all the gels excluding TPA. However, both the reaction rates and the phase purity of the fully crystalline material was dependent upon the composition of the organic additive mixture. The most crystalline materials were obtained from gels including the organic additives DAO and TBP. Indeed, the fastest nucleation and crystallisation rate were associated with the TBP/DAO synthesis system. In contrast, the addition of BAPZ to the reaction mixture had a detrimental effect on the reaction rates. The least crystalline materials were obtained from systems involving this organic additive. It appears that BAPZ affects the structure-directing properties of the other

organic additive in the reaction system. Synthesis involving TBA had mostly an intermediary effect on the reaction kinetics. Most interesting however, the longest nucleation period was experienced in the TBP/TBA system. This result was somewhat unexpected but must arise from disruptive processes which prevent the formation of stable nuclei. Overall, the results are in agreement with those reported in section 4.32 concerning the structure-directing capabilities of the organic additives.

The phase purity of the zeolites obtained after 75 hours varied with respect to the organic mixture used during synthesis. Pure ZSM-11 was synthesised from gels where DAO was one of the organic components, apart from the reaction involving BAPZ. In the latter synthesis a 30-40% pentasil material was obtained. Alternatively, when BAPZ was combined with TBA or TBP, MEL or 30-40% pentasil material, respectively, were synthesised. Overall, the zeolites with the highest pentasil content were obtained from systems involving BAPZ. This highlights again the disruptive effects of BAPZ during zeolite synthesis. A crystalline 20-30% pentasil material was also obtained from the TBA/TBP synthesis. The only other noticeable product development concerned the reaction involving TBP and DAO. Initially, a semi-crystalline materials with a pentasil content between 20-30% was synthesised after 49 hours. However, after 75 hours, x-ray analysis showed that the crystalline phase composed of highlycrystalline ZSM-11. A possible explanation for this result may relate to limitations associated with x-ray diffraction [34]. Alternatively, the structures of MEL and MFI are composed of similar structural building units [1]. It is feasible therefore, that a layer or shell of MEL type material may have crystallised around the initially synthesised pentasil material as depicted in Figure 4.11. Similar crystallisation processes such as the growth of zeolite X onto zeolite Y is known [35]. Without further work it is difficult to account for the various phase developments.

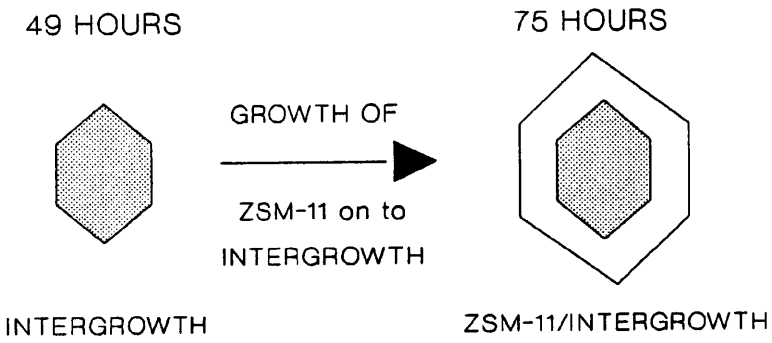


**Figure 4.11. Growth of ZSM-11 onto pentasil material during crystallisation.**

Chemical analysis was performed on the crystalline materials synthesised after 75 hours. Due to the similar chemical composition of the organic additives only a few conclusions could be drawn. The product $SiO_2/Al_2O_3$ ratio was approximately 65, irrespective of the organic additive component used. The $Na^+$ ion content, per unit cell, of the zeolite synthesised with TBP and TBA is 2.0. In contrast, 1.0 $Na^+$ ion per unit cell was associated with all the other crystalline materials.

Assuming the organic additives were intact, the zeolite synthesised with TBP and TBA had a 1:1, N:P molar ratio. This shows that during synthesis both organics were equally incorporated into the zeolite pore system. The total organic content of this material was 2.9 molecules per unit cell. A similar quaternary ion content was reported by Nagy et al.[24], which gave a near maximum pore-filling capacity. Using the N:P molar ratio, the DAO:TBP ratio of the respective crystalline material is 4:1. This reveals a preferential incorporation of the diamine into the intra-crystalline framework. This result highlights the efficiency of DAO as a structure-directing agent.

The micrographs of the crystalline products code numbers A to F are summarised in Figure 4.12. Irrespective of the organic content and phase purity all the crystalline materials were composed of monodispersed, spherical, polycrystalline aggregates. The surface of the crystals is smooth and without defects. This shows that the crystals were formed via a homogeneous nucleation and similar crystal growth processes. Spherical crystals readily form from highly saturated or supersaturated gels. A similar crystal morphology of ZSM-11 was reported by Kaucic et al.[17]. Some crystals show a clear imprint or contact surface of neighbouring crystals. This gives an indication of their crystal growth process. However, such a crystal morphology could have developed via a solution- or hydrogel-mediated process as outlined by Gabelica et al.[16]. Table 4.8. summarises the size distribution of the aggregated crystals as a function of the organic content. The results show no significant trends in the crystal size distribution as a function of the organic additives. The smallest crystals around 7-8μm in size are associated with the TBA/TBP synthesis. This may result from the extended nucleation period experienced by this reaction system as previously shown in Figure 4.10.

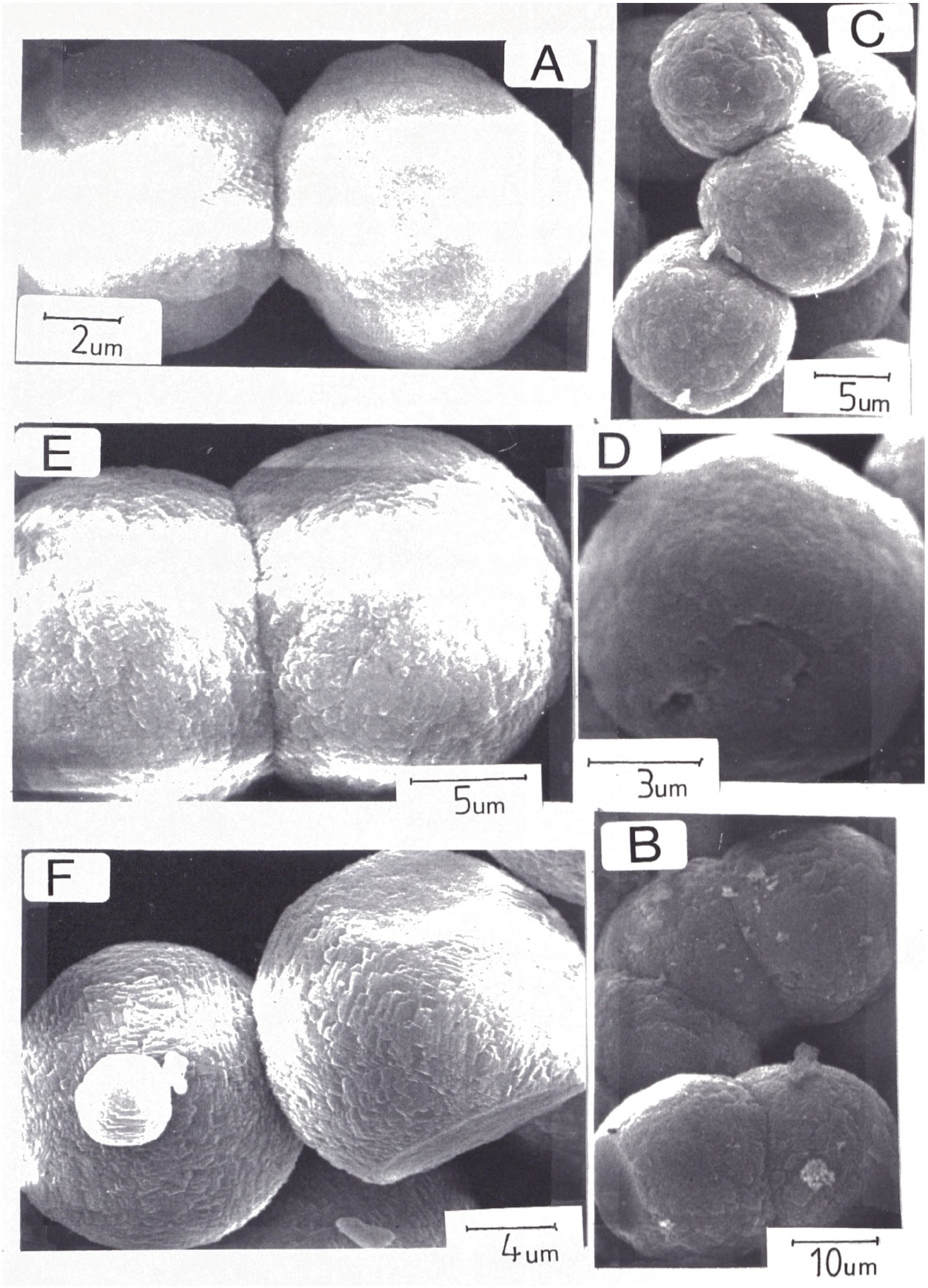


**Figure 4.12. SEMs of zeolites synthesised using mixtures of organic additives**

| CODE | A | B | C | D | E | F |
|---|---|---|---|---|---|---|
| ORGANIC MIX | TBP/TBA | TBP/BAPZ | TBA/BAPZ | DAO/TBA | BAPZ/DAO | TBP/DAO |
| CRYSTAL SIZES/um | 7-8 | 20-21 | 10 | 13-14 | 15-10 | 16-17 |

**Table 4.8. Crystal size evaluation of the mixed organic synthesis after 75 hours at 175°C with an initial $SiO_2/Al_2O_3$ of 70.**

In general, the largest crystals have the highest pentasil content and involve the organic additive BAPZ. Examples are the synthesis products from reactions B and E. Disruptive processes, results in the formation of relatively few stable nuclei. Consequently, larger crystals are synthesised as there is an ample supply of reactive species for crystal growth. Alternatively, as ZSM-5 type material is less difficult form and crystallises at a faster rate than ZSM-11 type materials.

## 4.4. Conclusions

ZSM-11 and pentasil materials were synthesised under the same reaction conditions with a range of organic additives of varying size and chemical nature. Similarities in the crystal size and morphology of these materials show that both nucleation and crystal growth processes are independent of the organic additive. This brings into question the general structure-directing role of the organic additive during zeolite synthesis.

In terms of product crystallinity, DAO and TBP were the most effective organic additives. This probably relates to the structure-directing qualities of these particular organic additives. The least crystalline materials were obtained from the BAPZ synthesis. BAPZ is a comparatively large and bulky organic additive with limited pore-filling ability. With regards to purity of ZSM-11, DAO was by far the most efficient while the most intergrown materials were associated with gels containing TBP. The relative siting of the organic influences phase purity. DAO is incorporated

along the pores of the ZSM-11, while quaternary ions occupy the channel intersections.

The incorporation of TBP into the pore system was seen as a disruptive process. In this respect TBA is less disturbing, producing a less intergrown ZSM-11 product. This is related to the more efficient pore-filling and/or charge-balancing nature of TBA. MAS NMR studies showed that TBA is incorporated intact into the pore system and sited at the channel intersections.

Irrespective of the organic content, a decrease in reaction temperature at the expense of reaction rates, promoted the formation of ZSM-11 over pentasil material. As discussed in Chapter 3, this may be related to the reduced thermal motion of the organic additive, which favours MEL formation, or the more demanding reaction conditions.

In agreement with section 3.33, the replacement of $Na^+$ with $K^+$ ions increased the nucleation rate and changed the crystal morphology of silicalite-2 using TBP as the organic additive. The $Na^+$ ions may form complexes with silicate ions which would normally be used in the formation of nuclei. Both the $M^+$ ion systems showed an optimum $OH^-/SiO_2$ ratio of 0.2, highlighting the influence of gel alkalinity on the synthesis of high-silica zeolites. This represents a level of supersaturation where stable nuclei are most rapidly formed together with a sufficient concentration of (alumino)silicate species for crystallisation.

In the mixed organic syntheses, the structure-directing properties of TPA were reiterated as, even with substantial increases in the DAO content of the gel, ZSM-5 was synthesised. ZSM-11 was the only crystalline product synthesised from other mixed organic gels containing DAO. In these reactions DAO was preferentially incorporated into the pore system of ZSM-11 . This highlight the efficiency of DAO as structure-directing agent for MEL synthesis. The reaction rates of zeolite synthesis with gels containing mixtures of TBP, TBA and BAPZ were more inhibited. This suggests that the organic additives compete for the (alumino)silicate species required for the formation of stable nuclei, which prolonges the nucleation period.

## REFERENCES.


1. G.T.Kokotailo & W.M.Meier, *Chem.Soc.Special Publ.*, **33** 133 (1980)

2. J.C.Védrine, A.Ardoux, G.Coudurier, P.Engelhardt, J.P. Gallez & G.Szabo in Proc.6th Int.Zeolite Conf., (Eds. Olson & Bisio, Butterworths) Reno, USA, 497 (1983)

3. G.T.Kokotailo, *US.Pat.* 4 229 424 (1980)

4. P.Chu, *US.Pat.* 3 709 979 (1973)

5. G.A.Jabolonski, L.B.Sand & J.A.Gard, *Zeolites*, **6** 396 (1986)

6. L.Y.Lou & L.B.Sand in Proc.6th Int.Zeolite Conf., (Eds. Olson & Bisio, Butterworths) Reno, USA, 887 (1983)

7. L.D.Rollmann & E.W.Valyocsik, *US.Pat.Appl.*, 4 139 600 (1979)

8. P.A.Jacobs & J.A.Martens in *Synthesis of High-Silica Aluminosilicate Zeolites*, Stud.Sur.Sci.Catal.No.**33**, (Publ.Elsevier) chpts.2-4 (1987)

9. E.Moretti, S.Contessa & M.Padovan, *La Chimica E L'Industria*, **67**, N1-2, 21 (1985)

10. W.J.Smith & E.M.Cooke, unpublished results (1989)

11. R.von Ballmoos & J.B.Higgins, *Collection of Simulated X-Ray Powder Patterns for Zeolites*, IZA Special Publication, (Butterworths, 1990)

12. P.A.Jacobs & J.A.Martens in *Synthesis of High-Silica Aluminosilicate Zeolites*, Stud.Sur.Sci.Catal.No.**33**, (Publ.Elsevier) chpt.4 (1987)

13. L.D.Rollmann, E.W.Valyocsik & J.A.Cooper, *Eur.Pat.Appl.*, 0 015 132 (1980)

14. S.G.Fegan & B.M.Lowe, *J.Chem.Soc.Farad.Trans.1.*, **82**, 801 (1986)

15. A.J.Blake, K.R.Franklin & B.M.Lowe, *J.Chem.Soc.Dalton Trans.*, 2513 (1988)

16. Z.Gabelica, E.G.Derouane & N.Blom in *Catalytic Materials, Relationship Between Structure and Reactivity*, ASC Symp.Ser.**248** (Eds.Whyte, Dalla Betta, Derouane & Baker) 219 (1984)

17. V.Kaucic, S.Gaspersic & S.Hocevar in *Zeolites:Facts, Figures, Future*, Proc.8th Int.Zeolite Conf.,(Eds. Jacobs & van Santen, Elsevier) Amsterdam, The Netherlands, 311 (1989)

18. E.W.Valyosik and L.D.Rollmann, *Zeolites*, **5** 123 (1985)

19. K.J.Chao, T.S.Tasi, M.S.Chen & I.Wang, *J.Chem.Soc.Farad.Trans.1*, **3**, 547 (1981)

20. M.L.Occelli, S.S.Pollack & J.V.Sanders in *Innovations in Zeolite Materials Science*, Stud.Surf.Sci.Catal.No.**37**, (Eds.Grobet, Mortier, Vansant & Schulz-Ekloff, Elsevier) 45 (1987)

21. J.C.Jansen in *Introduction to Zeolite Science and Practice*, Stud.Sur.Sci.Catal. No.**58**, (Eds.van Bekkum, Flanigen & Jansen, Elsevier) 77 (1991)

22. K.R.Franklin & B.M.Lowe, *Zeolites*, **8**, 501 (1988)

23. J.March in *Advanced Organic Chemistry: Reactions, Mechanisms and Structure*, 2nd Edn., 927 (Publ.McGraw-Hill, 1977)

24. J.B.Nagy, Z.Gabelica & E.G.Derouane, *Zeolites*, **3**, 43 (1983)

25. E.G.Derouane & J.B.Nagy, *Chem.Phys.Lett.*, **137**, No.4, 341 (1987)

26. K.Foger, J.V.Sanders & D.Seddon, *Zeolites*, **4**, 337 (1984)

27. D.M.Bibby, N.B.Milestone & L.P.Aldridge, *Nature*, **280**, 664 (1979)

28. B.Marler, *Zeolites*, **7**, 393 (1987)

29. A.Erdem & L.B.Sand, *J.Catal.*, **60**, 241 (1979)

30. R.D.Edelman, D.V.Kudalar, T.Ong, J.Warzywoda & R.W.Thompson, *Zeolites*, **9**, 496 (1989)

31. T.Kungang & X.Ruren in *Zeolites, Synthesis, Structure, Technology and Application*, Stud.Surf.Sci.Cata.No.**24**, (Eds.Drzaj, Hocevar & Pejovnik, Elsevier) 73 (1984)

32. Z.Gabelica, M.Cavez-Bierman, P.Bodart, A.Gourgue & J.B. Nagy in *Synthesis, Structure, Technology and Application*, Stud.Surf.Sci.Cata.No.**24**, (Eds.Drzaj, Hocevar & Pejovnik, Elsevier) 55 (1985)

33. S.G.Fegan & B.M.Lowe, *J.Chem.Soc.Farad.Trans.1.*, **82**, 785 (1985)

34. M.M.Treacey, *BZA Conf.*, Durham, plenary lecture (1991)

35. E.de Vos Burchant, J.C.Jansen & H.van Bekkum, *Zeolites*, **9**, 432 (1989)

# CHAPTER 5.

## The Characterisation of Pentasil Zeolites and Intergrowths

### 5.1. Introduction

A detailed theoretical framework definition of pentasil intergrowths was first discussed by Kokotailo et al.[1] and was outlined in section 1.2.2. Over recent years, with the advent of more sophisticated analytical methods, much effort has been devoted to the distinction of the subtle physical and chemical differences of these materials [2]. Details of these techniques are summarised in the following.

X-ray diffraction is a bulk technique which is routinely used to discriminate between discrete zeolite phases. However, it is unable to differentiate between physical mixtures and intergrowths of pentasil materials. The relative intensities of several XRD peaks have been used as a semi-quantitative measure of intergrowth content [2].

Alternatively, by measuring the rates and extents of adsorption of a series of molecules of different kinetic diameters the pore dimensions and diffusional characteristics of several zeolites have been distinguished [3]. An intermediate behaviour compared to that of the structural end members is predicted by intergrowth materials. The nature of the intra-crystalline pore structure and shape-selective properties of several zeolites have been directly correlated to the product distribution from several catalytic studies [4]. Recently, the *refined constraint index (CI*)* was used as a criterion for determining the structural nature of pentasil materials [5]. The reaction involves hydroisomerisation reaction of n-decane where CI* is defined as:

$$CI^* = \frac{\text{amount 2-methylnonane formed}}{\text{amount 5-methylnonane formed}}$$

Local intergrowths over a crystal region of approximately $0.1\mu m^2$ can be directly viewed by the combined use of HREM imaging and electron diffraction [6]. The existence of regular, random and isolated intergrowths can be discerned by the eye. This is the only analytical method which can positively identify intergrowths and

differentiate them from physical mixtures. However, as only small sample area can be studied, it is not possible to quantify the degree of structural defects of a given sample.

Recently, the dealuminated $^{29}Si$ MASNMR spectra of highly siliceous ZSM-5 and ZSM-11 were reported by Fyfe et al.[7]. The differences in the number of chemical shifts and relative intensities of the spectral lines reflect the number of non-equivalent silicon atoms. It is possible that a similar study of intergrowth materials may yield valuable structural information. However, the interpretation of such complicated spectra would be immensely difficult [8].

To date, no characterisation technique has been developed which can both positively identify and quantify intergrowth materials. To describe their physical and chemical behaviour as intermediate between ZSM-5 and ZSM-11 is perhaps over-simplified. The aim of this work was to appraise the value of several characterisation methods in deciphering the structural nature of a series of pentasil materials. This was achieved using x-ray analysis, sorption measurements, electron microscopy, *in-situ* FTIR and catalytic studies. Differences in the acidic nature and catalytic shape-selective properties of the zeolites was also assessed using the latter two methods.

## 5.2. Characterisation Procedures

A concise description of the experimental details is given in Chapter 2. This section outlines a more detailed view of the methods used.

### 5.2.1. Sample Origin

The synthesis procedure of zeolites used in this study is described in section 4.2. Table 5.1 gives the compositional and structural details of materials used in the study. The type of phase and its crystallinity was previously determined using routine x-ray methods as described in section 2.5. For the ease of discussion samples 1 and 2, phase types ZSM-5 and ZSM-11, will be referred to as ECMFI and ECMEL, respectively. Samples 3 and 4, suspected intergrowths, will be named as ECTBP and

ECTBA, respectively.

| Code Name | $SiO_2/Al_2O_3$ Ratio | Organic Used[b] | Phase Type | % Crys[d] | % $I_d$ |
|---|---|---|---|---|---|
| ECMFI | 48.1 | DAH | ZSM-5 | 89 | None |
| ECMEL | 46.1 | DAO | ZSM-11 | 95 | None |
| ECTBP | 51.2 | TBP | I [c] | 89 | 80-70 |
| ECTBA | 53.0 | TBA | I | 90 | 30-20 |

a - sample studied in FTIR experiments only
b - Organic additive used in synthesis
c - Intergrown
d - Data otained from routine XRD

**Table 5.1. Details of the calcined, hydrogen form pentasil phases used in this study.**

### 5.2.2. X-Ray Diffraction

There are many physical aspects of zeolites which affect the quality of the diffraction data obtained. Positions of the diffraction maxima, their intensity and shape are sensitive to sample factors. These factors include crystallite and particle size, the position of the sample in the diffractometer and crystallite orientation and absorption. In order to achieve a reproducible and quantitative determination of the intergrowth content several methods of sample preparation and data collection were attempted. The most successful method was based on analysis recommendations outlined in a publication by the International Centre for Diffraction Data [9] and using a CYGNUS DSM 2000 diffractometer.

Samples were carefully prepared in the same fashion assuring that the same amount of zeolite was used for each run. The materials were mounted and pressed into an aluminium powder holder so that the incoming x-rays were targeted on a smooth and flat powder surface. Quantification of the relative shifts in d-spacing and intensities was achieved by including an internal standard namely, silicon powder. This was mixed with the zeolite during sample preparation. The acquisition of the x-ray data and resolution improvements were achieved by increasing the sampling interval and by using the most appropriate slit width. Following background correction a peak-profiling method was used to assess accurately the d-spacing and peak areas of interest.

Together with the samples in question, a series of physical mixtures composed of the standards, ZSM-11 and ZSM-5 were analysed. The intergrowth content was estimated using the equation [2]:

$$\text{ZSM-5} = (100/0.5) \times (I_a / I_b)$$

where $I_a$ and $I_b$ refer to the peak area at the d-spacing, 3.64 and 3.84, respectively. The former peak was absent in ZSM-11, but for ZSM-5 the ratio of these peak areas was 0.5. Therefore, based on the standard material, this ratio corresponds arbitrarily to 100% ZSM-5.

### 5.2.3. Electron Microscopy

Transmission electron microscopy techniques require the sparing deposition of the zeolite onto a carbon-coated copper grid. The experimental details are given section 2.7. The analysis involves the reconstruction of diffracted beams to form an image [10]. The criteria required are that the sample area must be very thin and relatively flat and that the instrument operates at an optimum condition of defocus (to optimise the spherical abberation), illumination and the objective aperture. In this respect zeolites pose difficulties since crystals are rarely perfect. As a result a significant amount of the microscopist's time is required to find a suitable area or crystal fragment.

Lattice imaging represents a very powerful tool for the investigation of structural features on a nanometer scale. However, a serious difficulty in the analysis of zeolites stems from to their susceptibility to electron beam damage during setting up the experiment, i.e. optimising defocus conditions, and during the actual data acquisition. Consequently, this means that the area already viewed is useless for any further detailed information. A technique was developed, where the electron dose during data acquisition is deliberately kept to a minimum to reduce the beam damage. This led to an under-exposure of the film and the plates had to be developed using a novel *push-processing* technique [11].

To the untrained eye interpreting HREM images is a difficult process and often misleading. The ultimate photograph of the image does not necessarily correlate to the

actual material. As a result, a series of theoretical predictions of image contrast were calculated for a range of crystal thickness and defocus conditions [12,13]. Similarly, for the interpretation of the experimental electron diffraction patterns, a series of kinematical representations [11] were also calculated. This method generates both the arrangement and relative intensity of the electron diffraction spots along a chosen structural axis.

### 5.2.4. Sorption Measurements

The gravimetric sorption capacity of the zeolites was investigated using m-xylene as the probe molecule. The experimental details are outlined in section 2.9. The rate of uptake was carefully monitored over time. The total sorption capacity was taken as the weight gain after 24 hours. All measurements were performed at a sample temperature of 150°C using relative sorbate pressure of approximately 2.48 Torr at 0°C.

### 5.2.5. *In-Situ* Fourier Transform Infrared Studies

The acidic nature of zeolites was assessed using *in-situ* FTIR methods. The relative amounts of Brφnsted and Lewis acids were determined by the adsorption of pyridine at 150°C. The acidic nature of the materials was investigated by low temperature adsorption of hydrogen ($H_2$). Experimental details are given in section 2.6.

Pyridine bound to a Brφnsted acid site is associated with a band at 1545cm$^{-1}$ and that bound to a Lewis site with a band at 1450 cm$^{-1}$ [13]. The strength of a particular site can be estimated by systematically heating the sample and noting the relative changes of the frequencies and intensities of the two acid bands.

$H_2$ is a non-polar diatomic molecule and therefore infrared inactive. However, when adsorbed by the zeolite a dipole is induced by the electrostatic field experienced within the channels and cavities of the zeolite. The induced $H_2$ spectrum gives an indication of the number and strength of acid sites [14]. In this experiment, the perturbation of the hydroxyl (OH) and $H_2$ band frequencies were studied over a range of

$H_2$ pressures. The materials were assessed only in terms of Brønsted acidity as doubts have been cast over the use of $H_2$ as a probe for Lewis acidity [15].

### 5.2.6. Catalysis

The catalytic and shape-selective properties of the materials were investigated using the alkylation reaction of p-xylene with methanol. This reaction was used to differentiate the shape-selective properties of ZSM-5 and ECMEL [16]. A mixed (2:1) molar feed consisting methanol and p-xylene (total WHSV=3hr$^{-1}$) in a flow of dry nitrogen was admitted on the catalyst in a fixed bed reactor operating at a bed temperature of 315°C. The gaseous and liquid products at various stages of *time-on-stream* were analysed by gas chromatography. The experimental details of this study are outlined in section 2.10.

## 5.3. Results and Discussion

### 5.3.1. Evaluation of Intergrowth Content using X-Ray Diffraction

With improvements to the data acquisition and the use of peak profiling methods [9], fully resolved diffractograms of all the materials studied were obtained. Figures 5.1 shows the peak profiled x-ray data obtained for each sample and Figure 5.2 compares the XRDs of the standard materials and physical mixtures between 22.5 to 24.5, 2Θ. Samples ECMFI and ECMEL compare well to the standard materials ZSM-5 and ZSM-11, respectively, over this diffractional region. The data shows that many of the d-spacings associated with ECMFI are absent in ECMEL. This is due to the higher symmetry of the latter zeolite structure.

The x-ray diffraction patterns for ECTBA and ECTBP were very close to the physical mixtures 25:75 and 75:25 ZSM-5:ZSM-11, respectively. No unique d-spacings were associated with the intergrowths to differentiate them from the physical mixtures. However, several intensities of these samples were broader as compared to the structural end members. This results from the cumulative contribution of x-ray data from both ZSM-5 and ZSM-11 structural origins. Similar effects with x-ray analysis have

been reported concerning zeolite beta due to polymorphism [17,18].

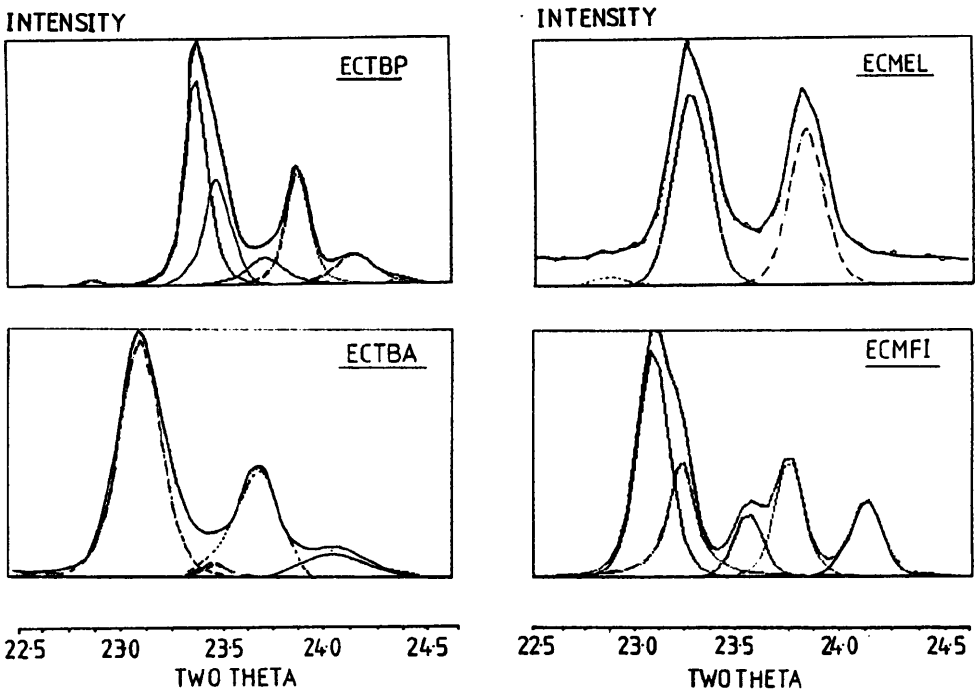


**Figure 5.1. XRD (peak profiled) data of ECMEL, ECMFI, ECTBA and ECTBP.**

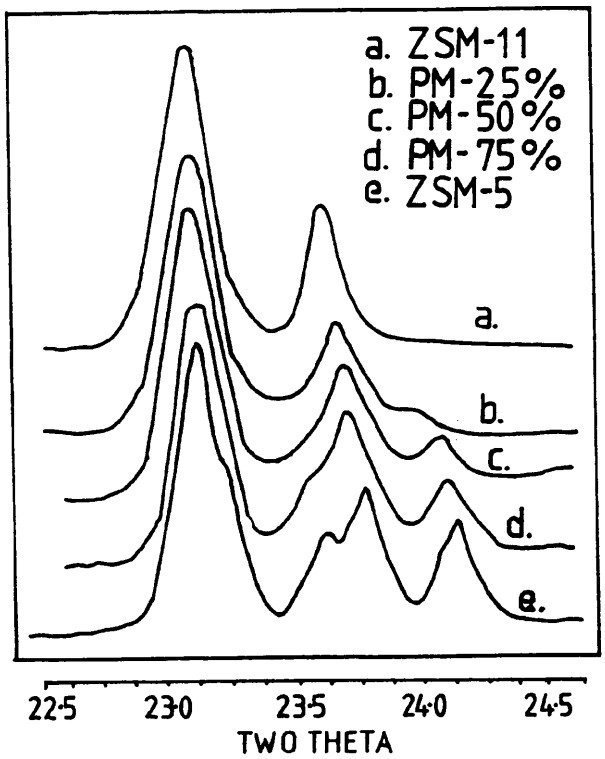


**Figure 5.2. XRD data of the standard materials and physical mixtures (PXn. % = physical mixture with percentage content of ZSM-5 to ZSM-11).**

A corresponding intensity transition at 2Θ between 42-45 from a doublet to a singlet with increasing ZSM-11 content of the sample was also noticed. This is illustrated in Figure 5.3. This trend was used by Jablonski et al.[19] as a quantitative measure of intergrowth content. In this study it was proven to be a rather inaccurate method for intergrowth quantification. The intensities were relatively small and, since they were collected at the higher angles of 2Θ, problems such as line broadening and absorption factors accompanied the data collection [9].

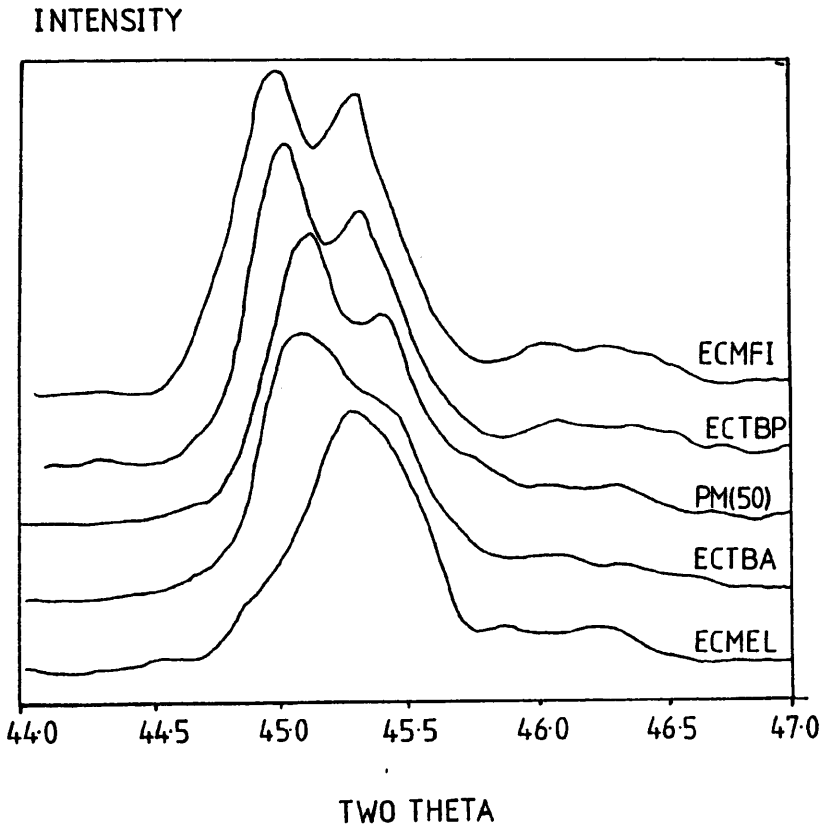


**Figure 5.3. Intensity transition associated with pentasil materials at higher angles of 2Θ (PX(50)=physical mixture 50:50, ZSM-11:ZSM-5).**

The percentage ZSM-5 content of the physical mixtures was evaluated with some accuracy to approximately, (+/- 10%) as depicted in Figure 5.4. The percentage error was estimated by calculating the standard deviation using the results obtained of the pure and physical mixtures.

From this correlation the percentage intergrowth content of ECTBA and ECTBP was estimated, respectively equal to, 30 and 70% (± 10%). Overall, the results agree with

similar studies reported in the literature [2]. In this respect XRD can be seen as a semi-qualitative method for the determination of phase purity [2]. Recently, Treacey [20] showed that the pentasil end members could not be distinguished from very high or low intergrown (I) materials i.e. 10% < I > 90% using similar x-ray methods. Consequently, ECMEL and ECMFI may not be structurally pure phases. However, in this study the limiting content of any one phase in the physical mixtures was 25%. Intensity differences with respect to these phases were still observable. Despite this, the accuracy of XRD in determining phase purity, especially at low intergrowth content, is questionable.

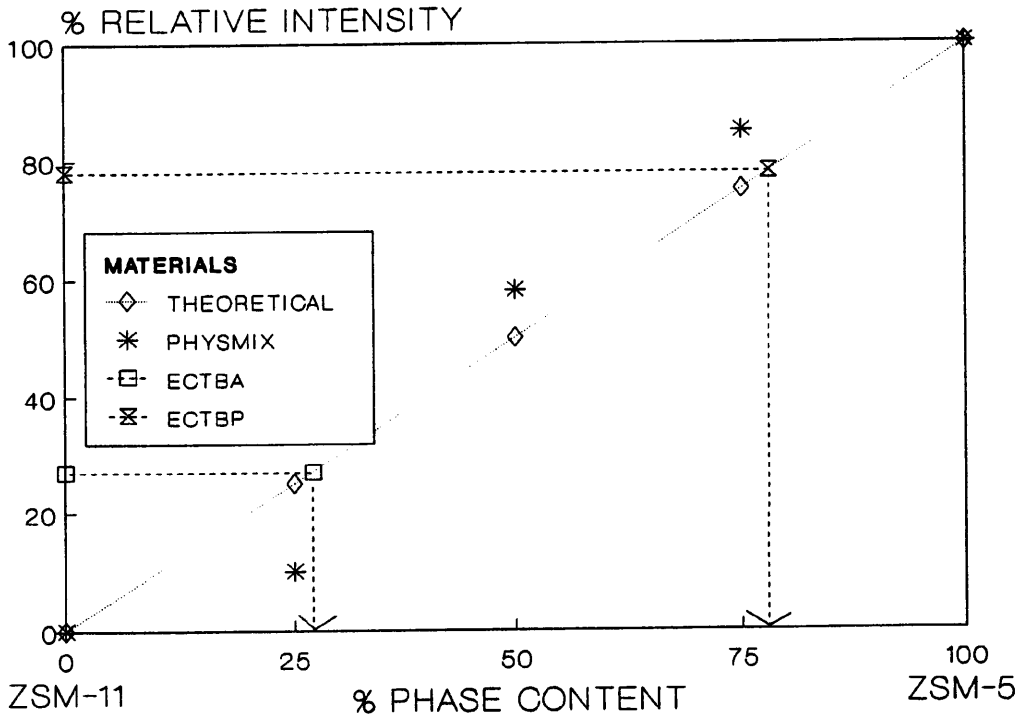


**Figure 5.4. Intergrowth estimation using x-ray analysis.**

### 5.3.2. A Study of the Structural Content of Pentasils using Electron Microscopy

The zeolites studied were sufficiently beam stable to allow the study of their structural content. As there is a practical limit to the amount of material that can be studied in the microscope, the results discussed below cannot be described as *truly representative* of a particular phase. The ZSM-5 materials have been extensively investigated and reported on in the literature [21]. As a result, it was not necessary to collect further data for this material. The crystal size morphological details, revealed by

TEM, of ECTBP, ECMEL and ECTBA are shown in Figures 5.5a, 5.6a and 5.7a respectively. ECTBP is composed of irregular-shaped and ovate aggregates between 2.5-3.00μm in diameter. The aggregates consist of a series of small lozenge-like crystallites approximately 450-500nm x 180-220nm in size.

In the case of the ovate aggregates the crystallites appear virtually linearly aligned to one another. Similarly, ovate aggregates 3.0 x 2.5μm in diameter are present in ECMEL and ECTBA. In addition, a large amount of small isolated single lozenge-shaped crystals approximately 280nm x 500nm in size are present in both samples.

The corresponding electron diffraction patterns and HREM images of the various types of crystal morphology in ECTBP, ECMEL and ECTBA were collected. The data are summarised in Figures 5.5b, 5.6b and 5.7b, respectively. Two distinct diffraction patterns for ECTBP were recorded, depending on the crystal morphology. A simple crystallographic representation of these arrays is given in Figure 5.8. It was found that triangular or rectangular electron diffraction pattern were associated with the ovate or irregular crystal aggregates, respectively.

The triangular lattice of diffraction spots is consistent with that expected from a projection along [010] of ZSM-11. This corresponds to the space group I4m2 [21] with the appropriate systematic absences (h+l= odd). It should be noted that ZSM-5 also yields a triangular lattice of spots along the [100]. In contrast, an essentially rectangular pattern is associated with the structural projection along [010] in ZSM-5. This complies with the space group Pnma, where only true absences occur when (h=0, l= odd) or (h= odd, l= 0). Other diffraction patterns along the [001] structural projection were also recorded, as illustrated in Figure 5.7d. However, the kinematical [001] axis projections for ZSM-5 and ZSM-11 are equivalent. Consequently, the origin of this information cannot be qualified based purely on diffraction data. ECTBP was studied on several occasions at length and at no time was evidence of intergrowth-type material located. Tentatively, this suggests that the specimen is a physical mixture of ZSM-5 and ZSM-11. This technique gives unequivocal qualitative evidence, therefore it is hazardous to give a quantitative estimate of the separate phases or of the intergrowth content.

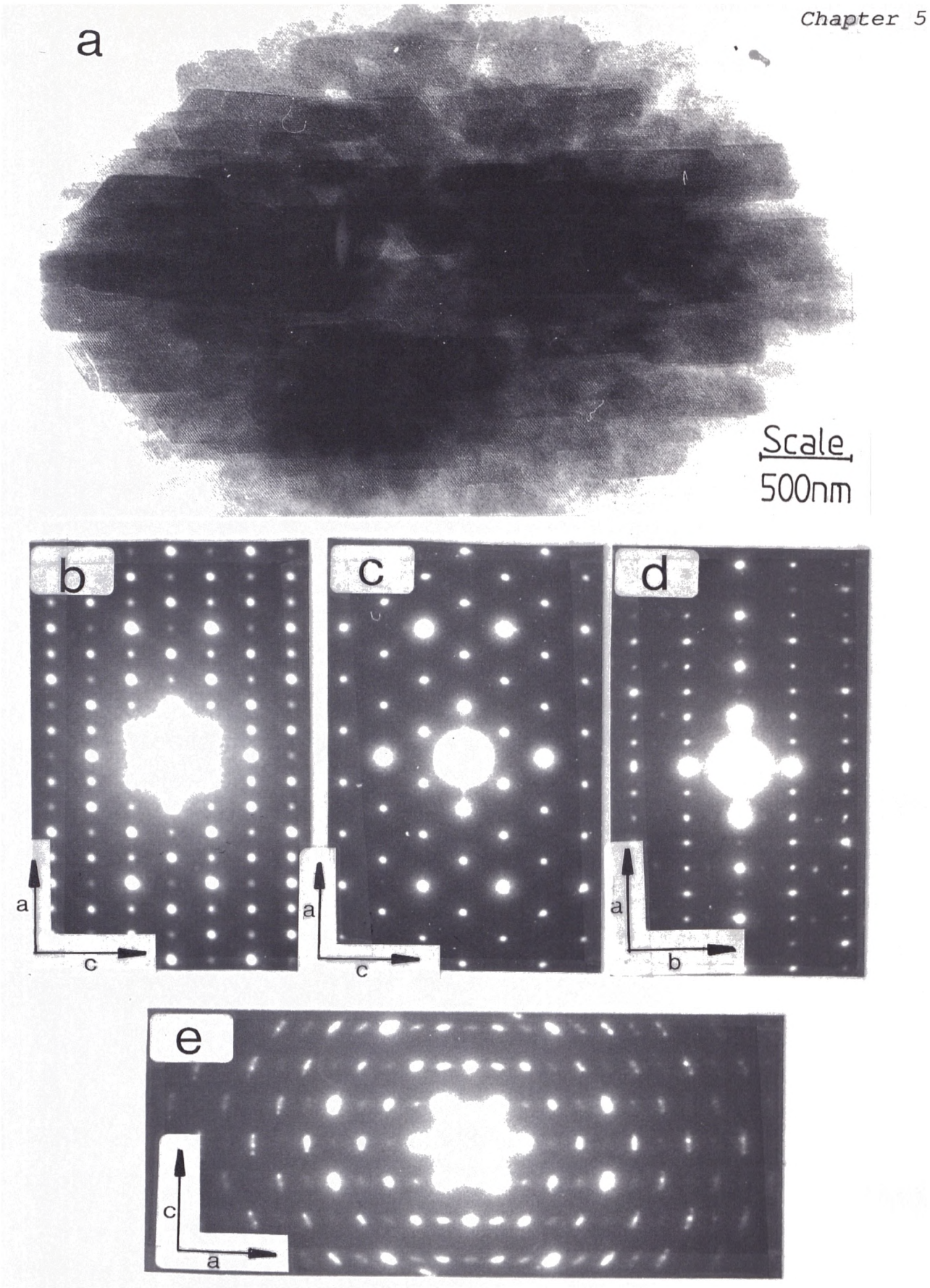


**Figure 5.5. a. TEM & b–e. ED series obtained for sample ECTBP.**

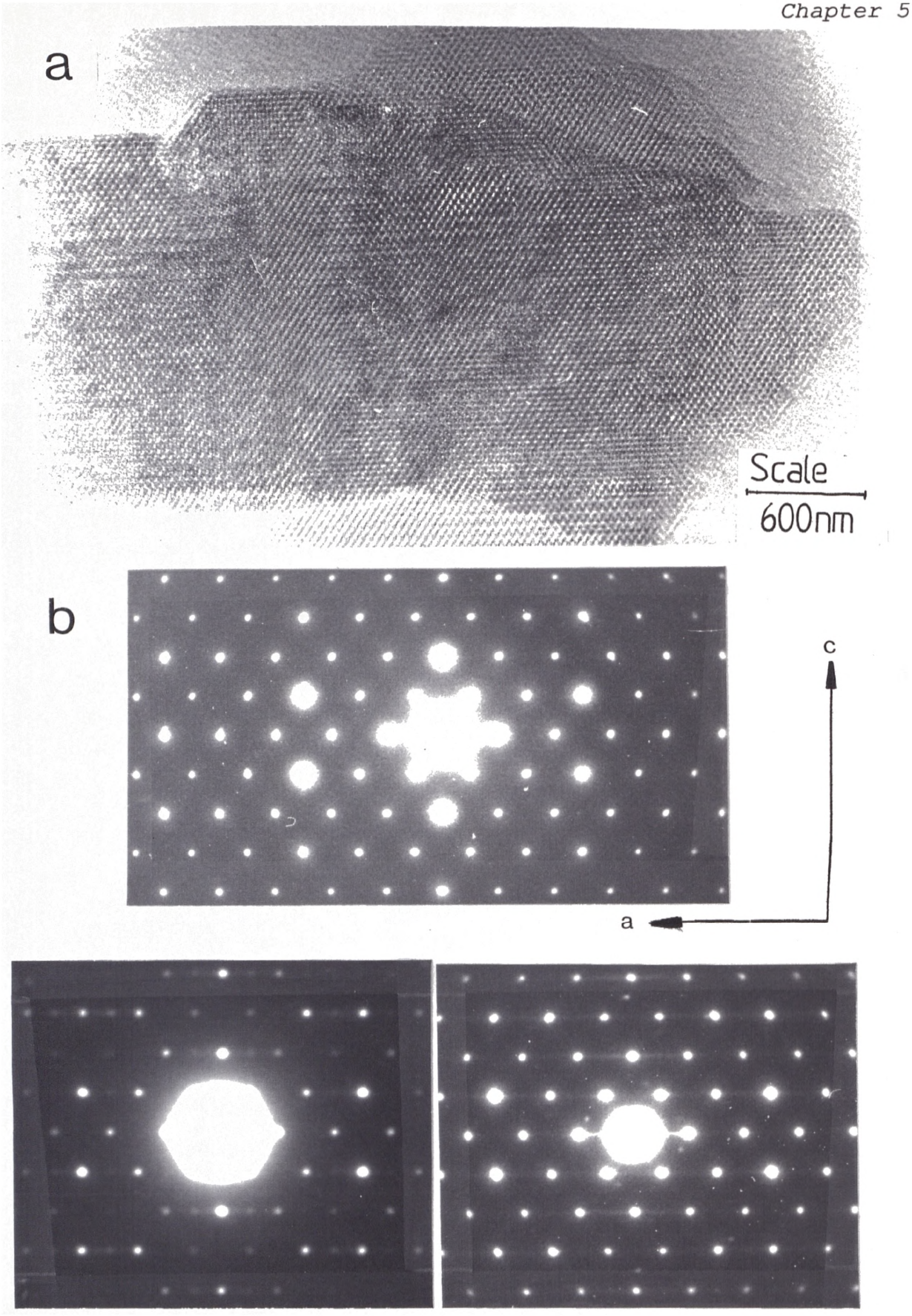


**Figure 5.6. a. TEM and b. ED series obtained for sample ECMEL.**

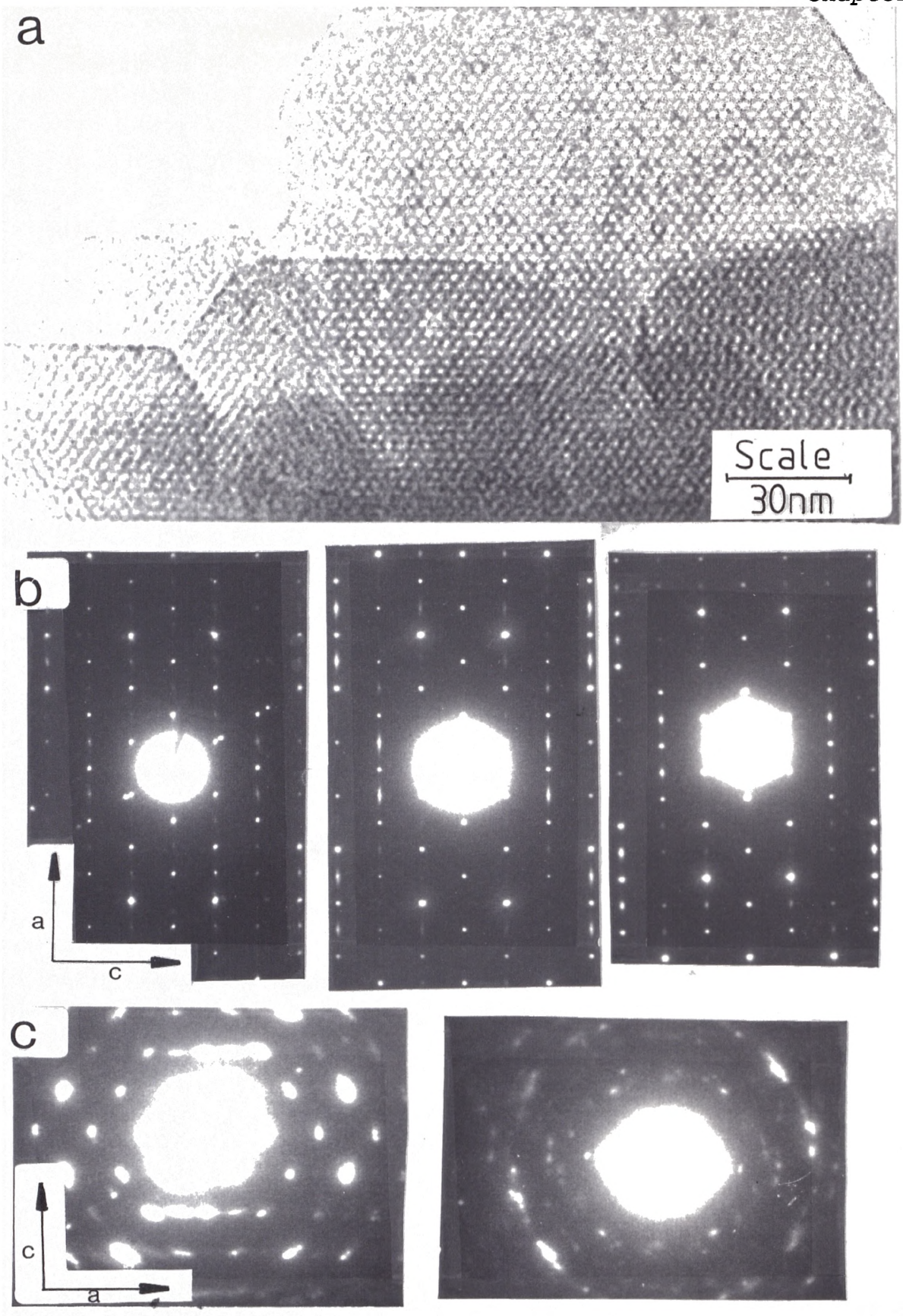


**Figure 5.7. a. TEM , b & c. ED series obtained for ECTBA.**

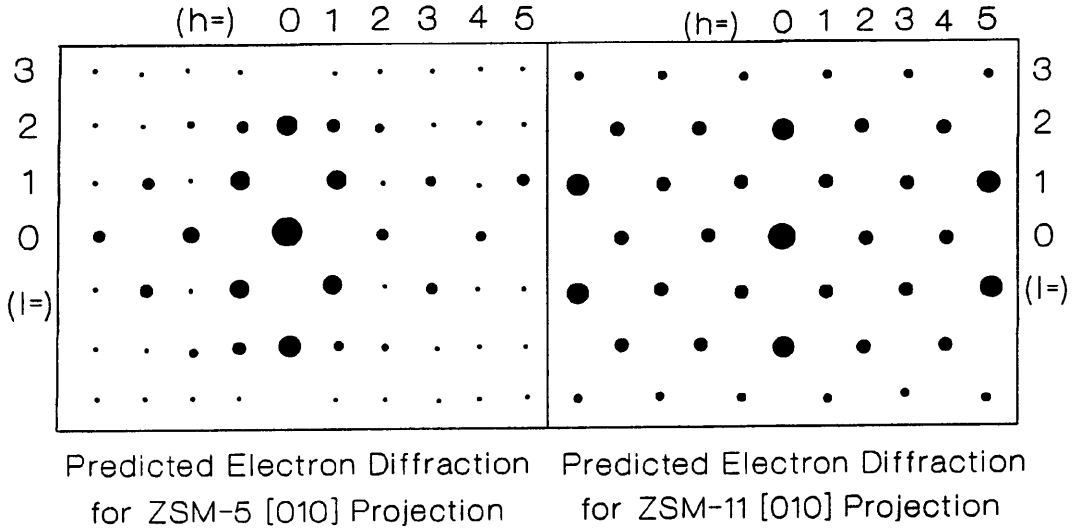


**Figure 5.8. A simplified version of the [010] zone axis projections for ZSM-5 and ZSM-11.**

A number of slightly rotated [010] zone axis projections were recorded from areas of the ovate aggregates of ECTBP. This data is given in Figure 5.5e. The measured rotational angle varies between 7-10°. In order to correlate HREM images and corresponding diffraction patterns, it is necessary to know precisely from where the diffraction pattern originates and how it physically relates to the orientation of the specimen. Recalling Figure 5.5a the ovate aggregates of ECTBP were constructed from linearly aligned, small, individual crystallites. The slight disorientation of adjacent crystals gives rise to the skewed lattice patterns.

With respect to ECMEL and ECTBA the diffraction information was only taken from a number of the small and regular single crystals as their physical nature was the most conducive to HREM imaging. These materials were composed of varying degrees of intergrowth, made apparent from the streaking nature of the electron diffraction patterns along the [010] [21].

The series of electron diffraction patterns for ECMEL and ECTBA are summarised in Figures 5.6b and 5.7b, respectively. The data shows the appearance and development of streaked diffraction spots along the a axis. Streaking of this kind, combined with an appearance of intensity maxima in positions h=0, l=1 and h=1, l=0, is indicative of

intergrowth occurrence [21]. This results from the inclusion of inversion (i) planes at irregular intervals in the structure of ZSM-11. Qualitatively, as the streaks develop into single-spot intensities, the percentage of (i) planes or ZSM-5 content of the zeolite increases.

In comparing the data of ECTBA and ECMEL there is a marked variation of intergrowth content between the materials. The level of intergrowth in the former material is much greater than the latter. The range of diffraction patterns obtained for ECTBA is shown in Figure 5.7b. They reveal a marked development from slight streaking to a broad streaking and eventually to *smudged* spot intensities. This trend is far less drastic in ECMEL.

Throughout this study there was no evidence of any *super-lattice* [21]. Such a material would display the regular or ordered occurrence of defect planes. It can be concluded therefore, that the intergrowth occurrence in ECTBA and ECMEL is random in nature. The diffraction studies concerning ECMEL support the view that XRD is not an accurate method for the determination of structural purity [20].

The only other noticeable features concerning ECTBA and ECMEL were associated with their multicrystalline nature. In a similar fashion to ECTBP, a rotation effect was visible along the [010] of ECMEL and ECTBA. In ECTBA this effect was most acute to the extent that spot intensities merged to form a series of ring patterns as illustrated in Figure 5.7c. Such a pattern arises from the random orientation of crystalline grains, all of which contribute to the diffraction data. The breadth and spottiness of the ring pattern depends on the size and number of crystals contributing to the pattern [10]. Such information is incoherent and difficult to decipher.

Recently, a similar rotational effect for Zeolite L was discussed by Terasaki et al.[22]. In the present study, similar methods [8] were used to generate an idealised view of the effects of relative orientation of two adjacent pentasil sheets on the channel system. Systematically, one pentasil sheet was rotated by 2.5° increments with respect to the other. Figure 5.9 shows a series of through-angle views generated using this procedure.

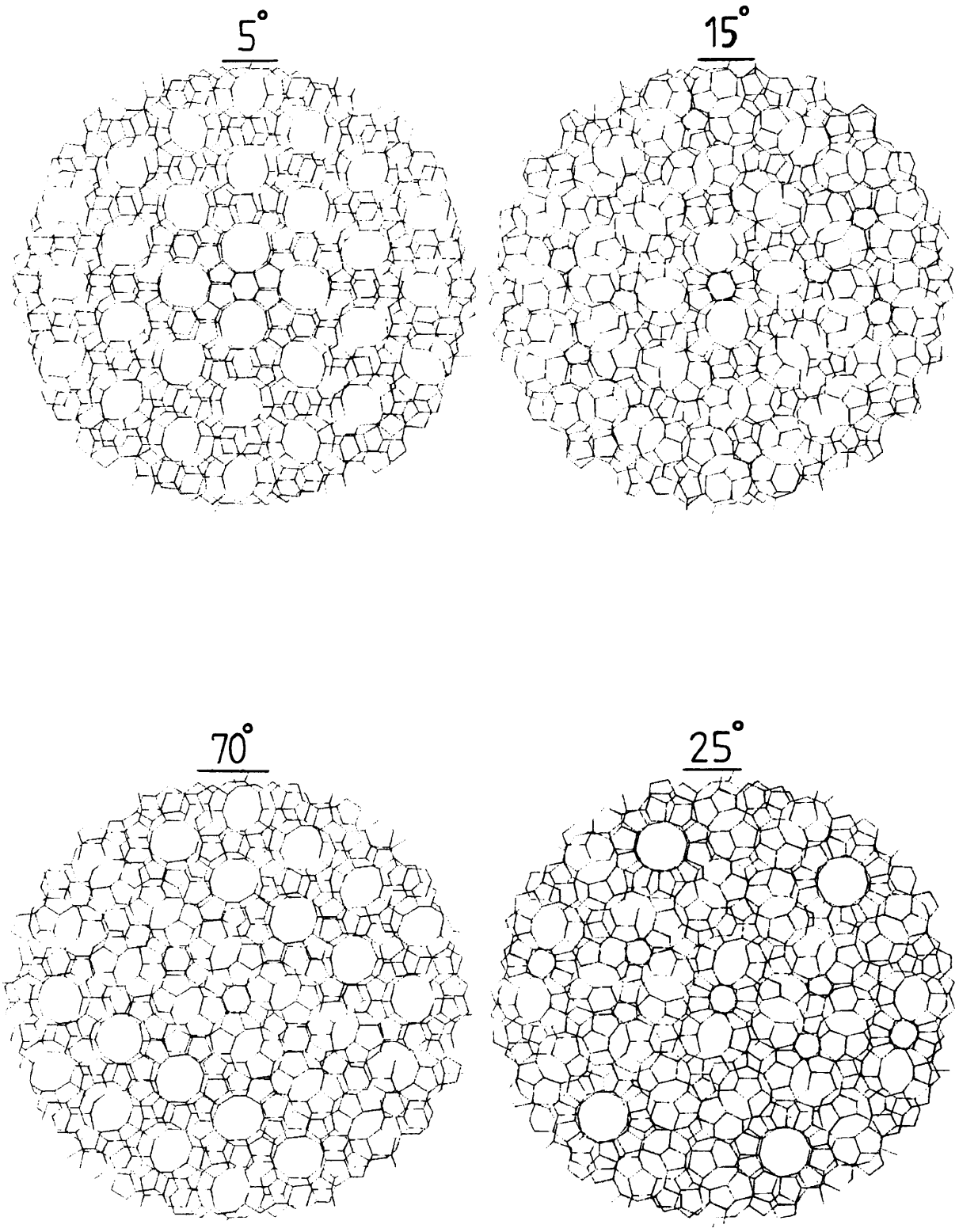


**Figure 5.9. Simple representation of rotated adjacent pentasil sheets.**

As the sheet is rotated about its axis most of the major pore systems are either partially or totally blocked. This would obviously impair the diffusional characteristics of the zeolite. However, for particular rotational angles such as 25.0° and 70° a series of periodic pseudo-secondary pore systems are generated. This is illustrated in Figure 5.9c and d, respectively. The estimated rotational angles for ECTBP, ECMEL and ECTBA are 13°, 17-15° and 12.5°, respectively. These angles do not relate to any generated secondary pore systems, but rather to the irregular and blocked projections.

In order to obtain a more accurate resolution a series of HREM images were collected over a series of defocus conditions on a selected specimen area. This procedure damages the zeolite framework, and on closer inspection it becomes obvious that most of the finer structural detail was lost. Where the specimen was sufficiently thin (< 100Å), clear and resolved images were observed. The primary and secondary channel systems of the zeolite framework could be readily recognised and correlated to the theoretical images. As discussed in section 1.22, pentasil layers are assembled via two symmetry operations namely reflection (σ) and/or inversion (i). This gives rise to the MEL and MFI structure types, respectively. The resultant major 10-MR channel system and surrounding 5- and 6-MR interchannel apertures are easily recognised from the HREM images along the [010]. By studying the relative arrangement of the larger 5-MR apertures, the σ and i symmetry is differentiated. These 5MR interchannel apertures in MFI follow a zig-zag path, while in MEL a linear course emerges. A simple structural representation and simulated HREM image of MEL and MFI are illustrated in Figure 5.10 and 5.11, respectively.

With respect to intergrown pentasil material, in regions of i symmetry, the larger of the interchannel 5-MR apertures trace a similar zig-zag path. The presence of a plane of σ symmetry cause a change in *phase* of the zig-zag trace, thus enabling defects to be readily identified. This is schematically illustrated in Figure 5.12. Figure 5.13 shows the HREM image with the corresponding diffraction pattern of the ZSM-5 type material associated with ECTBP. The major 10-MR channel system and the 5-MR and 6-MR interchannel apertures are highly resolved. The material is unfaulted and the adjacent (100) planes are all related by i symmetry. The larger 5-MRs follows a zig-zag path along the *a* direction.

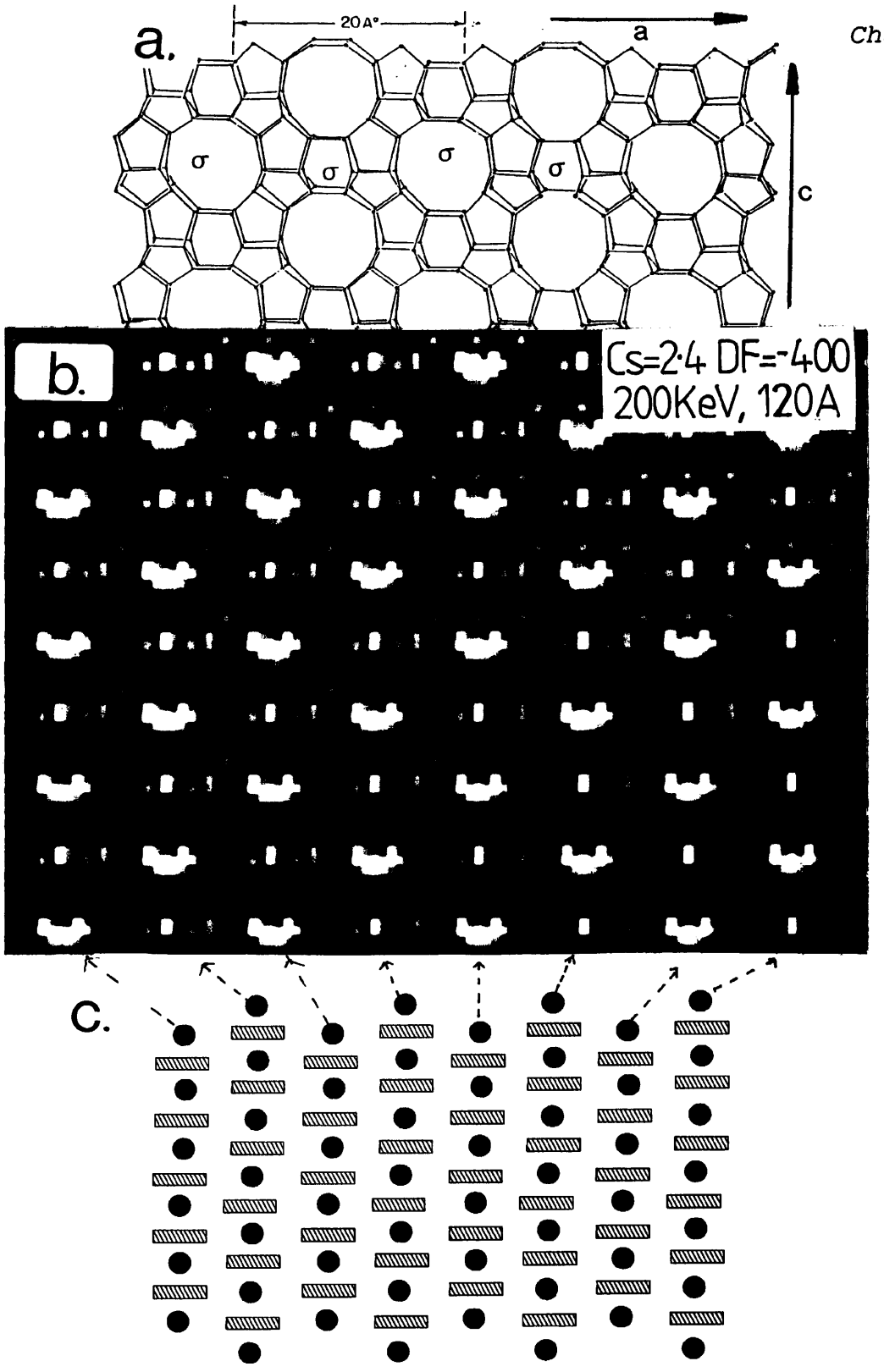


**Figure 5.10. Graphic representations of MEL a. schematic b. simulated image c. simplified interpretation. Si- and Al- $TO_4$ coincide with the line intersections.**

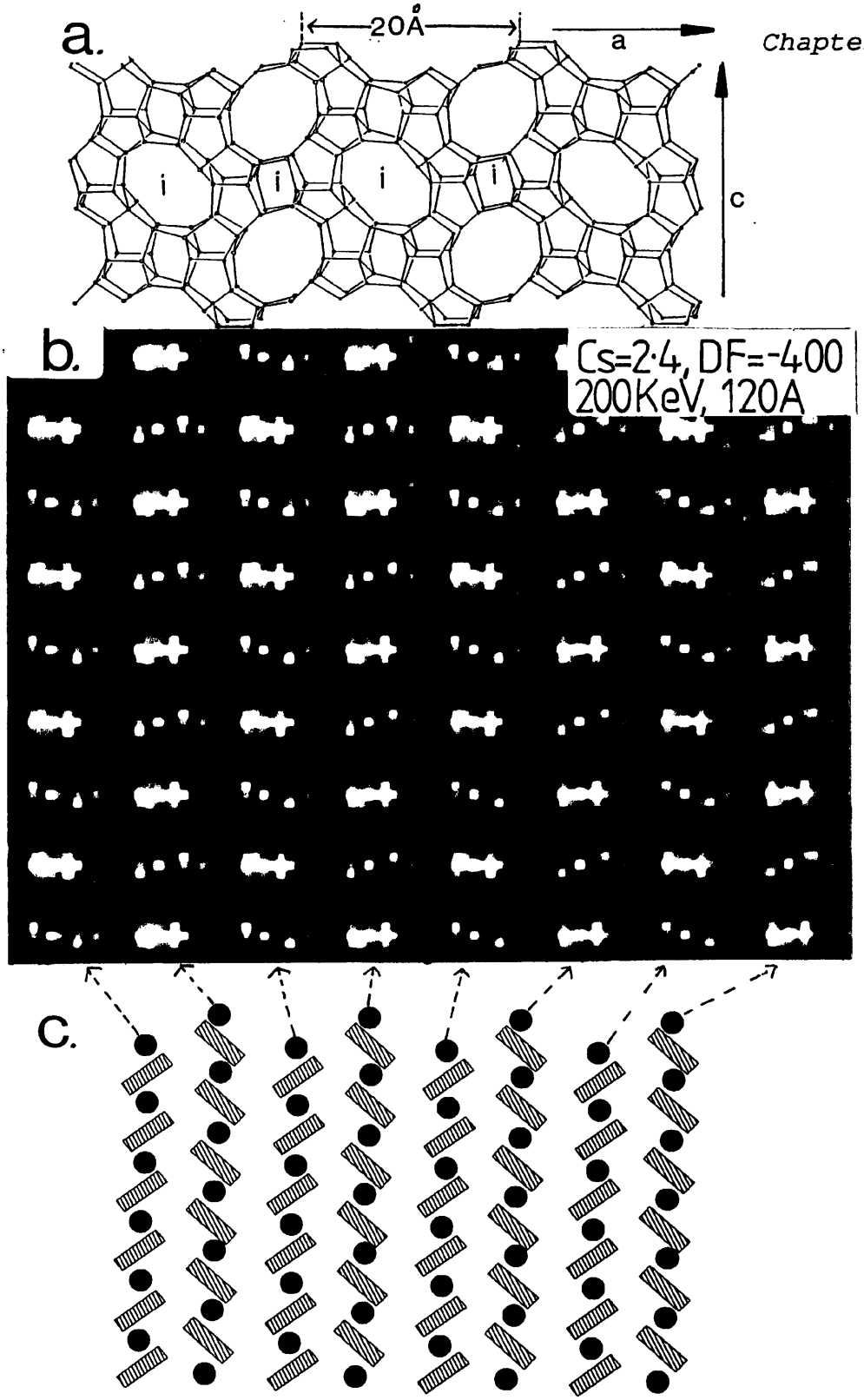


**Figure 5.11. Graphic representations of MFI, a. schematic b. simulated image c. simplified interpretation. Si- and Al- $TO_4$ coincide with the line intersections.**

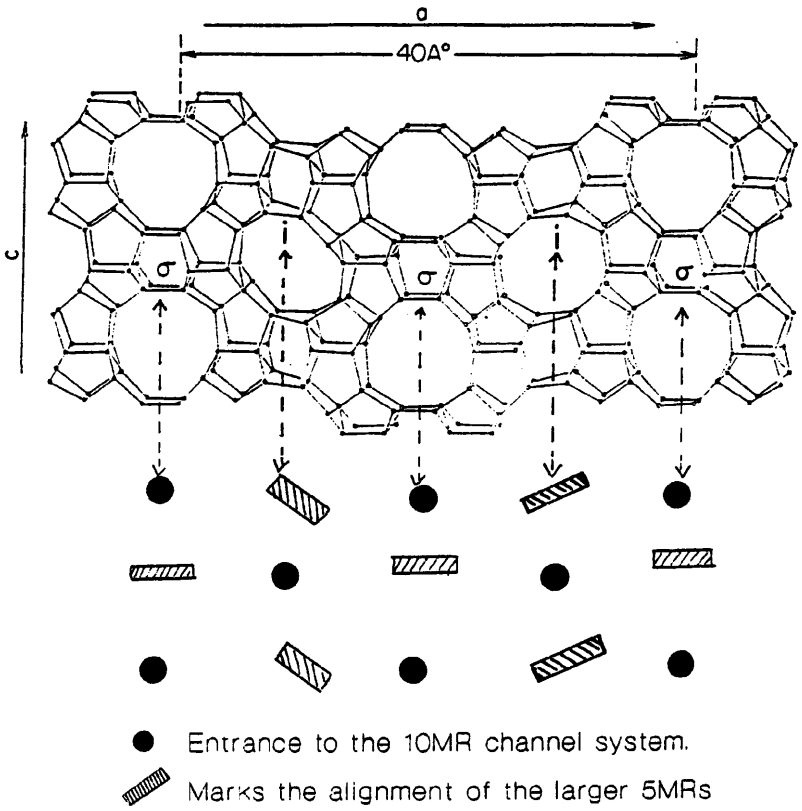


**Figure 5.12. Schematic and simple representation of a pentasil intergrowth. Si- and Al- $TO_4$ coincide with the line intersections.**

The HREM image of a ECTBA is given in Figure 5.14 and shows the improvement in image resolution by using the *push processing* method. The irregular occurrence of defect planes is easily deciphered from the rectified image. In the regions of σ symmetry the larger interchannel 5-MR apertures trace a linear path along the *a* direction until the line is broken by a series of i planes. This clearly shows the occurrence of intergrowths in ECTBA.

In the case of ECMEL several crystal areas of varying phase purity were investigated. An example of ZSM-11 and intergrown material are summarised in Figure 5.15. The σ (100) planes of the former crystal region are uninterrupted and the larger 5-MR aperture series follows a linear path. In the intergrown material, regions of both i and σ symmetry occur throughout the material.

These results show that HREM imaging is a useful tool for the structural characterisation of zeolites.

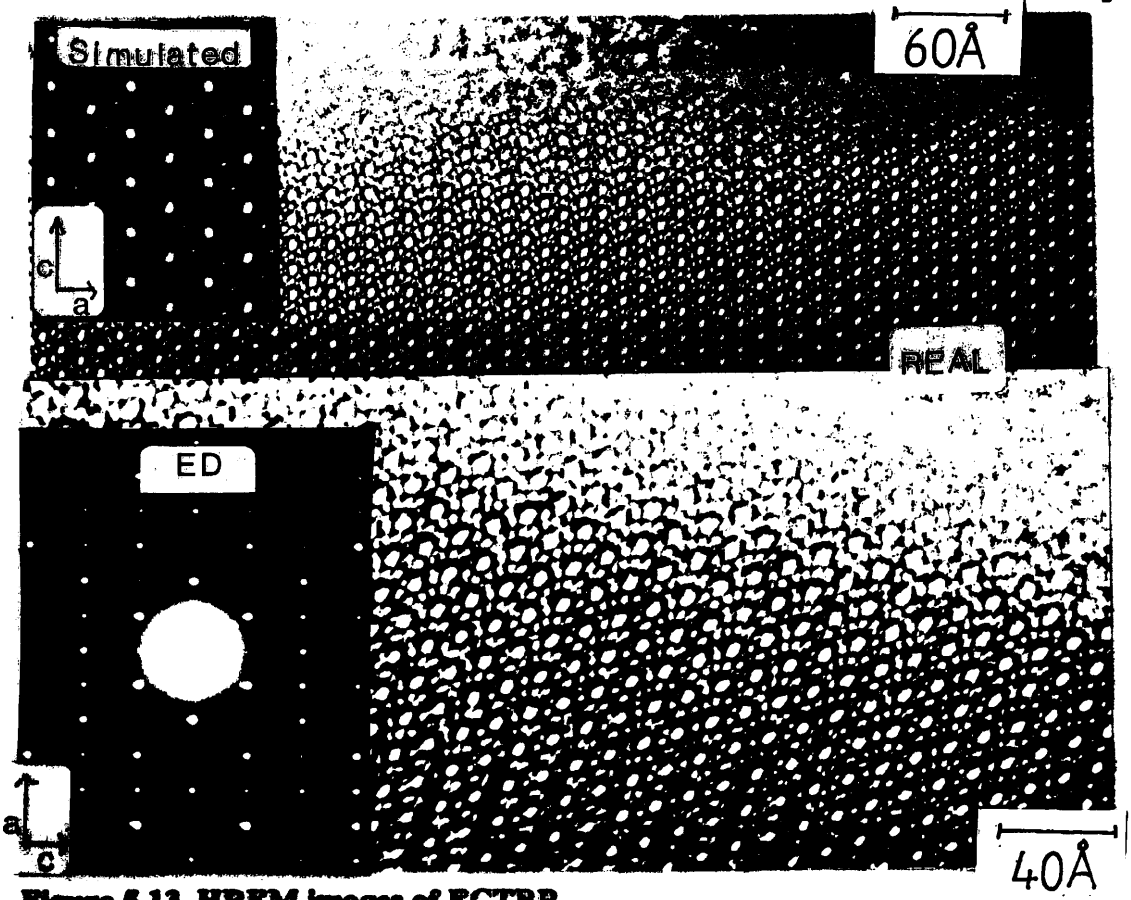


**Figure 5.13. HREM images of ECTBP.**

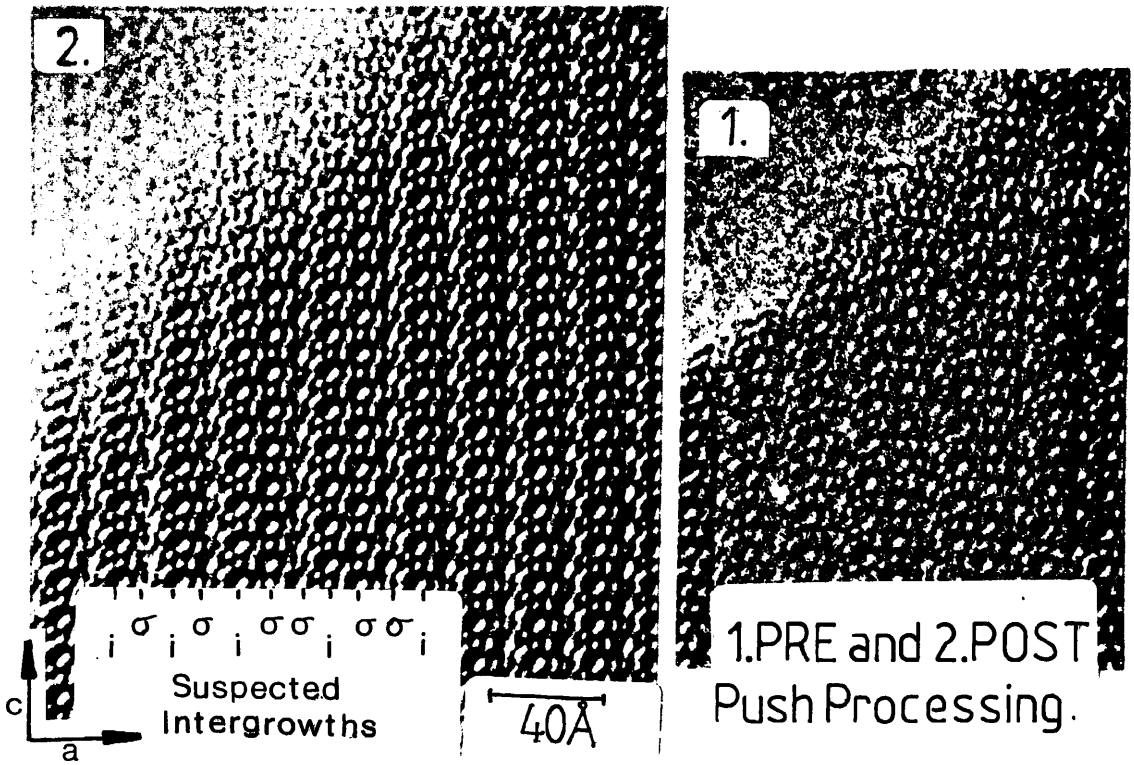


**Figure 5.14. HREM images of ECTBA.**

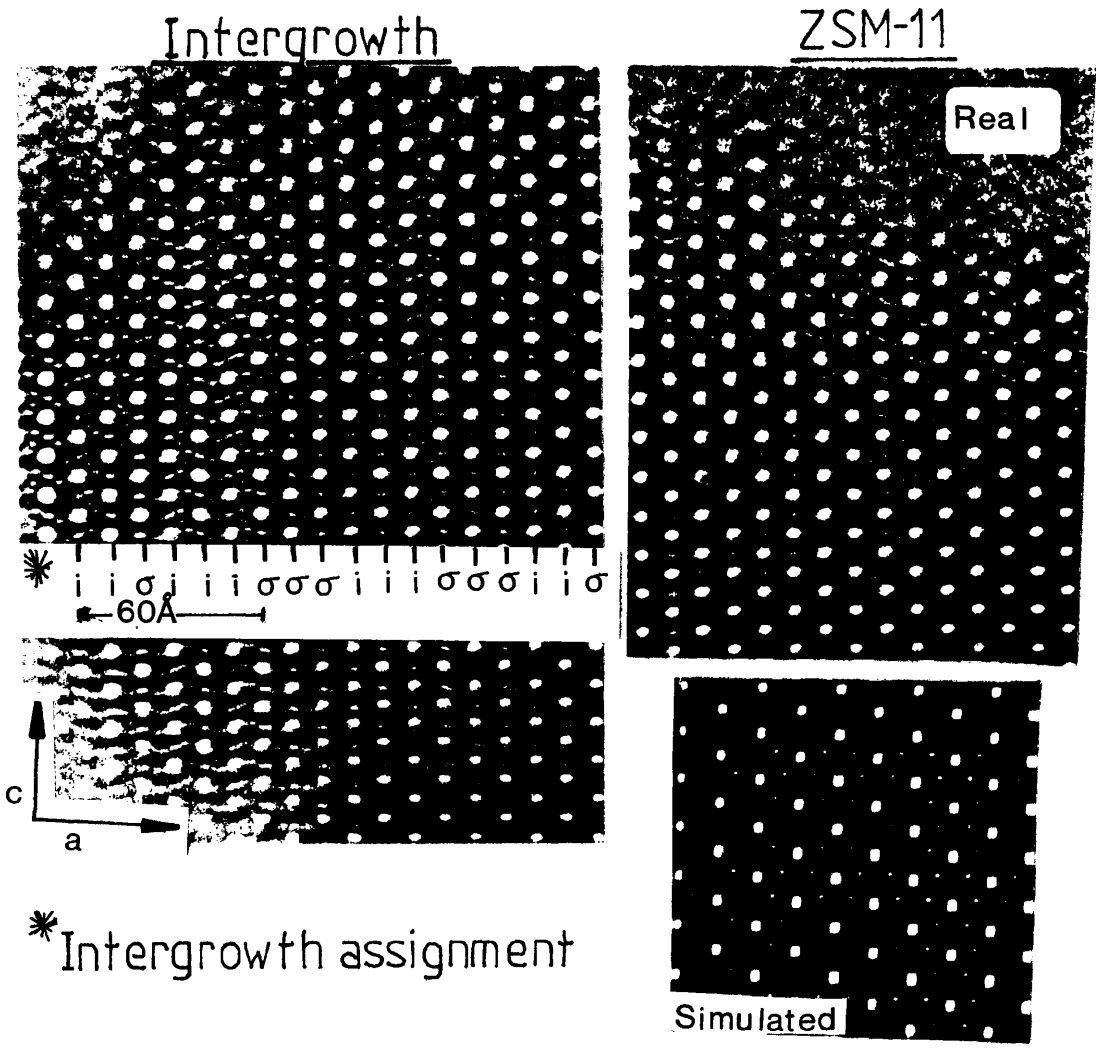


**Figure 5.15. HREM images of ECMEL.**

### 5.3.3. Evaluation of Phase Purity using the Sorption of M-Xylene

The relative unit cell sorption capacity for m-xylene was used as a semi-qantitative method to determine the intergrowth content. Due to equipment availability, ECTBA was not studied. Results are summarised in Figure 5.17.

After eight hours, the total capacities to m-xylene were 3.65, 3.05, 2.75 and 2.90 molecules per unit cell, for ECMEL, a physical mixture (50:50, ECMEL:ECMFI), ECMFI and ECTBP, respectively. As described in section 1.22, the channel system of ZSM-11 gives rise to two types of channel intersection. One has the same volume as

those in ZSM-5, while the other has a volume which is 30% greater [23]. This accounts for the greater m-xylene capacity of ECMEL. The uptake of m-xylene of the physical mixture and ECTBP followed a predictable trend. That of the former sample was 50% of that of ECMEL, and that of the latter sample was 25% greater than that of ECMFI. These results compare with the studies of Li-Feng et al.[3] who used a range of sorbates to differentiate the sorption capacities of several high-silica zeolites.

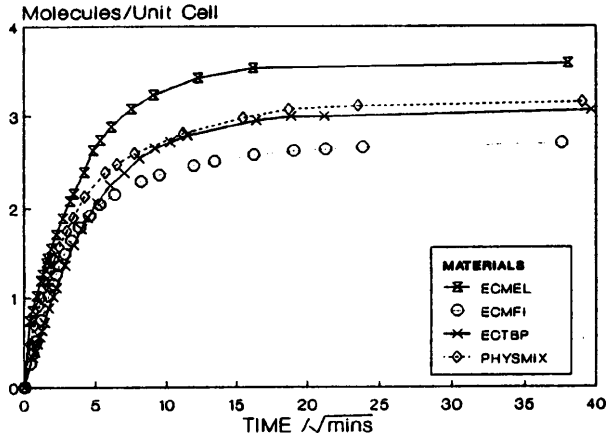


**Figure 5.17. M-xylene sorption data of pentasil materials.**

The kinetic size of m-xylene (6.8Å) appears to be too large to penetrate the channels (5.2-5.5Å). It has been suggested that the molecule enters the zeolite channels by undergoing isomerisation to the smaller para isomer. Such processes occur on the crystal outer surface sites [24]. However, as sorption was recorded at 120°C, isomerisation processes were presummed negligible. Alternatively, via steric juggling or by being compressed by the electric field experienced within the channel network, m-xylene invades the zeolite pore system [25].

Assuming crystal size homogeneity, the relative rates of uptake of m-xylene gives a qualitative determination of channel size and tortuosity. In this work the rate of m-xylene uptake went as follows,

**ECMEL > PHYSMIX > ECTBP > ECMFI**

and Figure 3.18 represents the relative uptake after 60 minutes of exposure to m-xylene of these materials. The results show that the tortuous channels in ECMFI deterred the uptake of m-xylene and that this method can differentiate channel systems.

Foger suggested that the occurrence of planar faults in ZSM-5 or ZSM-11 should have no influence on its sorption behaviour as they are parallel to the [010] channel system [26]. The disruption caused to the other major channel system along [100] was not mentioned. As a result, it is unwise to suggest that the sorption behaviour of an inter-growth would equate to that of a physical mixture of structural end members. A more comprehensive study using a range of sorbates of varying dimensions might prove sucessful in determining structural anomalies. Nonetheless, the results showed that from a simple sorption experiment a semi-quantitative determination of phase purity can be achieved.

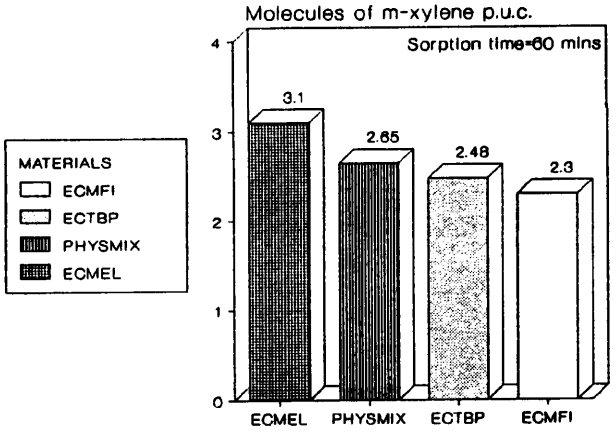


**Figure 5.18. Relative uptake of m-xylene after 60 minutes exposure to m-xylene.**

### 5.3.4. Assessment of the Acidic Nature of Pentasils using *In-Situ* FTIR Methods

The FTIR spectra of the calcined hydrogen forms of ECMEL, ECMFI, ECTBP and ECTBA are illustrated in Figure 5.19. The data consists of two distinct absorbance bands, common to all the materials, at approximately 3740 and 3610cm$^{-1}$. The fundamental stretching vibrations of both internal and external silanol species are associated with the band at 3740cm$^{-1}$. The band around 3612cm$^{-1}$ is connected with framework OH or Brφnsted acid sites. In agreement with similar studies of Qin et al.[27] the relative intensity of this band is equivalent in each of the samples and independent of phase type or method of synthesis. The spectra of the samples only differ with respect to the relative intensities of the silanol and OH absorbance bands. Such variations depend upon several factors such as the organic additive used in synthesis, crystal size [27], framework aluminium content [28], and the presence of unreacted amorphous material or hydroxyl defect acid sites [26].

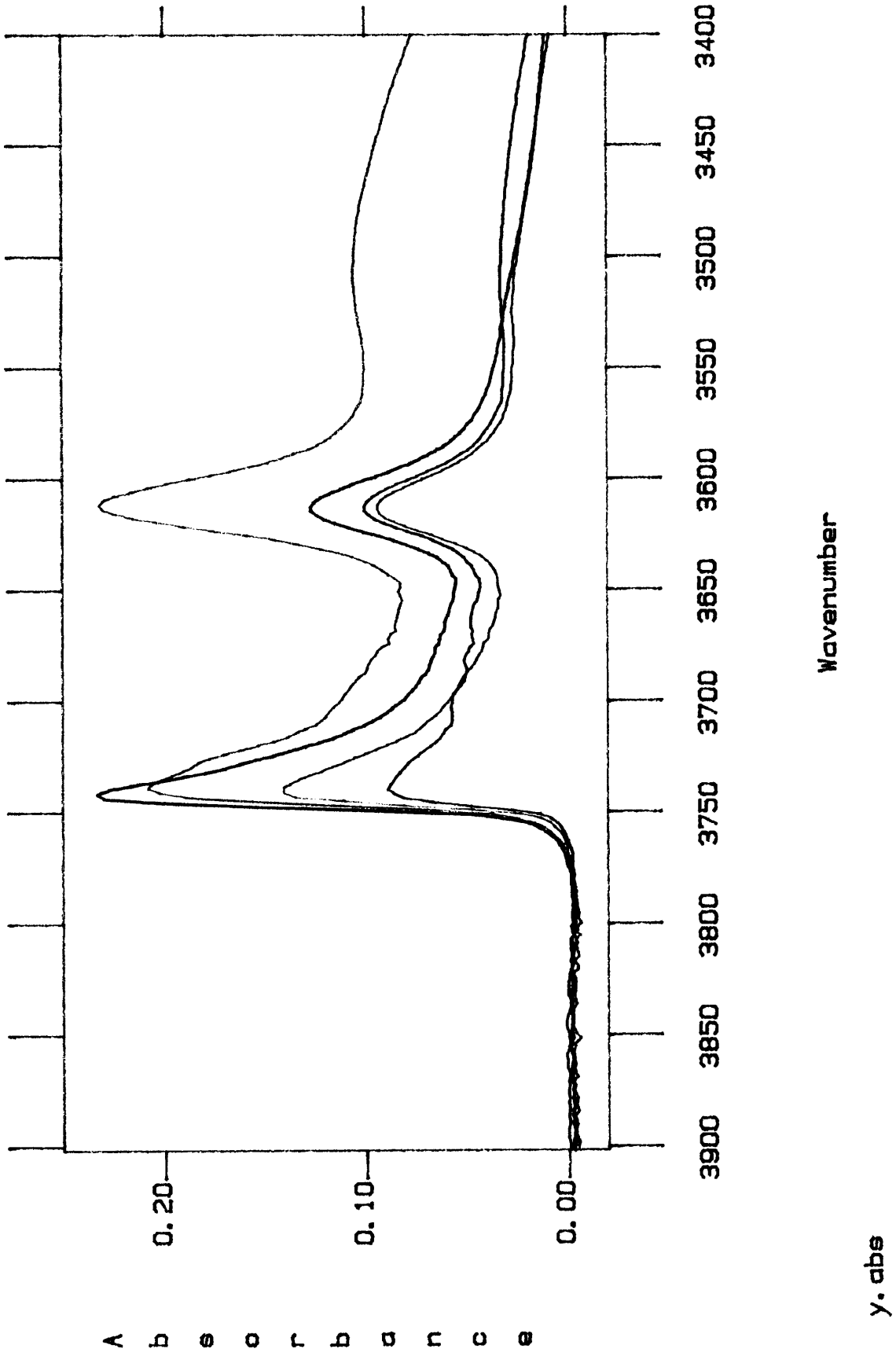


Figure 5.19. Comparison of the OH spectra of the hydrogen form pentasil materials. Key: yellow-ECTBP, blue-ECTBA, red-ECMEL and green-ECMFI.

After the adsorption of pyridine at 150°C, the intensity of the OH band ($3610cm^{-1}$) was removed, as exemplified by ECTBA in Figure 5.20. This corresponded to the appearance of a series of bands in the region of deformation vibrations. The absorbance bands due to chemisorbed pyridine for each sample are shown in Figure 5.21. The band around $1545cm^{-1}$ is attributed to the C-C stretching vibration of the pyridinium ions, $PyH^+$, showing the presence of Brφnsted acidity. Lewis acid sites are indicated by the presence of a band at around $1454cm^{-1}$ arising from the C-C stretch of a coordinatively bonded pyridine complex, PyL. The band at $1495cm^{-1}$ is common to pyridine linked to both Brφnsted and Lewis acid centres.

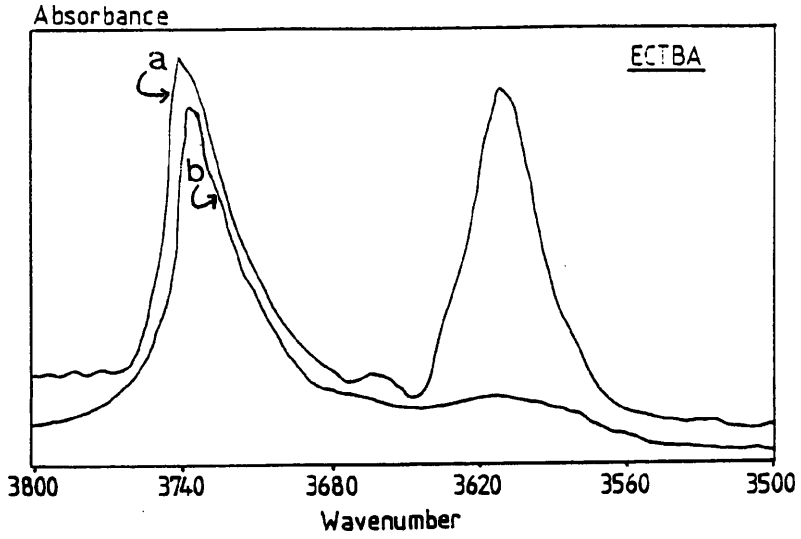


**Figure 5.20. Effect of on the OH spectra of ECTBA, a.before and b.after pyridine adsorption at 150°C.**

Figure 5.22 represents a study of the Brφnsted and Lewis acidity with the thermal desorption of pyridine from the various samples. This casts some light on the strength of the acid sites associated with the zeolite. The intensity values given represent the ratio of the integrated peak area from the pyridine spectrum obtained after heating at the chosen temperature to the peak area in the original spectrum prior to pyridine adsorption. The results show that an increase in the desorption temperature leads to a removal of approximately the same quantity of $PrH^+$ species from all zeolites. This corresponded to a reappearance of the OH band around $3610cm^{-1}$. In agreement with others [28], this suggests that the Brφnsted character of the materials was equivalent.

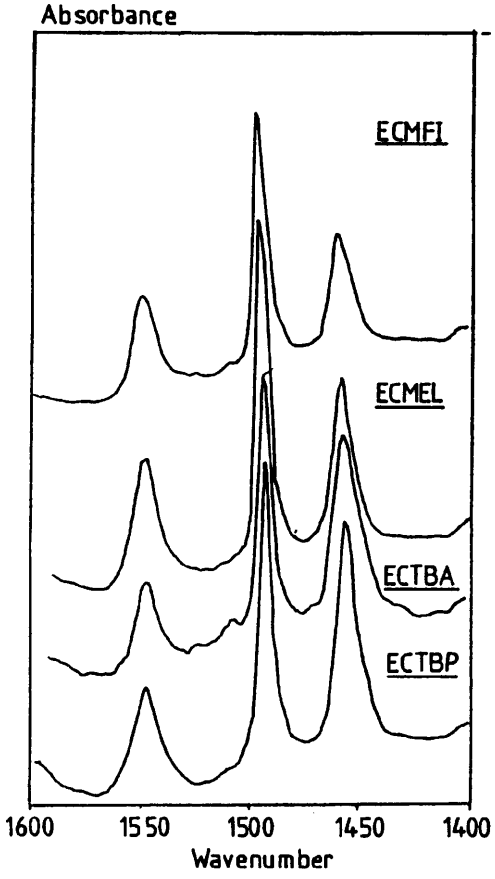


**Figure 5.21. FTIR spectra of pyridine adsorbed at 150°C on the pentasil zeolites.**

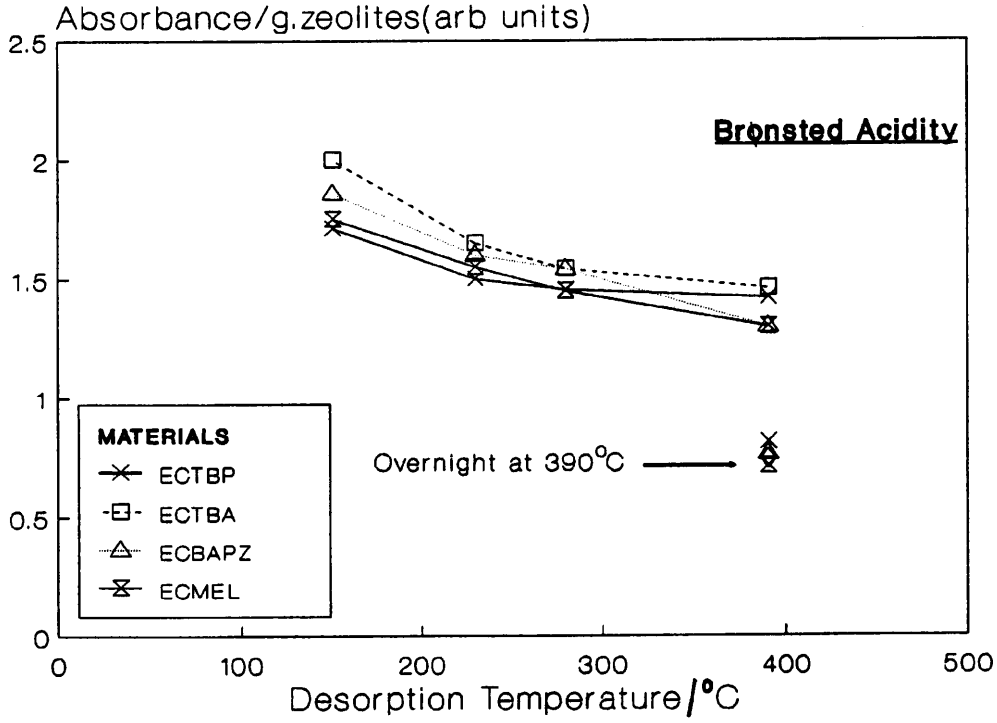


**Figure 5.22. Changes in Bronsted acid site populations as a function of pyridine desorption temperature.**

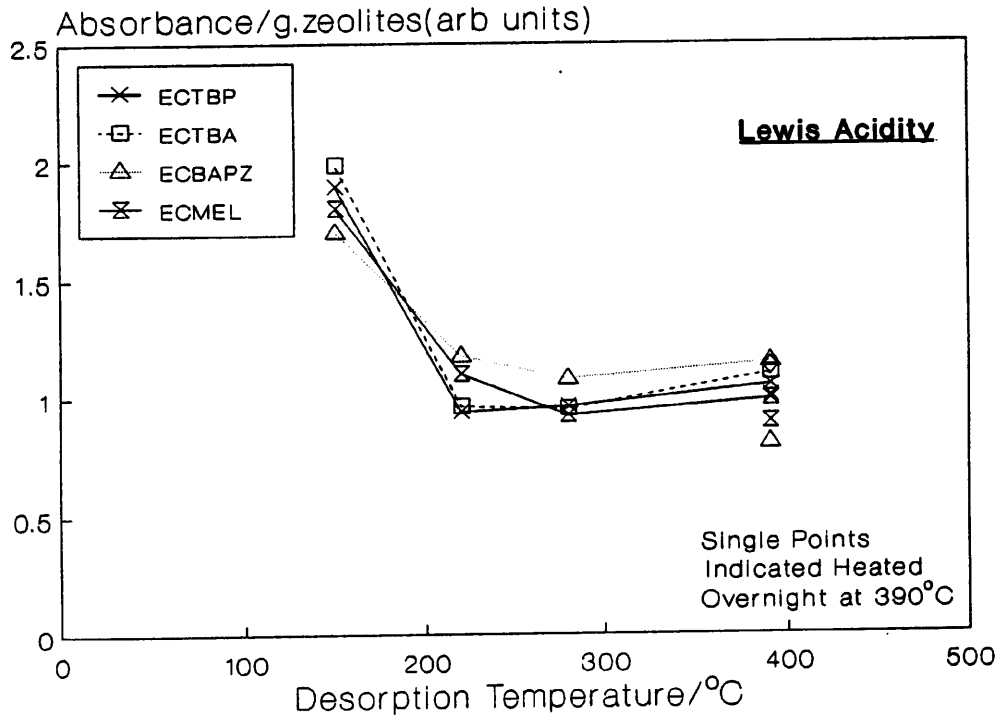


**Figure 5.23. Changes in Lewis acid site populations as a function of pyridine desorption temperature.**

Some slight differences in the Lewis acidity between samples were apparent from this experiment. On the initial adsorption of pyridine at 150°C a greater number of PyL sites were associated with zeolites synthesised with quaternary compounds (ECTBA and ECTBP) as opposed to diamines (ECMEL and ECMFI). However, after desorption at 280°C, equivalent numbers of PyL sites were associated with all the samples. After prolonged heating at 390°C the number of PyL sites increased slightly, indicating that pyridine was bound to strong Lewis acid sites. On closer inspection as shown in Figure 5.23, this band consisted of the major PyL intensity at 1455cm$^{-1}$ with a newly developed shoulder around 1445cm$^{-1}$. The development of PyL vibrational frequencies has been reported by others [15]. It was suggested that, due to the stronger acidic nature of the Lewis sites [29], desorbing pyridine is attracted from the weaker Brφnsted site [30]. Alternatively, such variations originate from, either sites of varying acidity, or from dislodged aluminium occurring at elevated temperatures [31,17]. However, pyridine is a strong base and is not capable of discriminating subtle differences in acidic properties of the materials.

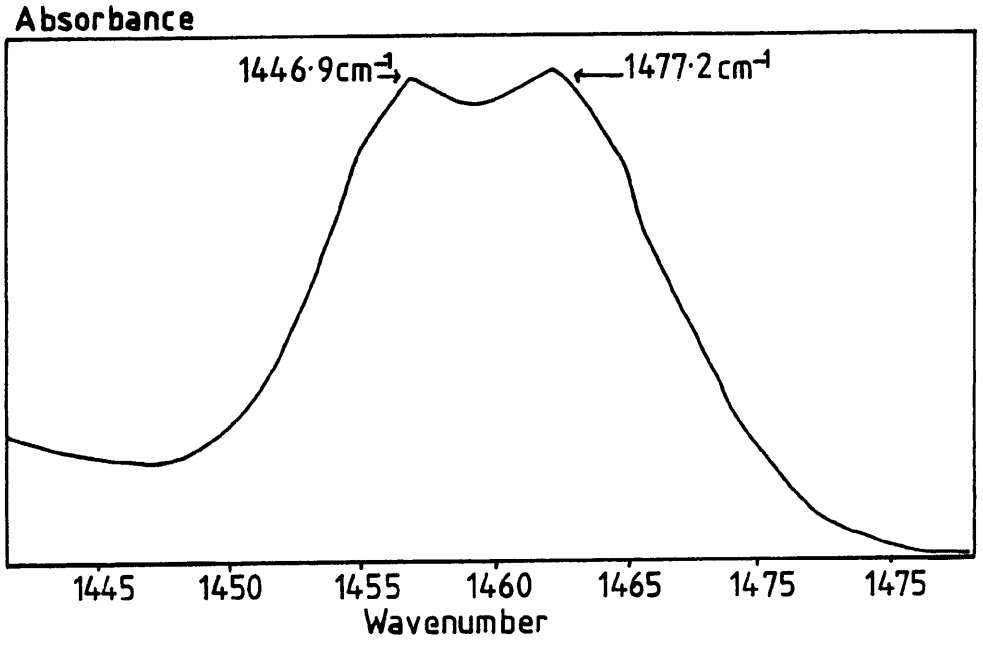


**Figure 5.23. Effect on the PyL band of ECTBA after prolonged heating at 390°C for eight hours.**

Figure 5.24 exemplifies the OH spectra of the acid form of ECMEL absorbed over a range of pressures at 77K. Hydrogen ($H_2$) molecules interacts with the Brφnsted acid sites, which is illustrated by the displacement of the band at 3613cm$^{-1}$. The dis placement bands at 3576 and 3485cm$^{-1}$, represent $H_2$-OH interactions. By increasing the $H_2$ pressure more sites interact, as first reported by Thompson [15], and the intensity of the 3485cm$^{-1}$ OH band increases. Figure 5.25, shows the induced $H_2$ spectra of ECMEL composed of two bands around 4110 and 4130cm$^{-1}$. The changes in their relative intensity with respect to hydrogen pressure match those of the 3576 and 3485cm$^{-1}$ OH bands, respectively. In agreement with Thompson [15] all the materials in this study, independent of their structural nature, interacted with $H_2$ in a similar manner. This is illustrated in Figure 5.26, showing the OH spectra of all the materials after $H_2$ sorption at 750 Torr. The $H_2$ spectra can be interpreted in terms of a clustering effect. At low pressures a virtual 1:1, $H_2$:OH coordination is assumed. At higher pressures, a number of $H_2$ molecules cluster around the OH. This results in an increase in the perturbation of the OH band together with a net decrease in the interaction of each $H_2$ molecule. Consequently, the intensity of the 3485cm$^{-1}$ band increases and the 4110cm$^{-1}$ $H_2$ band is displaced by the 4130cm$^{-1}$ [15].

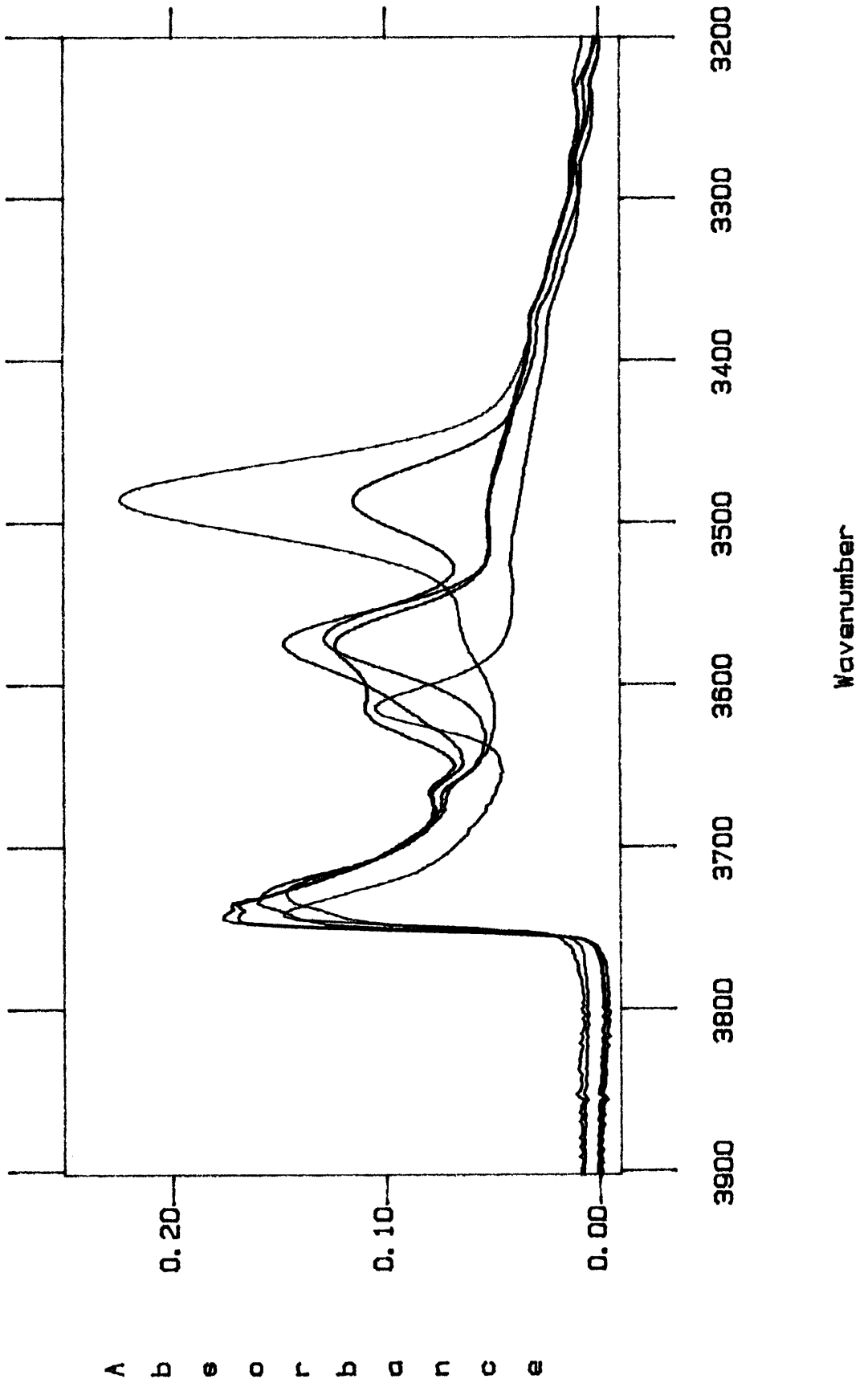


Figure 5.24. Corresponding OH spectra of ECMEL with increasing $H_2$ pressure.Key:purple-original spectra, red-11.7, blue-34, black-288 and yellow-750 Torr.

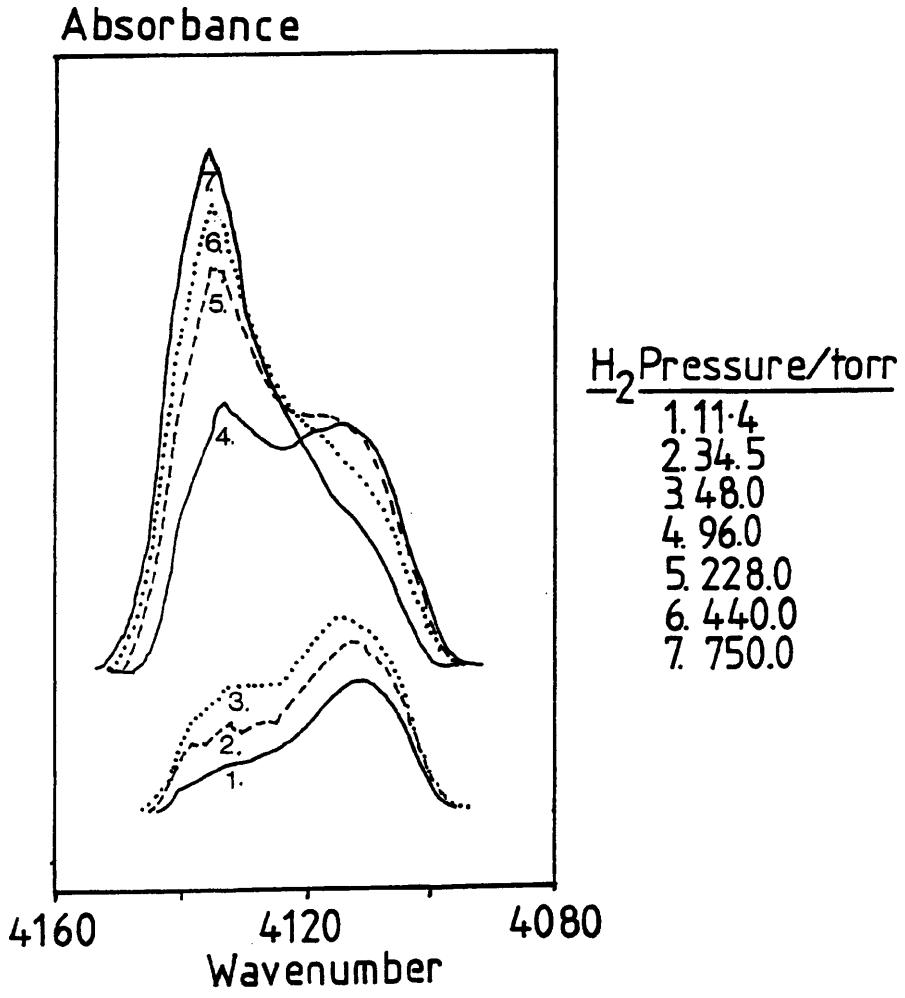


**Figure 5.25. Induced $H_2$ spectra of ECMEL with increasing $H_2$ pressure.**

An important characteristic of zeolite catalysts is their ability to stabilise reaction intermediates. This is attained by strong electric fields arising from charges associated with the zeolite framework and any counter ions. By measuring the total $H_2$ band area as a function of pressure, the molar absorption extinction coefficient (A) can be determined. It is proportional to the infrared intensity of a vibrational band induced by an electric field. The derivation of A and the methodology involved is summarised in Appendix V. Figure 5.27 shows the plot of P/S versus P, for ECMEL, ECMFI, ECTBA and ECTBP. P is the pressure (Pa) of $H_2$ and S represents the corresponding total $H_2$ band intensity obtained from a zeolite disc of given mass(g) and cross-sectional area ($m^2$).

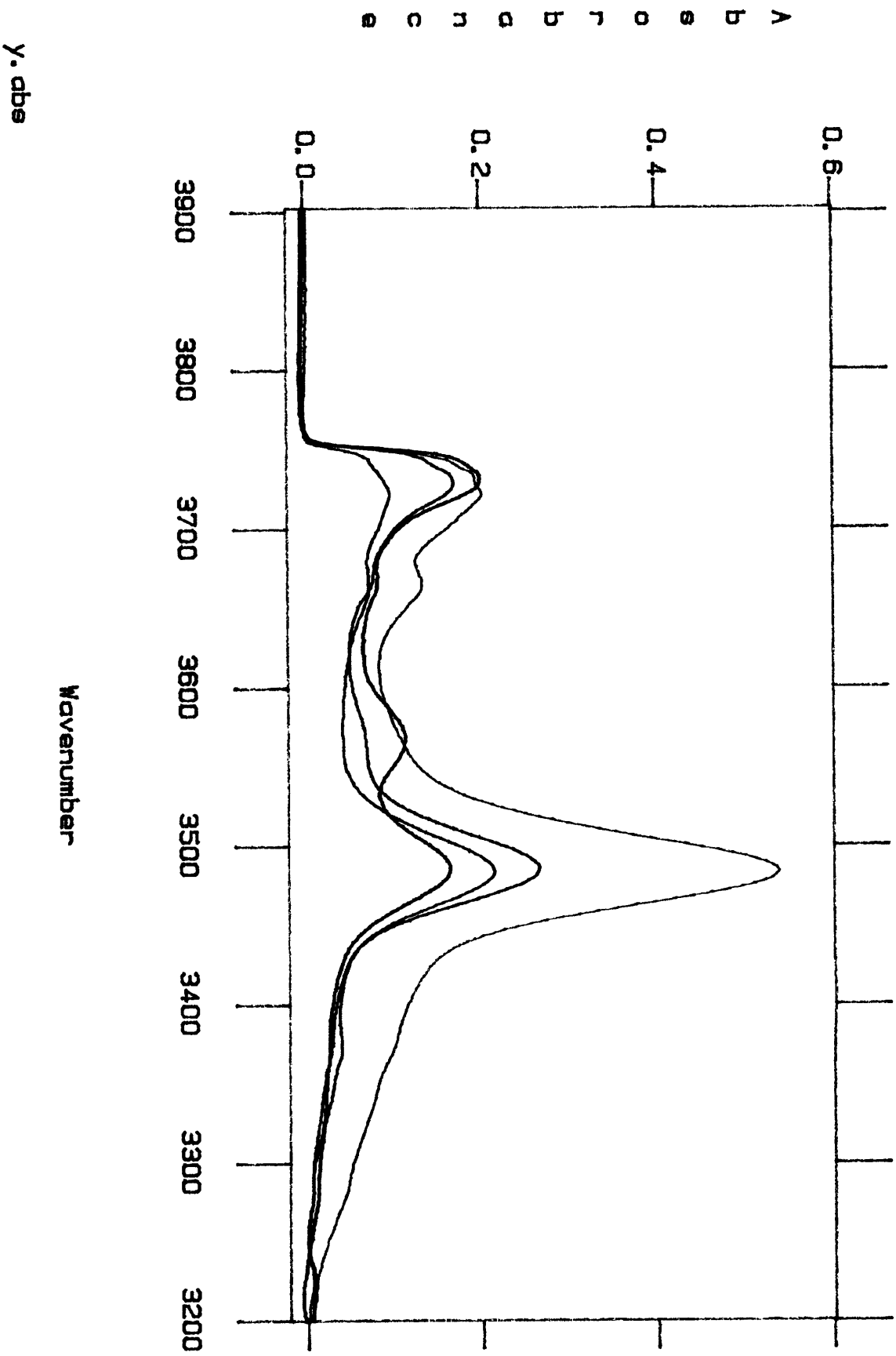


Figure 5.26. Comparison of OH spectra of pentasil materials after $H_2$ adsorption at 750 Torr. Key: yellow-ECTBP, blue-ECTBA, red-ECMEL and green-ECMFI.

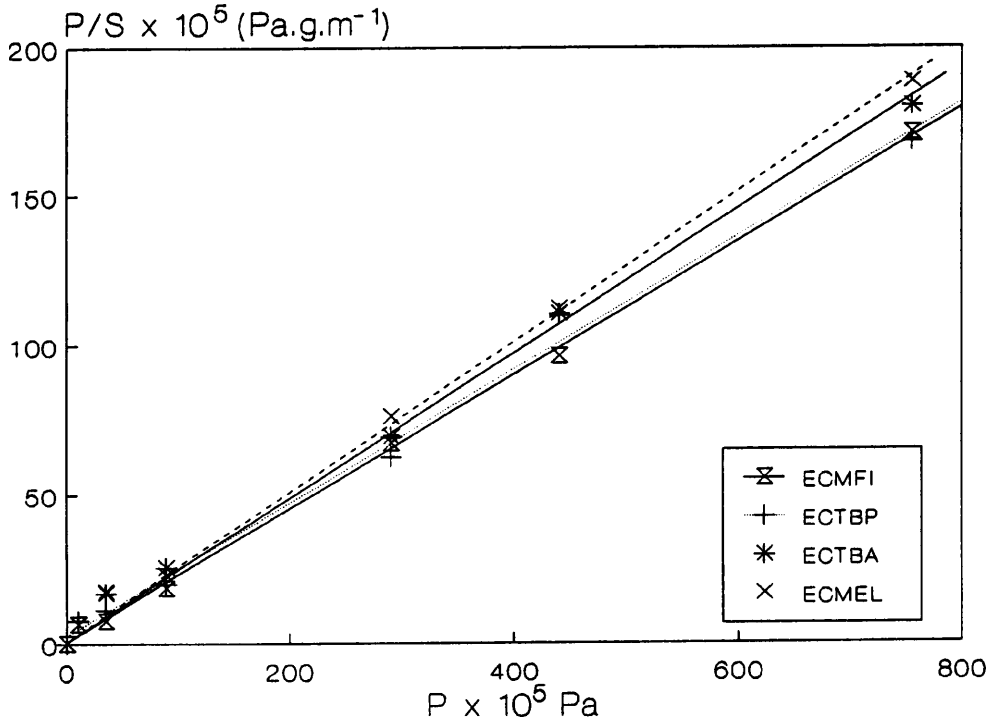


**Figure 5.27. A study of the change in $H_2$ band intensity with the pressure $H_2$ on pentasil materials.**

The materials show a comparable linear response in $H_2$ band intensity with respect to $H_2$ pressure. A is directly calculated from the gradient of the corresponding lines as given in Table 3.2.

| Sample | A/m.mol$^{-1}$ |
|---|---|
| ECMEL | 655 |
| ECMFI | 665 |
| ECTBP | 680 |
| ECTBA | 686 |

**Table 3.2. The molar extinction coefficient (A)of pentasil materials.**

The values for A are comparable and independent of zeolite structure. Similar values for pentasil materials were obtained by Thompson [15] corresponding to an electric field between 1.8 and 1.9 x $10^9$ V.m$^{-1}$.

Both the pyridine and hydrogen studies have shown that, irrespective of structure, the zeolites in this study have comparable Brφnsted and Lewis acidity.

### 5.3.6. Catalytic Evaluation of Pentasil Zeolites

Unless otherwise stated, the results in this section refer to the activated catalysts. The zeolites studied were ECTBA, ECTBP, ECMFI, ECMEL and a physical mixture (PHYSMIX, 1:1,ECMEL:ECMFI). All the materials have near-equivalent crystal size and morphology and aluminium contents (Si/Al≈50) as listed in Table 5.1. The alkylation of p-xylene was a useful probe reaction to investigate the shape-selective properties of the zeolites. Substantial differences in their respective aromatic product distributions were found.

The conversion of p-xylene with respect to time-on-stream of the various materials is summarised in Figure 5.28. Generally, all the zeolites showed a similar activity and high conversion (65-90%) of p-xylene. However, over the reaction period the catalysts deactivated according to the order:

**INCREASING ACTIVITY**

**ECTBA < ECTBP < ECMFI < PHYSMIX(1:1) = ECMEL**

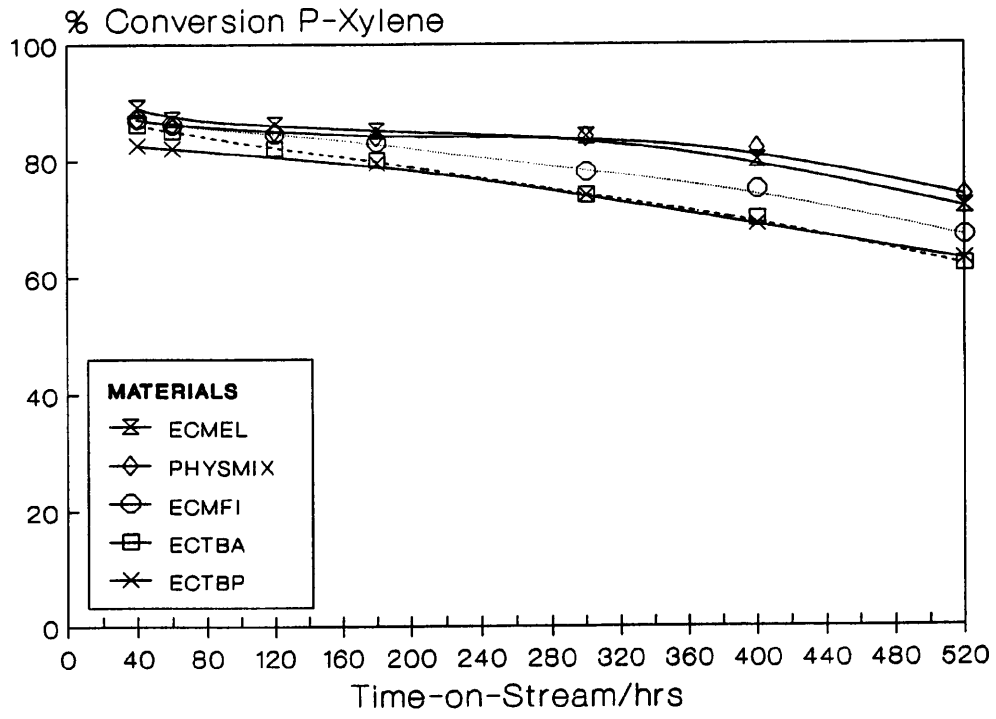


**Figure 5.28. Conversion of p-xylene with respect to time-on-stream.**

At high conversions, p-xylene underwent isomerisation forming a near thermodynamic distribution of o- and m-xylenes on all the catalysts. This supports the view that, independent of the zeolite structure, all the materials have similar Brφnsted and Lewis acidity. This is in agreement with the FTIR results reported in the previous section.

At lower p-xylene conversions the product selectivity for each catalyst was more distinct. The data show that the isomerisation of p-xylene is more favoured on ZSM-11 type materials. This is in agreement with Derouane et al.[16], who used the same reaction to study the shape-selective properties of pentasils. The accepted mechanistic route [25] for acid catalysed xylene isomerisation involves a monomolecular 1,2-methyl-shift in the protonated xylene as illustrated in Figure 5.29.

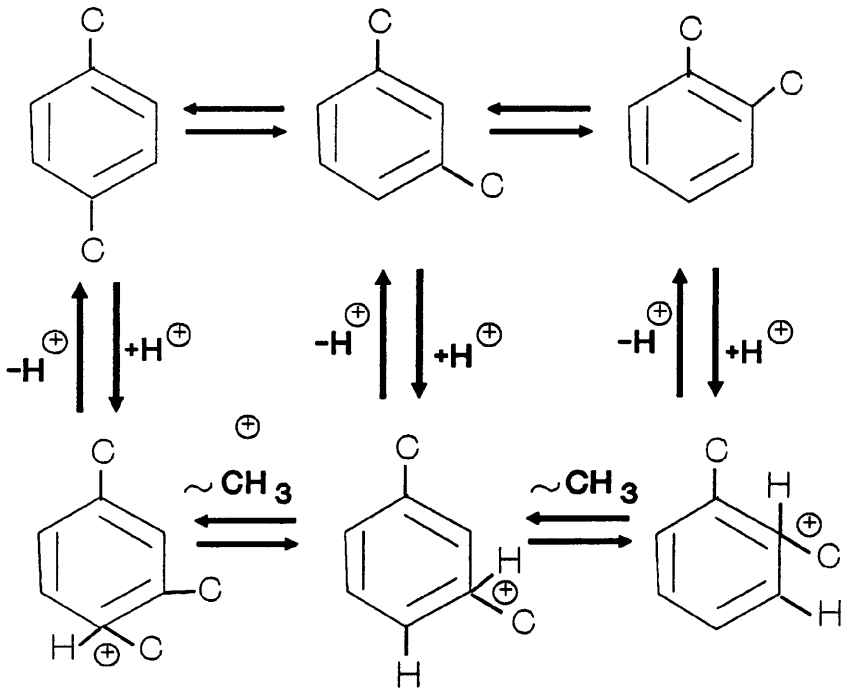


**Figure 5.29. Proposed acid catalysed xylene isomerisation mechanism [24].**

Xylene isomerisation also occurs during the bimolecular transalkylation process [24]. In ZSM-5 or ZSM-11 the spatial restraints for the transition state for the bimolecular process means that the major transformation is likely to occur via the monomolecular methyl shift process.

By studying the aromatic alkylated product distribution in more detail, significant differences in the shape-selective character of the catalysts were discovered. Table 5.3 gives the details of the product distributions for each catalyst after 60 minutes on stream. The yields are listed as molar percentages and as the xylene content in the product is not included, these values may be considered as selectivities (see Appendix V).

For a *global* appreciation the total C9 and C10 product selectivities were calculated by summing the percentage yields for each carbon number. Figures 5.30 and 5.31 show total C9 (trimethylbenzenes, TMB and ethyltoluenes, ET) and C10 (tetramethylbenzenes, TEMB and dimethylethyltoluene, DMET) selectivities as a function of p-xylene conversion for each catalyst.

| Product Distributions [a] | | ECMEL | ECMFI | PHYSMIX | ECTBA | ECTBP |
|---|---|---|---|---|---|---|
| Benzene (C6) | | 1.34 | 0.45 | 0.47 | 0.22 | 0.22 |
| Toluene (C7) | | 4.48 | 5.63 | 4.99 | 5.09 | 4.55 |
| Ethyl Toluenes (C8) | | 3.56 | 5.35 | 4.47 | 5.00 | 5.48 |
| Trimethyl benzenes (C9) | 124 | 51.29 | 45.00 | 48.15 | 52.26 | 45.41 |
| | 135 | 3.04 | 1.72 | 2.43 | 2.10 | 1.90 |
| | 123 | 1.91 | 0.99 | 1.58 | 1.19 | 1.16 |
| Dimethylethyl benzenes (C9) | | 16.38 | 21.00 | 19.58 | 20.50 | 23.27 |
| Tetramethyl benzenes (C10) | 1245 | 11.03 | 14.80 | 12.05 | 10.05 | 13.04 |
| | 1235 | 5.20 | 3.63 | 4.56 | 2.55 | 3.50 |
| | 1234 | 1.77 | 1.43 | 1.72 | 1.04 | 1.47 |

a- Xylenes excluded all values in Mol%

**Table 5.3. Aromatic product distribution after 60 minutes.**

For all samples, the main aromatic products were C9 compounds showing a non-equilibrium TMB distribution, as depicted in Figure 5.32. The largest amount of a single product was 1,2,4-TMB, as shown in Figure 5.33. Neglecting isomerisation processes, this arose from the monoalkylation of the p-xylene. However, the yield and

selectivity of the other bulkier TMBs (1,2,3 and 1,3,5) was low, as reflected in Figure 5.34. The total C9 selectivity was highest on ECMEL and lowest on ECMFI. PHYMIX followed an intermediate pattern, while ECTBA and ECTBP show similar selectivity to ECMEL and ECMFI, respectively.

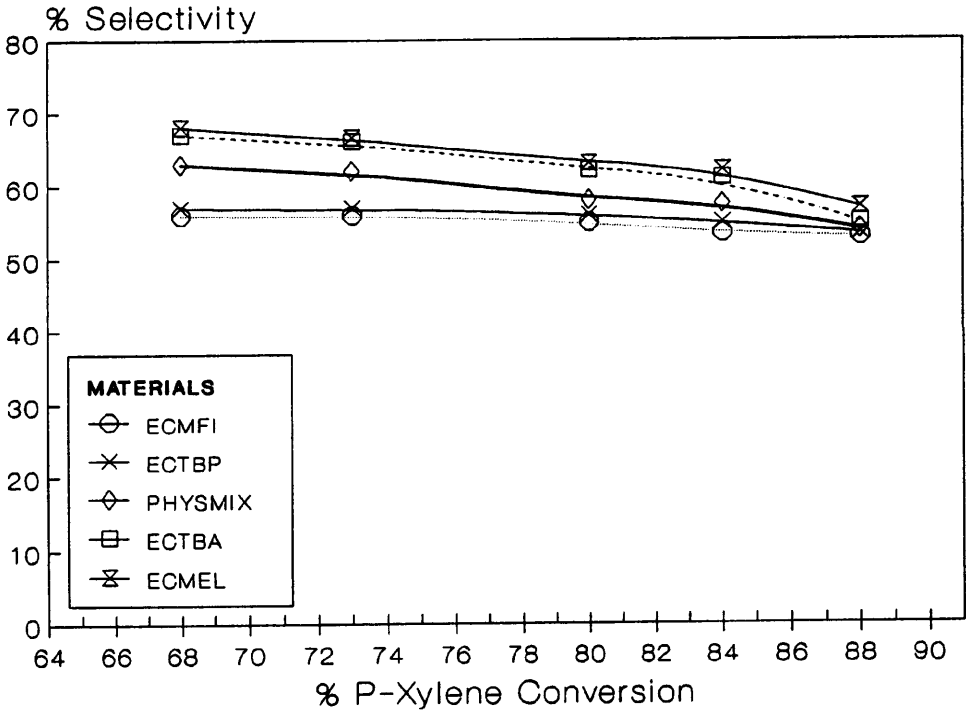


**Figure 5.30. Global C9 selectivity with respect to p-xylene conversion.**

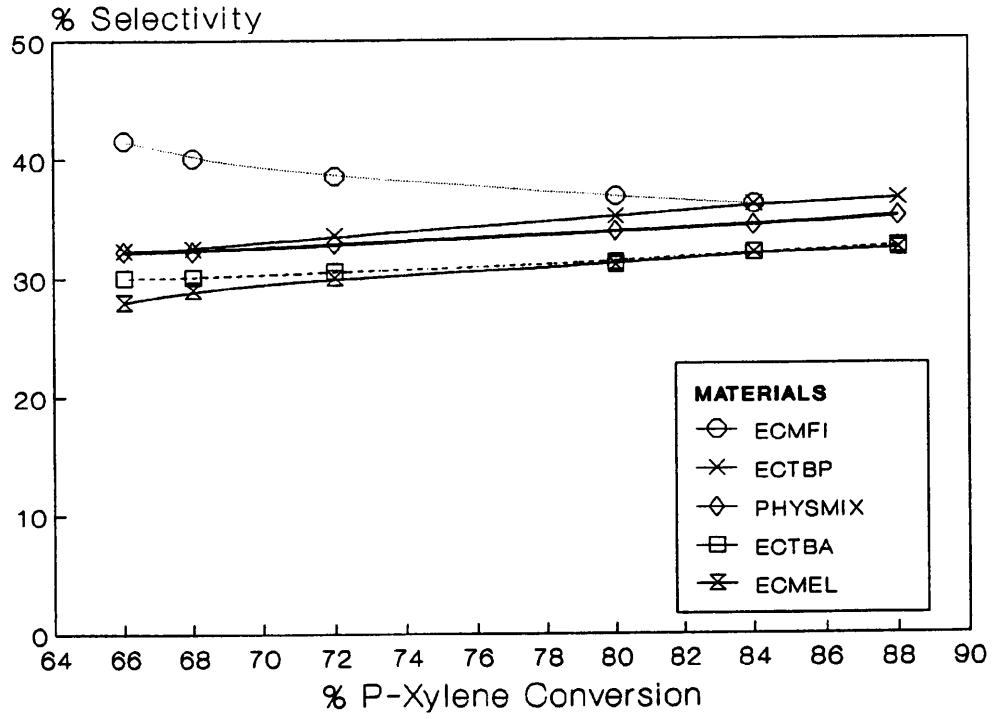


**Figure 5.31. Global C10 selectivity with respect to p-xylene conversion.**

A reversed trend was observed for the total C10 product distribution. Here the major products were the tetramethylbenzenes (TEMB). ECMFI showed a very high selectivity to 1,2,4,5-TEMB, while higher yields of the bulkier isomers, 1,2,3,4- and 1,2,3,5-TEMB were favoured on ECMEL. It should be noted that no significant yields of products above C10 were obtained in any of the zeolites. This is characteristic of pentasil materials [33]. Figures 5.35 and 5.36 reveal the differences in the TEMB selectivity of all the catalysts studied. As the TEMBs are very large molecules, it has been suggested that their formation occurs at the non-selective surface of the crystal. However, a high selectivity to 1,2,4,5-TEMB suggests that TEMBs are formed internally. Consequently, the more sterically hindered and bulkier isomers are unable to diffuse out and become subject to isomerisation and dealkylation.

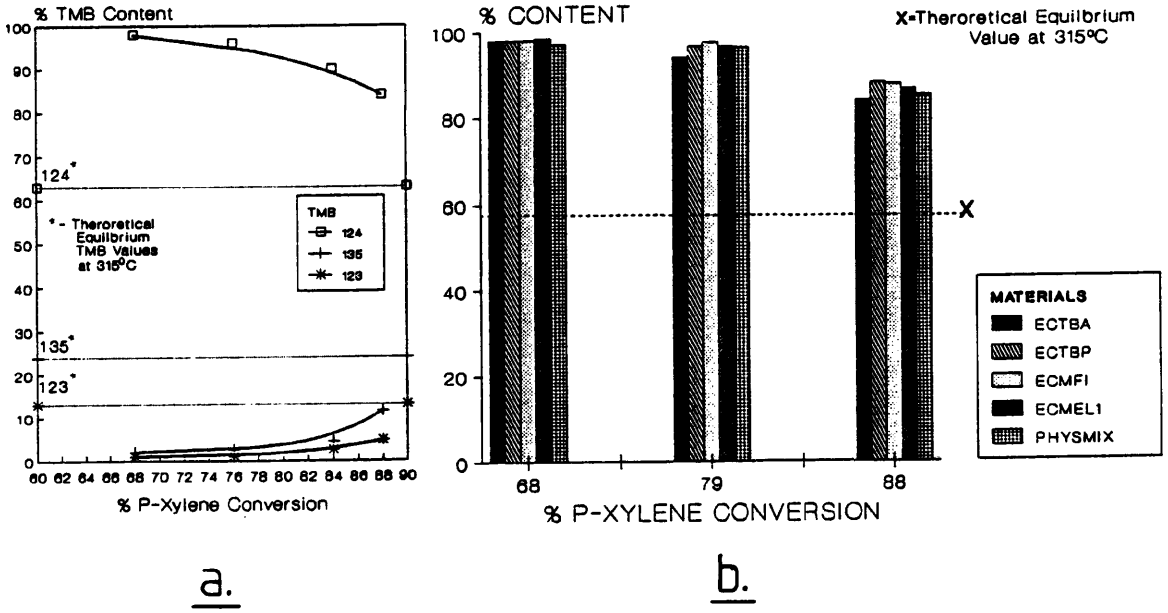


**Figure 5.32. Representations of the non-equilbrium TMBs yeild with respect to p-xylene conversion a. the TMB product distribution with ECMEL and b. percentage 1,2,4TMB content with respect to p-xylene conversion for each catalyst.**

Due to marked differences in the shape-selective properties of the catalysts an estimate of the phase purity was calculated. This was based on the *global* C10, C9 and C8 product distributions at 80% p-xylene conversion. The results are illustrated in Figure 5.37. The estimated intergrowth content, from these data for ECTBP and ECTBA, is between 75-90% and 8-20%, respectively. These

results compare reasonably well with the XRD data reported in section 5.31. This suggests that studies of shape-selective catalysis can be used as a criterion to determine phase purity.

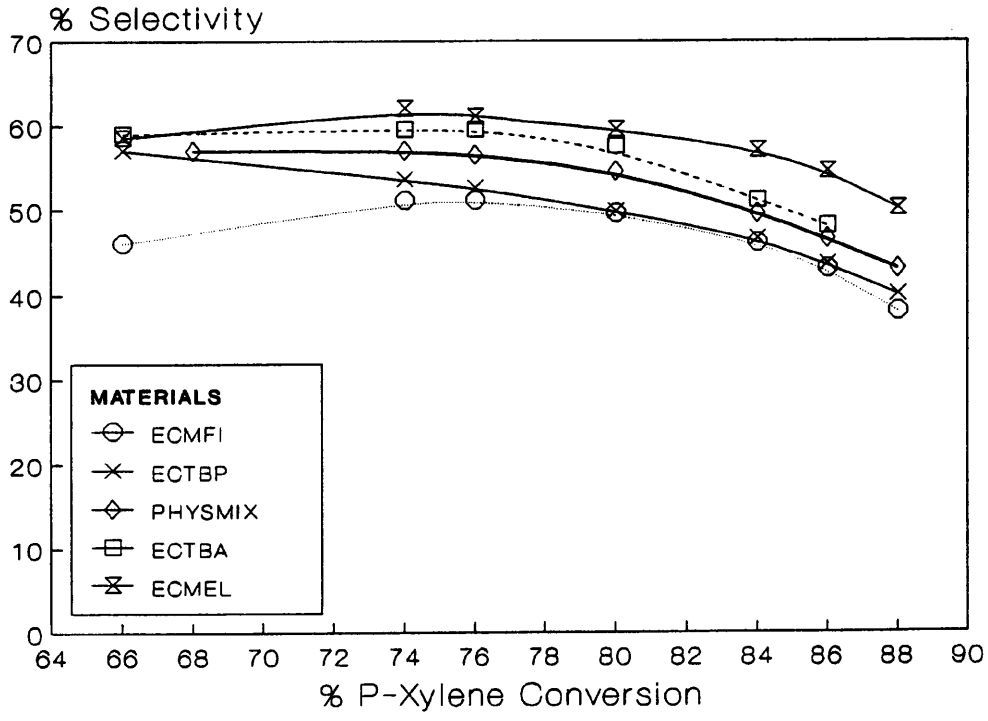


**Figure 5.33. Comparison of 1,2,4-TMB selectivity of each zeolite.**

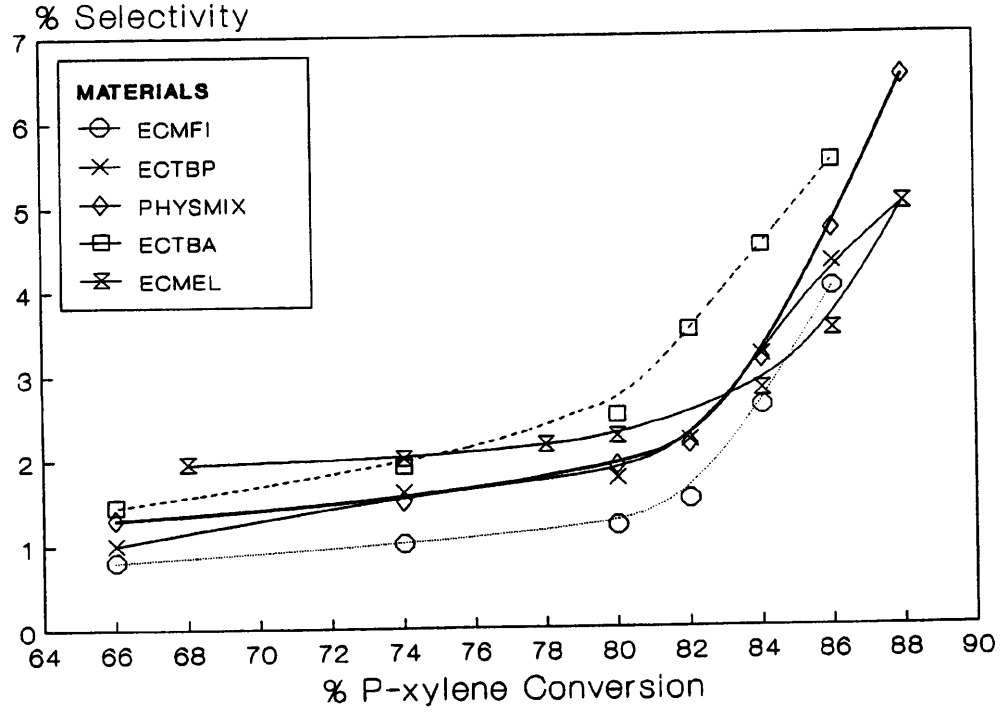


**Figure 5.34. Comparison of 1,3,5- and 1,2,3-TMB selectivity of each zeolite.**

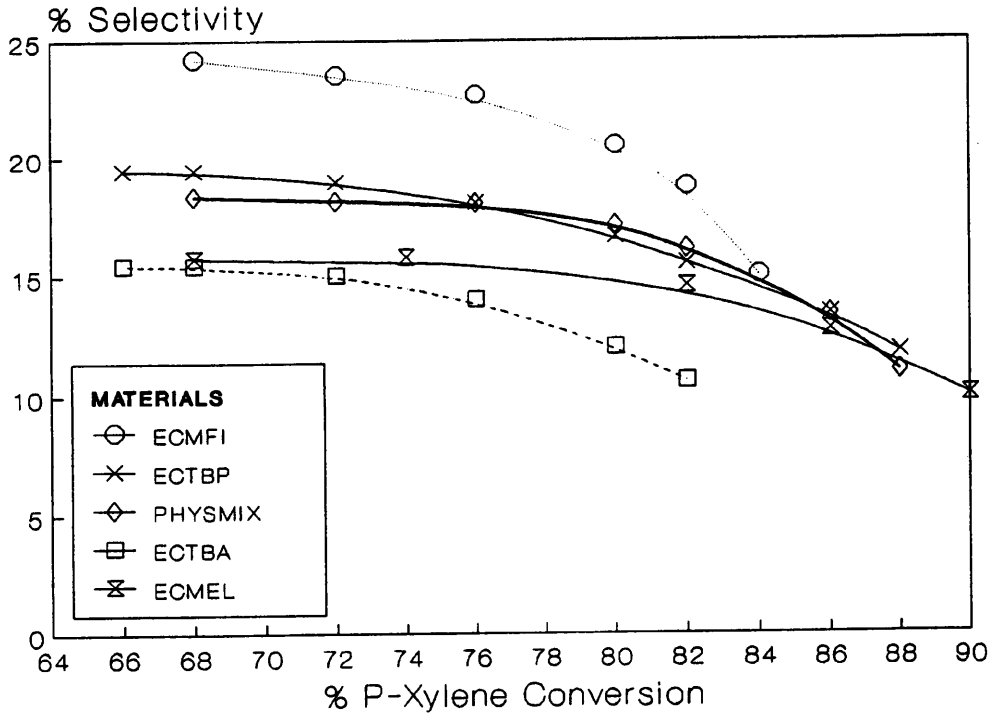


**Figure 5.35. Percentage product selectivity of 1,2,4,5-TEMB.**

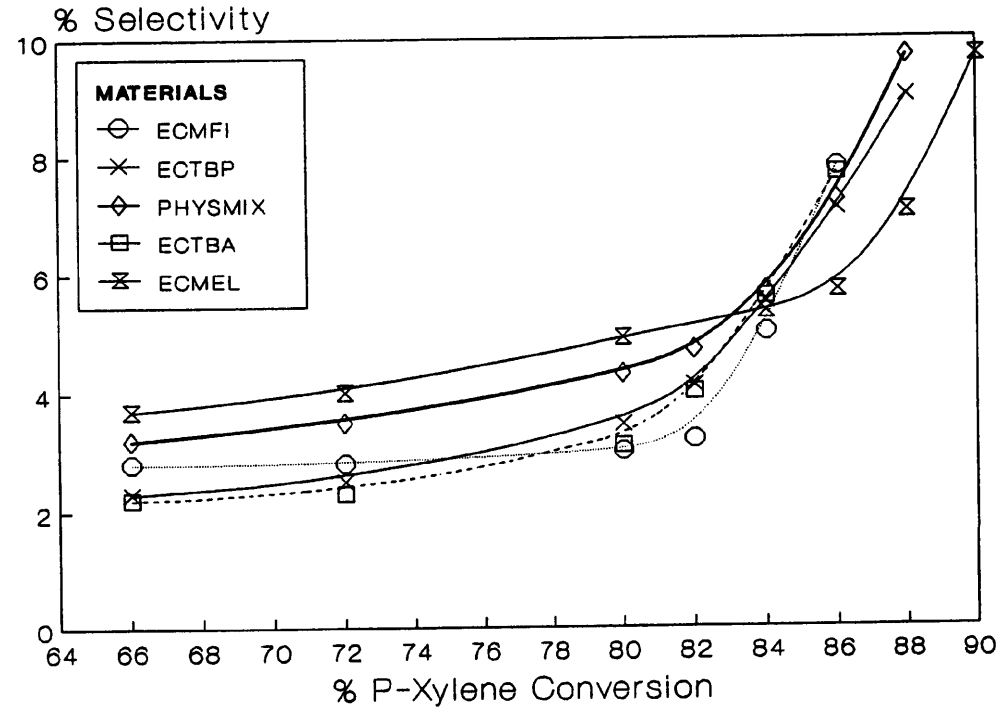


**Figure 5.36. Percentage product selectivity of 1,2,3,4- and 1,2,3,5-TEMB.**

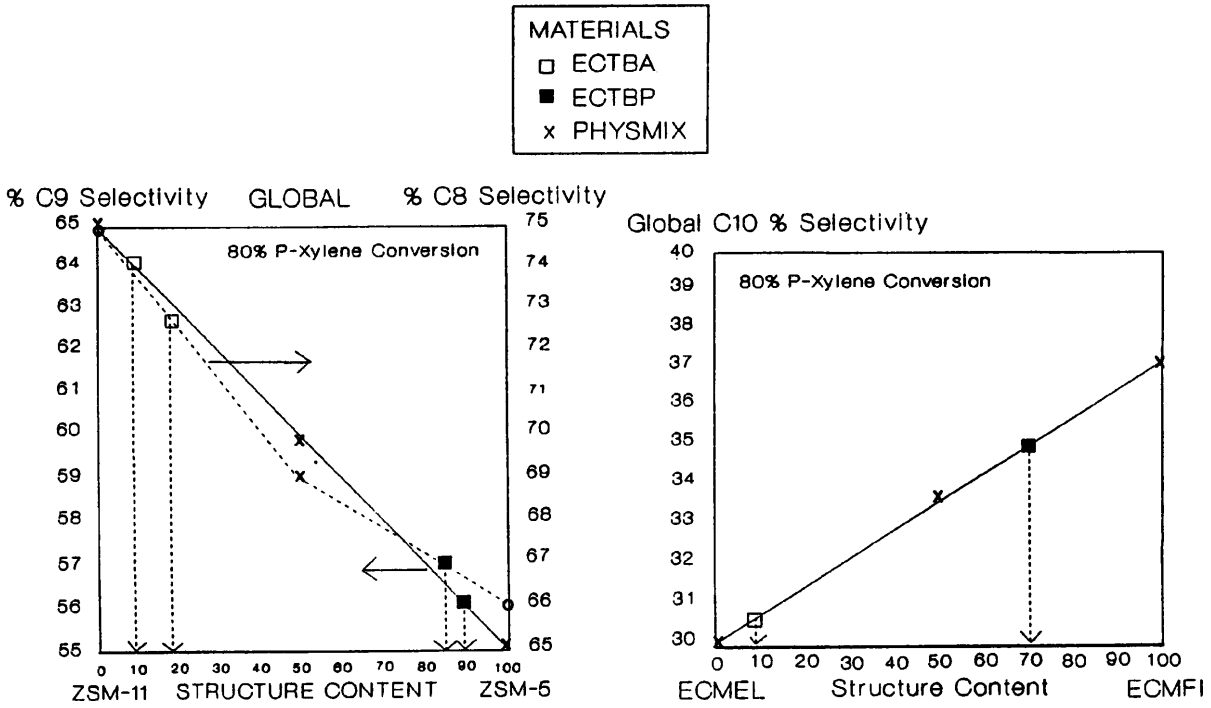


**a. Global C8 and C9.** **b. Global C10**

**Figure 5.37. Estimation of phase purity based on the global product distributions.**

The TMB and TEMB products arise primarily from the direct alkylation on the benzene ring of the xylene molecule. In addition, TMB and toluene are also formed during xylene disproportionation via the transalkylation process [25] as illustrated in Figure 5.38. The theory of *molecular traffic control* [16] was used to explain the enhanced selectivity to mono- and dialkylation in ZSM-11 over ZSM-5. The model predicts that the larger free volume at some channel intersections with more relaxed steric constraints in ZSM-11 enhances the probability of a reactive collision between a xylene molecule and a methanol molecule. However, it seems unlikely that a reactant and product molecules are able to follow a preferred diffusive pathway [32].

A correlation between selectivity and intra-crystalline free space can be readily accounted for in terms of the mechanisms involved. Disproportionation of xylene involves a large diphenylmethane-type intermediate as shown in Figure 5.38. It is

suggested that this intermediate can form more readily in some of the less sterically strained cavities available in ZSM-11, but not in ZSM-5. Consequently, in the more restricted and tortuous environment of ZSM-5 the products of xylene alkylation experience a longer residence time, which allows for dealkylation and isomerisation processes to occur until a more rapidly diffusing product is formed.

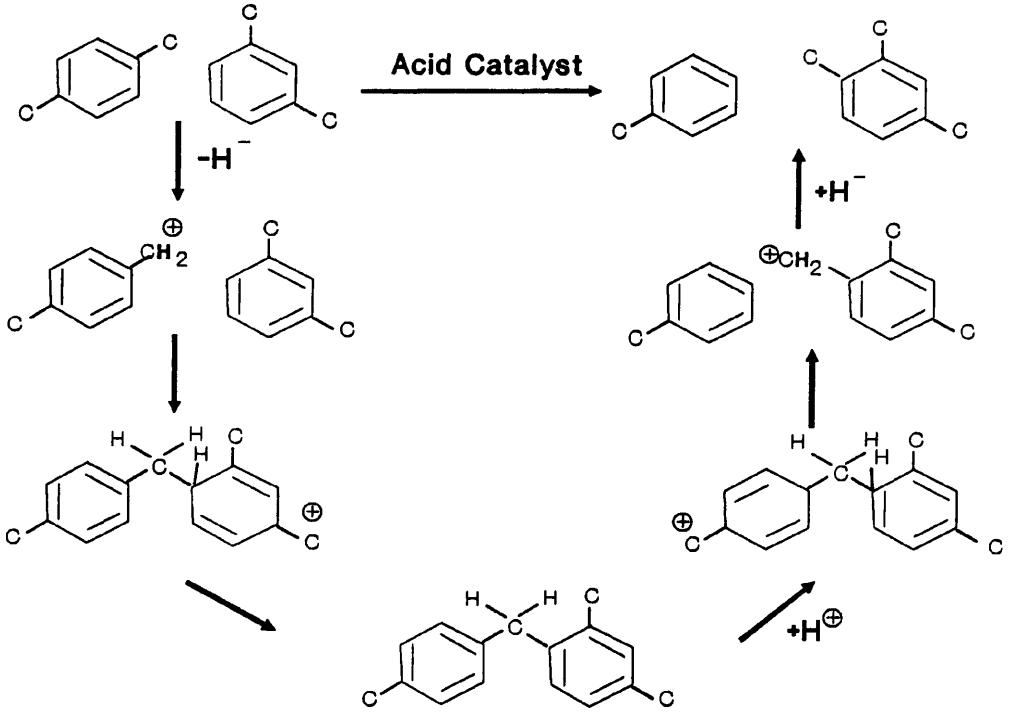


**Figure 5.38. The proposed acid catalysed xylene disproportiontion mechanism [24].**

The selectivity and product distribution of the aromatic ethylated products ie. dimethylethylbenzene (DMEB) and ethyltoluene (ET), were a more sensitive probe for distinguishing structural differences. For example, in contrast to ECMEL, a significantly larger selectivity for ethyl-substituted aromatics was obtained over ECMFI. This is revealed in Figure 5.39.

More noticeable, ECTBA and ECTBP showed the highest selectivity to the aromatic methylethyl derivatives. The largest single ethylated product was 1,2-dimethyl-4-ethyl benzene as illustrated in Figure 5.40 and Table 5.3. This high selectivity suggests that the distribution of the ethyl derivatives cannot be accounted for by a non-shape-selective external crystal surface.

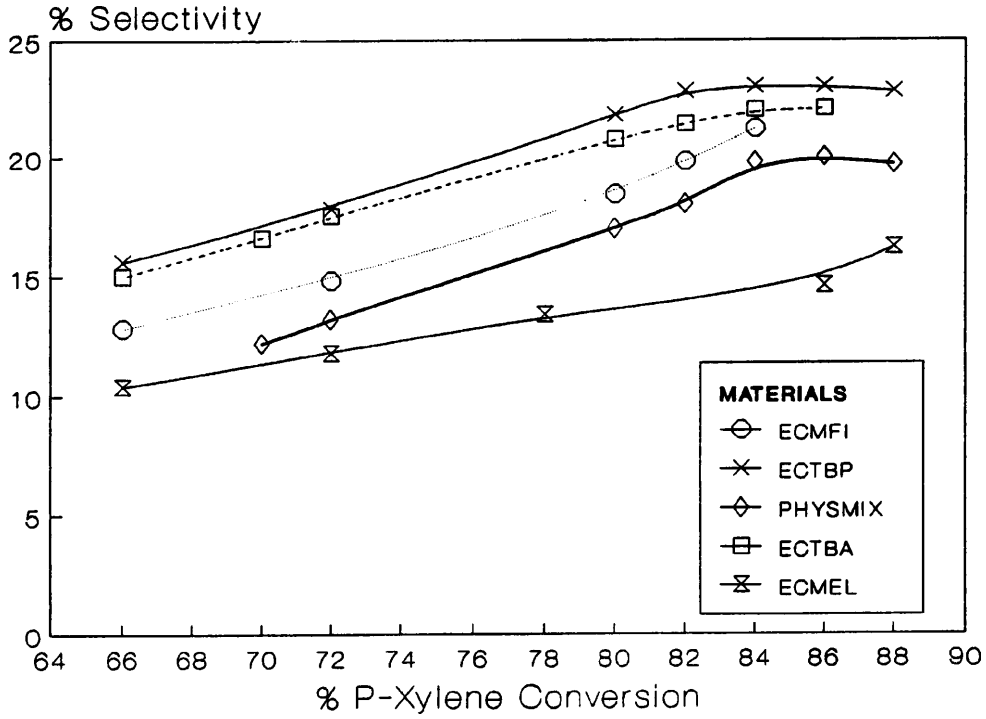


**Figure 5.39. Selectivity of catalysts to aromatic ethylated products.**

Classically, benzene ring alkylation takes place on the acidic site, while side-chain alkylation by methanol requires basic sites [34]. Quantum calculations have revealed that the latter process occurs more favourably by the simultaneous action of basic and acidic sites in a well defined configuration such as the restricted environment in ZSM-5 [35]. It is more likely that a protonated xylene, rather than a free methonium ($+CH_3$) species, is involved in the alkylation process because of the relative carbenium ion stabilities [36]. The aromatic carbenium ion is of greater stability due to inductive effects imposed by the benzene ring.

It is difficult to explain the enhanced DMEB selectivity of ECTBA and ECTBP without further catalytic studies. The shape-selective behaviour of ECTBP was very similar to that of ECMFI apart from its enhanced selectivity to DMEB. XRD and electron microscopy studies revealed that ECTBP is a physical mixture of ZSM-5 and ZSM-11. Therefore, the selectivity differences are not due to structural anomalies such as intergrowths.

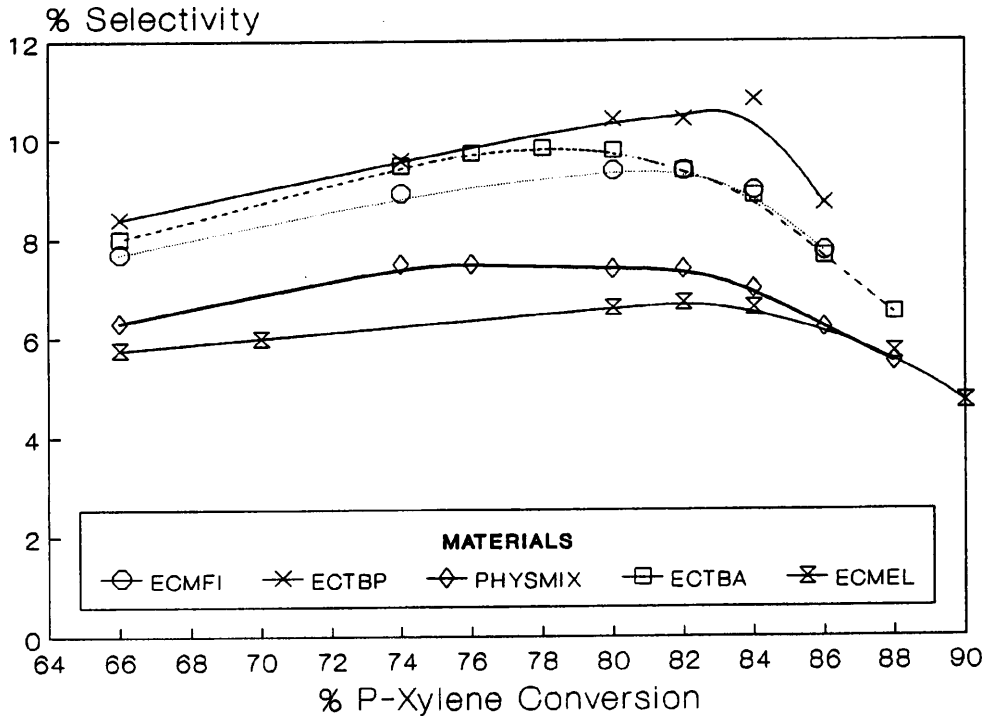


**Figure 5.40. Product selectivity of the catalysts to 1,2-dimethyl-4-ethylbenzene.**

ECTBP and ECMFI were synthesised using tetrabutylphosphonium bromide and diaminohexane, respectively. Chemical analysis of the calcined and ammonium form of both materials revealed that all the organic additive had been removed from the ECMFI. In contrast, an amount of residual phosphorus (1.0% mol/wt) was present in ECTBP. The addition of modifiers such as magnesium, boron and phosphorus is known to affect the selectivity, acidity, diffusive and coking properties [37] of zeolite catalysts. The phosphorus content of ECTBP is significant and may well play a role in the shape-selective properties of the sample ECTBP.

There are no reports on the catalytic shape-selective properties of known intergrowth materials. Consequently, it is difficult to predict the behaviour of ECTBA. Most of the shape-selective properties ECTBA were equivalent to a ZSM-11 rich physical mixture. However, the selectivity in ECTBA to C10 products was noticeably lower, while it was higher to 1,2,4-TMB and 1,2-dimethyl-4-ethyl benzene. It is possible that a disrupted or intergrown framework inhibits the diffusion of the bulkier C10 isomers.

Such effects would favour dealkylation and disproportionation processes. Alternatively, the coking mechanism associated with intergrowths may be very different to the structurally pure materials. This would alter both their acidic and shape-selective properties.

A difference in the catalytic activity of the regenerated ECTBA catalyst compared to the other samples was found. Figure 5.41 shows the conversion of p-xylene (315°C, WHSV=6.0hr$^{-1}$) with respect to time-on-stream for all the materials. ECMEL, ECMFI and ECTBP all follow the same deactivation path and after an initially high activity assume a fairly constant p-xylene conversion between 5-25%. In contrast ECTBA remains at a higher p-xylene conversion (>30%) for most of the run. This suggests that the coking processes occurring in ECTBA are dissimilar to coke lay-down in the other materials.

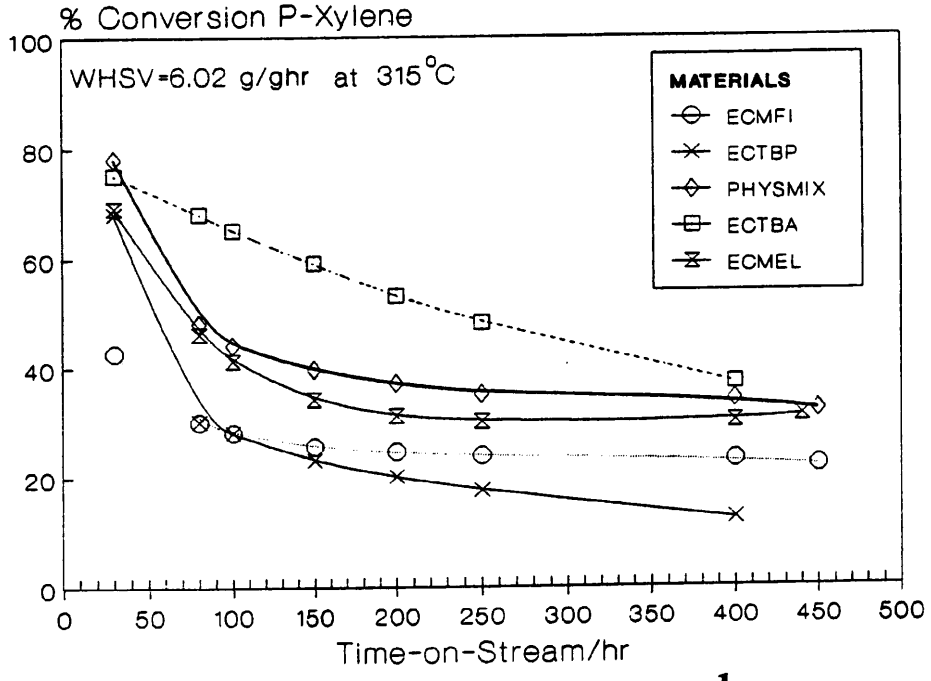


**Figure 5.41. Conversion of p-xylene at 315°C(WHSV=6hr$^{-1}$) on the regenerated catalysts.**

Both the pyridine and hydrogen *in-situ* FTIR studies revealed that the Brφnsted and Lewis acidty of the materials was equivalent. The TEM studies highlighted the multi-crystalline nature of the zeolites consisting of similarly sized aggregated crystals. However, there are several subtle differences in the crystalline nature of the materials which are summarised in the following.

1. The aggregates associated with ECTBP and ECTBA were composed of regularily aligned crystallites while ECMFI and ECMEL were more random in nature.
2. There was a significant amount of small single crystals associated with ECMEL and ECTBA.
3. Electron diffraction studies showed a marked range of inter- and intra-crystalline intergrowth content of ECTBA, while in ECMEL the intergrowth variation and content was small.

Most observations reported by other workers concern the effects of crystal size, rather than orientation on the shape selectivity of zeolites [38]. The size of the crystals effects the ratio of outer to the inner acid sites. The physically random or regular nature of the crystalline aggregates will alter the inter- and intra-crystalline diffusional properties of the zeolites. As a result, the acidic and shape-selective properties will be affected. This further complicates the interpretation of the catalytic results. Consequently, without further studies only these suggestions can be given to explain these data.

The study stresses the sensitivity of catalysis as a method of detecting subtle structural effects on shape-selective properties. Moreover, these results show that intergrowths cannot be assumed to behave as physical mixtures.

## 5.4. Conclusions

Only by using a variety of analytical techniques was the structural nature of ZSM-11, ZSM-5 and intergrowth materials distinguished. XRD proved a semi-quantitative technique in estimating the phase purity. However, XRD results cannot distinguish intergrowth structures from physical mixtures and there is a limit to which phase purity can be determined.

Qualitatively, electron microscopy was demonstrated to be a very useful tool in identifying the structural content of pure and intergrown materials. Physical mixtures were readily distinguished from intergrown materials which related to the morphology and polycrystallinity of the samples. These data also assisted in the interpretation of the

catalysis results. Electron diffraction data revealed that ECTBA was composed of material with a range of intergrowth content. In contrast to the conclusion suggested x-ray analysis, electron diffraction showed ECMEL was not purely composed of ZSM-11, but was also associated with small regions of intergrowth of ZSM-5 in ZSM-11. Intergrowths were also discernible to the eye on the HREM images. Adjacent areas of i and σsymmetry were observed by studying the arrangement of the interchannel pore systems.

Sorption studies revealed that intergrowth materials had intermediate behaviour to end members for the uptake to m-xylene. The study was not comprehensive, but showed that the structural differences altered the relative up-take of the sorbate.

Independent of their structures the materials had an showed similar Brφnsted and Lewis acidity. Therefore their catalytic behaviour could be based on their shape-selectivity in the alkylation of p-xylene with methanol. Xylene isomerisation and alkylation was favoured on ZSM-11 rather than ZSM-5 type materials. This is a function of the spatial requirements of the intermediate species and the larger pore volumes experienced at some intersections in ZSM-11. The intergrowth content was estimated using the selectivity of the materials from a range of alkylated products. In this respect the selectivity of the intergrowth compared well to the physical mixture.

In agreement with previous work [16], this catalytic study revealed that in contrast to ZSM-11, ZSM-5 type materials show a higher selectivity to ethylated products. This relates to the geometric and stability requirements of the intermediate species. Although no unique reaction products were associated with the intergrown sample ECTBA, together with ECTBP, an unpredictable selectivity to certain ethylated products was noticed. Such behaviour probably relates to their diffusional characteristics. For the physical mixture (ECTBP), this may be related to the polycrystallinity or chemical modification of the material. The diffusional characteristics of the intergrowth sample (ECTBA), may relate to differences in both inter- and intra-crystallinity. These results highlight the sensitivity of catalysis as a method to differentiate the structural characteristic of zeolites.

## REFERENCES


1. G.T.Kokotailo & W.M.Meier, *Chem.Soc.Spec.Publ.*, **33**, 133 (1980)

2. P.A.Jacobs & J.A.Martens in *Synthesis of High-Silica Aluminosilicate Zeolites*, Stud.Surf.Sci.Catal.No.33, (Publ. Elsevier) 180 (1987)

3. C.Li-feng, T.Waker & L.V.C.Rees, *J.Chem.Soc.Farad.Trans.1*, **85**, 33 (1989)

4. P.A.Jacobs & J.A.Martens, *Pure Appl.Chem.*, **58** No.10, 1329 (1986)

5. J.A.Martens, M.Tielen, P.A.Jacobs & J.Weitkamp, *Zeolites*, **4**, 98 (1984)

6. H.W.Zanbergen & D.van Dyck in *Zeolites: Facts, Figures, Future*. Proc.8th Int. Zeolites Conf., (Eds.Jacobs & van Santen, Elsevier) Amsterdam, The Netherlands 599 (1989)

7. C.A.Fyfe, G.T.Kokotailo, G.J.Kennedy & C.De Shutter, *J.Chem.Soc.Chem. Commun.*, 306 (1985)

8. S.A.Ramdas. B.P. Research, unpublished work.

9. *Methods and Practices in X-Ray Powder Diffraction*, JCPDS, Ed.R.Jenkins (1990)

10. G.Thomas & M.J.Goringe in *Transmission Electron Microscopy of Materials*, (Publ.J.Wiley & Sons, 1979)

11. A.Wright, UMIST, unpublished results

12. M.A.O'Keefe & P.R.Buseck, *Nature*, **274**, 322 (1978)

13. J.H.C.Hoof & J.W.Roelofsen in *Introduction to Zeolite Science and Practice*, Stud.Surf.Sci.Catal.No.**58**, (Eds.van Bekkum, Flanigen & Jansen, Elsevier) chpt.7 (1991)

14. V.B.Kazansky in *Structure and Reactivity of Modified Zeolites*, Stud.Sur.Sci. Catal. No.**18**, (Eds.Jacobs, Jaeger, Jiru, Kazansky & Schulz-Ekloff, Elsevier) 61 (1984)

15. N.Thompson, Ph.D Thesis, UMIST (1991)

16. E.G.Derouane, P.Dejaifve & Z.Gabelica, *J.Chem.Soc.Disc.Farad.Soc.*, **72**, 331 (1981)

17. J.B.Higgins, R.B.La Pierre, J.L.Schlenker, A.C.Rohrman, J.D.Wood, G.T.Kerr & J.Rohrbaugh, *Zeolites*, **8**, 446 (1988)

18. M.M.Treacy & J.M.Newsam, *Nature*, **332**, 249 (1988)

19. G.A.Jablonski, L.B.Sand & J.A.Gard, *Zeolites*, **6**, 398 (1986)

20. M.M.Treacey. *BZA Conf.*, Durham, plenary lecture (1991)

21. G.R.Millward, S.Ramdas, J.M.Thomas, *J.Chem.Soc.Farad.Trans.2*, **79**, 1075 (1983)

22. O.Terasaki, J.M.Thomas & S.Ramdas, *J.Chem.Soc.Chem.Commun.*, 216 (1984)

23. J.M.Thomas & G.R.Millward, *J.Chem.Soc.Chem.Comm.*, 1382 (1982)

24. D.H.Olson & W.O.Haag in *Catalytic Materials:Relationship Between Structure and Reactivity*, (Eds.Whyte, Dalla Betta, Derouane & Buker) ACS Sym.**248**, 275 (1983)

25. L.V.C.Rees & J.Dwyer, *Chem.Ind.*, **7**, 252-269 (1984)

26. K.Foger, J.V.Sanders & D.Seddon, *Zeolites*, **4**, 337 (1984)

27. G.Qin, L.Zheng. Y.Xie & C.Wu, *J.Catal.*, **95**, 609 (1985)

28. V.B.Kazansky, L.M.Kustov & V.Y.Borokov, *Zeolites*, **3**, 77 (1983)

29. A.Auroux, V.Bolis, P.Wierzchowski, P.Gravelle & J.Védrine, *J.Chem.Soc.Farad. Trans.1*, **75**, 165 (1979)

30. N.Y.Topsoe, K.Pedresen & E.G.Derouane, *J.Catal.*, **70**, 41, (1981)

31. A.S,Medin, V.Yu.Borovkov, V.B.Kazansky, A.G. Pelmentschikov & G.M. Zhidomirov, *Zeolites*, **10**, 668 (1990)

32. A.K.Nowak, private commun., (KSLA, Amsterdam 1991)

33. P.Dejaifve, A.Aurdoux, P.C.Védrine, Z.Gabelica & E.G.Derouane, *J. Catal.*,**70**, 123 (1981)

34. Y.Ono in *Catalysis by Zeolites*, Stud.Sur.Sci.Catal.No.**5**., (Eds.Imelik, Naccache, Ben Taarit, Védrine, Coudurier & Praliand, Elsevier) 19 (1980)

35. H.Itoh, A.Miyamoto & Y.Murakami, *J.Catal.*, **64**, 248 (1980)

36. P.Sykes, *A Guide to Mechanisms in Organic Chemistry*, 4th Edn. (Publ.Longmann,1985)

37. L.B.Young, S.A.Butter & W.W.Kaeding, *J.Catal.*, **76**, 418 (1982)

38. H.J.Doelle, J.Heering & L.Riekert, *J.Catal.*, **71**, 27 (1981)

# CHAPTER 6.

## Future Work

This work has been concerned with the synthesis and characterisation of high-silica zeolites. In particular the role of the organic additive during zeolite synthesis was investigated. Chapter 3 describes how the structure-directing properties of DAO can be modified by altering the reaction conditions. Synthesis variables such as the reaction temperature, the gel pH and aluminium content, the nature of the silica source and the $M^+$ ion affected both the reaction rates and phase development. The chemical and physical nature of DAO was dependent upon the structure and composition of the frameworks synthesised.

Further research should involve a more in depth study following the involvement of DAO in the gel phase, in the nucleation process and its incorporation into the pore system of the zeolite. This could be assessed using a combination of $^{29}Si$, $^{27}Al$, $^{13}C$ and $^{15}N$ solution and MAS NMR. An interesting line of investigation would be to detect at what stage in the reaction protonation of the diamine occurs and how such protonation relates to the incorporation of aluminium into the framework or to the development of defect sites.

In this study the chemical and physical nature of DAO sited in several pore systems of zeolites was investigated using CP-MAS NMR. However, the influence of the $M^+$ ions on the chemical shift and multiplicity of the resonances was not fully evaluated. DAO was shown to be a useful organic additive as a range of zeolites were synthesised with and without the presence $M^+$ ions in the reaction gel. Therefore a comprehensive $^{1}H$, $^{13}C$, $^{15}N$ and $^{23}Na$ MASNMR study of all these *as-made* zeolites would be of use in determining the pore-filling character of DAO.

Chapters 4 and 5 discussed the synthesis and characterisation of pentasil and related intergrown materials. The dependence of phase purity and intergrowth content was related to the nature of the organic additive and the reaction temperature. Recently, den Ouden et al.[1, 2], discussed the interactions of an occluded TMA molecule in a

sodalite cage. The molecule was shown to be mobile within the sodalite cage. These findings differ from the classical approach to *templating*, where the organic additive is seen as fixed within the zeolite pore system. Such mobility of the incorporated organic additive may be related to the formation of framework defects such as intergrowths. In this respect, two complementary methods for studying the interactions of organic material with zeolites are Molecular Dynamics and solid state $^{2}H$ and $^{13}C$ CP-MAS NMR [1,3,4]. With the correct choice of parameters Molecular dynamics offers a theoretical appraisal to framework-*template* interactions and CP-MAS NMR studies show very detailed information concerning the molecular mobility of organic materials.

The difficulties in distinguishing physical mixtures of ZSM-5 and ZSM-11 from intergrowths was discussed at length in Chapter 5. Only with a combination of analytical techniques was the structural content of the materials fully assessed. In future studies it would be useful to develop a synthesis method from which zeolites of varing intergrowth content with the same composition are predictably synthesised. This approach requires the synthesis of zeolites using a range of gel compositions and reaction temperatures using TBP, TBA, BAPZ and DAO as the organic additive. Furthermore, in order to assist in their analysis, the crystals synthesised should have uniform dimensions, greater than 10μm, and have a regular morphology e.g. tablet-like. Consequently, such materials would be more readily characterised by sorption, catalysis and microscopy.

In this study the diffusional characteristics of the pentasils was only briefly assessed. Future work should involve an assessment of the kinetic diffusivity of these materials. This requires a careful determination of the rate of uptake of a range of sorbates with varying dimensions. Consequently, diffusional differences between physical mixtures and intergrowths may become apparent. The shape-selectivity of these catalysts was addressed in this work using the methylation of p-xylene as a test reaction at high p-xylene conversions. However, it may prove more useful to investigate shape-selectivity at lower conversion (< 10%). Under such conditions the primary products of the reaction should relate more to the structural environment in which they were produced. Alternatively, the generation of coke within and at the surface of a zeolite is

directly related to its diffusional properties. Further work might involve an investigation into the composition of the external and internal coke products of pure and intergrown pentasils.

The electron microscopy was shown to be an accurate method in distinguishing the structural nature of several pentasil materials. These studies could be extended in several ways. By recording the electron diffraction patterns of gel samples throughout the synthesis period it may be possible to follow intergrowth development during crystallisation. A follow-up to this experiment would be to use the scanning tunnelling electron microscopy (STEM). This technique offers a method of estimating the chemical content of individual crystals. Consequently, the relationship between chemical and structural composition could be investigated.

## REFERENCES

1. C.J.J.Ouden, K.P.Datema, F.Viser, M.Mackay & M.F.M.Post, *Zeolites*, in press (1991)

2. C.J.J.Ouden, Ph.D Thesis (Uni.Eindhoven, 1991)

3. S.Hayashi, K.Suzuki & K.Hayamizu, *J.Chem.Soc.Farad.Trans.*, **85**(9), 2973 (1989)

4. A.J.Vega & Z.Lutz, *Zeolites*, **8**, 19 (1988)

## APPENDIX I

### Calculation of Reaction Stoichiometry and the Initial $OH^-/SiO_2$ Ratio

It is convenient to represent zeolite synthesis compositions in terms of reaction stoichiometries, these are conveniently expressed in terms of oxides. To fully illustrate the derivation of the reaction stoichiometry and the initial $OH^-/SiO_2$ ratio the calculations for gel preparation 4.21 are highlighted.

| Ingredients | Weights/g | Mol. Weights/g |
|---|---|---|
| $Al(NO_3)_3.9H_2O$ | 16.20 | 375.14 |
| Colloidal Silica (40% wt/wt) | 192.00 | 60.09 |
| BAPZ | 64.98 | 200.33 |
| NaOH | 20.52 | 40.00 |
| $H_2O$ | 512.00 | 18.00 |
| $HNO_3$ (70% wt/wt) | 20.83 | 63.01 |

The respective molar amounts can be represented in a tabular form.

| | $Al^{3+}$ | $SiO_2$ | BAPZ | $Na^+$ | $H_2O$ |
|---|---|---|---|---|---|
| $Al^{3+}$ | 0.0432 | – | – | – | 0.3888 |
| $SiO_2$ | – | 1.2781 | – | – | 6.4200 |
| BAPZ | – | – | 0.3244 | – | – |
| $Na^+$ | – | – | – | 0.5130 | – |
| $H_2O$ | – | – | – | – | 28.8888 |
| $HNO_3$ | – | – | – | – | 0.3480 |
| Total | 0.0432 | 1.2761 | 0.3244 | 0.5130 | 36.0449 |

Normalising the molar content with respect to Al;

| Al | Si | BAPZ | Na | $H_2O$ |
|---|---|---|---|---|
| 1.0 | 29.6 | 7.5 | 11.9 | 834.4 |

and this can be formally represented by the oxide stoichiometry:

$$Al_2O_3 - 59.2SiO_2 - 15.0(BAPZ)_2O - 11.9Na_2O - 1668.8\ H_2O$$

To calculate the initial $OH^-/SiO_2$ ratio it assumed that:

$$Al(NO_3)_3 + 2H_2O \text{ ----------} \rightarrow AlO_2^- + 3HNO_3 + H^+$$

each $Al(NO_3)_3$ liberates an equivalent of $4H^+$. For this particular example the total number of $OH^-$ can be calculated by summing:

- moles ex. $Na^+OH^-$ = 0.5130
- moles ex. $Al(NO_3)_3$ = - (4 x 0.0432) = - 0.1728
- moles ex. $HNO_3$ = -0.2314

therefore the total moles of $OH^-$ = 0.513 - (0.1728+0.2314)

= 0.1088

and the initial $OH^-/SiO_2$ ratio = 0.1088/1.2781 = 0.09

# APPENDIX II

## Unit Cell Calculations

Chemical analysis gives data concerning the elemental chemical composition of a zeolite in terms of weight percent (wt%). A typical calculation for the unit cell content of ZSM-11 can be summarised as follows. Table III.1 lists the elemental composition of *as-made* ZSM-11 synthesised with DAO in terms of weight and mole percents.

| | ELEMENT | | | | |
|---|---|---|---|---|---|
| | Si | Al | Na | C | N |
| WT % | 37.9 | 0.9 | 0.1 | 7.8 | 1.9 |
| MW | 28.0 | 27.0 | 23.0 | 12.0 | 14.0 |
| MOLE % (WT%/MW) | 1.35 | 0.03 | 0.004 | 0.65 | 0.14 |

**Table III.1. Elemental composition of *as-made* ZSM-11**

The relevent molar ratios for this sample are:

1. Si/Al=1.35/0.03=45.0
2. C/N=0.65/0.15=4.3
3. $Na^+$/Si=0.004/1.35=0.003
4. $Na^+$/Al=0.004/0.03=0.13
5. DAO/Si=(0.54/8)/1.35=0.05

The C/N ratio is near the theoretical value of 4, consequently DAO can be assumed in tact. The DAO/Si ratio takes into account the eight carbon of the diamine chain. There are 96 T-atoms per unit cell of ZSM-11. The number of Si T-atoms per unit cell of ZSM-11 is,

$$Si(T) + Al(T) = 96.$$

Using the Si/Al molar ratio,

a. $Si + Si/45 = 96$
b. $45Si + Si = 4320$
c. $Si = 4320/46 = 93.9$

this shows ZSM-11 consists of 93.9 Si and 2.1 Al T-atoms.

Using the $Na^+$/Si molar ratio the number of $Na^+$ species per unit cell of ZSM-11 is,

a. $93.9 \times 0.003 = 0.3$

Similarily using the DAO/Si molar ratio, the number of DAO molecules per unit cell of ZSM-11 is

a. $93.9 \times 0.05 = 4.7$

ZSM-11 contains 0.3 Na puc and 4.7 intact DAO molecules per unit cell.

# APPENDIX III

## Literature X-Ray Diffraction Data

Unless otherwise stated the following information was taken from Collected Simulated X-ray Diffraction Patterns published under the authorsis of the IZA.

## TON Diethylamine Theta-1

COMPOSITION: $Si_{24}O_{48}(C_2H_5)_2NH$
Synthetic

CRYSTAL DATA: Orthorhombic Cmc2$_1$ (36)
a = 13.859 b = 17.420 c = 5.038
α = 90.00 β = 90.00 γ = 90.00
X-ray single crystal refinement Rw = 0.056

REFERENCE: B. Marler
Zeolites 7, 393-397 (1987)

| 2θ | d | I rel | h | k | l | 2θ | d | I rel | h | k | l | 2θ | d | I rel | h | k | l |
|---|---|---|---|---|---|---|---|---|---|---|---|---|---|---|---|---|---|
| 8.15 | 10.845 | 100.0 | 1 | 1 | 0 | 30.43 | 2.937 | 2.2 | 3 | 3 | 1 | 45.37 | 1.998 | 1.7 | 0 | 8 | 1 |
| 10.16 | 8.710 | 22.6 | 0 | 2 | 0 | 30.80 | 2.903 | 2.6 | 0 | 6 | 2 | 47.81 | 1.903 | 2.3 | 0 | 6 | 2 |
| 12.78 | 6.930 | 23.3 | 2 | 0 | 0 | 31.89 | 2.806 | 0.6 | 1 | 5 | 1 | 48.59 | 1.874 | 4.8 | 7 | 3 | 0 |
| 16.35 | 5.423 | 9.9 | 2 | 2 | 0 | 32.18 | 2.782 | 1.4 | 3 | 5 | 2 | 48.77 | 1.867 | 0.5 | 3 | 5 | 2 |
| 16.55 | 5.356 | 1.1 | 1 | 3 | 0 | 32.72 | 2.737 | 2.6 | 5 | 1 | 0 | 49.44 | 1.844 | 0.7 | 4 | 8 | 0 |
| 19.43 | 4.569 | 6.4 | 1 | 1 | 1 | 33.02 | 2.713 | 1.8 | 4 | 2 | 1 | 49.76 | 1.832 | 0.8 | 7 | 1 | 1 |
| 20.35 | 4.361 | 49.3 | 0 | 2 | 1 | 35.64 | 2.519 | 9.3 | 0 | 0 | 2 | 51.17 | 1.785 | 2.8 | 3 | 9 | 0 |
| 20.39 | 4.355 | 8.7 | 0 | 4 | 0 | 35.69 | 2.516 | 2.6 | 0 | 8 | 1 | 52.07 | 1.756 | 0.6 | 7 | 3 | 1 |
| 24.11 | 3.691 | 6.2 | 2 | 2 | 1 | 36.62 | 2.454 | 1.6 | 1 | 1 | 2 | 52.88 | 1.731 | 1.0 | 4 | 8 | 1 |
| 24.14 | 3.687 | 9.7 | 2 | 4 | 0 | 36.91 | 2.435 | 6.7 | 3 | 5 | 1 | 53.89 | 1.701 | 0.7 | 6 | 6 | 1 |
| 24.26 | 3.670 | 38.6 | 1 | 3 | 1 | 37.39 | 2.405 | 1.9 | 5 | 1 | 1 | 55.07 | 1.668 | 0.7 | 4 | 6 | 2 |
| 24.63 | 3.615 | 31.3 | 3 | 3 | 0 | 37.68 | 2.388 | 1.2 | 4 | 4 | 1 | 55.75 | 1.649 | 1.3 | 0 | 2 | 3 |
| 25.71 | 3.465 | 21.3 | 4 | 0 | 0 | 38.06 | 2.365 | 6.0 | 2 | 6 | 1 | 56.50 | 1.629 | 2.5 | 7 | 5 | 1 |
| 26.38 | 3.379 | 1.3 | 1 | 5 | 0 | 40.25 | 2.240 | 1.8 | 5 | 3 | 1 | 57.51 | 1.603 | 1.5 | 2 | 8 | 2 |
| 26.68 | 3.342 | 4.1 | 3 | 1 | 1 | 43.80 | 2.067 | 2.6 | 3 | 3 | 2 | 57.52 | 1.602 | 2.3 | 1 | 3 | 3 |
| 27.06 | 3.296 | 4.5 | 0 | 4 | 1 | 44.51 | 2.036 | 1.5 | 4 | 6 | 1 | 58.74 | 1.572 | 0.5 | 3 | 1 | 3 |
| 27.71 | 3.219 | 1.6 | 4 | 2 | 0 | 44.88 | 2.020 | 1.3 | 1 | 5 | 2 | 58.95 | 1.567 | 0.9 | 0 | 4 | 3 |
| 30.03 | 2.975 | 1.6 | 2 | 4 | 1 | 45.13 | 2.009 | 0.8 | 3 | 7 | 1 | | | | | | |

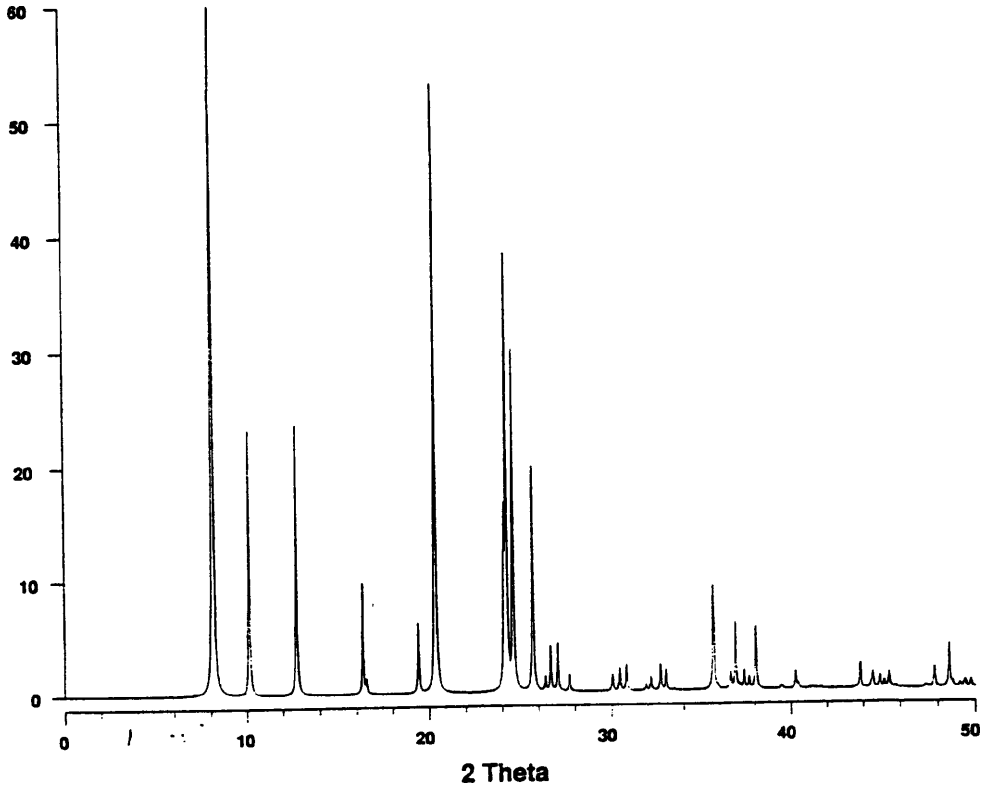

# MFI Calcined ZSM-5

| 2θ | d | I rel | h | k | l | 2θ | d | I rel | h | k | l | 2θ | d | I rel | h | k | l |
|---|---|---|---|---|---|---|---|---|---|---|---|---|---|---|---|---|---|
| 7.93 | 11.153 | 37.1 | -1 | 0 | 1 | 21.82 | 4.074 | 2.1 | 0 | 2 | 3 | 30.64 | 2.918 | 1.0 | 5 | 1 | 3 |
| 7.94 | 11.132 | 100.0 | 0 | 1 | 1 | 22.20 | 4.005 | 2.8 | 3 | 4 | 0 | 31.22 | 2.865 | 1.1 | -2 | 5 | 3 |
| 8.01 | 11.033 | 31.9 | 1 | 0 | 1 | 23.10 | 3.851 | 44.9 | 0 | 5 | 1 | 31.35 | 2.853 | 0.6 | 2 | 5 | 3 |
| 8.80 | 10.054 | 47.8 | 0 | 2 | 0 | 23.19 | 3.836 | 1.0 | 3 | 3 | 2 | 31.55 | 2.836 | 0.6 | -5 | 4 | 2 |
| 8.90 | 9.939 | 51.7 | 2 | 0 | 0 | 23.27 | 3.823 | 16.2 | -5 | 0 | 1 | 32.15 | 2.784 | 0.7 | -7 | 0 | 1 |
| 9.07 | 9.753 | 13.9 | -1 | 1 | 1 | 23.42 | 3.798 | 18.3 | 5 | 0 | 1 | 32.74 | 2.735 | 1.6 | -3 | 6 | 2 |
| 9.14 | 9.673 | 14.1 | 1 | 1 | 1 | 23.69 | 3.756 | 8.2 | -5 | 1 | 1 | 32.88 | 2.724 | 1.2 | 3 | 6 | 2 |
| 9.86 | 8.971 | 1.4 | 1 | 2 | 0 | 23.84 | 3.732 | 10.5 | 5 | 1 | 1 | 33.46 | 2.678 | 1.3 | 0 | 6 | 3 |
| 11.01 | 8.035 | 1.2 | 0 | 2 | 1 | 23.94 | 3.718 | 1.4 | -3 | 0 | 3 | 33.78 | 2.654 | 0.9 | -1 | 0 | 5 |
| 11.88 | 7.450 | 1.1 | -2 | 1 | 1 | 23.98 | 3.711 | 23.1 | 0 | 3 | 3 | 34.34 | 2.612 | 1.6 | -5 | 5 | 2 |
| 12.00 | 7.378 | 0.6 | 2 | 1 | 1 | 24.07 | 3.697 | 0.9 | 5 | 2 | 0 | 34.55 | 2.596 | 1.1 | 5 | 5 | 2 |
| 13.25 | 6.684 | 7.3 | 0 | 0 | 2 | 24.20 | 3.678 | 2.1 | 3 | 0 | 3 | 34.66 | 2.588 | 0.9 | -3 | 7 | 1 |
| 13.96 | 6.343 | 11.0 | 0 | 1 | 2 | 24.35 | 3.656 | 7.6 | -3 | 1 | 3 | 35.16 | 2.552 | 0.6 | -5 | 1 | 4 |
| 14.61 | 6.062 | 0.7 | -1 | 1 | 2 | 24.61 | 3.618 | 8.2 | 3 | 1 | 3 | 35.17 | 2.552 | 0.9 | -1 | 5 | 4 |
| 14.79 | 5.991 | 13.7 | 0 | 3 | 1 | 24.77 | 3.595 | 1.0 | -2 | 5 | 1 | 35.73 | 2.513 | 1.6 | 0 | 8 | 0 |
| 14.85 | 5.964 | 2.7 | -3 | 0 | 1 | 24.82 | 3.587 | 0.5 | 2 | 5 | 1 | 36.15 | 2.485 | 1.1 | 8 | 0 | 0 |
| 14.99 | 5.909 | 4.9 | 3 | 0 | 1 | 25.54 | 3.488 | 1.5 | -2 | 3 | 3 | 36.17 | 2.483 | 1.4 | 0 | 3 | 5 |
| 15.50 | 5.718 | 5.0 | -3 | 1 | 1 | 25.71 | 3.465 | 0.9 | 2 | 3 | 3 | 36.34 | 2.472 | 0.7 | 7 | 4 | 0 |
| 15.63 | 5.669 | 5.0 | 3 | 1 | 1 | 25.80 | 3.454 | 1.0 | 3 | 2 | 3 | 36.36 | 2.471 | 0.6 | -3 | 1 | 5 |
| 15.89 | 5.577 | 2.0 | -2 | 0 | 2 | 25.85 | 3.446 | 3.1 | -3 | 4 | 2 | 37.24 | 2.414 | 1.3 | 0 | 7 | 3 |
| 15.92 | 5.566 | 6.1 | 0 | 2 | 2 | 26.02 | 3.425 | 4.2 | 3 | 4 | 2 | 37.50 | 2.399 | 0.8 | -5 | 6 | 2 |
| 16.02 | 5.532 | 1.3 | 3 | 2 | 0 | 26.22 | 3.399 | 1.2 | -1 | 5 | 2 | 37.63 | 2.390 | 0.9 | -7 | 1 | 3 |
| 16.07 | 5.517 | 1.4 | 2 | 0 | 2 | 26.59 | 3.352 | 0.7 | 5 | 1 | 2 | 37.65 | 2.389 | 0.7 | 3 | 5 | 4 |
| 16.50 | 5.374 | 1.5 | -2 | 1 | 2 | 26.60 | 3.351 | 2.8 | 0 | 6 | 0 | 37.83 | 2.378 | 0.9 | 5 | 3 | 4 |
| 16.66 | 5.320 | 2.0 | 2 | 1 | 2 | 26.91 | 3.313 | 2.7 | 6 | 0 | 0 | 41.45 | 2.178 | 0.7 | 0 | 7 | 4 |
| 17.24 | 5.143 | 0.6 | -2 | 3 | 1 | 27.05 | 3.297 | 5.2 | 0 | 1 | 4 | 45.09 | 2.011 | 3.3 | 0 | 10 | 0 |
| 17.32 | 5.119 | 1.1 | 2 | 3 | 1 | 27.37 | 3.258 | 0.6 | -1 | 1 | 4 | 45.14 | 2.009 | 3.5 | 0 | 8 | 4 |
| 17.64 | 5.027 | 3.6 | 0 | 4 | 0 | 27.44 | 3.251 | 1.1 | 0 | 6 | 1 | 45.22 | 2.005 | 0.9 | -8 | 0 | 4 |
| 17.85 | 4.969 | 5.4 | 4 | 0 | 0 | 27.44 | 3.250 | 0.8 | -5 | 2 | 2 | 45.33 | 2.001 | 1.1 | -8 | 4 | 3 |
| 18.20 | 4.873 | 0.7 | 1 | 4 | 0 | 27.70 | 3.220 | 0.7 | 5 | 2 | 2 | 45.64 | 1.988 | 4.7 | 10 | 0 | 0 |
| 18.86 | 4.705 | 0.6 | 0 | 4 | 1 | 28.14 | 3.171 | 0.6 | 0 | 2 | 4 | 45.73 | 1.984 | 0.8 | 8 | 4 | 3 |
| 19.24 | 4.613 | 2.2 | -1 | 3 | 2 | 28.43 | 3.140 | 1.1 | -2 | 1 | 4 | 45.76 | 1.983 | 1.5 | 8 | 0 | 4 |
| 19.32 | 4.596 | 1.5 | 1 | 3 | 2 | 29.22 | 3.057 | 3.0 | -5 | 3 | 2 | 46.50 | 1.953 | 1.4 | -3 | 4 | 6 |
| 20.37 | 4.359 | 2.2 | -1 | 0 | 3 | 29.46 | 3.032 | 3.4 | 5 | 3 | 2 | 46.69 | 1.945 | 0.5 | 8 | 2 | 4 |
| 20.41 | 4.350 | 1.9 | 0 | 1 | 3 | 29.88 | 2.990 | 0.7 | 3 | 6 | 0 | 46.80 | 1.941 | 0.8 | 3 | 4 | 6 |
| 20.48 | 4.337 | 1.3 | 1 | 0 | 3 | 29.93 | 2.985 | 6.7 | 0 | 5 | 3 | 47.29 | 1.922 | 0.8 | -5 | 8 | 3 |
| 20.74 | 4.282 | 0.8 | -3 | 2 | 2 | 29.95 | 2.984 | 4.1 | -5 | 0 | 3 | 47.48 | 1.915 | 0.6 | -3 | 9 | 3 |
| 20.86 | 4.259 | 2.6 | -2 | 4 | 1 | 30.17 | 2.962 | 0.9 | -1 | 3 | 4 | 47.53 | 1.913 | 0.7 | 5 | 8 | 3 |
| 20.92 | 4.246 | 3.4 | 2 | 4 | 1 | 30.28 | 2.952 | 2.7 | -5 | 1 | 3 | 47.63 | 1.909 | 0.8 | 3 | 9 | 3 |
| 20.94 | 4.242 | 0.7 | 3 | 2 | 2 | 30.30 | 2.949 | 1.9 | 5 | 0 | 3 | 48.55 | 1.875 | 1.4 | -5 | 3 | 6 |

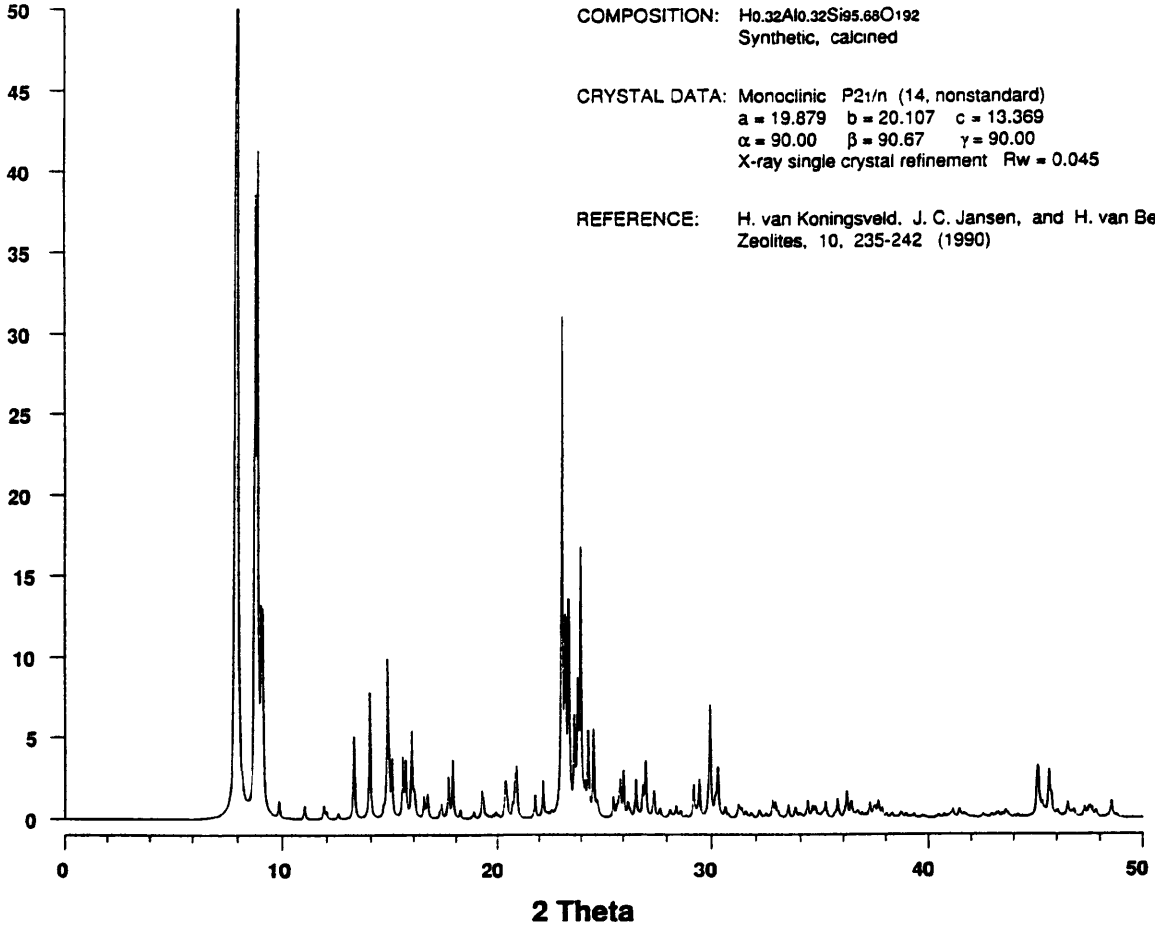


COMPOSITION: $H_{0.32}Al_{0.32}Si_{95.68}O_{192}$
Synthetic, calcined

CRYSTAL DATA: Monoclinic $P2_1/n$ (14, nonstandard)
a = 19.879 b = 20.107 c = 13.369
α = 90.00 β = 90.67 γ = 90.00
X-ray single crystal refinement Rw = 0.045

REFERENCE: H. van Koningsveld, J. C. Jansen, and H. van Bekkum
Zeolites, 10, 235-242 (1990)

# MEL — Calcined ZSM-11

COMPOSITION: $Si_{96}O_{192}$
Synthetic, calcined, dealuminated

CRYSTAL DATA: Tetragonal $I\bar{4}m2$ (119)
a = 20.067 b = 20.067 c = 13.411
α = 90.00 β = 90.00 γ = 90.00
X-ray synchrotron Rietveld refinement Rp = 0.13

REFERENCE: C. A. Fyfe, H. Gies, G. T. Kokotailo, C. Pasztor, H. Strobl, and D. E. Cox
J. Am. Chem Soc. 111, 2470-2474 (1989)

| 2θ | d | I rel | h | k | l | 2θ | d | I rel | h | k | l | 2θ | d | I rel | h | k | l |
|---|---|---|---|---|---|---|---|---|---|---|---|---|---|---|---|---|---|
| 6.23 | 14.190 | 2.4 | 1 | 1 | 0 | 25.56 | 3.485 | 2.6 | 3 | 2 | 3 | 40.96 | 2.203 | 1.0 | 7 | 5 | 2 |
| 7.93 | 11.150 | 100.0 | 1 | 0 | 1 | 26.25 | 3.394 | 2.1 | 5 | 1 | 2 | 43.53 | 2.079 | 1.3 | 8 | 3 | 3 |
| 8.81 | 10.034 | 53.6 | 2 | 0 | 0 | 26.59 | 3.353 | 2.4 | 0 | 0 | 4 | 45.14 | 2.008 | 3.6 | 8 | 0 | 4 |
| 11.87 | 7.458 | 3.9 | 2 | 1 | 1 | 26.65 | 3.345 | 2.8 | 6 | 0 | 0 | 45.19 | 2.007 | 4.7 | 10 | 0 | 0 |
| 13.20 | 6.706 | 9.2 | 0 | 0 | 2 | 27.33 | 3.263 | 0.6 | 1 | 1 | 4 | 46.09 | 1.969 | 0.9 | 8 | 2 | 4 |
| 14.61 | 6.063 | 0.7 | 1 | 1 | 2 | 28.06 | 3.180 | 2.0 | 2 | 0 | 4 | 47.33 | 1.921 | 1.2 | 8 | 5 | 3 |
| 14.80 | 5.986 | 15.4 | 3 | 0 | 1 | 29.17 | 3.062 | 7.8 | 5 | 3 | 2 | 48.57 | 1.875 | 2.4 | 5 | 3 | 6 |
| 15.90 | 5.575 | 8.0 | 2 | 0 | 2 | 29.92 | 2.986 | 9.6 | 5 | 0 | 3 | 49.49 | 1.842 | 0.7 | 3 | 0 | 7 |
| 17.25 | 5.140 | 3.6 | 3 | 2 | 1 | 30.15 | 2.964 | 2.7 | 3 | 1 | 4 | 51.36 | 1.779 | 0.9 | 10 | 5 | 1 |
| 17.68 | 5.017 | 7.1 | 4 | 0 | 0 | 31.25 | 2.862 | 2.2 | 5 | 2 | 3 | 51.77 | 1.766 | 1.1 | 10 | 3 | 3 |
| 18.76 | 4.730 | 1.6 | 3 | 3 | 0 | 31.53 | 2.838 | 0.6 | 5 | 5 | 0 | 53.80 | 1.704 | 0.6 | 5 | 2 | 7 |
| 19.26 | 4.609 | 3.7 | 3 | 1 | 2 | 34.31 | 2.613 | 2.3 | 5 | 5 | 2 | 54.76 | 1.676 | 0.8 | 0 | 0 | 8 |
| 20.35 | 4.363 | 3.2 | 1 | 0 | 3 | 35.16 | 2.552 | 1.4 | 5 | 1 | 4 | 55.03 | 1.669 | 2.2 | 8 | 0 | 6 |
| 22.22 | 4.001 | 0.6 | 2 | 1 | 3 | 35.80 | 2.508 | 1.4 | 8 | 0 | 0 | 55.11 | 1.667 | 0.9 | 8 | 5 | 5 |
| 22.59 | 3.935 | 1.2 | 5 | 1 | 0 | 36.08 | 2.490 | 1.6 | 3 | 0 | 5 | 56.74 | 1.623 | 0.7 | 12 | 0 | 2 |
| 23.01 | 3.865 | 1.2 | 3 | 3 | 2 | 36.13 | 2.486 | 0.8 | 6 | 3 | 3 | 58.91 | 1.568 | 0.9 | 8 | 8 | 4 |
| 23.13 | 3.845 | 52.6 | 5 | 0 | 1 | 37.26 | 2.413 | 1.3 | 7 | 0 | 3 | 59.92 | 1.544 | 0.7 | 8 | 7 | 5 |
| 23.94 | 3.717 | 22.8 | 3 | 0 | 3 | 37.45 | 2.402 | 1.5 | 5 | 3 | 4 | | | | | | |
| 24.80 | 3.590 | 5.1 | 5 | 2 | 1 | 38.93 | 2.313 | 0.8 | 8 | 3 | 1 | | | | | | |

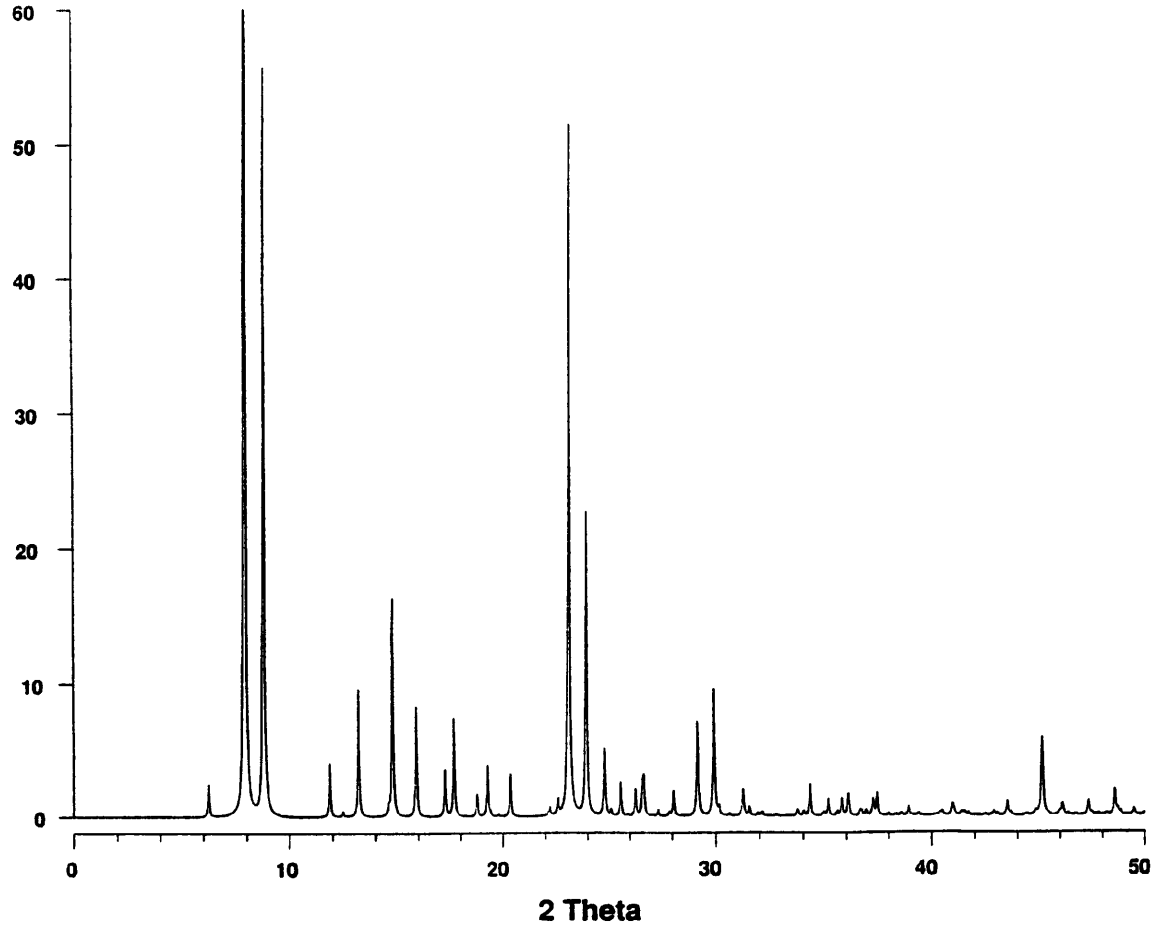

# ZSM-48

Eur. Pat. Appl. 0 015 132 (MOBIL, 1980).

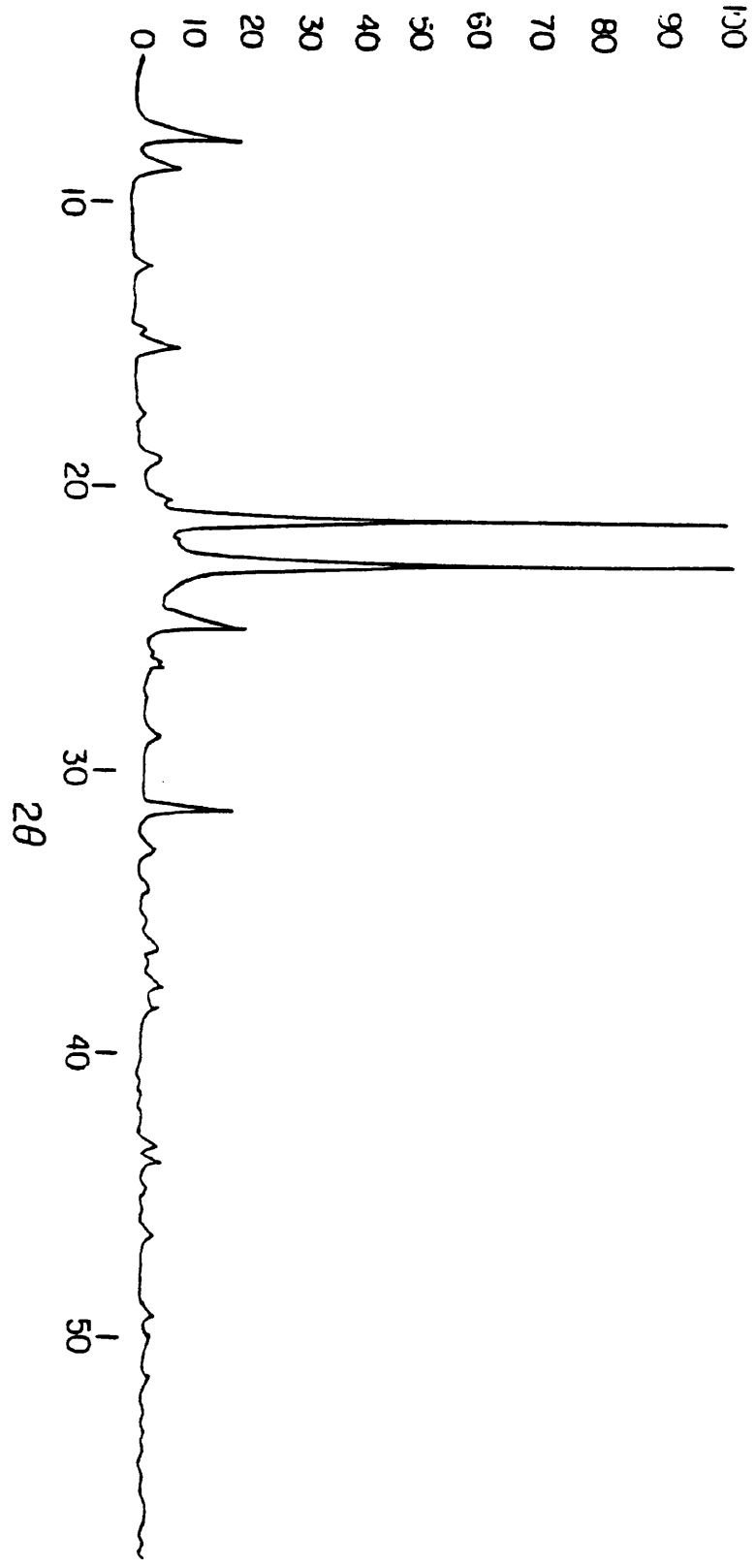


| 2θ | D | INT |
|---|---|---|
| 7.42 | 11.91 | 15 |
| 8.60 | 10.28 | 7 |
| 12.26 | 7.22 | 3 |
| 14.42 | 6.14 | 2 |
| 15.06 | 5.88 | 6 |
| 17.47 | 5.08 | 1 |
| 19.01 | 4.67 | 4 |
| 21.18 | 4.19 | 84 |
| 22.77 | 3.91 | 100 |
| 24.73 | 3.60 | 13 |
| 25.75 | 3.46 | 2 |
| 26.15 | 3.41 | 3 |
| 26.38 | 3.38 | 4 |
| 27.65 | 3.23 | 1 |
| 28.84 | 3.10 | 3 |
| 31.33 | 2.86 | 13 |
| 32.88 | 2.72 | 2 |
| 34.05 | 2.63 | 2 |
| 35.48 | 2.53 | 1 |
| 36.30 | 2.47 | 3 |
| 37.70 | 2.39 | 3 |
| 38.40 | 2.34 | 2 |
| 43.25 | 2.09 | 3 |
| 43.83 | 2.07 | 4 |
| 44.82 | 2.02 | 1 |
| 46.37 | 1.96 | 2 |
| 49.22 | 1.85 | 2 |
| 50.12 | 1.82 | 1 |
| 51.57 | 1.77 | 1 |

# MOR Mordenite

COMPOSITION: $Na_8Al_8Si_{40}O_{96}(H_2O)_{24}$
Challis, Idaho, USA

CRYSTAL DATA: Orthorhombic Cmcm (63)
a = 18.11 b = 20.53 c = 7.528
α = 90.00 β = 90.00 γ = 90.00
X-ray single crystal refinement R = 0.07

REFERENCE: V. Gramlich
PhD Dissertation, ETH, Zurich (1971)
and personal communication

| 2θ | d | I rel | h | k | l |
|---|---|---|---|---|---|
| 6.51 | 13.581 | 100.0 | 1 | 1 | 0 |
| 8.61 | 10.265 | 14.9 | 0 | 2 | 0 |
| 9.77 | 9.055 | 58.5 | 2 | 0 | 0 |
| 13.45 | 6.584 | 38.9 | 1 | 1 | 1 |
| 13.63 | 6.492 | 26.2 | 1 | 3 | 0 |
| 14.59 | 6.071 | 11.6 | 0 | 2 | 1 |
| 15.30 | 5.791 | 9.7 | 3 | 1 | 0 |
| 17.28 | 5.133 | 0.6 | 0 | 4 | 0 |
| 17.59 | 5.042 | 2.6 | 2 | 2 | 1 |
| 18.19 | 4.877 | 3.9 | 1 | 3 | 1 |
| 19.34 | 4.590 | 3.3 | 3 | 1 | 1 |
| 19.61 | 4.528 | 1.1 | 4 | 0 | 0 |
| 19.61 | 4.527 | 20.4 | 3 | 3 | 0 |
| 19.88 | 4.465 | 0.6 | 2 | 4 | 0 |
| 20.95 | 4.241 | 1.3 | 0 | 4 | 1 |
| 21.45 | 4.142 | 4.5 | 4 | 2 | 0 |
| 22.20 | 4.004 | 39.4 | 1 | 5 | 0 |
| 22.92 | 3.880 | 0.7 | 3 | 3 | 1 |
| 23.16 | 3.840 | 14.2 | 2 | 4 | 1 |
| 23.64 | 3.764 | 6.7 | 0 | 0 | 2 |
| 24.53 | 3.629 | 3.6 | 4 | 2 | 1 |
| 24.98 | 3.567 | 1.9 | 5 | 1 | 0 |
| 25.20 | 3.534 | 3.9 | 0 | 2 | 2 |
| 25.63 | 3.476 | 68.5 | 2 | 0 | 2 |
| 26.04 | 3.422 | 4.5 | 0 | 6 | 0 |
| 26.25 | 3.395 | 39.8 | 3 | 5 | 0 |
| 27.09 | 3.292 | 4.2 | 2 | 2 | 2 |
| 27.49 | 3.245 | 11.2 | 1 | 3 | 2 |
| 27.68 | 3.223 | 42.8 | 5 | 1 | 1 |
| 27.87 | 3.201 | 26.5 | 5 | 3 | 0 |
| 28.28 | 3.156 | 3.5 | 3 | 1 | 2 |
| 28.66 | 3.115 | 3.1 | 0 | 6 | 1 |
| 28.85 | 3.095 | 3.3 | 4 | 4 | 1 |
| 30.35 | 2.946 | 5.4 | 2 | 6 | 1 |
| 30.88 | 2.896 | 1.7 | 6 | 2 | 0 |
| 30.90 | 2.894 | 11.2 | 4 | 0 | 2 |
| 30.90 | 2.894 | 7.4 | 3 | 3 | 2 |
| 32.65 | 2.743 | 2.6 | 1 | 5 | 2 |
| 33.15 | 2.703 | 2.8 | 6 | 2 | 1 |
| 33.15 | 2.702 | 5.2 | 1 | 7 | 1 |
| 33.98 | 2.638 | 1.4 | 3 | 7 | 0 |
| 34.97 | 2.566 | 4.8 | 0 | 8 | 0 |
| 35.61 | 2.521 | 0.5 | 4 | 4 | 2 |
| 35.61 | 2.521 | 13.1 | 3 | 5 | 2 |
| 36.39 | 2.469 | 0.9 | 2 | 8 | 0 |
| 36.41 | 2.468 | 1.0 | 1 | 1 | 3 |
| 36.54 | 2.459 | 5.2 | 8 | 4 | 1 |
| 36.86 | 2.439 | 0.9 | 5 | 3 | 2 |
| 36.86 | 2.438 | 1.8 | 2 | 8 | 2 |
| 36.54 | 2.336 | 0.7 | 1 | 3 | 3 |
| 39.54 | 2.279 | 1.0 | 5 | 7 | 0 |
| 40.40 | 2.233 | 2.0 | 4 | 8 | 0 |
| 41.27 | 2.186 | 1.6 | 2 | 4 | 3 |
| 41.67 | 2.168 | 0.9 | 6 | 6 | 1 |
| 41.82 | 2.160 | 1.7 | 3 | 7 | 2 |
| 44.11 | 2.053 | 4.7 | 0 | 10 | 0 |
| 44.11 | 2.053 | 0.8 | 3 | 9 | 1 |
| 44.13 | 2.052 | 0.6 | 5 | 1 | 3 |
| 44.51 | 2.036 | 3.2 | 7 | 3 | 2 |
| 44.92 | 2.018 | 4.6 | 4 | 4 | 3 |
| 45.42 | 1.997 | 2.8 | 8 | 4 | 1 |
| 45.95 | 1.975 | 0.7 | 5 | 3 | 3 |
| 45.96 | 1.975 | 0.6 | 2 | 6 | 3 |
| 46.45 | 1.955 | 6.4 | 6 | 8 | 0 |
| 46.58 | 1.950 | 0.6 | 5 | 7 | 2 |
| 46.95 | 1.935 | 1.4 | 9 | 1 | 1 |
| 47.07 | 1.930 | 0.8 | 9 | 3 | 0 |
| 47.34 | 1.920 | 4.8 | 4 | 8 | 2 |
| 47.97 | 1.896 | 0.6 | 6 | 2 | 3 |
| 47.98 | 1.896 | 1.0 | 1 | 7 | 3 |
| 48.09 | 1.892 | 0.8 | 7 | 5 | 2 |
| 48.36 | 1.882 | 8.6 | 0 | 0 | 4 |
| 48.70 | 1.870 | 2.1 | 5 | 9 | 1 |
| 48.86 | 1.864 | 1.1 | 1 | 1 | 4 |
| 50.39 | 1.811 | 4.6 | 10 | 0 | 0 |
| 50.64 | 1.803 | 1.0 | 1 | 11 | 1 |
| 50.89 | 1.794 | 6.8 | 7 | 1 | 3 |
| 52.67 | 1.738 | 0.9 | 4 | 0 | 4 |
| 53.11 | 1.725 | 1.6 | 7 | 7 | 2 |
| 53.33 | 1.718 | 1.8 | 9 | 3 | 2 |
| 53.48 | 1.713 | 0.5 | 4 | 2 | 4 |
| 53.82 | 1.703 | 0.8 | 1 | 5 | 4 |
| 54.02 | 1.698 | 1.9 | 8 | 8 | 0 |
| 54.38 | 1.687 | 1.6 | 5 | 7 | 3 |
| 55.04 | 1.668 | 0.7 | 7 | 9 | 1 |
| 55.05 | 1.668 | 2.0 | 0 | 12 | 1 |
| 55.86 | 1.646 | 0.6 | 3 | 5 | 4 |
| 56.74 | 1.622 | 2.6 | 5 | 3 | 4 |
| 57.71 | 1.597 | 3.9 | 8 | 4 | 3 |
| 59.34 | 1.557 | 0.7 | 0 | 12 | 2 |
| 59.76 | 1.548 | 3.9 | 8 | 8 | 2 |

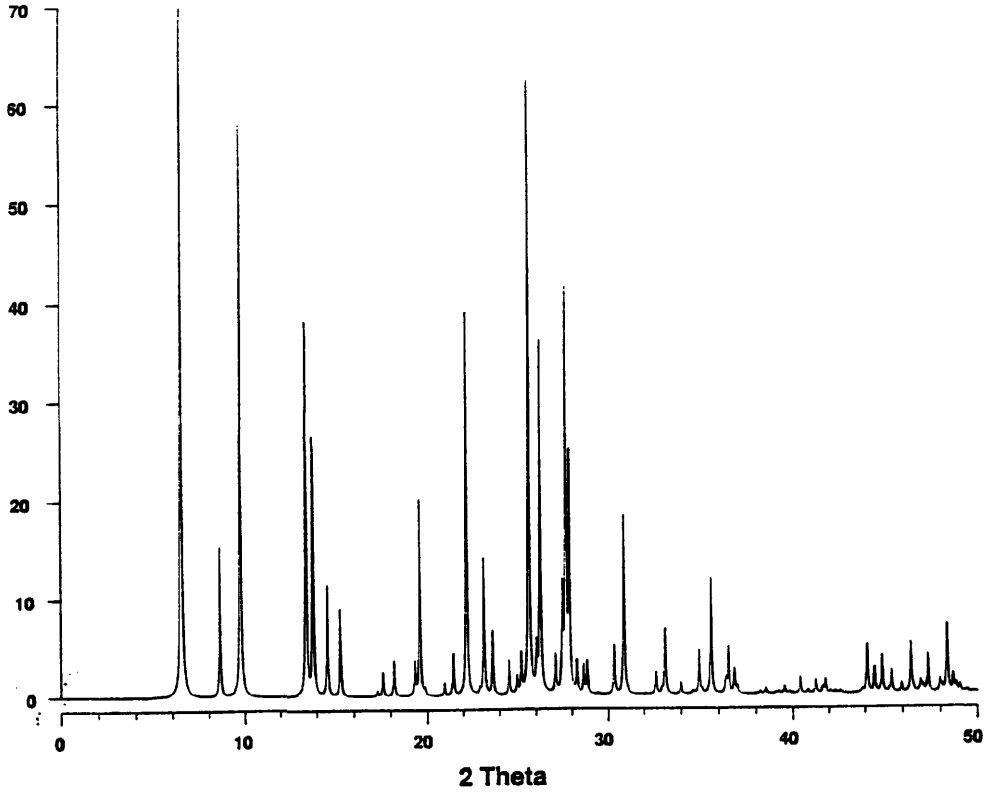

# FER Ferrierite

COMPOSITION: $Na_{1.5}Mg_2Al_{5.5}Si_{30.5}O_{72}(H_2O)_{18}$
Kamloops Lake, British Columbia

CRYSTAL DATA: Orthorhombic Immm (71)
a = 19.16 b = 14.13 c = 7.49
α = 90.00 β = 90.00 γ = 90.00
X-ray single crystal refinement R = 0.11

REFERENCE: P. A. Vaughan
Acta Cryst. 21, 983-990 (1966)

| 2θ | d | I rel | h | k | l |
|---|---|---|---|---|---|
| 7.78 | 11.370 | 46.1 | 1 | 1 | 0 |
| 9.23 | 9.578 | 100.0 | 2 | 0 | 0 |
| 12.53 | 7.063 | 9.8 | 0 | 2 | 0 |
| 12.89 | 6.875 | 14.4 | 1 | 0 | 1 |
| 13.38 | 6.617 | 9.1 | 0 | 1 | 1 |
| 15.23 | 5.819 | 22.6 | 3 | 1 | 0 |
| 15.59 | 5.685 | 2.7 | 2 | 2 | 0 |
| 17.87 | 4.963 | 4.7 | 1 | 2 | 1 |
| 18.53 | 4.789 | 2.2 | 4 | 0 | 0 |
| 19.41 | 4.573 | 1.5 | 1 | 3 | 0 |
| 22.21 | 4.003 | 23.8 | 3 | 2 | 1 |
| 22.30 | 3.986 | 7.1 | 0 | 3 | 1 |
| 22.43 | 3.964 | 19.0 | 4 | 2 | 0 |
| 22.92 | 3.879 | 13.2 | 4 | 1 | 1 |
| 23.47 | 3.790 | 15.7 | 3 | 3 | 0 |
| 23.76 | 3.744 | 3.4 | 0 | 0 | 2 |
| 24.07 | 3.698 | 6.2 | 5 | 1 | 0 |
| 25.04 | 3.557 | 14.1 | 1 | 1 | 2 |
| 25.22 | 3.532 | 26.2 | 0 | 4 | 0 |
| 25.54 | 3.487 | 32.9 | 3 | 0 | 2 |
| 26.13 | 3.411 | 5.6 | 5 | 0 | 1 |
| 26.91 | 3.314 | 6.5 | 2 | 4 | 0 |
| 26.95 | 3.308 | 0.6 | 0 | 2 | 2 |
| 27.95 | 3.193 | 1.1 | 6 | 0 | 0 |
| 28.33 | 3.151 | 1.4 | 1 | 4 | 1 |
| 28.34 | 3.149 | 12.0 | 3 | 1 | 2 |
| 28.55 | 3.127 | 1.6 | 2 | 2 | 2 |
| 29.07 | 3.071 | 9.4 | 5 | 2 | 1 |
| 30.07 | 2.972 | 5.7 | 5 | 3 | 0 |
| 30.30 | 2.950 | 2.2 | 4 | 0 | 2 |
| 30.87 | 2.897 | 4.5 | 1 | 3 | 2 |
| 31.10 | 2.875 | 0.6 | 6 | 1 | 1 |
| 31.47 | 2.842 | 0.7 | 4 | 4 | 0 |
| 32.91 | 2.722 | 3.3 | 4 | 2 | 2 |
| 33.35 | 2.687 | 0.8 | 7 | 1 | 0 |
| 33.91 | 2.644 | 3.4 | 0 | 5 | 1 |
| 34.08 | 2.631 | 0.6 | 5 | 1 | 2 |
| 34.72 | 2.584 | 2.7 | 3 | 5 | 0 |
| 34.91 | 2.570 | 0.6 | 7 | 0 | 1 |
| 34.92 | 2.569 | 1.0 | 0 | 4 | 2 |
| 36.04 | 2.492 | 0.6 | 6 | 3 | 1 |
| 36.20 | 2.482 | 1.1 | 2 | 4 | 2 |
| 37.00 | 2.429 | 2.6 | 6 | 3 | 2 |
| 38.03 | 2.366 | 3.0 | 7 | 3 | 0 |
| 38.54 | 2.336 | 0.6 | 1 | 2 | 3 |
| 38.92 | 2.314 | 1.9 | 4 | 5 | 1 |
| 39.82 | 2.264 | 1.1 | 4 | 4 | 2 |
| 40.05 | 2.252 | 0.7 | 8 | 1 | 1 |
| 40.26 | 2.240 | 0.7 | 1 | 5 | 2 |
| 41.28 | 2.187 | 0.6 | 4 | 1 | 3 |
| 42.04 | 2.149 | 1.6 | 2 | 3 | 3 |
| 42.67 | 2.119 | 0.5 | 3 | 5 | 1 |
| 42.80 | 2.113 | 2.4 | 4 | 5 | 0 |
| 44.24 | 2.047 | 1.1 | 9 | 0 | 1 |
| 44.50 | 2.036 | 0.6 | 5 | 5 | 1 |
| 45.22 | 2.005 | 2.9 | 5 | 2 | 3 |
| 45.31 | 2.002 | 1.7 | 6 | 4 | 2 |
| 45.78 | 1.982 | 1.1 | 8 | 4 | 0 |
| 46.16 | 1.966 | 1.3 | 9 | 2 | 1 |
| 46.61 | 1.949 | 2.0 | 0 | 7 | 1 |
| 46.84 | 1.940 | 1.7 | 9 | 3 | 0 |
| 47.24 | 1.924 | 2.0 | 3 | 7 | 0 |
| 48.63 | 1.872 | 5.5 | 0 | 0 | 4 |
| 50.26 | 1.815 | 0.9 | 6 | 3 | 3 |
| 51.16 | 1.786 | 2.4 | 5 | 7 | 0 |
| 51.19 | 1.784 | 2.4 | 7 | 2 | 3 |
| 51.26 | 1.782 | 0.7 | 3 | 1 | 4 |
| 51.50 | 1.775 | 1.4 | 8 | 5 | 1 |
| 51.67 | 1.769 | 1.0 | 1 | 7 | 2 |
| 53.19 | 1.722 | 0.8 | 9 | 3 | 2 |
| 54.97 | 1.670 | 0.7 | 5 | 1 | 4 |
| 55.36 | 1.660 | 1.0 | 3 | 8 | 1 |
| 55.46 | 1.657 | 0.8 | 4 | 3 | 0 |
| 55.56 | 1.654 | 0.8 | 0 | 4 | 4 |
| 56.33 | 1.633 | 0.7 | 11 | 3 | 0 |
| 56.67 | 1.624 | 1.0 | 7 | 7 | 0 |
| 56.85 | 1.620 | 1.0 | 9 | 0 | 3 |
| 57.06 | 1.614 | 1.0 | 6 | 5 | 3 |
| 57.76 | 1.598 | 0.9 | 12 | 0 | 0 |
| 58.24 | 1.584 | 0.5 | 5 | 3 | 4 |
| 59.08 | 1.564 | 0.5 | 5 | 6 | 3 |
| 59.71 | 1.549 | 1.0 | 2 | 7 | 3 |

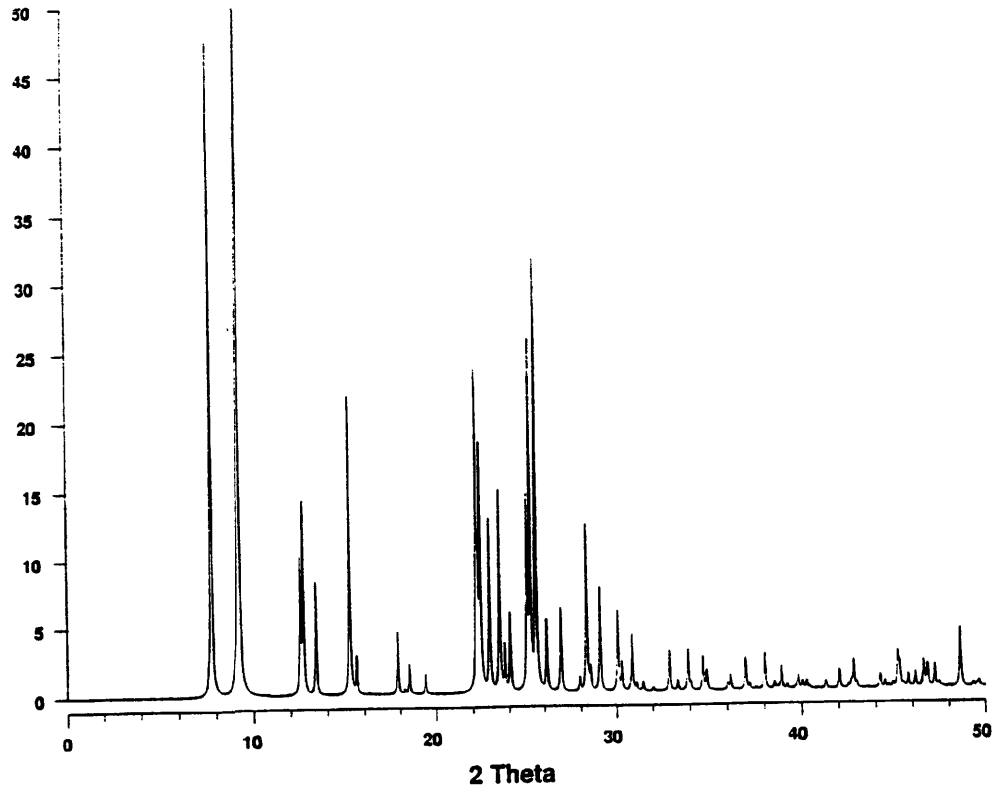

# APPENDIX IV

## Catalysis Calculations

The following notes summarise the conversion and selectivity relationships used in chapter 5.

1. **Percentage conversion** of the liquid feed consisting of p-xylene (PX) and methanol (MeOH),

$$= \frac{\text{Moles C in (PX+MeOH) - Moles C out (PX+MeOH)}}{\Sigma \text{ Moles C feed as PX and MeOH}} \times 100$$

2. **Percentage Yield** of a particular component product P was based on the conversion of PX and MeOH as follows,

$$= \frac{\text{Moles C as P out}}{\text{Moles C of feed converted}} \times 100$$

3. **Percentage Selectivity** of P for this particular study was related to the yields of aromatic liquid products excluding the xylene contribution. Therefore the percentage selectivity for a particular component, P, can be represented as follows,

$$= \frac{\text{Yield of P (mole\%)}}{\Sigma \text{ Yields C6 to C10 (mole\%)}} \times 100$$

# APPENDIX V

## Calculation of the Molar Extinction Coefficient

One experimental form of the Beer-Lambert law for light absorption is:

$$A = (n.l)^{-1}. f \log (Ii/If)\, dv \qquad (1)$$

where

A = molar absorption extinction coefficient ($m.mol^{-1}$),
n = moles of absorbing molecules per unit volume ($mol.m^{-3}$),
l = sample thickness (m)
Ii, If = initial and final light intensities
$v$ = radiation wavenumber ($m^{-1}$)

Equation 1 can be rewritten as:

$$A.M_H = S$$

where

$M_H$ = moles $H_2$ adsorbed per unit weight ($mol.g^{-1}$),
$S = (W/A)^{-1}. f \log (Ii/If)\, dv$ ($m.g^{-1}$),
W = weight of zeolite disc (g),
a = disc cross-sectional area ($m^2$).

To make further progress the adsorption of $H_2$ under the experimental conditions used, is assumed to follow a Langmuir-type adsorption, at which point the following relationship is valid,

$$S = A.M_H = A.K.M_{AF}.P\,(1 + KP)^{-1} \qquad (2)$$

where

K = adsorption equilibrium constant,
$M_{AF}$= moles of framework aluminium per unit weight ($mol.g^{-1}$),
P = equilibrium $H_2$ pressure (Pa).

According to equation 2 plots of P/S versus P should be linear since,

$$P/S = 1(A.K.M_{AF})^{-1} + P.(A.M_{AF})^{-1}.$$

For a series of pressure measurements the combined integrated $H_2$ peak areas were obtained for the 4129 and 4108$cm^{-1}$ bands for a range of zeolites of known disc weight and cross-sectional area. From these experimental values plots were obtained of P/S versus P this gives a series of straight lines with slopes = $(A.M_{AF})^{-1}$. Since $M_{AF}$ is known from chemical analysis, A can be calculated from the plot.